Crystal Plasticity Modeling of
Fully Lamellar Titanium Aluminide Alloys

Vom Promotionsausschuss der
Technischen Universität Hamburg
zur Erlangung des akademischen Grades

Doktor-Ingenieur (Dr.-Ing.)

genehmigte Dissertation

von
Jan Eike Schnabel
(geb. Butzke)

aus
Neumünster

2018

Acknowledgments

Crystal Plasticity Modeling of Fully Lamellar Titanium Aluminide Alloys

Jan Eike Schnabel

Abstract

In the present thesis, a thermomechanically coupled, defect density based crystal plasticity model is presented. This model accounts for the evolution of dislocation densities and twinned volume fractions on different slip and twinning systems during plastic deformation and thermal recovery. Considering the evolution of dislocation densities and twinned volume fractions allows a physics based formulation of the work hardening model and enables a physically meaningful representation of dissipation and stored energy of cold work in the applied thermomechanical framework. In the course of this thesis, the presented crystal plasticity model was applied to investigate several aspects of the plastic deformation behavior of fully lamellar titanium aluminide alloys. After calibrating the work hardening model to fit experimental results, it was successfully used to relate specifics of the macroscopic stress-strain response of fully lamellar titanium aluminides to the work hardening interactions on the microscale. By combining numerical studies and experimental findings from literature, it was further possible to identify and consequently model the relative contribution of the different coexisting microstructural interfaces to the macroscopic yield strength. With this microstructure sensitive model formulation, the influence of the microstructural parameters on the inhomogeneous microplasticity of fully lamellar titanium aluminides was studied. Due to its defect density based formulation, the model enabled trends in the static recovery behavior to be investigated. Finally, the model was extended in order to account for the anomalous dependence of the yield strength of fully lamellar titanium aluminides on temperature.

Kristallplastizitätsmodellierung lamellarer Titanaluminidlegierungen

Jan Eike Schnabel

Zusammenfassung

In der vorliegenden Arbeit wird ein thermomechanisch gekoppeltes, defektdichtebasiertes Kristallplastizitätsmodell vorgestellt. Dieses Modell berücksichtigt die Entwicklung von Versetzungsdichten und Zwillingsvolumenfraktionen auf verschiedenen Gleit- und Zwillingssystemen in Folge von plastischer Verformung und Erholungsvorgängen. Die Berücksichtigung von Versetzungsdichten und Zwillingsvolumenfraktionen erlaubt eine physikalisch motivierte Modellierung des Verfestigungsverhaltens und ermöglicht eine physikalisch sinnvolle Darstellung der Dissipation und der in Form von Defekten im Kristallgitter gespeicherten Energie im Rahmen der hier angewandten thermomechanischen Modellierung. Im Rahmen dieser Arbeit wurde das vorgestellte Kristallplastizitätsmodell angewendet um verschiedene Aspekte des plastischen Verformungsverhaltens lamellarer Titanaluminidlegierungen zu untersuchen. Nach der Kalibrierung des Verfestigungsmodells gegen experimentelle Ergebnisse wurde dieses erfolgreich angewendet um charakteristische Merkmale der makroskopischen Spannungs-Dehnungsantwort lamellarer Titanaluminide mit den Verfestigungsinteraktionen auf der Mikroskala in Beziehung zu setzen. Durch die Kombination numerischer Studien und experimenteller Ergebnisse aus der Literatur war es außerdem möglich den relativen Beitrag der verschiedenen koexistierenden mikrostrukturellen Grenzflächen zur makroskopischen Fließspannung zu identifizieren und folglich zu modellieren. Mit dieser mikrostruktursensitiven Modellformulierung wurde der Einfluss der mikrostrukturellen Parameter auf die inhomogene Mikroplastizität von lamellaren Titanaluminiden untersucht. Aufgrund der defektdichtebasierten Formulierung ermöglichte das Modell die Untersuchung von Trends im statischen Erholungsverhalten. Schließlich wurde das Modell um die Temperaturanomalie des Fließpunkts lamellar Titanaluminidlegierungen erweitert.

Contents

List of symbols

A_α	dislocation accumulation coefficient of slip system α
$A_{\alpha,0}$	reference accumulation coefficient of slip system α
a	unit cell base length
$\boldsymbol{b}$	Burgers vector
b_α	magnitude of the Burgers vector of slip system α
$\boldsymbol{C}$	right Cauchy-Green tensor
$\boldsymbol{C}_E$	right Cauchy-Green tensor in intermediate configuration
$C_{\beta\alpha}$	hardening interaction coefficient
c	height of unit cell
c_p	heat capacity
D	grain size
$\mathcal{D}$	dissipation
$\mathcal{D}_{\text{therm}}$	thermal part of the dissipation
$\mathcal{D}_{\text{mech}}$	mechanical part of the dissipation
E	Young's modulus
$\boldsymbol{F}$	deformation gradient
$\boldsymbol{F}_E$	elastic part of the deformation gradient
$\boldsymbol{F}_P$	plastic part of the deformation gradient
f	total twinned volume fraction
f_β	twinned volume fraction on twinning system β
G	shear modulus
g_β	twinning rate on twinning system β
$h_{\alpha\beta}$	hardening interaction coefficient
$h_{\beta\beta'}$	hardening interaction coefficient
J	Jacobian
J_E	Jacobian in intermediate configuration
K	bulk modulus
K_C	Hall-Petch coefficient for colony boundary strengthening
K_D	Hall-Petch coefficient for γ domain boundary strengthening
K_L	Hall-Petch coefficient for γ/γ lamella boundary strengthening
K_{α_2}	Hall-Petch coefficient for γ/α_2 lamella boundary strengthening
k_D	resolved Hall-Petch coefficient for γ domain boundary strengthening
k_C	resolved Hall-Petch coefficient for colony boundary strengthening
k_L	resolved Hall-Petch coefficient for lamella boundary strengthening
k_B	Boltzmann constant
$\boldsymbol{L}$	velocity gradient
$\boldsymbol{L}_E$	elastic part of the velocity gradient
$\boldsymbol{L}_P$	plastic part of the velocity gradient
$\boldsymbol{M}_E$	Mandel stress
N^{tw}	number of twinning systems
N^{sl}	number of slip systems
$\boldsymbol{n}$	slip/twinning plane normal

$\boldsymbol{n}_\alpha$	slip plane normal of slip system α
$\boldsymbol{n}_\beta$	twinning plane normal of twinning system β
n	strain rate sensitivity exponent
p_α	dislocation accumulation exponent
$\boldsymbol{Q}$	heat flux vector
Q_R	activation energy for static recovery
q_α	recovery exponent
$q_{\alpha\alpha\prime}$	hardening interaction coefficient between slip systems
q_n	plastic internal variables
$\boldsymbol{R}$	rotation matrix
R_α	recovery rate of slip systems α
$R_{\alpha,0}$	reference recovery rate of slip systems α
r	external heat supply per unit mass
r_i	inner radius of hexagon
$\boldsymbol{S}$	2$^{\text{nd}}$ Piola-Kirchhoff stress
$\boldsymbol{S}_E$	2$^{\text{nd}}$ Piola-Kirchhoff stress in intermediate configuration
$\boldsymbol{s}$	slip/twinning direction
$\boldsymbol{s}_\alpha$	slip direction of slip system α
$\boldsymbol{s}_\beta$	twinning direction of twinning system β
$\boldsymbol{U}_{\text{RVE}}$	matrix of the displacements of the RVE's master nodes
$\boldsymbol{U}_{\text{dummy}}$	matrix of the averaged displacements of the dummy element
$\boldsymbol{u}$	vector of nodal displacements
u	nodal displacement
V_{α_2}	volume fraction of α_2 phase
V_γ	volume fraction of γ phase
$\boldsymbol{X}$	position of material point in the reference configuration
$\boldsymbol{x}$	position of material point in the current configuration
α_t	thermal expansion coefficient
$\gamma_M^{\text{I--III}}$	matrix orientation variants of the γ phase
$\gamma_T^{\text{I--III}}$	twin orientation variants of the γ phase
γ_T	twinning shear
$\overline{\gamma}_\alpha$	accumulated shear on slip system α
$\overline{\gamma}_\beta$	accumulated shear on twinning system β
$\Delta\tau_\alpha^Y$	work hardening increment of slip system α
$\Delta\tau_{\alpha,s|s}^Y$	work hardening increment of slip system α due to slip-slip interaction
$\Delta\tau_{\alpha,s|t}^Y$	work hardening increment of slip system α due to slip-twin interaction
$\Delta\tau_\beta^T$	work hardening increment of twinning system β
$\Delta\tau_{\beta,t|t}^T$	work hardening increment of twinning system β due to twin-twin interaction
$\Delta\tau_{\beta,t|s}^T$	work hardening increment of twinning system β due to twin-slip interaction
Δt	time interval
$\Delta\gamma$	shear increment
ε	internal energy
ε_x	strain in x direction
ε_y	strain in y direction
ε_z	strain in z direction
ζ	randomization constant
η	entropy
θ	absolute temperature
κ	thermal conductivity

λ	Lamé constant
λ_C	colony size
λ_L	lamella thickness
λ_L^γ	γ lamella thickness
$\lambda_L^{\alpha_2}$	α_2 lamella thickness
λ_D	domain size
λ_{α_2}	spacing of α_2 lamellae
μ	Lamé constant
ν	Poisson's ratio
ν_α	slip shear rate on slip systems α
ν_0	reference shear rate
ξ	internal entropy production
$\rho_{\alpha,0}^{\text{dis}}$	initial dislocation density in undeformed state
ρ_α^{dis}	dislocation density on slip system α
ρ^{dis}	total dislocation density
$\rho_{\alpha,\text{sat}}^{\text{dis}}$	saturation dislocation density
$\rho_{\alpha,\text{min}}^{\text{dis}}$	minimum dislocation density for static recovery
$\rho_{\text{ref}}^{\text{dis}}$	reference dislocation density
ρ_0	density in reference configuration
$\boldsymbol{\sigma}$	Cauchy stress tensor
$\sigma_{0.2}$	0.2% yield stress
σ_R	0.2% yield stress for $D \to \infty$
τ_{twin}	critical resolved shear stress of twinning systems in the γ phase
τ_{ordinary}	critical resolved shear stress of ordinary slip systems in the γ phase
τ_{super}	critical resolved shear stress of super slip systems in the γ phase
$\tau_{\text{prismatic}}$	critical resolved shear stress of prismatic slip systems in the α_2 phase
τ_{basal}	critical resolved shear stress of basal slip systems in the α_2 phase
$\tau_{\text{pyramidal}}$	critical resolved shear stress of pyramidal slip systems in the α_2 phase
τ	resolved shear stress/Schmid stress
τ_α	resolved shear stress on slip system α
τ_β	resolved shear stress on twinning system β
τ_α^Y	current strength of slip system α
τ_β^T	current strength of twinning system β
$\tau_{\alpha,0}^Y$	initial strength of slip system α
$\tau_{\beta,0}^T$	initial strength of twinning system β
$\tau_{\text{long},0}$	initial strength of longitudinal slip and twinning systems
$\tau_{\text{mix},0}$	initial strength of mixed slip and twinning systems
$\tau_{\text{trans},0}$	initial strength of transversal slip and twinning systems
$\tau_{\text{mix},0}^{\alpha_2}$	initial strength of mixed slip systems in α_2 phase
$\tau_{\text{trans},0}^{\alpha_2}$	initial strength of transversal slip systems in α_2 phase
$\tau_{\text{long},0}^\gamma$	initial strength of longitudinal slip and twinning systems in γ phase
$\tau_{\text{mix},0}^\gamma$	initial strength of mixed slip systems in γ phase
$\tau_{\text{trans},0}^\gamma$	initial strength of transversal slip and twinning systems in γ phase
$\tau_{\alpha,R}$	lattice resistance to slip
$\tau_{\beta,R}$	lattice resistance to twinning
τ_R	lattice resistance to slip and twinning in γ phase
$\boldsymbol{\varphi}$	function of motion
φ	loading angle of polysynthetically twinned crystals
φ_i	orientation angle of lamella plane in a colony

ψ	Helmholtz free energy
ψ_E	thermo-elastic part of the Helmholtz free energy
ψ_P	thermo-plastic part of the Helmholtz free energy

1 Introduction and research objectives

The search for new lightweight structural materials for advanced high temperature applications strongly promoted research on intermetallic aluminide alloys over the last decades [5]. These alloys consist of one or more of the intermetallic phases (hence the attribute *inter-metallic*) that occur in the Ni–Al, Ti–Al or Fe–Al phase diagrams for high aluminum contents of several 10% (hence the name *aluminides*) [6]. Although nickel aluminides, titanium aluminides and iron aluminides each have their own specific properties [5, 6], all intermetallic aluminide alloys share some common features like, e.g., their beneficial combination of a low density and promising thermomechanical properties which renders them interesting for high temperature lightweight applications [5, 7]. On the other hand, intermetallic aluminide alloys usually suffer from their inherent brittleness which causes challenges in manufacturing and thus complicates their implementation to industrial applications [5]. Among the most prominent intermetallic aluminide material systems – i.e. the mentioned nickel aluminides, iron aluminides and titanium aluminides – so far only titanium aluminide alloys reached a sufficient state of development for large scale industrial applications [5–10].

1.1 General introduction to γ based titanium aluminides

Most technically relevant titanium aluminides are two phase alloys that mainly consist of the intermetallic γ phase (TiAl) but also contain a minor volume fraction of the intermetallic α_2 phase (Ti_3Al) [11]. These γ based titanium aluminide alloys – in the following simply referred to as γ TiAl alloys – exhibit compositions in the range of

$$Ti - (42 - 49)Al - (0 - 10)X(at.\%), \tag{1.1}$$

where X are ternary alloying elements like, e.g., Cr, Nb, V, Mn, Ta, Mo, W, Si, C and B [11]. Their high aluminum content results in a low density (3.8-4.2 g/cm^3) and a good oxidation resistance [5, 6, 9, 12, 13]. Further, γ TiAl alloys are characterized by a high melting point, high specific strengths and Young's modulus, and a (compared to conventional Ti alloys) good resistance to titanium fire [5, 9, 12]. Figure 1.1 illustrates the specific yield strength of TiAl alloys over temperature compared to competing structural materials.

1.1.1 Industrial application potential

Due to their comparatively low density paired with good thermomechanical properties, γ TiAl alloys were early on identified as potential materials to replace titanium (≈ 4.4 g/cm^3) and nickel based alloys (8-8.5 g/cm^3) in high temperature lightweight applications, e.g., in turbo and aero engines. The 1st generation alloys (Ti-48Al-1V-(0.1C) [15]) and 2nd generation alloys (Ti-(45-48)Al-(1-3)X-(2-5)Y-(<1)Z where X=Cr, Mn, V; Y=Nb, Ta, W, Mo; Z= Si, B, C [9]) were, however, limited to service temperatures of 650°C–750°C due to issues with oxidation [5] and limited creep resistance [9]. With the development of the 3rd generation (i.e. 5-10% Nb containing) γ TiAl alloys, the service temperature range was further increased, ultimately paving the way for applications with temperatures of up to 750°C–850°C [5, 7, 9, 10, 13].
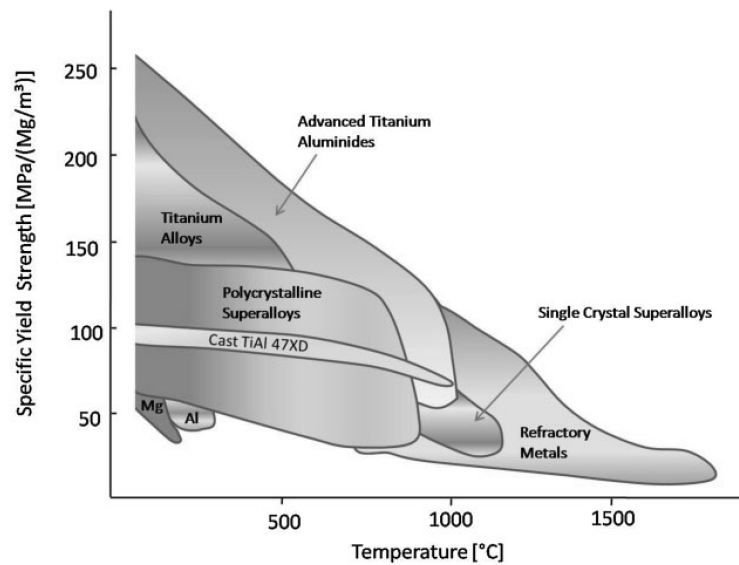
Figure 1.1. Density normalized yield strength of different structural metallic materials as a function of temperature. Reproduced with permission from [14]. Copyright ©2013 Wiley-VCH Verlag GmbH & Co. KGaA.

While the recent implementation as structural materials for turbine blades in aircraft engines probably is the most prominent example of their industrial use[1], γ TiAl alloys are suitable for a variety of other high temperature applications like, e.g., exhaust valves and turbo charger wheels in combustion engines [6, 8–10, 15, 16] or blade disks and casings in compressors and turbines of aircraft engines [8].

Compared to conventional materials, γ TiAl alloys have the potential to reduce the weight of such components by 20–50% [5]. Reducing the weight of components with high rotational velocities (e.g. turbine blades or turbo charger wheels) or high accelerations (e.g. exhaust valves) further opens up possibilities for secondary weight reduction in the supporting structure. Thus, the effective weight saving potential by the implementation of γ TiAl alloys in such applications is even higher.

1.1.2 Microstructures in γ TiAl alloys

Two phase γ TiAl alloys can be processed to different microstructures which all have their own mechanical characteristics [11, 17]. Following [17], the possible microstructures can be categorized into near γ, duplex, nearly lamellar and fully lamellar microstructures. Figure 1.2 shows the mid-section of the binary Ti–Al phase diagram and indicates the temperature regions from which the respective microstructures can be obtained by quenching.

Among the possible microstructures in γ TiAl alloys, duplex and (nearly/fully) lamellar microstructures have the highest technical relevance [12] and are thus most commonly investigated. While duplex microstructures show an improved ductility as compared to lamellar microstructures, they suffer from a low fracture toughness and a low creep resistance [9, 17]. Although exhibiting a poor ductility, TiAl alloys with fully lamellar microstructures are superior when it comes to creep or fatigue resistance and fracture toughness [6, 9, 12, 13, 17, 18] and, thus, are in the focus of current research and this thesis.

---

[1] Aircraft engines with γ TiAl low pressure turbine blades: General electrics – GEnx[TM]; Pratt & Whitney – PW1000G[TM]; CFM International – LEAP[TM] [10]
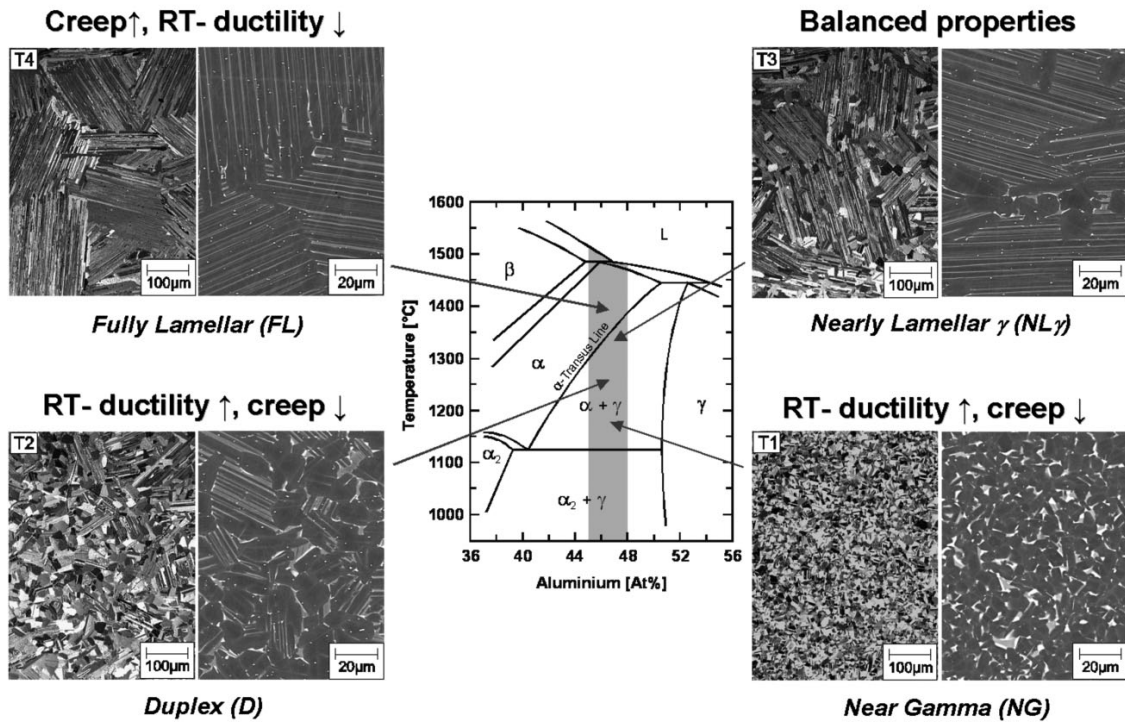
Figure 1.2. Mid-section of the Ti–Al phase diagram with different microstructures that can be obtained in two phase γ TiAl alloys. The microstructures are categorized into *near γ* (equiaxed γ grains with a small volume fraction of α_2 grains), *duplex* (globular γ grains and lamellar ($\alpha_2 + \gamma$) colonies), *nearly lamellar* (lamellar ($\alpha_2 + \gamma$) colonies and a small volume fraction of γ grains) and *fully lamellar* (only lamellar ($\alpha_2 + \gamma$) colonies). The left parts of the microstructural images are light-optical microscope images, whereas the right halves are scanning electron microscopy (SEM) images in which the γ phase appears dark and the α_2 phase shows a light contrast. Reproduced with permission from [14]. Copyright ©2013 Wiley-VCH Verlag GmbH & Co. KGaA.

Due to their promising combination of properties for the intended applications, fully lamellar TiAl alloys attract considerable research attention in the fields of alloy development and process optimization as a result of which their formability and processability is continuously improved (see, e.g., [9, 10, 15, 19, 20]). Further, the strong effect of the dense arrangement of microstructural interfaces in fully lamellar TiAl alloys on their macroscopic properties like, e.g., their yield strength, their creep and fatigue behavior or their fracture mechanics was studied extensively[2]. These studies aimed to better understand the complex micromechanics of fully lamellar TiAl in order to ultimately identify combinations of microstructural parameters that yield the most balanced properties for certain applications. In order to support the understanding of the various micromechanical interactions in fully lamellar TiAl and their influence on the macroscopic material's behavior, numerical simulations – especially in the field of crystal plasticity – proved helpful in the past (see Chapter 3 for details).

---

[2]As the experimental studies are too numerous to be discussed here, the reader is referred to [11] for a comprehensive evaluation of the available experimental studies and the corresponding findings.

1.2 Research objectives

Despite the advances in understanding and modeling the (micro)mechanics of fully lamellar TiAl alloys, there are still unresolved issues especially when it comes to predicting the macroscopic mechanical behavior from microstructural parameters (e.g. colony size or lamella thickness, see Figure 1.2). The present thesis is dedicated to address some of these issues by providing a computational model of the deformation behavior of fully lamellar TiAl alloys. This model is supposed to capture

- the microstructure sensitive yield strength between room and operating temperature,

- the work hardening behavior with particular emphasis on the interactions between slip and twinning systems and

- the recovery of work hardening during annealing at elevated temperatures.

These objectives cover different topics of engineering interest. First of all, the yield strength is the most important property for dimensioning structural components. In fully lamellar TiAl, the yield strength is dominated by the dense arrangement of microstructural interfaces. Thus, determining the yield strength of fully lamellar TiAl as a function of microstructural parameters and temperature is by no means trivial.

The work hardening behavior, on the other hand, is of significant importance in all technical applications and processes that incorporate considerable plastic deformation. Generally two types of respective applications can be distinguished: the ones that aim to benefit from the introduced work hardening (e.g. surface treatments like shot peening [21]) and the ones that are negatively affected by work hardening (e.g. forming). For both types of applications, the recovery behavior (i.e. the reduction of the introduced work hardening due to annealing processes at elevated temperatures) is of particular interest. In applications in which it is intended to benefit from the introduced work hardening, recovery due to heat input during processing or in operation is obviously unfavorable whereas in applications that are negatively affected by work hardening, systematic heat treatment can be applied to reduce necessary forming forces.

A well-designed micromechanical model enables to predict the respective material's behavior for a given load/annealing history. Consequently, such models can be used to identify the most beneficial combination of microstructural parameters for an intended application and enable to optimize the load/annealing path. Further, micromechanical models enable to study aspects of the respective micromechanics which can not be separately investigated in experiments.

These modeling objectives all have their own particular challenges some of which are related to the constitutive modeling itself while others arise from lacking experimental data.

1.2.1 Challenges in micromechanical modeling of fully lamellar TiAl

Modeling the microstructure sensitive yield strength is complicated by the fact that the finite element method (FEM), as the preferred numerical solution technique, does not explicitly involve length scales. Thus, a way has to be found to incorporate effects like e.g. Hall-Petch strengthening which explicitly depend on microstructural lengths. Further, the highly different length scales that coexist in fully lamellar microstructures raise questions regarding their spatial discretization.

Challenges in modeling the work hardening of fully lamellar TiAl arise from the high number of simultaneously activated deformation systems and their work hardening interactions. In this, the interactions between slip and twinning systems are of special interest.

The aim to account for the recovery of work hardening imposes certain restrictions on the work hardening model. Since the recovery of work hardening results from the reduction of defects in the material, the work hardening model has to be formulated in dependence of the current defect density in the material which evolves with deformation and temperature.

1.2.2 Challenges due to lacking experimental data

The reported experimental studies pursue research objectives that do not necessarily coincide with the above sketched objectives of this thesis. Consequently, the reported data are often incomplete with respect to the research objectives addressed here. A typical example is the microstructural characterization of tested specimens. While the microstructural parameters (lamella thickness, colony size etc.) are required for microstructure sensitive modeling, they are often not (or at least incompletely) reported in studies that do not explicitly intend to investigate their influence on the material's behavior.

Further, it is not straight forward and sometimes not even possible to experimentally separate certain simultaneously acting micromechanical effects in fully lamellar TiAl alloys. Thus, the corresponding parameters of the micromechanical model that will be presented in the course of this thesis have to be derived indirectly from experimental results by an iterative calibration procedure.

1.3 Outline of this thesis

In Chapter 2, a brief introduction to the specifics of fully lamellar microstructures in γ TiAl alloys is given. As a necessary foundation for crystal plasticity modeling, the crystallography and correspondingly the deformation mechanisms of fully lamellar TiAl alloys are described. Chapter 3 gives an overview of the state of the art in micromechanical modeling of fully lamellar TiAl before a defect density based, thermomechanically coupled crystal plasticity model and its implementation into finite elements is presented. Parts of this Chapter were previously published in [1–4].

In Chapter 4, the work hardening part of this crystal plasticity model is detailed in terms of hardening interactions between slip and twinning systems. This hardening model is then calibrated against experimental results from literature. Subsequently, the calibrated material model is applied to gain deeper insight into the anisotropic work hardening behavior of fully lamellar TiAl. Parts of this Chapter were previously published in [2, 3].

In Chapter 5, the dominant effect of the different coexisting microstructural interfaces on the macroscopic strength of fully lamellar TiAl is described. The respective part of the crystal plasticity model is detailed and a procedure is shown which enables to separate the relative contributions of different types of microstructural interfaces to the macroscopic strength by a combination of simulations and experiments from literature. Parts of this Chapter were previously published in [1, 2].

In Chapter 6, the calibrated crystal plasticity model is applied to study the typical inhomogeneous microplasticity in polycrystals of fully lamellar TiAl and its sensitivity to changes in microstructure. Parts of this Chapter were previously published in [3].

Chapter 7 deals with the static recovery behavior. The respective part of the crystal plasticity model is calibrated against experiments and subsequently applied to study the characteristics of the static recovery behavior of fully lamellar TiAl alloys. Parts of this Chapter were previously published in [3].

In Chapter 8, the model is extended about the temperature dependent yield strength. In this, the yield stress temperature anomaly that is typically observed in intermetallic alloys is taken into account in a phenomenological way by making the Hall-Petch parameters a function of

temperature. The extended model reproduces well the temperature dependent yield strength of fully lamellar TiAl alloys and allows to rationalize discrepancies in the findings of different experimental studies. Parts of this Chapter were previously published in [1].

Finally, Chapter 9 summarizes the findings of this thesis and gives a brief outlook on possible future work.

2 Crystallography and micromechanics of fully lamellar TiAl alloys

In this chapter, the characteristics of fully lamellar microstructures are briefly explained. Further, the crystallography and correspondingly the available deformation systems of fully lamellar TiAl alloys are introduced.

2.1 Fully lamellar microstructures

As shown in Figure 2.1, fully lamellar microstructures consist of grain-shaped lamellar colonies. These colonies are formed by numerous parallel γ lamellae with a minor fraction of dispersed α_2 lamellae. In analogy to conventional polycrystalline materials, neighboring colonies (grains) are separated by colony boundaries (grain boundaries) and have a different orientation of their lamella plane (crystal orientation). Typical colony sizes λ_C range from some $10\,\mu m$ to more than $1000\,\mu m$ whereas the lamella thickness λ_L is adjustable between a few $10\,nm$ and some µm by alloying and processing [11, 12, 22, 23].
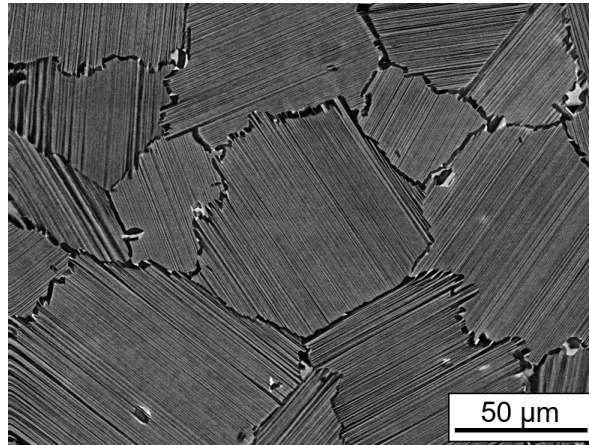
Figure 2.1. Scanning electron microscopy (SEM) image of a fully lamellar microstructure in a Ti-42Al-8.5Nb alloy. The microstructure consists of lamellar ($\alpha_2 + \gamma$) colonies which are distinguished by the orientations of their lamella planes. Picture courtesy of Dr. M.W. Rackel, Institute of Materials Research, Materials Physics, Helmholtz-Zentrum Geesthacht

As illustrated schematically in Figure 2.2, the γ lamellae are further subdivided into ordered domains (see e.g. [24] for details) with typical domain sizes λ_D of a few $10\,\mu m$ [23, 24], that is, the aspect ratio of the lamellae is much higher than sketched in Figure 2.2.

2.1.1 Polysynthetically twinned crystals

By remelting rods of fully lamellar TiAl in an optical floating zone furnace, it is possible to produce samples with unidirectionally solidified microstructures that are formed by γ and α_2 lamellae of only one specific orientation [25, 26]. Since these so called polysynthetically
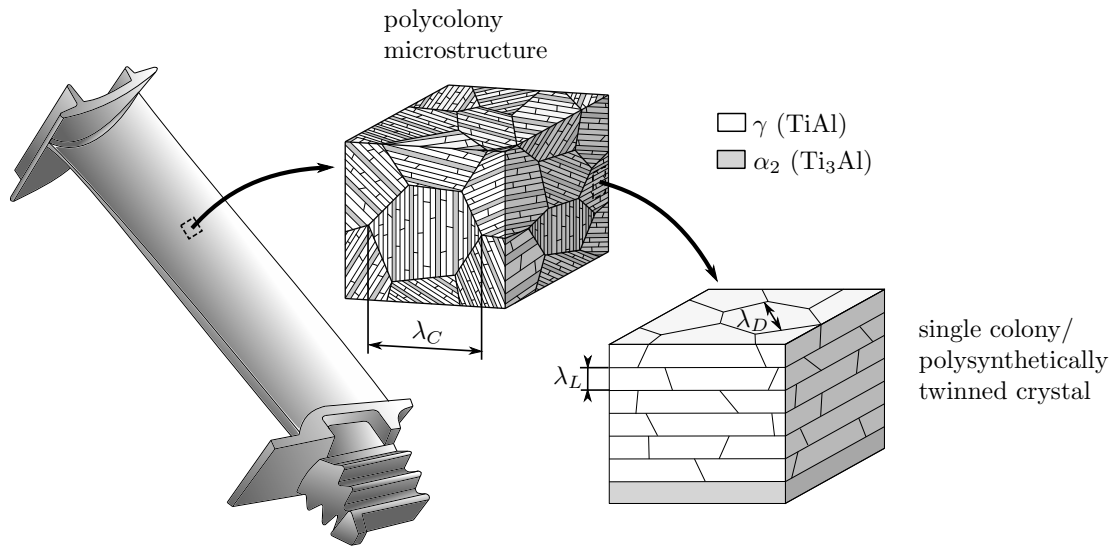
Figure 2.2. Schematic illustration of a fully lamellar microstructure. λ_C: colony size; λ_L: lamella thickness; λ_D: domain size.

twinned crystals do not contain any colony boundaries, they were frequently used to gain insight into the complex micromechanics of a single colony without the disturbing influence of neighboring colonies. Consequently, a polysynthetically twinned crystal is to a polycolony microstructure what a single crystal is to a conventional polycrystalline material. The terms *polysynthetically twinned crystal* and *polycolony microstructure* are thus used in the following to distinguish these two types of lamellar microstructures.

2.2 Crystallography

2.2.1 Lattices

The intermetallic γ phase (TiAl) exhibits the tetragonal L1$_0$ lattice depicted in Figure 2.3 which is basically an FCC lattice with alternating layers of Ti and Al atoms [11]. Due to the alternating Ti and Al layers, the unit cell's height c is slightly bigger than its base length a. For a better readability, the $\frac{c}{a}$ ratio is, however, neglected in the description of deformation systems and the standard Miller index notation for cubic lattices is used (see Appendix A.1). Like in FCC lattices, plastic deformation of the γ phase is accomplished by slip and twinning on the {111} planes. In contrast to FCC structures, slip systems with a non-zero c component are, however, not crystallographically equivalent to those without a c component. In order to make these so called super slip systems distinguishable from the ordinary slip systems (i.e. those that do not involve a c component), a modified Miller index notation with a mixed parenthesis is usually applied (see, e.g., [11]). In this, $\langle uvw]$ denotes the subset of crystallographically equivalent directions that all have the same c component (i.e. the same index w). Making use of this modified notation, lattice restoring super slip can be described by $\langle 10\bar{1}]$ translations (cf. Figure 2.3). These translations may, e.g., be achieved by two identical superpartial dislocations $1/2\langle 10\bar{1}]$ between which a disordered surface – a so called antiphase boundary – emerges [11]. Once both partial dislocations passed, the lattice is restored.

In total, four ordinary slip systems with Burgers vectors $\boldsymbol{b} = \frac{1}{2}\langle 1\bar{1}0]$ and eight super slip systems with Burgers vectors $\boldsymbol{b} = \langle 10\bar{1}]$ can be identified [11]. Further, there exist four twinning systems in the {111} planes of the γ phase with Burgers vectors $\boldsymbol{b} = \frac{1}{6}\langle 11\bar{2}]$ of the
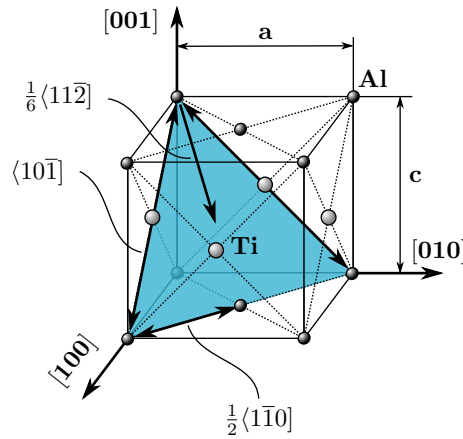
Figure 2.3. Tetragonal L1$_0$ lattice of the γ phase (TiAl) with slip and twinning systems in the {111} planes. The lattice exhibits four ordinary slip systems: $\boldsymbol{b} = \frac{1}{2}\langle 1\bar{1}0]$; eight super slip systems: $\boldsymbol{b} = \langle 10\bar{1}]$ and four twinning systems: $\boldsymbol{b} = \frac{1}{6}\langle 11\bar{2}]$.

twinning partial dislocations [11].

The intermetallic α_2 phase (Ti$_3$Al) exhibits the hexagonal D0$_{19}$ lattice depicted in Figure 2.4 [11]. Although the $\frac{c}{a}$ ratio of this unit cell is close to 0.8, standard Miller-Bravais index notation (see Appendix A.2) is used for better readability. In this hexagonal lattice, plastic deformation can be accomplished by slip with Burgers vectors $\boldsymbol{b} = 1/3\langle 11\bar{2}0\rangle$ on prismatic {1$\bar{1}$00} planes, by slip with Burgers vectors $\boldsymbol{b} = 1/3\langle \overline{11}26\rangle$ on pyramidal {11$\bar{2}$1} planes and by slip with Burgers vectors $\boldsymbol{b} = 1/3\langle 11\bar{2}0\rangle$ on the basal (0001) plane [11, 27].
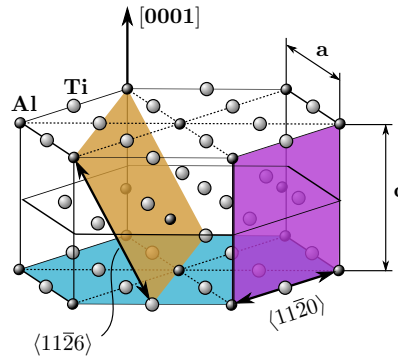
Figure 2.4. Hexagonal D0$_{19}$ lattice of the α_2 phase (Ti$_3$Al) with prismatic $1/3\langle 11\bar{2}0\rangle\{1\bar{1}00\}$, pyramidal $1/3\langle \overline{11}26\rangle\{11\bar{2}1\}$ and basal $1/3\langle 11\bar{2}0\rangle(0001)$ slip systems.

2.2.2 Orientation relation between the γ and the α_2 phase

The specific alignment of the γ and the α_2 phase into parallel lamellae results from the eutectoid phase transformation shown in Figure 1.2 (see [11] for details on the $\alpha \rightarrow \alpha + \gamma \rightarrow \alpha_2 + \gamma$ phase formation sequence). As a result of the formation process, there is a strict orientation relation between both phases within each colony that can be described by

$$\{111\}_\gamma \parallel (0001)_{\alpha_2} \qquad \text{and} \qquad \langle 1\bar{1}0]_\gamma \parallel \langle 11\bar{2}0\rangle_{\alpha_2} \tag{2.1}$$

where $\parallel$ denotes co-planar or parallel respectively [11, 24]. This means, the close-packed

planes of both phases (i.e. the $\{111\}_\gamma$ planes in the γ lamellae and the $(0001)_{\alpha_2}$ plane in the α_2 lamellae) align co-planar during formation while the close-packed directions in these planes align parallel. The interface between the close-packed planes forms the lamella boundary. The dense arrangement of crystallographic interfaces within each colony (see Figure 2.2) does, however, not only involve interfaces between the γ and the α_2 phase (γ/α_2 lamella boundaries) but also contains interfaces between neighboring γ lamellae (γ/γ lamella boundaries) and between domains within each γ lamella (γ/γ domain boundaries). These γ/γ interfaces result from the fact, that six different γ orientation variants exist which fulfill the orientation relation given in (2.1) [24]. These different γ orientation variants can be described in terms of rotations of the γ lattice by a multiple of 60° about the $[111]_\gamma/[0001]_{\alpha_2}$ direction as it is depicted in Figure 2.5.
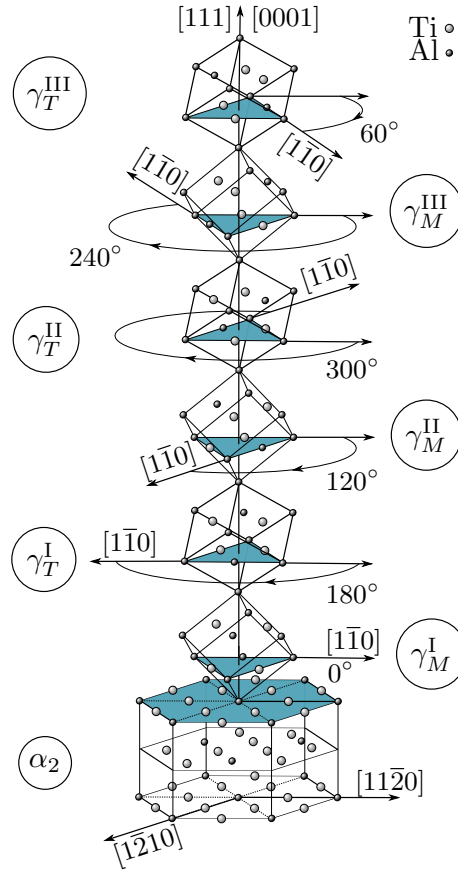
Figure 2.5. Orientation relation between the hexagonal lattice of the α_2 phase and the tetragonal lattice of the γ phase in lamellar colonies. $\gamma_M^{\mathrm{I-III}}$: matrix orientations; $\gamma_T^{\mathrm{I-III}}$: twin orientations. Following Butzke & Bargmann [1].

Three of these γ orientation variants are so called matrix orientations that can be expressed in terms of the orientation relation between their $[1\bar{1}0]_\gamma$ direction and the $\langle 11\bar{2}0\rangle_{\alpha_2}$ directions in the basal plane of the α_2 phase as follows [24]:

$$\gamma_M^{\mathrm{I}} : [1\bar{1}0]_\gamma \uparrow\uparrow [11\bar{2}0]_{\alpha_2},$$
$$\gamma_M^{\mathrm{II}} : [1\bar{1}0]_\gamma \uparrow\uparrow [1\bar{2}10]_{\alpha_2},$$
$$\gamma_M^{\mathrm{III}} : [1\bar{1}0]_\gamma \uparrow\uparrow [\bar{2}110]_{\alpha_2}.$$

Here, ↑↑ denotes parallel directions. The three remaining γ orientation variants denote the corresponding twin orientations which are described in terms of the orientation relation between their $[1\bar{1}0]_\gamma$ direction and the $\langle11\bar{2}0\rangle_{\alpha_2}$ directions in the basal plane of the α_2 phase as follows [24]:

$$\gamma_T^{\mathrm{I}} : [1\bar{1}0]_\gamma \uparrow\downarrow [11\bar{2}0]_{\alpha_2},$$
$$\gamma_T^{\mathrm{II}} : [1\bar{1}0]_\gamma \uparrow\downarrow [1\bar{2}10]_{\alpha_2},$$
$$\gamma_T^{\mathrm{III}} : [1\bar{1}0]_\gamma \uparrow\downarrow [\bar{2}110]_{\alpha_2}.$$

In this, ↑↓ denotes anti-parallel directions. Thus, each twin orientation is described by a 180° rotation of the corresponding matrix orientation about the $[111]_\gamma/[0001]_{\alpha_2}$ direction [24]. Since it has been found that all domains within a single γ lamella are either of matrix or of twin type [6, 11, 24], a lamella is called matrix or twin lamella correspondingly.

2.2.3 Morphological classification of deformation systems

So far, the deformation systems of the single phases were described either in groups of crystallographically equivalent slip planes (e.g. basal, prismatic and pyramidal slip in the α_2 phase) or grouped by deformation mechanisms (e.g. ordinary slip, super slip and twinning in the γ phase). However, since the $(111)_\gamma$ plane of all γ domains and the $(0001)_{\alpha_2}$ plane of all α_2 lamellae within a single colony are always strictly co-planar to the lamella interfaces, the deformation systems of both phases can alternatively be classified according to their orientation with respect to the lamella plane as introduced in [28]. With the slip/twinning direction $\boldsymbol{s}$ and the slip/twinning plane normal $\boldsymbol{n}$, all deformation systems in lamellar microstructures can be uniquely categorized to be either

- longitudinal ($\boldsymbol{s} \parallel$ lamella plane; $\boldsymbol{n} \perp$ lamella plane),
- mixed ($\boldsymbol{s} \parallel$ lamella plane; $\boldsymbol{n} \not\perp$ lamella plane) or
- transversal ($\boldsymbol{s} \nparallel$ lamella plane; $\boldsymbol{n} \not\perp$ lamella plane)

where $\parallel$ and $\nparallel$ refer to parallel and non-parallel respectively whereas $\perp$ and $\not\perp$ refer to perpendicular and non-perpendicular. These different morphological deformation modes are illustrated in Figure 2.6.

longitudinal   mixed   transversal
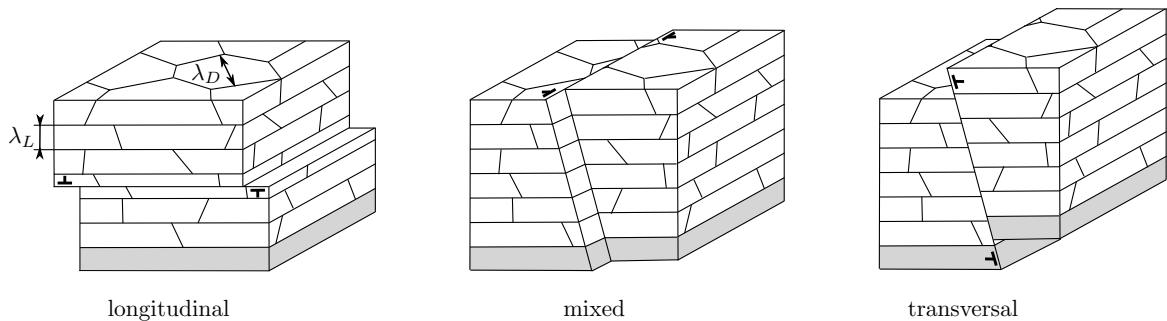
Figure 2.6. Schematic illustration of the morphological deformation modes of the lamellae. The morphological classification was introduced in [28]. λ_L: lamella thickness; λ_D: domain size. Following [29].

Table 2.1 gathers all deformation systems of the γ and the α_2 phase with their mechanism based and their morphological classification.

Table 2.1. Slip and twinning systems in the tetragonal γ and hexagonal α_2 phase with morphological classification according to [28]. Although both phases exhibit a $\frac{c}{a}$ ratio $\neq 1$, standard Miller index respectively Miller-Bravais index notation is used for a better readability. Throughout this thesis, the index α is used for slip systems whereas the index β is used for twinning systems.

γ phase				
system	mechanism	morphology	index	
$1/2[1\bar{1}0](111)$	ordinary slip	longitudinal	1	
$[01\bar{1}](111)$	super slip	longitudinal	2	
$[10\bar{1}](111)$	super slip	longitudinal	3	
$1/2[1\bar{1}0](\bar{1}\bar{1}1)$	ordinary slip	mixed	4	
$[01\bar{1}](\bar{1}11)$	super slip	mixed	5	
$[10\bar{1}](1\bar{1}1)$	super slip	mixed	6	
$1/2[110](1\bar{1}1)$	ordinary slip	transversal	7	α
$1/2[\bar{1}\bar{1}0](\bar{1}11)$	ordinary slip	transversal	8	
$[01\bar{1}](\bar{1}\bar{1}1)$	super slip	transversal	9	
$[\bar{1}0\bar{1}](\bar{1}\bar{1}1)$	super slip	transversal	10	
$[0\bar{1}\bar{1}](1\bar{1}1)$	super slip	transversal	11	
$[\bar{1}0\bar{1}](\bar{1}11)$	super slip	transversal	12	
$1/6[11\bar{2}](111)$	twinning	longitudinal	1	
$1/6[\bar{1}1\bar{2}](\bar{1}11)$	twinning	transversal	2	β
$1/6[1\bar{1}\bar{2}](1\bar{1}1)$	twinning	transversal	3	
$1/6[\bar{1}\bar{1}2](\bar{1}\bar{1}1)$	twinning	transversal	4	
α_2 phase				
system	mechanism	morphology	index	
$1/3\langle11\bar{2}0\rangle(0001)$	basal slip	longitudinal	1-3	
$1/3\langle11\bar{2}0\rangle\{1\bar{1}00\}$	prismatic slip	mixed	4-6	α
$1/3\langle\bar{1}\bar{1}26\rangle\{11\bar{2}1\}$	pyramidal slip	transversal	7-12	

2.3 Plastic anisotropy

Crystalline phases generally behave anisotropic during both elastic and plastic deformation [30]. As long as a polycrystalline material does not exhibit a pronounced texture, the anisotropy of its crystalline phases is, however, not visible in its macroscopic mechanical response. The micromechanics of polycrystalline materials is still strongly affected by the anisotropy of the single phases as it is the case for fully lamellar TiAl alloys. In the context of crystal plasticity, the plastic anisotropy on the microscale is thus of major interest and is briefly described in the following for the single α_2 and γ phase as well as for the lamellar colonies.

2.3.1 Plastic anisotropy of single phases

Most crystals exhibit certain symmetries which are characteristic for their lattice structure. Thus, their distinct plastic anisotropy can usually be described in terms of crystallographically equivalent slip and twinning planes [30]. Besides the kinematic restriction to deform by shear on these crystallographic planes, the plastic anisotropy of a crystal is mainly determined by the critical resolved shear stresses and the hardening behavior of its available deformation

systems acting along these planes.

Crystallographically equivalent deformation systems are generally believed to exhibit the same critical resolved shear stress. This means that, e.g., all prismatic slip systems in the α_2 phase share the same critical resolved shear stress. Further groups of deformation systems with the same critical resolved shear stresses are pyramidal and basal slip in the α_2 phase and twinning, ordinary slip and super slip in the γ phase.

Experimentally, the anisotropy of crystalline phases is naturally best investigated in single crystal specimens. Consequently, the anisotropy of the γ and the α_2 phase was frequently investigated by tests with γ and α_2 single crystals. These single crystal studies allowed to determine the elastic constants of both phases (see, e.g., [31, 32]) as well as the critical resolved shear stresses of their different plastic deformation systems (see, e.g., [27, 33–36]). However, such single crystals can only be grown for compositions that deviate significantly from the composition of ($\alpha_2 + \gamma$) two phase alloys [11]. While γ single crystals are obtained for Al-rich compositions (e.g. Ti-56 at. % Al in [33]) , α_2 single crystals are obtained for Al-lean compositions (e.g. Ti-24.4 at. % Al in [27]).

Since it has been found that the strengths of the plastic deformation systems in both phases strongly dependent on the Al content [11, 12, 37, 38], the available single crystal results are, however, only of limited help to understand and describe the plastic deformation of two phase γ TiAl alloys. This is best illustrated by comparing the relative strength of deformation systems in the γ phase as it was determined in single crystal experiments [33] to the findings from two phase alloys [37]. Tests with Al-rich γ single crystals revealed that their plastic deformation is favorably accommodated by super slip for most crystal orientations indicating that the critical resolved shear stresses of the ordinary slip and the twinning systems were higher than those of the super slip systems [11, 33, 39]. In contrast, the γ phase in two phase alloys was found to mainly deform by ordinary slip and twinning while super slip systems are less preferably activated [11, 37, 39]. Thus, in two phase alloys the critical resolved shear stresses τ_{twin} of twinning systems and τ_{ordinary} of ordinary slip systems in the γ phase are generally believed to be lower than the critical resolved shear stresses τ_{super} of the super slip systems [11, 37].

The critical resolved shear stresses of the slip systems in the α_2 phase were also found to be highly composition dependent. There is, however, evidence that the critical resolved shear stresses of prismatic slip systems are generally lowest, followed by basal and pyramidal slip, i.e. $\tau_{\mathrm{prismatic}} < \tau_{\mathrm{basal}} < \tau_{\mathrm{pyramidal}}$ [27, 35, 36].

In spite of the observed trends in the relative strengths of the different deformation systems in two-phases alloys, their critical resolved shear stresses could not be quantified uniquely so far. While micromechanical testing, e.g., micropillar compression or nanoindentation has the potential to finally determine the strengths of deformation systems of the single phases within two phase alloys, it creates its own challenges with specimen preparation and interpretation of the obtained results especially in fully lamellar microstructures [40, 41].

2.3.2 Plastic anisotropy of single colonies/polysynthetically twinned crystals

There is general agreement that the microstructural interfaces in fully lamellar TiAl – namely lamella, domain and colony boundaries – are strong barriers for dislocation motion and twin propagation and thus all give rise to Hall-Petch strengthening, i.e. the yield strength increases with decreasing lamella thickness λ_L, domain size λ_D and colony size λ_C [11, 18, 23, 42–49]. Consequently, the inherent plastic anisotropy of the γ and the α_2 phase is superimposed by the severe strengthening effect of these microstructural interfaces as it will be discussed in more detail in Chapter 5. The effective anisotropy of the lamellar colonies was thus frequently investigated by experiments with differently oriented polysynthetically twinned crystals (see

e.g. [25, 26, 50–52]) and more recently by micropillar compression of single colonies within actual polycolony microstructures [40, 53]. Figure 2.7 shows the anisotropic yield strength of polysynthetically twinned crystals as obtained from different experimental studies.
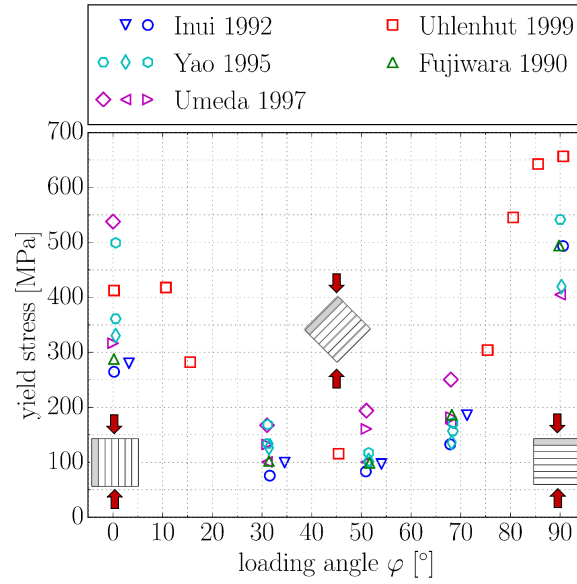
Figure 2.7. Yield stress of differently oriented polysynthetically twinned crystals under uniaxial loading. The loading angle φ is defined between the uniaxial load and the lamella plane (i.e. $\varphi=0°$: loading parallel to lamella plane and $\varphi=90°$: loading perpendicular to lamella plane). Experimental results taken from [25, 26, 50–52]

In Figure 2.7, the yield strength of polysynthetically twinned crystals tested in the strongest orientation (90° between lamella plane and uniaxial load) is $\approx$ 5–7 times higher than in the weakest orientation (45° between lamella plane and uniaxial load). The actual difference between the yield strength in the strongest and the weakest orientation depends on the ratio between lamella thickness λ_L and domain size λ_D as it will be discussed in more detail in Chapter 5. In general, the experiments with differently oriented polysynthetically twinned crystals/single colonies allow to identify two principal deformation modes [25, 40, 52, 54, 55]:

- the hard deformation mode which requires activation of deformation systems on crystallographic planes that cross the lamella interfaces (mixed and transversal systems) and

- the soft deformation mode which requires activation of deformation systems on crystallographic planes that are parallel to the lamella interfaces (longitudinal systems).

As it will be discussed in more detail in Chapter 4, hard mode deformation was mainly found near 0° and 90° orientations whereas soft mode deformation dominates for intermediate loading angles between 15° and 75°.

As shown in [25], the yield stress of polysynthetically twinned crystals also varies between specimens that are loaded parallel to the lamella plane (i.e. $\varphi=0°$) but are rotated around the $[111]_\gamma/[0001]_{\alpha_2}$ direction. However, due to the rotational symmetries that result from the coexistence of the six γ orientation variants (cf. Figure 2.5), the variation of the yield stress of $\varphi=0°$ specimens with the angle between the $[1\bar{1}0]_{\gamma_M^I}$ and the loading direction is insignificant especially in comparison to the strong anisotropy that is caused by the lamella interfaces (cf. Figure 2.7). Thus, most experimental studies which are reported in the literature – and

consequently the corresponding simulations which will be presented in the course of this thesis – have been carried out with the $[1\bar{1}0]_{\gamma_M^I}$ direction fixed either parallel or perpendicular to the loading direction (for $\varphi=0°$) while varying φ.

As a result of the strong plastic anisotropy of the single colonies, there is a pronounced localization of plastic deformation within weakly oriented colonies of polycolony microstructures as it will be discussed in Chapter 6.

3 Modeling framework

3.1 State of the art

In the following, the state of the art in crystal plasticity modeling of fully lamellar TiAl and the generation of representative volume elements (RVEs) of lamellar microstructures is briefly reviewed.

3.1.1 Crystal plasticity models of fully lamellar TiAl

With the continuous progress in alloy development and the increasing application potential of fully lamellar TiAl alloys, modeling their deformation behavior soon became of interest. Since the macroscopic mechanical behavior of fully lamellar TiAl alloys is strongly affected by their intricate microstructure and crystallography [11], a respective constitutive model has to take into account the underlying anisotropic micromechanics. On continuum scale, the anisotropic micromechanics of crystalline materials is frequently described by crystal plasticity models. Since crystal plasticity models explicitly consider the kinematics of a crystal's plastic deformation in terms of shear on individual crystallographic planes, they have been successfully applied to a variety of problems in the field of crystal mechanics [56]. In combination with the finite element method (FEM) as a common solution technique, the abbreviation CPFEM (crystal plasticity finite element method/modeling) is frequently used. In the following, the reported crystal plasticity models for fully lamellar TiAl alloys are briefly reviewed in chronological order.

The first successful applications of the crystal plasticity framework to fully (and nearly) lamellar TiAl have been reported between 1995 and 1997 by Kad, Dao & Asaro [57–59] and Kad & Asaro [60]. In these works, a 2D CPFEM formulation was presented which describes the complex crystallography of the lamellar colonies by a homogenized single crystal model (i.e. without explicitly considering the lamellae). This was done by replacing the deformation systems of the numerous γ and α_2 lamellae by a set of only three slip systems that reflect the principal deformation modes of the lamellar colonies, namely the soft mode deformation (parallel to lamella interfaces) and the hard mode deformation (across the lamella interfaces). The soft mode deformation was described by a 2D projection of the $[1\bar{1}0](111)$ slip system of the γ phase whereas two hard mode deformation systems were introduced by 2D projections of two of the pyramidal $\langle\bar{1}\bar{1}26\rangle\{11\bar{2}1\}$ slip systems in the α_2 phase. The work hardening behavior was modeled by a linear hardening law whereas latent hardening was neglected. Since this 2D single-phase model does not require an explicit spatial discretization of the lamellae and takes into account only three slip systems, it is computationally highly efficient. Thus, it was successfully applied to investigate how the anisotropy of the single colonies affect the micro strain fields and the macroscopic stress strain response of polycolony microstructures. However, describing the kinematics of the lamellar colonies by a single phase crystal plasticity model with only three slip systems does not allow detailed modeling of work hardening interactions. Further, such a model naturally prevents investigation of details in the microstrain fields that may arise within the single colonies.

Almost at the same time, a CPFEM model of a polysynthetically twinned crystal was developed by Parteder, Siegmund, Fischer & Schlögl [61] and Schlögl & Fischer [62–64] in which

the γ and the α_2 lamellae were explicitly considered. The initial 2D CPFEM formulation, presented in [61], incorporated all slip systems of the γ phase and explicitly considered the 6 γ orientation variants. At this stage, the model did, however, not incorporate twinning of the γ lamellae and treated the α_2 lamellae as purely elastic. Thus, the model was extended to a 3D CPFEM formulation [62–64] which incorporated the twinning systems of the γ lamellae as well as basal, prismatic and pyramidal slip in the α_2 lamellae. Deformation of the γ lamellae by super slip was, however, not considered anymore. The critical resolved shear stresses for the γ phase were determined following Hall-Petch arguments. This model was able to precisely reproduce the anisotropic strength of polysynthetically twinned crystals and consequently allowed investigation of the respective yield loci. However, the parameters of the applied hypersecans hardening law were chosen without validation due to a lack of experimental data on the hardening behavior of polysynthetically twinned crystals. Further, no hardening was assumed for the twinning systems and hardening interactions were considered between slip systems only.

In the work of Lebensohn, Uhlenhut, Hartig & Mecking [28], Lebensohn [65] and Uhlenhut [52], the plastic deformation of polysynthetically twinned crystals was modeled by a visco-plastic self-consistent (VPSC) crystal plasticity formulation (cf. [66]). In this work, the morphological classification, described in Section 2.2.3, was introduced and the relative strength of deformation systems of different morphological classes was investigated. By assuming that all deformation systems of a morphological class have the same strength, i.e. by neglecting potential differences in strength that result from the crystallography of the single phase, this model reproduced the anisotropic yield strength of polysynthetically twinned crystals as well as their relative transversal strains very well. While the different γ orientation variants were explicitly considered in this model, the α_2 phase, as the minority phase, was neglected completely.

Grujicic & Zhang [67] presented a 2D CPFEM model that closely followed the ideas of Kad et al. [57–60] and that was later used by Grujicic & Cao [68] in combination with a cohesive zone model to investigate fracture in fully lamellar microstructures. The idea of Kad et al. [57–60] to model the plastic deformation behavior of the lamellar colonies by a homogenized single phase model was then transferred to a 3D CPFEM formulation by Grujicic & Batchu [69] which was subsequently applied in [70] again together with a cohesive zone approach to analyze the fracture behavior of polycolony microstructures. In this 3D CPFEM model, the strength and hardening behavior of the deformation systems that were chosen to represent the lamellar colonies in the homogenized single phase model were for the most part taken to be identical to the values that were previously determined from γ and α_2 single crystal simulations. These single crystal simulations were calibrated against single crystal experiments via a numerical optimization algorithm. After adjusting the strength of hard (mixed and transversal) deformation modes against experiments with polysynthetically twinned crystals by numerical optimization, the homogenized single phase model reproduced their plastic deformation behavior well. However, since the critical resolved shear stresses of the deformation systems of both phases strongly change with composition (cf. Section 2.3.1), taking the parameters of the soft mode (longitudinal) deformation systems from single crystal experiments, is somewhat questionable.

Another 3D CPFEM approach that described the deformation of the lamellar colonies in a homogenized way was reported by Brockmann [71]. The homogenized single phase model of Brockmann [71] was set up in terms of small deformations and rotations. The anisotropic deformation of the lamellar colonies was represented by a set of 4 groups of deformation systems – namely ordinary slip systems of the γ phase, prismatic and pyramidal slip systems of the α_2 phase and an interlamellar deformation mode that was assumed to act in the basal plane of the α_2 phase. The critical resolved shear stresses of the considered slip systems were assigned according to findings from γ and α_2 single crystals and the strengthening effect of

the lamella interfaces was considered in terms of a Hall-Petch type correction. Further, linear work hardening was assumed. With this single phase model it was possible to efficiently analyze the arising micro strain fields in a 3D duplex microstructure with more than hundred lamellar colonies.

The modeling activities of Werwer & Cornec [72, 73] and Werwer [29] aimed on analyzing the deformation behavior of polysynthetically twinned crystals for higher plastic strains (not only near the yield point). Therefore, the authors developed a 3D CPFEM model which explicitly considered all slip and twinning systems of the γ and the α_2 phase in separate lamellae. With the experimental results on the hardening behavior of differently oriented polysynthetically twinned crystals, reported by Uhlenhut [52], the applied linear hardening law was calibrated. In this calibration process it was assumed that deformation systems of the same morphological class do not only have the same strength (as stated by Lebensohn et al. [28]) but may also be described by the same set of hardening parameters. With this assumption, not only the anisotropic yield strength (as in most previous studies) but also the anisotropic work hardening behavior of differently oriented polysynthetically twinned crystals was reproduced sufficiently well. However, certain specifics of the experimental stress strain curves – especially at higher strains – did not appear in the simulations due to the simplicity of the applied hardening law. By considering all deformation systems in the γ lamellae, it was possible to investigate the specific role of the strength of super slip systems on the deformation behavior of polysynthetically twinned crystals [73].

What is particularly interesting about the work of Werwer & Cornec [29, 72, 73] is the way in which the authors realized to model the rotation of the representative volume element (RVE) of the polysynthetically twinned crystal with respect to the uniaxial load as it is necessary when its anisotropy shall be analyzed. Instead of changing the loading direction or altering the lamella orientation of the RVE, the authors implemented the whole RVE within a single finite element – a so-called dummy element – and introduced a rotational relation between the averaged nodal displacements of this dummy element and the deformation of the RVE (see Section 3.6.2 for details). This allows to change the angle between the uniaxial loading (applied to the dummy element) and the lamella plane of the RVE without changing the geometrical set up. In [29], this FE^2-like idea was extended to model polycolony microstructures. In these calculations, the colonies were represented by hexahedral finite elements in each of which a complete, randomly oriented RVE of a polysynthetically twinned crystal was implemented using the described rotational relation between the nodal displacements of the dummy elements and the embedded RVEs. This two scale modeling approach was later successfully applied by Kabir [74], Kabir, Chernova & Bartsch [75] and Cornec, Kabir & Huber [76] to reproduce and study the macroscopic stress strain response of duplex and fully lamellar microstructures.

In the work of Roos, Chaboche, Gélébart & Crépin [77], a multi scale crystal plasticity model of TiAl alloys with potentially different microstructures is reported. In this model, three scales exist: the macro (i.e. the structural) scale, the meso scale of the lamellar colonies and if applicable the γ and α_2 grains, and the micro scale of the lamellae within the colonies. The crystal plasticity formulation is solved on the meso scale for the globular γ and α_2 grains and on the micro scale for the lamellar colonies. The respective results are passed to the next higher scale. On the micro scale all 6 γ orientation variants and the α_2 phase with all their deformation systems were explicitly considered.

Further, the crystal plasticity model of Kowalczyk-Gajewska [78] is worth mentioning here as it was the first crystal plasticity model of γ TiAl which accounts for the work hardening of slip and twinning systems due to evolving twins in a more physical way than the afore mentioned models. While this contribution to work hardening was commonly modeled by a linear hardening interaction law, in [78] a Hall-Petch type relation was introduced based on

ideas from [79].

In the work of Zambaldi [41] and Zambaldi, Roters & Raabe [80] a 3D CPFEM model was presented which models the plastic deformation of the lamellar colonies by a homogenized single phase model with 18 effective deformation systems (instead of the 108 deformation systems in the 6 γ variants + the α_2 phase). Like in the models of Kad et al. [57–60], Grujicic et al. [67–70] and Brockmann [71], these 18 deformation systems are chosen in such a way that they represent the principal deformation modes of the lamellar colonies. This set of deformation systems involves 3 effective longitudinal slip systems and 3 effective longitudinal twinning systems in the $(111)_\gamma$ plane, 6 effective transversal pyramidal slip systems of the α_2 phase and 6 effective mixed slip systems of the γ phase. With the same critical resolved shear stresses assigned to all systems of the same morphological class, the model was able to sufficiently reproduce the anisotropic yield strength and relative transversal strain of polysynthetically twinned crystals/single colonies and was successfully applied to model the macroscopic stress strain behavior of polycolony microstructures. However, the strength of the different deformation systems was not modeled in a microstructure sensitive way plus the hardening law of the model was not calibrated against experiments.

Finally, Ilyas & Kabir [81] only recently presented a temperature sensitive CPFEM model of fully lamellar TiAl. In order to capture the (anomalous) temperature dependence of the yield strength (see Chapter 8 for details), the authors made the strain rate sensitivity exponent of the applied classical flow rule a function of temperature. This model was then calibrated to successfully reproduce the temperature dependent yield strength of differently oriented polysynthetically twinned crystals reported in [37]. As it has been experimentally observed in [46], the temperature dependent yield strength of polysynthetically twinned crystals is, however, strongly influenced by the spacing of the different microstructural interfaces (see Chapter 8 for details). Although showing promising results, the model from [81] is not formulated in a microstructure sensitive way and is thus not (yet) capturing the experimentally observed effect of the different microstructural interfaces on the temperature dependent yield strength of differently oriented polysynthetically twinned crystals. A comparison to the respective experimental results from [46] was thus not given in [81].

Further reviews of crystal plasticity (and other) modeling approaches for TiAl alloys can be found in [41] and [82].

Reviewing the reported crystal plasticity models, it appears that there are basically two modeling strategies:

1. describing the plastic deformation of the lamellar colonies by explicitly considering the complete crystallography of the α_2 phase and the 6 γ orientation variants in separate lamellae [28, 29, 52, 61–65, 72–77, 81] or

2. describing the plastic deformation of the lamellar colonies in a homogenized single phase model by only considering deformation systems that reflect their principal deformation modes (i.e. without explicitly considering the lamellae) [41, 57–60, 67–71, 80].

The comparison of the reported crystal plasticity models allows to formulate the following common questions:

Crystallography:

- Is it necessary to separately model the α_2 phase and the six orientation variants of the γ phase or is it sufficient to set up a homogenized single phase model?

- Which deformation systems are relevant and thus have to be considered?

Yield strength:

- How can the strengthening effect by lamella, domain and colony boundaries be modeled?

- What are the relative strengths of deformation systems in the γ phase (ordinary/super slip, twinning) and in the α_2 phase (prismatic, basal and pyramidal slip)?

Work hardening:

- How can the self hardening behavior of different deformation mechanisms (slip and twinning) be described?

- How can the work hardening interactions between deformation systems, i.e. slip/slip, slip/twin and twin/twin interactions be described?

While most of these questions can naturally not be answered unambiguously since the answer strongly depends on the pursued modeling strategy and the intended accuracy of the model predictions, some of them are apparently harder to tackle than others. One of the most prominent issues with modeling fully lamellar TiAl is the strengthening effect by lamella, domain and colony boundaries. While being discussed in many numerical as well as experimental contributions, the relative effect of these three types of microstructural interfaces is not yet clarified, consequently inhibiting a microstructure sensitive prediction of the yield point. Another issue appears to be the work hardening behavior which has not been modeled in detail so far since most studies were mainly interested in predicting the yield point. Further, it is striking that the vast majority of the reported models are either limited to room temperature or isothermal conditions and are thus obviously inadequate to describe the material's behavior at service temperature or for thermal cycling. To the best of the author's knowledge, so far only a single study was published that explicitly dealt with crystal plasticity modeling of fully lamellar TiAl at elevated temperatures, i.e. [81]. Apart from this, the high temperature behavior of γ TiAl alloys was so far only addressed by modeling their creep deformation behavior [83–85], however, in a quite phenomenological way.

3.1.2 Generating representative volume elements of lamellar microstructures

Besides a constitutive model of the plastic deformation behavior, a geometrical representation and derived from that a discretization of a representative part of the lamellar microstructure is needed in order to solve the boundary value problem by FEM. The aim of this section is thus to review the state of the art in generating respective geometries for FEM analyses.
Lamellar microstructures are not exclusively found in TiAl alloys but can be obtained in various alloy systems like e.g. Pb–Sn, Fe–C, Al–Cu or Cu–Ag for eutectic or eutectoid compositions. Besides TiAl alloys, the most prominent examples of commercial structural materials with lamellar microstructures are probably pearlitic steels and two-phase titanium alloys like Ti-6Al-4V. While the parallel arrangement of the lamellae into regions of different lamella orientations, i.e. into colonies, is a common feature of lamellar microstructures, additional, material specific features may occur, like e.g. the domain structure of the γ lamellae in TiAl or the waviness of the cementite lamellae in pearlite colonies. However, the techniques that can be used to generate RVEs of lamellar microstructures are in most cases not material specific. Thus, differences in the crystallography or in the geometrical details of lamellar microstructures from different alloy systems do not prevent these methods from being applied.
Following [4], the methods for RVE generation may be grouped into

- experimental methods that aim to create a digital representation of the microstructure from imaging techniques like, e.g., SEM,

- physics based methods that aim to generate RVEs of a microstructure based on the physical processes that caused its formation and

- geometry based methods that solely aim to capture relevant geometrical features of the microstructure (usually in an idealized way), neglecting irregularities of the real microstructures as they would be captured by experimental methods and ignoring the formation process as it would be considered in physics based methods.

Microstructure reconstruction from experimental data

The most common technique for the 3D reconstruction of microstructures is the so called serial sectioning technique. In serial sectioning techniques, thin layers of the material are sequentially removed by grinding or by a focused ion beam (FIB). After removing a layer of material, the exposed surface is scanned using, e.g., SEM. From the series of scans, a layered reconstruction of the 3D microstructure can be obtained. A review of the details of serial sectioning techniques can be found in [4].

3D reconstructions of lamellar microstructures by serial sectioning were to date only reported for pearlite colonies in pearlitic steels [86–89] and arrangements of several α laths in Ti-6Al-4V [90, 91]. While these studies enabled investigation of microstructural details like e.g. the waviness of the cementite lamellae in pearlite colonies, they also revealed the difficulties in capturing the intricate details of lamellar microstructures by serial sectioning techniques.

In [86], the authors reported problems with aligning the scans of the 2D sections in the reconstruction process. These problems resulted from pronounced changes in the morphology of the investigated pearlite colonies along the thickness of the successively removed material layers. As a result, many interconnections of the branched cementite lamellae were lost in the reconstruction process. When aiming to capture intricate microstructural features like, e.g., the lamellae in fully lamellar TiAl (often with a thickness $\lambda_L < 100$ nm) or the mentioned branching of the cementite lamellae in pearlite colonies by serial sectioning techniques, the thickness of the removed material layers has to be in the range of a few 10 nm (instead of the often reported > 100 nm). While such small slice thicknesses are achievable by suitable milling techniques (e.g. FIB), the number of sections that are needed to resolve a complete colony (with a diameter of some 10µm to several 100 µm) increases accordingly. Storing and processing the corresponding big amount of data is a formidable task which creates its own challenges.

While the described problems result from the inevitable information loss due to the successive removal of material layers of finite thickness, i.e. the serial sectioning process itself, capturing all microstructural details within a single 2D section may also cause certain difficulties. Due to the significantly different length scales that coexist in lamellar microstructures, an extreme resolution would be necessary to capture a representative number of colonies while still being able to resolve their lamellar substructure. Thus, capturing all microstructural features in a single scan is often impeded (see e.g. Fig. 2.1), consequently further increasing the amount of data that have to be stored and processed.

In summary it can be stated that experimental reconstruction of lamellar microstructures (especially for submicron lamella thicknesses) remains challenging but has the potential to grant unique insight into their intricate 3D details.

Physics based microstructure generation

Due to the complexity of the eutectic respectively eutectoid phase transformations that lead to the creation of lamellar microstructures, a physics based generation of the corresponding RVEs is not yet state of the art. A first, even though still two dimensional, RVE of single

ferrite-pearlite colonies was generated by a phase-field modeling approach in [92]. The results of the phase-field simulation subsequently served as input for FEM calculations.

More recently, 3D large scale phase-field simulations of eutectic solidification of ternary Al–Ag–Cu alloys were reported [93, 94]. These simulations were able to precisely reproduce the intricate cobblestone microstructure that is characteristic for these alloys. Consequently, such phase-field simulations might also help to better understand the eutectic respectively eutectoid formation process of lamellar microstructures and could ultimately be used for a physics based RVE generation.

Geometrical methods

Due to the high aspect ratio of the lamellae (in TiAl often $\frac{\lambda_C}{\lambda_L}$ >500), a one to one discretization of a representative set of colonies would require a very high number of finite elements. In combination with the computationally expensive micromechanical constitutive models, this would result in unpleasantly high computational costs. Thus, neither experimental nor physics based methods – which per definition yield a one to one representation of the microstructure – are widely used for the generation of RVEs for FEM based modeling of lamellar microstructures. In fact, most reported RVEs of lamellar microstructures are based on purely geometrical considerations and include some kind of geometric simplification or multi-scale approach to reasonably limit the computational costs.

As it became clear in the review of the reported crystal plasticity models for fully lamellar TiAl (see Section 3.1.1), these models are usually set up and calibrated in two steps, beginning with the constitutive behavior of a single colony and subsequently transferring the results to the micromechanics of a polycolony microstructure. Accordingly, two types of RVEs can be distinguished for lamellar microstructures:

- RVEs of single colonies that consist of a representative number of lamellae and

- RVEs of polycolony microstructures that consist of a representative set of differently oriented colonies.
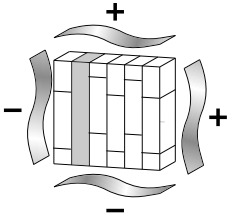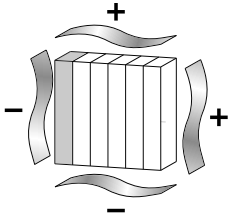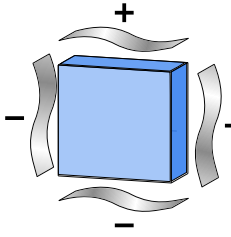
The specific appearance of the reported RVEs is, however, directly related to the pursued modeling strategy, i.e. whether or not it is intended to explicitly model the constitutive behavior of the individual lamellae (cf. Section 3.1.1). While constitutive models that explicitly consider the micromechanics of the different lamellae obviously require lamellar RVEs, there is no need for an explicit geometrical representation of the lamellae in RVEs for homogenized single phase models. Moreover, some authors aim to set up RVEs that reproduce the microstructural details as realistic as possible, while others decide to create structured RVEs of reduced complexity. Thus, the reported geometry based RVEs can be categorized to be

- *lamellar* or *homogeneous* and

- *realistic* or *structured.*
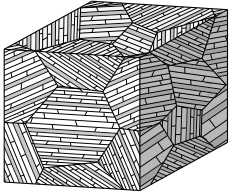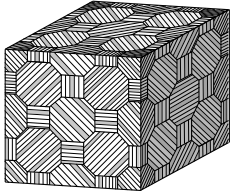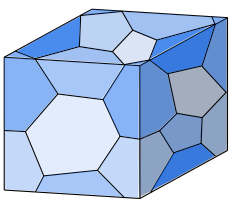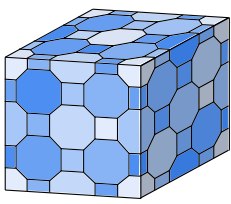
Table 3.1 illustrates this categorization scheme and summarizes literature in which respective kinds of RVEs were presented.

As mentioned above, micromechanical modeling of materials with lamellar microstructures usually starts with modeling the manageable constitutive behavior of the single colonies. However, the corresponding RVEs of single colonies are not only needed for model calibration but were also used to study their micromechanics (like e.g. their plastic anisotropy) and play a role in the context of multi scale modeling. The geometry of such single colony RVEs is usually quite simple and thus generally enables structured meshing.

Table 3.1. Schematic illustration of different types of reported RVEs of lamellar microstructures categorized by level of detail. *Homogeneous* and *lamellar* refer to whether or not the lamellae are explicitly considered in the RVE (and correspondingly in the constitutive model). The categories *realistic* and *structured* indicate whether it is intended to represent the microstructural details as realistic as possible or in a simplified (i.e. structured) way. Figures taken from Bargmann et al.[4].

single lamellar colonies			
	realistic		structured
lamellar		**modeled details** domains in TiAl (3D: [1, 29, 62, 63, 72, 78, 83, 95]; 2D: [61])		**resolved phases** TiAl (α_2 + 6 γ orientations [29, 77, 78]; α_2 + 2 homogenized γ matrix and twin variants [29, 75]); pearlitic steel (ferrite + cementite [96–98]); Ti-6242 (α + β [99])
homogeneous	**not applicable**			**calibration of homogenized constitutive model** TiAl [71, 80]

polycolony microstructures			
	realistic		structured
lamellar		**colony geometry** Voronoi-based [100]		**colony geometry** hexagonal (2D) [83, 101, 102]
homogeneous		**colony geometry** Voronoi-based [97, 103, 104]		**colony geometry** truncated rhombic dodecahedral [71]; hexahedral [29, 72, 75, 105, 106]; hexagonal (2D) [57, 67, 68]; rhombo hexagonal dodecahedral [80]

RVEs of polycolony microstructures are naturally more complex and thus need more sophisticated tools to be created. In general, the single colonies have a similar shape as the grains in conventional polycrystalline materials. In the case of fully lamellar TiAl, the shape of the colonies is in fact determined by the shape of the parent α phase grains in which the lamellae form during the eutectoid phase transformation (cf. Figure 1.2). Thus, the geometry of the colonies can basically be obtained by the same techniques that are used to create RVEs of conventional polycrystalline materials (e.g. Voronoi tessellation). Most reported polycolony

RVEs are, however, created using more or less complex, space-filling geometries like simple hexahedra, hexagonal prisms or truncated rhombic dodecahedra to represent the colony boundaries. As it becomes clear from Table 3.1, only a few of the reported polycolony RVEs explicitly incorporated the lamellae. In all of the respective studies, the number of lamellae per colony was drastically reduced as compared with real microstructures in order to limit the number of elements that are needed for their discretization.

In summary it can be stated that the significantly different length scales that coexist in lamellar microstructures (lamella thickness $\ll$ colony size) currently impede the use of realistic RVEs for FEM simulations. As a result, most reported constitutive models treat the lamellar colonies in a homogenized way or apply some kind of multiscale approach.

3.2 Crystal plasticity

Crystal plasticity models aim to reproduce the plastic anisotropy of crystalline materials by explicitly considering the kinematics of their crystallographic lattices and their work hardening characteristics. A review of the reported crystal plasticity models can be found in [56]. In the following section, the crystal plasticity framework that is used throughout this thesis is presented.

3.2.1 Kinematics

The crystal plasticity model presented here is formulated in terms of finite strain theory, i.e. for large deformations. In this, the motion of a material point from its initial position $\boldsymbol{X}$ in the undeformed, stress-free reference configuration of a solid body to its current position $\boldsymbol{x}$ in the deformed (current) configuration at time t is described by

$$\boldsymbol{\varphi}(\boldsymbol{X}, t) := \boldsymbol{x}. \tag{3.1}$$

With the function of motion $\boldsymbol{\varphi}$ of the material points of a solid body between its reference and its current configuration, the deformation of infinitesimal line elements in that body is described by the deformation gradient $\boldsymbol{F}$

$$\boldsymbol{F} := \operatorname{Grad} \boldsymbol{\varphi}(\boldsymbol{X}, t), \text{ i.e. } F_{ij} = \frac{\partial \varphi_i}{\partial X_j} \text{ for } i, j = 1, 2, 3 \tag{3.2}$$

where Grad is the gradient with respect to reference configuration. In the context of large strain plasticity, the deformation gradient $\boldsymbol{F}$ is commonly assumed to be decomposable into two parts (see, e.g., [107])

$$\boldsymbol{F} = \boldsymbol{F}_E \cdot \boldsymbol{F}_P. \tag{3.3}$$

Here, $\boldsymbol{F}_P$ represents the deformation of a crystal due to inelastic shear on its crystallographic planes whereas $\boldsymbol{F}_E$ represents the elastic deformation of the lattice and its rigid body rotations.

As illustrated in Figure 3.1, the multiplicative split of the deformation gradient introduces an intermediate configuration which is described by a transformation of the reference configuration by $\boldsymbol{F}_P$. Since it is usually assumed that the inelastic shear on crystallographic planes does not alter the appearance of the lattice, the intermediate configuration is assumed to be isoclinic, i.e. the shear direction $\boldsymbol{s}$ and the shear plane normal $\boldsymbol{n}$ do not change between reference and intermediate configuration.

With the multiplicative split of the deformation gradient $\boldsymbol{F}$, i.e. Equation (3.3), the right Cauchy-Green tensor can be defined in the reference configuration, reading
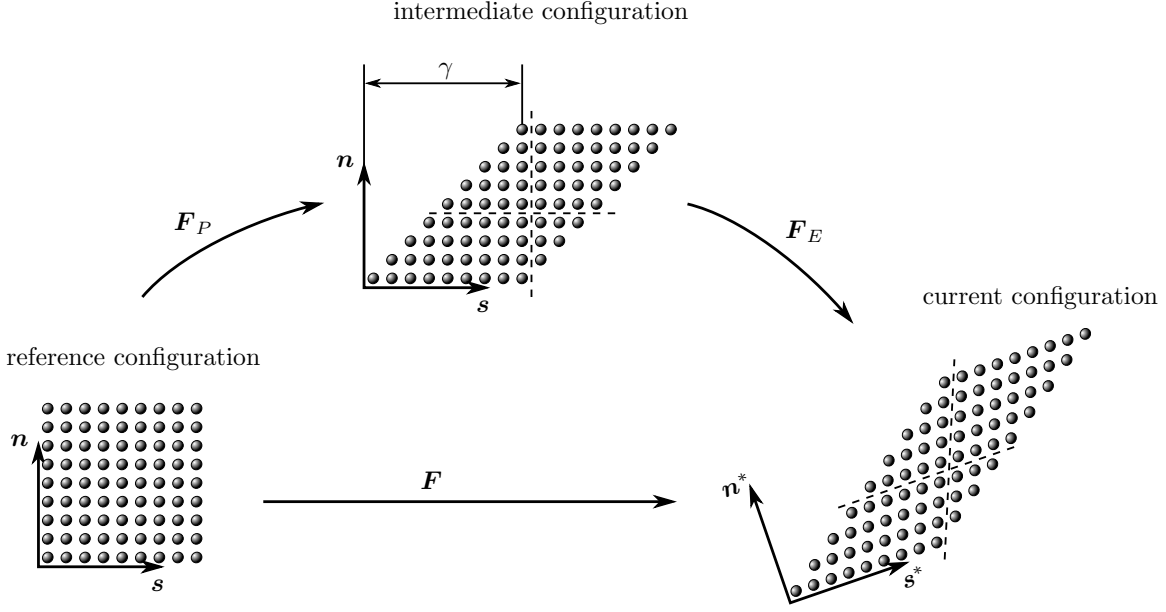
Figure 3.1. Decomposition of the deformation gradient $\boldsymbol{F}$ into an elastic part $\boldsymbol{F}_E$ and a plastic part $\boldsymbol{F}_P$. The decomposition introduces an intermediate configuration which is assumed to be isoclinic, i.e. the shear direction $\boldsymbol{s}$ and the shear plane normal $\boldsymbol{n}$ do not change between reference and intermediate configuration. Following [41].

$$\boldsymbol{C} := \boldsymbol{F}^T \cdot \boldsymbol{F} \tag{3.4}$$

as well as in the intermediate configuration, indicated by the subscript E

$$\boldsymbol{C}_E := \boldsymbol{F}_E^T \cdot \boldsymbol{F}_E. \tag{3.5}$$

The evolution $\dot{\boldsymbol{F}}$ of the deformation gradient $\boldsymbol{F}$ is given by

$$\boldsymbol{L} = \dot{\boldsymbol{F}} \cdot \boldsymbol{F}^{-1} \tag{3.6}$$

where $\boldsymbol{L}$ is the velocity gradient. With the multiplicative split of the deformation gradient $\boldsymbol{F}$ given in Equation (3.3), its evolution reads $\dot{\boldsymbol{F}} = \dot{\boldsymbol{F}}_E \cdot \boldsymbol{F}_P + \boldsymbol{F}_E \cdot \dot{\boldsymbol{F}}_P$. The inverse of $\boldsymbol{F}$ reads $\boldsymbol{F}^{-1} = \boldsymbol{F}_P^{-1} \cdot \boldsymbol{F}_E^{-1}$. Inserting this into Equation (3.6) yields

$$
\begin{aligned}
\boldsymbol{L} &= \left[\dot{\boldsymbol{F}}_E \cdot \boldsymbol{F}_P + \boldsymbol{F}_E \cdot \dot{\boldsymbol{F}}_P \right] \cdot \boldsymbol{F}_P^{-1} \cdot \boldsymbol{F}_E^{-1} \\
&= \underbrace{\dot{\boldsymbol{F}}_E \cdot \boldsymbol{F}_E^{-1}}_{\boldsymbol{L}_E} + \boldsymbol{F}_E \cdot \underbrace{\dot{\boldsymbol{F}}_P \cdot \boldsymbol{F}_P^{-1}}_{\boldsymbol{L}_P} \cdot \boldsymbol{F}_E^{-1}
\end{aligned} \tag{3.7}
$$

with $\boldsymbol{L}_E$ and $\boldsymbol{L}_P$ being the elastic and the plastic part of the velocity gradient. With this, the evolution of the plastic deformation gradient is given by

$$\dot{\boldsymbol{F}}_P = \boldsymbol{L}_P \cdot \boldsymbol{F}_P. \tag{3.8}$$

In order to capture the kinematics of a crystal's plastic deformation, the plastic velocity gradient $\boldsymbol{L}_P$ is defined in terms of shear rates on individual crystallographic planes in crystal plasticity models. Based on the definition from [107] which was extended in [108] to account

for twinning, the plastic velocity gradient is defined as

$$\boldsymbol{L}_P = \dot{\boldsymbol{F}}_P \cdot \boldsymbol{F}_P^{-1} = \left[1 - \sum_{\beta}^{N^{\mathrm{tw}}} f_\beta\right] \underbrace{\sum_{\alpha}^{N^{\mathrm{sl}}} \nu_\alpha \left[\boldsymbol{s}_\alpha \otimes \boldsymbol{n}_\alpha\right]}_{\text{slip}} + \underbrace{\sum_{\beta}^{N^{\mathrm{tw}}} \gamma_T g_\beta \left[\boldsymbol{s}_\beta \otimes \boldsymbol{n}_\beta\right]}_{\text{twinning}}. \tag{3.9}$$

In this, the shear rate on slip system α and the twinning rate on twinning system β are denoted by ν_α and g_β, f_β denotes the twinned volume fraction of twinning system β and γ_T denotes the material specific twinning shear ($\gamma_T = 1/\sqrt{2}$ in TiAl [11]). The product of twinning rate g_β and twinning shear γ_T yields the shear rate on twinning system β. N^{sl} and N^{tw} denote the number of slip systems and the number of twinning systems respectively. The sum of the twinned volume fractions f_β has to be limited to $\sum_{\beta}^{N^{\mathrm{tw}}} f_\beta \leq 1$ as this means that the volume is twinned completely.

In the present definition of $\boldsymbol{L}_P$ (Equation (3.9)), the reorientation of the crystal lattice due to twinning and subsequent slip or twinning within twinned regions is not considered. This assumption is reasonable since twins in fully lamellar TiAl alloys are generally very thin, see, e.g., [55].

3.2.2 Stress measures

As an important stress measure, the second Piola-Kirchhoff stress $\boldsymbol{S}$ in the reference configuration is defined by

$$\boldsymbol{S} := J\boldsymbol{F}^{-1} \cdot \boldsymbol{\sigma} \cdot \boldsymbol{F}^{-T} \tag{3.10}$$

where $J = \det \boldsymbol{F} > 0$ is the Jacobian and $\boldsymbol{\sigma}$ denotes the Cauchy stress tensor.

As a result of the decomposition of the deformation gradient, i.e. Equation (3.3), the second Piola-Kirchhoff stress can also be defined with respect to the intermediate configuration, again indicated by the subscript E reading

$$\boldsymbol{S}_E := J_E \boldsymbol{F}_E^{-1} \cdot \boldsymbol{\sigma} \cdot \boldsymbol{F}_E^{-T} \tag{3.11}$$

with $J_E = \det \boldsymbol{F}_E > 0$. Correspondingly, the Mandel stress defined in the intermediate configuration is given by

$$\boldsymbol{M}_E = \boldsymbol{C}_E \cdot \boldsymbol{S}_E. \tag{3.12}$$

The resolved shear stress τ that acts on a slip or twinning system can now be determined by the following representation of Schmid's law[3]

$$\tau := \boldsymbol{s} \cdot \boldsymbol{M}_E \cdot \boldsymbol{n}. \tag{3.13}$$

Once the resolved shear stress τ on any slip or twinning system reaches levels close to its strength, plastic deformation starts. This has to be modeled by an appropriate flow respectively twinning rule.

---

[3]The slip/twinning direction $\boldsymbol{s}$ and the slip/twinning plane normal $\boldsymbol{n}$ are defined as unit vectors in cartesian coordinates. Thus, the Miller-Bravais notation for hexagonal lattices have to be transformed according to Appendix A.2.

3.2.3 Flow rule

The arising slip shear rate ν_α on a slip system α depends on the ratio between the resolved shear stress τ_α (see Equation (3.13)) and its current strength τ_α^Y. The slip shear rates ν_α are thus described via the viscoplastic powerlaw [109]

$$\nu_\alpha = \nu_0 \left| \frac{\tau_\alpha}{\tau_\alpha^Y} \right|^n \mathrm{sign}(\tau_\alpha). \tag{3.14}$$

The parameters, ν_0 and n are the reference shear rate and the strain rate sensitivity exponent. For high values of n, this formulation asymptotically approaches the rate independent case. Since Equation (3.14) defines the slip shear rate ν_α to be positive or negative depending on the sign of the resolved shear stress τ_α, the accumulated slip shear $\overline{\gamma}_\alpha$ on slip system α is defined by

$$\overline{\gamma}_\alpha = \int |\nu_\alpha| \, \mathrm{d}t. \tag{3.15}$$

The parameters that were used for Equation 3.14 are not varied throughout this thesis. Their values are given in Table 3.2.

Table 3.2. Model parameters for flow and twinning rule, i.e. equations (3.14) and (3.16)

symbol	value	unit
ν_0	0.001	$[\frac{1}{s}]$
n	50	$[-]$

Choosing the strain rate sensitivity exponent n as high as 50, makes Equation (3.14) relatively insensitive to the applied strain rate.

3.2.4 Twinning rule

From a continuum point of view, the shear of a crystal lattice due to evolving twins can be described in the same way as for slip systems, except that twinning shear can only act in one direction which is the twinning direction. To ensure that twinning is unidirectional and that the total twinned volume fraction does not exceed the limit of $f = \sum_\beta^{N^{\mathrm{tw}}} f_\beta \leq 1.0$ (as it is required by Equation (3.9)), the relation of resolved shear stress τ_β and twinning rate g_β is modeled via (cf. [108])

$$g_\beta = \begin{cases} \frac{\nu_0}{\gamma_T} \left[\frac{\tau_\beta}{\tau_\beta^T} \right]^n & \text{for } \tau_\beta > 0 \text{ and } f < 1.0 \\ 0 & \text{else} \end{cases}. \tag{3.16}$$

Herein, τ_β^T denotes the current twinning resistance of twinning system β and the reference twinning rate is determined by dividing the reference shear rate ν_0 by twinning shear γ_T [63, 108]. The corresponding parameters that were used throughout this thesis are given in Table 3.2.

The accumulated twinning shear $\overline{\gamma}_\beta$ on twinning system β is determined by the time integration of the twinning shear rate which is given by the product between twinning shear γ_T and twinning rate g_β and thus reads

$$\overline{\gamma}_\beta = \int \gamma_T g_\beta \mathrm{d}t. \tag{3.17}$$

3.2.5 Defect density evolution

On the atomic scale, the plastic deformation of crystalline materials is accomplished by the discrete motion and propagation of defects like dislocations or twins. In crystal plasticity – as a continuum model – the plastic deformation of a crystal's lattice is, however, represented by continuous shear on its crystallographic planes, i.e. single dislocations or twins are not explicitly considered. Since the density of defects in a deformed volume is a direct measure for the stored energy of cold work and is closely related to work hardening and recovery processes, an additional set of internal variables for the defect densities and the corresponding evolution equations is introduced in the following.

The twinned volume fractions f_β on systems β and the total twinned volume fraction $f = \sum_\beta^{N^{\text{tw}}} f_\beta$ defined earlier, directly reflect the density of twins in the deformed volume. Analogically, the dislocation densities ρ_α^{dis} on systems α as well as the corresponding total dislocation density $\rho^{\text{dis}} = \sum_\alpha^{N^{\text{sl}}} \rho_\alpha^{\text{dis}}$ are introduced in the following.

Dislocation density evolution   The evolution of dislocation densities ρ_α^{dis} on slip systems α is modeled by a generation/recovery formulation proposed in [110–112]

$$\dot{\rho}_\alpha^{\text{dis}} = A_\alpha \left(\rho_\alpha^{\text{dis}} \right) |\nu_\alpha| - R_\alpha \left(\rho_\alpha^{\text{dis}}, \theta \right) \quad \text{with} \quad \rho_\alpha^{\text{dis}}|_{t=0} = \rho_{\alpha,0}^{\text{dis}}. \tag{3.18}$$

The first term on the right hand side of Equation (3.18) represents the dislocation accumulation due to shear on slip system α ($|\nu_\alpha| > 0$) whereas the second term describes thermal recovery processes. Herein, $A_\alpha \geq 0$ is described by (cf. [110, 111])

$$A_\alpha = A_{\alpha,0} \left[1 - \left[\frac{\rho_\alpha^{\text{dis}}}{\rho_{\alpha,\text{sat}}^{\text{dis}}} \right]^{p_\alpha} \right], \tag{3.19}$$

where $A_{\alpha,0} \geq 0$ is the reference accumulation coefficient, $\rho_{\alpha,\text{sat}}^{\text{dis}}$ is the saturation value for the dislocation density and $p_\alpha > 0$ is a constant. In [111], the reference accumulation coefficient $A_{\alpha,0}$ was declared to be temperature dependent which is, however, neglected here for the sake of simplicity.

Equation (3.19) represents the competition between dislocation accumulation and (athermal) annihilation which – in case no thermal recovery occurs (i.e. $R_\alpha = 0$) – will eventually lead to a steady state value of the dislocation density as ρ_α^{dis} approaches a certain saturation value $\rho_{\alpha,\text{sat}}^{\text{dis}}$ [113–115]. In this case, A_α approaches zero and plastic flow leads to no further increase in the dislocation density ρ_α^{dis}.

The thermal recovery term in Equation (3.18) is described by an Arrhenius type law (cf. [39, 111, 115])

$$R_\alpha = R_{\alpha,0} \exp \left(-\frac{Q_R}{k_B \theta} \right) \left\langle \frac{\rho_\alpha^{\text{dis}} - \rho_{\alpha,\text{min}}^{\text{dis}}}{\rho_{\text{ref}}^{\text{dis}}} \right\rangle^{q_\alpha} \tag{3.20}$$

where $R_{\alpha,0}$ denotes the reference recovery rate, Q_R is the activation energy for static recovery, k_B denotes the Boltzmann constant, $\rho_{\alpha,\text{min}}^{\text{dis}}$ is the minimum dislocation density for recovery to take place, $\rho_{\text{ref}}^{\text{dis}}$ is a reference dislocation density and the exponent $q_\alpha > 0$ is a constant. The parenthesis $\langle x \rangle$ denotes a function which is 0 for $x < 0$ and x for $x \geq 0$ and thus ensures that recovery only takes place if $\rho_\alpha^{\text{dis}} \geq \rho_{\alpha,\text{min}}^{\text{dis}}$.

Evolution of twinned volume fraction   The twinned volume fractions f_β evolve directly with the corresponding twinning rates, i.e.

$$\dot{f}_\beta = g_\beta. \tag{3.21}$$

While it has been observed in [83] that twins in the γ phase are relatively stable under annealing at temperatures close to the service conditions of TiAl alloys, it has been claimed in [11] that twins can easily recover at elevated temperatures. Due to the contradictory statements from [83] and [11], a potential reduction of the twinned volume fractions due to thermal recovery is for the moment neglected in the model.

3.2.6 Critical resolved shear stress

The critical resolved shear stresses, i.e. the strengths, of slip and twinning systems are the most important state variables of crystal plasticity models since they denote the onset of plastic deformation and evolve with work hardening. In a general form, the slip and twinning system strengths τ_α^Y and τ_β^T in equations (3.14) and (3.16) can be written as follows:

$$\tau_\alpha^Y = \tau_{\alpha,0}^Y + \Delta\tau_\alpha^Y, \tag{3.22}$$

$$\tau_\beta^T = \tau_{\beta,0}^T + \Delta\tau_\beta^T. \tag{3.23}$$

Herein, $\tau_{\alpha,0}^Y$ and $\tau_{\beta,0}^T$ denote the initial slip and twinning system strengths while the terms $\Delta\tau_\alpha^Y$ and $\Delta\tau_\beta^T$ denote their incremental increase with plastic deformation, i.e. represent work hardening. The dependence of the initial slip and twinning system strengths $\tau_{\alpha,0}^Y$ and $\tau_{\beta,0}^T$ on microstructural lengths (Hall-Petch strengthening) is modeled in Chapter 5. In Chapter 4, $\Delta\tau_\alpha^Y$ and $\Delta\tau_\beta^T$ are detailed as functions of dislocation densities ρ_α^{dis} and twinned volume fractions f_β in order to account for work hardening interactions between slip and twinning systems.

3.3 Thermomechanics and temperature evolution

In the present modeling approach, it is intended to consider the coupling between thermal and mechanical fields as it, e.g., appears in the form of thermal stresses or dissipative heat from plastic deformation. Thus, the thermomechanical coupling as it follows from continuum thermodynamics is presented in the following.

3.3.1 Continuum thermodynamics

The procedure of thermomechanical coupling closely follows the line of arguments presented in, e.g., [116–118] and is thus just briefly recalled here. By assuming conservation of mass and taking into account the balance of momentum, the first law of thermodynamics – i.e. the balance of total energy – reduces to the balance of internal energy ε which reads

$$\rho_0\dot{\varepsilon} = -\operatorname{Div}\boldsymbol{Q} + \frac{1}{2}\boldsymbol{S} : \dot{\boldsymbol{C}} + \rho_0 r. \tag{3.24}$$

In Equation (3.24), ρ_0 is the density in reference configuration, $\boldsymbol{Q}$ is the heat flux vector (described by Fourier's law, i.e. $\boldsymbol{Q} = -\kappa\operatorname{Grad}\theta$ with thermal conductivity κ and temperature θ) and r is the external heat supply per unit mass. The operator Div denotes the divergence with respect to the reference configuration, i.e. $\operatorname{Div}\boldsymbol{Q} = \sum_{i=1}^{3}\frac{\partial Q_i}{\partial X_i}$.

The second balance equation that is relevant for the thermomechanical coupling is the balance of entropy η which reads

$$\rho_0 \dot{\eta} = -\operatorname{Div}\left(\frac{\boldsymbol{Q}}{\theta}\right) + \rho_0 \left[\frac{r}{\theta} + \xi\right]. \tag{3.25}$$

In this, ξ denotes the internal entropy production. With the second law of thermodynamics, i.e. $\xi \geq 0$, Equation (3.25) is rewritten as

$$\rho_0 \dot{\eta} + \operatorname{Div}\left(\frac{\boldsymbol{Q}}{\theta}\right) - \rho_0 \frac{r}{\theta} \geq 0 \tag{3.26}$$

typically referred to as the Clausius–Duhem inequality. As link between the internal energy ε and the entropy η, the Helmholtz free energy ψ is introduced in its common form $\psi = \varepsilon - \eta\theta$. Multiplying the Clausius–Duhem inequality (Equation (3.26)) by θ and inserting the Helmholtz free energy and subsequently the balance of internal energy (Equation (3.24)) leads to

$$\rho_0 \theta \dot{\eta} + \theta \operatorname{Div}\left(\frac{\boldsymbol{Q}}{\theta}\right) - \rho_0 r \geq 0 \qquad \text{with } \dot{\psi} = \dot{\varepsilon} - \dot{\eta}\theta - \eta\dot{\theta}$$

$$\rho_0 \left[\dot{\varepsilon} - \dot{\psi} - \eta\dot{\theta}\right] + \theta \operatorname{Div}\left(\frac{\boldsymbol{Q}}{\theta}\right) - \rho_0 r \geq 0 \qquad \text{with } (3.24)$$

$$\rho_0 \left[-\dot{\psi} - \eta\dot{\theta}\right] + \theta \operatorname{Div}\left(\frac{\boldsymbol{Q}}{\theta}\right) - \operatorname{Div}\boldsymbol{Q} + \frac{1}{2}\boldsymbol{S} : \dot{\boldsymbol{C}} \geq 0 \qquad \text{exploit } \operatorname{Div}\boldsymbol{Q} = \frac{\boldsymbol{Q}}{\theta} \cdot \operatorname{Grad}\theta + \theta \operatorname{Div}\left(\frac{\boldsymbol{Q}}{\theta}\right)$$

$$\rho_0 \left[-\dot{\psi} - \eta\dot{\theta}\right] - \frac{\boldsymbol{Q}}{\theta} \cdot \operatorname{Grad}\theta + \frac{1}{2}\boldsymbol{S} : \dot{\boldsymbol{C}} \geq 0. \tag{3.27}$$

As a result of the multiplicative split of the deformation gradient, the stress power $\frac{1}{2}\boldsymbol{S} : \dot{\boldsymbol{C}}$ can be decomposed into an elastic and a plastic part by $\frac{1}{2}\boldsymbol{S} : \dot{\boldsymbol{C}} = \frac{1}{2}\boldsymbol{S}_E : \dot{\boldsymbol{C}}_E + \boldsymbol{M}_E : \boldsymbol{L}_P$ as, e.g., shown in [119]. This leads to

$$\rho_0 \left[-\dot{\psi} - \eta\dot{\theta}\right] - \frac{\boldsymbol{Q}}{\theta} \cdot \operatorname{Grad}\theta + \frac{1}{2}\boldsymbol{S}_E : \dot{\boldsymbol{C}}_E + \boldsymbol{M}_E : \boldsymbol{L}_P \geq 0. \tag{3.28}$$

For the present thermo-elasto-plastic problem, the Helmholtz free energy is additively split into a thermo-elastic and a thermo-plastic part, reading

$$\psi(\boldsymbol{C}_E, \theta, q_n) = \psi_E(\boldsymbol{C}_E, \theta) + \psi_P(\theta, q_n) \tag{3.29}$$

where the thermo-elastic part ψ_E is assumed to be a function of $\boldsymbol{C}_E$ and absolute temperature θ and the thermo-plastic part ψ_P is assumed to depend on θ and – in the moment not further detailed – plastic internal variables q_n. The corresponding time derivative reads

$$\dot{\psi} = \frac{\partial\psi}{\partial\boldsymbol{C}_E} : \dot{\boldsymbol{C}}_E + \frac{\partial\psi}{\partial\theta}\dot{\theta} + \sum_n \frac{\partial\psi}{\partial q_n}\dot{q}_n. \tag{3.30}$$

Inserting this time derivative into Equation (3.28) yields

$$\left[\frac{1}{2}\boldsymbol{S}_E - \rho_0 \frac{\partial\psi}{\partial\boldsymbol{C}_E}\right] : \dot{\boldsymbol{C}}_E - \rho_0 \left[\frac{\partial\psi}{\partial\theta} + \eta\right]\dot{\theta} + \boldsymbol{M}_E : \boldsymbol{L}_P - \rho_0 \sum_n \frac{\partial\psi}{\partial q_n}\dot{q}_n - \frac{\boldsymbol{Q}}{\theta} \cdot \operatorname{Grad}\theta \geq 0. \tag{3.31}$$

Since Equation (3.31) must hold for any choice of $\dot{\boldsymbol{C}}_E$ and $\dot{\theta}$, $\frac{1}{2}\boldsymbol{S}_E - \rho_0 \frac{\partial\psi}{\partial\boldsymbol{C}_E} = 0$ and $\frac{\partial\psi}{\partial\theta} + \eta = 0$ must hold [120]. From this, it follows

$$\boldsymbol{S}_E = 2\rho_0 \frac{\partial \psi}{\partial \boldsymbol{C}_E} \qquad \text{and} \tag{3.32}$$

$$\eta = -\frac{\partial \psi}{\partial \theta}. \tag{3.33}$$

As a remainder of Equation (3.31)), the reduced dissipation inequality is obtained to be

$$\mathcal{D} = \underbrace{\boldsymbol{M}_E : \boldsymbol{L}_P - \rho_0 \sum_n \frac{\partial \psi}{\partial q_n} \dot{q}_n}_{\mathcal{D}_{\text{mech}}} - \underbrace{\frac{\boldsymbol{Q}}{\theta} \cdot \text{Grad}\,\theta}_{\mathcal{D}_{\text{therm}}} \geq 0 \tag{3.34}$$

where $\mathcal{D}_{\text{mech}}$ and $\mathcal{D}_{\text{therm}}$ are the mechanical and the thermal part of dissipation $\mathcal{D}$.

3.3.2 Temperature evolution

Since mechanical dissipation (see Equation (3.34)) leads to an increase in temperature, a thermomechanically coupled formulation of the temperature evolution is derived in the following. The Helmholtz free energy ψ was defined earlier to be a function of the elastic right Cauchy-Green tensor $\boldsymbol{C}_E$, the absolute temperature θ and the plastic internal variables q_n. Following the principle of equipresence, the entropy η a priori is also a function of these quantities and its time derivative reads

$$\dot{\eta} = \frac{\partial \eta}{\partial \boldsymbol{C}_E} : \dot{\boldsymbol{C}}_E + \frac{\partial \eta}{\partial \theta}\dot{\theta} + \sum_n \frac{\partial \eta}{\partial q_n}\dot{q}_n \qquad \text{with (3.33)}$$

$$\Rightarrow \dot{\eta} = -\frac{\partial^2 \psi}{\partial \boldsymbol{C}_E \partial \theta} : \dot{\boldsymbol{C}}_E - \frac{\partial^2 \psi}{\partial \theta^2}\dot{\theta} - \sum_n \frac{\partial^2 \psi}{\partial q_n \partial \theta}\dot{q}_n. \tag{3.35}$$

Inserting the Helmholtz free energy ψ into the balance of internal energy, Equation (3.24), and making use of Equations (3.30), (3.32), (3.33) and (3.35) yields

$$\rho_0 \dot{\varepsilon} = -\text{Div}\,\boldsymbol{Q} + \frac{1}{2}\boldsymbol{S} : \dot{\boldsymbol{C}} + \rho_0 r \qquad \text{with } \dot{\psi} = \dot{\varepsilon} - \dot{\eta}\theta - \eta\dot{\theta}$$

$$\Rightarrow \rho_0 \left[\dot{\psi} + \dot{\eta}\theta + \eta\dot{\theta}\right] = -\text{Div}\,\boldsymbol{Q} + \frac{1}{2}\boldsymbol{S} : \dot{\boldsymbol{C}} + \rho_0 r \qquad \text{with (3.30)}$$

$$\Rightarrow \rho_0 \left[\frac{\partial \psi}{\partial \boldsymbol{C}_E} : \dot{\boldsymbol{C}}_E + \frac{\partial \psi}{\partial \theta}\dot{\theta} + \sum_n \frac{\partial \psi}{\partial q_n}\dot{q}_n + \dot{\eta}\theta + \eta\dot{\theta}\right] = -\text{Div}\,\boldsymbol{Q} + \frac{1}{2}\boldsymbol{S} : \dot{\boldsymbol{C}} + \rho_0 r \qquad \text{with (3.33)}$$

$$\Rightarrow \rho_0 \left[\frac{\partial \psi}{\partial \boldsymbol{C}_E} : \dot{\boldsymbol{C}}_E + \sum_n \frac{\partial \psi}{\partial q_n}\dot{q}_n + \dot{\eta}\theta\right] = -\text{Div}\,\boldsymbol{Q} + \frac{1}{2}\boldsymbol{S} : \dot{\boldsymbol{C}} + \rho_0 r \qquad \text{with (3.32)}$$

$$\Rightarrow \frac{1}{2}\boldsymbol{S}_E : \dot{\boldsymbol{C}}_E + \rho_0 \left[\sum_n \frac{\partial \psi}{\partial q_n}\dot{q}_n + \dot{\eta}\theta\right] = -\text{Div}\,\boldsymbol{Q} + \frac{1}{2}\boldsymbol{S} : \dot{\boldsymbol{C}} + \rho_0 r \qquad \text{with } \frac{1}{2}\boldsymbol{S} : \dot{\boldsymbol{C}} = \frac{1}{2}\boldsymbol{S}_E : \dot{\boldsymbol{C}}_E + \boldsymbol{M}_E : \boldsymbol{L}_P$$

$$\Rightarrow \rho_0 \left[\sum_n \frac{\partial \psi}{\partial q_n}\dot{q}_n + \dot{\eta}\theta\right] = -\text{Div}\,\boldsymbol{Q} + \boldsymbol{M}_E : \boldsymbol{L}_P + \rho_0 r \qquad \text{with (3.35) and again (3.32)}$$

$$\Rightarrow \rho_0 \left[\sum_n \frac{\partial \psi}{\partial q_n}\dot{q}_n + \left[-\frac{\partial^2 \psi}{\partial \theta^2}\dot{\theta} - \sum_n \frac{\partial^2 \psi}{\partial q_n \partial \theta}\dot{q}_n\right]\theta\right] = -\text{Div}\,\boldsymbol{Q} + \boldsymbol{M}_E : \boldsymbol{L}_P + \frac{1}{2}\theta\frac{\partial \boldsymbol{S}_E}{\partial \theta} : \dot{\boldsymbol{C}}_E + \rho_0 r \qquad \text{rearrange}$$

$$\Leftrightarrow -\rho_0 \theta \frac{\partial^2 \psi}{\partial \theta^2}\dot{\theta} = -\text{Div}\,\boldsymbol{Q} + \boldsymbol{M}_E : \boldsymbol{L}_P - \rho_0 \sum_n \frac{\partial \psi}{\partial q_n}\dot{q}_n + \frac{1}{2}\theta\frac{\partial \boldsymbol{S}_E}{\partial \theta} : \dot{\boldsymbol{C}}_E + \rho_0 r$$

$$+ \rho_0 \theta \sum_n \frac{\partial^2 \psi}{\partial q_n \partial \theta} \dot{q}_n. \tag{3.36}$$

Defining the heat capacity as $c_p = -\theta \frac{\partial^2 \psi}{\partial \theta^2}$ finally yields the equation for the temperature evolution

$$\rho_0 c_p \dot{\theta} = -\operatorname{Div} \boldsymbol{Q} + \underbrace{\boldsymbol{M}_E : \boldsymbol{L}_P - \rho_0 \sum_n \frac{\partial \psi}{\partial q_n} \dot{q}_n}_{D_{\mathrm{mech}}} + \frac{1}{2} \theta \frac{\partial \boldsymbol{S}_E}{\partial \theta} : \dot{\boldsymbol{C}}_E + \rho_0 r + \rho_0 \theta \sum_n \frac{\partial^2 \psi}{\partial q_n \partial \theta} \dot{q}_n. \tag{3.37}$$

3.3.3 Helmholtz free energy

In the previous sections, the Helmholtz free energy ψ was assumed to be a function of the elastic Cauchy-Green strain tensor $\boldsymbol{C}_E$, the absolute temperature θ and the so far not further specified plastic internal variables q_n. Assuming $\frac{\partial \psi}{\partial q_n} > 0$ (see [111]), it becomes clear from Equations (3.34) and (3.37) that an increase of the plastic internal variables q_n (i.e. $\dot{q}_n > 0$) reduces the part of the plastic stress power $\boldsymbol{M}_E : \boldsymbol{L}_P$ which is dissipated to heat. Consequently, the plastic internal variables are related to the stored energy of cold work. Since the defect densities within a plastically deformed volume are directly related to the stored energy of cold work, they are a natural choice for the plastic internal variables, enabling a physically meaningful representation of mechanical dissipation and temperature evolution.

While the contribution of dislocations to the stored energy of cold work is directly proportional to the dislocation densities $\rho_\alpha^{\mathrm{dis}}$, the contribution of twins to the stored energy of cold work is given by the fixed energy per twin/matrix interface [11]. Since twin growth is accomplished by propagation of the twin/matrix interface, the respective energy per twin does not change with its size. Thus, the contribution of twin/matrix interfaces to the stored energy of cold work can only be assessed if the discrete number of twins is known. However, in the presented model twins are considered in terms of twinned volume fractions f_β and their number is thus not known. Therefore, the contribution of twins to the stored energy of cold work is neglected in the following by assuming that the Helmholtz energy is no function of the twinned volume fraction. With the dislocation densities $\rho_\alpha^{\mathrm{dis}}$ as the only plastic internal variables, the Helmholtz free energy from equation (3.29) is rewritten as

$$\rho_0 \psi := \rho_0 \psi_E(\boldsymbol{C}_E, \theta) + \rho_0 \psi_P(\rho_\alpha^{\mathrm{dis}}, \theta). \tag{3.38}$$

The thermo-elastic part of the Helmholtz free energy $\rho_0 \psi_E$ is assumed to follow a Neo-Hookean type behavior[4] [118, 121]

$$\rho_0 \psi_E = \frac{\mu}{2} \left[\operatorname{tr} \boldsymbol{C}_E - 3 \right] + \frac{\lambda}{2} \ln^2 J_E - \mu \ln J_E - 3\alpha_t K [\theta - \theta_0] \frac{\ln J_E}{J_E} \tag{3.39}$$

$$+ \rho_0 c_p \left[\theta - \theta_0 - \theta \ln \left[\frac{\theta}{\theta_0} \right] \right] - [\theta - \theta_0] S_0,$$

where α_t denotes the (temperature dependent) thermal expansion coefficient. The Lamé constants $\mu = \frac{E}{2(1+\nu)}$ and $\lambda = \frac{\nu E}{(1+\nu)(1-2\nu)}$ and the bulk modulus $K = \frac{E}{3-6\nu}$ are herein defined in terms of the (temperature dependent) Young's modulus E and the (temperature dependent)

---

[4]In this, the elastic anisotropy of the single phases as it was determined, e.g., in [31, 32] is neglected since the elastic deformation remains small as compared to the plastic deformation.

Poisson's ratio ν. Finally, θ_0 and S_0 denote the reference temperature and the reference entropy density.

Following [110, 111], the thermo-plastic part of the Helmholtz free energy $\rho_0\psi_P$ reads

$$\rho_0\psi_P = aG\sum_{\alpha}^{N^{\mathrm{sl}}} b_\alpha^2\rho_\alpha^{\mathrm{dis}}. \tag{3.40}$$

Herein, $G = \frac{E}{2[1+\nu]}$ denotes the (temperature dependent) shear modulus and b_α is the (temperature dependent) magnitude of the Burgers vector of slip system α. The material specific constant is chosen to $a \approx 0.5$ which is typical for TiAl alloys [11].

With this thermomechanical definition of the Helmholtz free energy and the relations (3.32) and (3.37), the governing equations – i.e. the balance of linear momentum and the temperature evolution equation – read

$$0 = \mathrm{Div}\left(\boldsymbol{F}_E\underbrace{\left[\mu[\boldsymbol{I} - \boldsymbol{C}_E^{-1}] + \left[\lambda\ln J_E - \frac{3\alpha_t K}{J_E}[\theta - \theta_0][1 - \ln J_E]\right]\boldsymbol{C}_E^{-1}\right]}_{\boldsymbol{S}_E}\right) + \rho_0\boldsymbol{b} \tag{3.41}$$

$$\rho_0 c_p\dot{\theta} = -\mathrm{Div}\,\boldsymbol{Q} + \boldsymbol{M}_E : \boldsymbol{L}_P - a\sum_{\alpha}^{N^{\mathrm{sl}}}\left[G - \theta\frac{dG}{d\theta}\right]b_\alpha^2\dot{\rho}_\alpha^{\mathrm{dis}} + \rho_0 r + \frac{1}{2}\theta\frac{\partial\boldsymbol{S}_E}{\partial\theta} : \dot{\boldsymbol{C}}_E \tag{3.42}$$

where $\boldsymbol{b}$ are the body forces per unit mass. In this, the temperature dependence of the magnitude of the Burgers vector is neglected.

3.3.4 Temperature dependent model parameters

The temperature dependent model parameters that are used throughout this thesis are summarized in Table 3.3. The parameters in Table 3.3 were obtained by linear interpolation of experimental data from literature. If no single phase parameters were reported, the corresponding parameters of two phase alloys were used.

3.4 Implementation into FEM

In this section, the implementation of the presented defect density based, thermomechanically coupled crystal plasticity model into the commercial FE software ABAQUS is presented.

3.4.1 Algorithmic formulation

The evolution of state variables in the crystal plasticity model introduced above is defined in terms of rates which have to be transformed into an algorithmic formulation before being implemented into FEM. Therefore, the temporal evolution of the state variables is discretized in time intervals

$$\Delta t = t_{n+1} - t_n \tag{3.43}$$

between state n and state $n + 1$. With this time discretization, the shear rates ν_α on slip systems α and the twinning rates g_β on twinning systems β are described in terms of shear increments

$$\Delta\gamma = \gamma_{n+1} - \gamma_n \tag{3.44}$$

Table 3.3. Temperature dependent model parameters that were used throughout this thesis. The reported experiments were carried out in the indicated temperature range. If no parameters for the single phases are available, the parameters of two phase alloys were used instead.

γ phase			
symbol	value	temp. range [°C]	composition	ref.
E	$173.59\,\text{GPa} - 0.0342[T - T_0]\,\frac{\text{GPa}}{\text{°C}}$	$T_0 = 25 < T < 935$	Ti-50Al	[122]
ν	$0.234 + 6.7 \cdot 10^{-6}[T - T_0]\,\frac{1}{\text{°C}}$	$T_0 = 25 < T < 847$	Ti-50Al	[122]
$\frac{c}{a}$	$1.00356 + 7.2 \cdot 10^{-6}[T - T_0]\,\frac{1}{\text{°C}}$	$T_0 = 20 < T < 1450$	Ti-46Al-1.9Cr-3Nb	[123]
a	$0.3997\,\text{nm}$			[11]

α_2 phase			
symbol	value	temp. range [°C]	composition	ref.
E	$147.05\,\text{GPa} - 0.0525[T - T_0]\,\frac{\text{GPa}}{\text{°C}}$	$T_0 = 25 < T < 954$	Ti-27.6Al	[122]
ν	$0.295 - 5.9 \cdot 10^{-5}[T - T_0]\,\frac{1}{\text{°C}}$	$T_0 = 25 < T < 954$	Ti-27.6Al	[122]
$\frac{c}{a}$	$0.804 \approx const.$	$T_0 = 20 < T < 1450$	Ti-46Al-1.9Cr-3Nb	[123]
a	$0.5765\,\text{nm}$			[11]

γ/α_2 phase combined			
symbol	value	temp. range [°C]	composition	ref.
ρ_0	$4.219\,\frac{\text{g}}{\text{cm}^3} - 1.579 \cdot 10^{-4}[T - T_0]\,\frac{\text{g}}{\text{cm}^3\,\text{°C}}$	$T_0 = 25 < T < 1150$	Ti-45.5Al-8Nb	[124]
c_p	$0.6207\,\frac{\text{J}}{\text{g\,°C}} + 1.5897 \cdot 10^{-4}[T - T_0]\,\frac{\text{J}}{\text{g[°C]}^2}$	$T_0 = 20 < T < 900$	Ti-45.5Al-8Nb	[125]
κ	$15.35\,\frac{\text{W}}{\text{m\,°C}} + 1.364 \cdot 10^{-2}[T - T_0]\,\frac{\text{W}}{\text{m[°C]}^2}$	$T_0 = 100 < T < 900$	Ti-47Al-4(Nb,W,B)	[125]
α_t	$8.936 \cdot 10^{-6}\,\frac{1}{\text{°C}} + 3.4 \cdot 10^{-9}[T - T_0]\,\frac{1}{[\text{°C}]^2}$	$T_0 = 100 < T < 900$	Ti-47Al-4(Nb,W,B)	[125]

and read

$$\nu_\alpha = \frac{\Delta\gamma_\alpha}{\Delta t} \qquad \text{and} \tag{3.45}$$

$$g_\beta = \frac{1}{\gamma_T}\frac{\Delta\gamma_\beta}{\Delta t}. \tag{3.46}$$

Analogically, the evolution of dislocation densities ρ_α^{dis} and twinned volume fractions f_β are defined by the discrete form

$$\dot{\rho}_\alpha^{\text{dis}} = \frac{\rho_{\alpha,n+1}^{\text{dis}} - \rho_{\alpha,n}^{\text{dis}}}{\Delta t} \qquad \text{and} \tag{3.47}$$

$$\dot{f}_\beta = \frac{f_{\beta,n+1} - f_{\beta,n}}{\Delta t}. \tag{3.48}$$

With this, a forward Euler form is obtained from Equations (3.18) and (3.21) which reads

$$\rho_{\alpha,n+1}^{\text{dis}} = \rho_{\alpha,n}^{\text{dis}} + A_{\alpha,0}\left[1 - \left[\frac{\rho_{\alpha,n}^{\text{dis}}}{\rho_{\alpha,\text{sat}}^{\text{dis}}}\right]^{p_\alpha}\right]|\Delta\gamma_\alpha| - R_{\alpha,0}\exp\left(-\frac{Q_R}{k_B\theta_{n+1}}\right)\left\langle\frac{\rho_{\alpha,n}^{\text{dis}} - \rho_{\alpha,\text{min}}^{\text{dis}}}{\rho_{\text{ref}}^{\text{dis}}}\right\rangle^{q_\alpha}\Delta t \qquad \text{and} \tag{3.49}$$

$$f_{\beta,n+1} = f_{\beta,n} + \frac{1}{\gamma_T}\Delta\gamma_\beta. \tag{3.50}$$

In order to derive an algorithmic representation of the evolution equation for the plastic deformation gradient $\boldsymbol{F}_P$ from Equation (3.9), the discrete form

$$\dot{\boldsymbol{F}}_P = \frac{\boldsymbol{F}_{P,n+1} - \boldsymbol{F}_{P,n}}{\Delta t} \tag{3.51}$$

is introduced. With Equation (3.51), a forward Euler form of Equation (3.9) is derived which analogous to [126] reads

$$\boldsymbol{F}_{P,n+1} = \text{uni}\left(\boldsymbol{I} + \left[1 - \sum_{\beta}^{N^{\text{tw}}} f_{\beta,n+1}\right] \sum_{\alpha}^{N^{\text{sl}}} \Delta\gamma_\alpha \left[\boldsymbol{s}_\alpha \otimes \boldsymbol{n}_\alpha\right] + \sum_{\beta}^{N^{\text{tw}}} \Delta\gamma_\beta \left[\boldsymbol{s}_\beta \otimes \boldsymbol{n}_\beta\right]\right) \cdot \boldsymbol{F}_{P,n}. \tag{3.52}$$

In this, the unimodular part $(\text{uni}(\boldsymbol{A}) = \boldsymbol{A}/\det(\boldsymbol{A})^{1/3}$ for any second-order tensor $\boldsymbol{A})$ was taken of both sides while requiring $\det(\boldsymbol{F}_P) = 1$ in order to enforce the plastic incompressibilty (see [126]).

3.4.2 Implementation as user material subroutine

In the presented algorithmic form, the model was implemented into the commercial FE-code ABAQUS via an UMAT user material subroutine. In every time step, ABAQUS hands over the deformation gradient and the temperature and requests the user to return the corresponding Cauchy stress tensor (STRESS) and the volumetric heat generation (RPL). Further, ABAQUS requires the stress tangents with respect to strain (DDSDDE) and temperature (DDSDDT) as well as the tangents of the volumetric heat generation with strain (DRPLDE) and temperature (DRPLDT).

In order to identify the internal state variables – namely the accumulated shears $\gamma_{\alpha,n+1}$ and $\gamma_{\beta,n+1}$, dislocation densities $\rho_{\alpha,n+1}^{\text{dis}}$, twinned volume fractions $f_{\beta,n+1}$ and the plastic deformation gradient $\boldsymbol{F}_{P,n+1}$ – at the end of the current time step, the algorithmic formulation of the evolution equations as it was derived in the previous section has to be solved iteratively as shown in Figure 3.2. Once this iterative procedure converged, the Cauchy stress tensor is calculated and handed over to ABAQUS via the STRESS array. In the implemented UMAT subroutine, the derivatives that are necessary to determine the volumetric heat generation (RPL) and the required tangents (DDSDDE,DDSDDT,DRPLDE and DRPLDT) are set up numerically in terms of a finite difference approximation. Therefore, the iterative procedure in Figure 3.2 has to be solved again multiple times for systematic perturbations of the deformation gradient and the temperature. In this, the number of necessary iteration loops was reduced by applying the scheme reported in [127] which allows to determine the tangents with respect to strain by only 6 systematic perturbations of the deformation gradient $\boldsymbol{F}$ (instead of individually perturbing each of its 9 components).
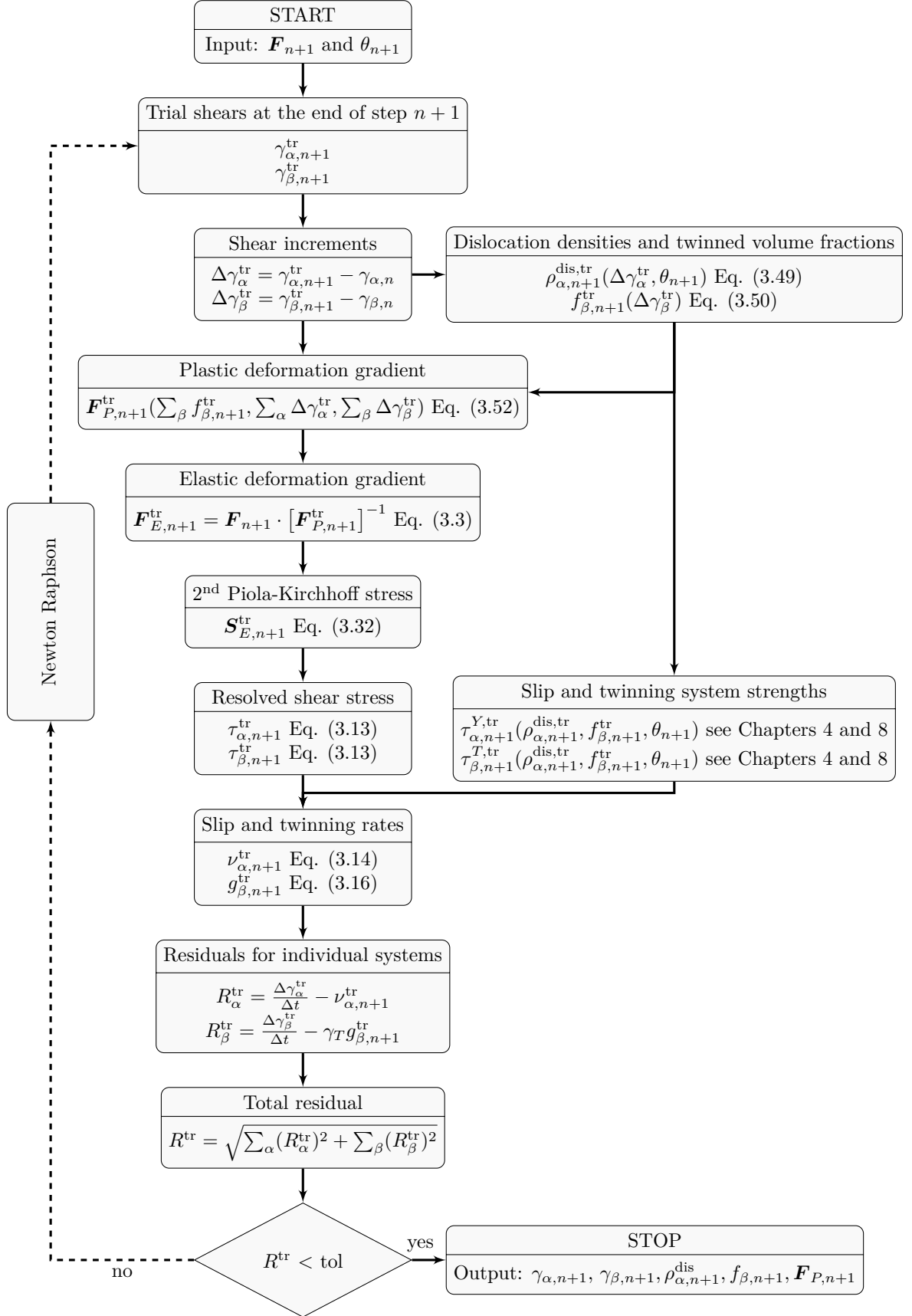
Figure 3.2. Flow chart for iteratively determining the state variables of the crystal plasticity model

3.5 Representative volume elements and discretization

The constitutive model presented in the previous section incorporates all features that are relevant to describe the crystal mechanics of the γ as well as the α_2 phase. However, the model was formulated in a single crystal plasticity framework. Thus, the crystal plasticity model has to be applied to an appropriate geometrical representation, namely an RVE, of the lamellar microstructure in order to capture the kinematic constraints that arise between neighboring lamellae and between neighboring colonies.

In the following, two periodic RVEs are set up to serve as geometrical input for the intended FE analyses – one of a polysynthetically twinned crystal and one of a polycolony fully lamellar microstructure.

3.5.1 Representative volume element of a polysynthetically twinned crystal

As shown in [73] by comparing simulation results with different RVEs, it is sufficient to model only seven lamellae, namely one α_2 lamella and one lamella for each γ orientation variant, to capture the influence of the crystallography of a polysynthetically twinned crystal on its deformation behavior. In the present thesis, a periodic RVE of a polysynthetically twinned crystal is set up in terms of a single α_2 lamella and an alternating sequence of 3 γ matrix and 3 γ twin lamellae each subdivided into domains to account for the different matrix and twin orientations that occur along the γ lamellae. The volume fraction V_{α_2} of the α_2 phase is considered by adjusting the thickness of the α_2 lamella accordingly. The remaining volume ($V_\gamma = 1 - V_{\alpha_2}$) is assumed to be divided equally between the 6 γ orientation variants so that the γ lamellae all have the same thickness. This set up is schematically shown in Figure 3.3.
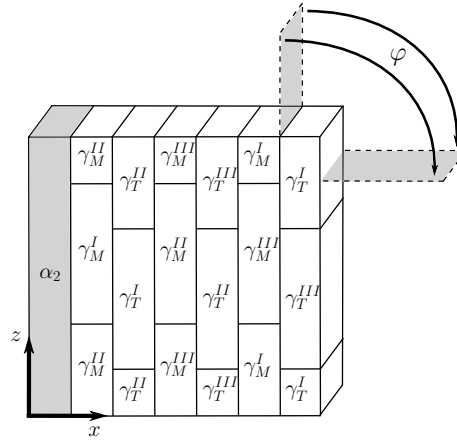
Figure 3.3. RVE of polysynthetically twinned crystal. φ: angle between uniaxial load and lamella plane; $\gamma_{M/T}^{I-III}$: six orientation variants of γ phase according to Figure 2.5 (three matrix and three twin orientations). Figure taken from Schnabel & Bargmann [2].

The RVE was discretized using linear hexahedral elements with a temperature degree of freedom (C3D8T) and was subjected to periodic boundary conditions (see Section 3.6.1). The orientation of the RVE with respect to the applied uniaxial load (angle φ in Figure 3.3) was realized as described in Section 3.6.2.

3.5.2 Representative volume element of a polycolony microstructure

The periodic RVE of a polycolony microstructure that is used throughout this thesis is based on a 2D Voronoi tesselation where the Voronoi cells are supposed to represent the outlines of the lamellar colonies. In order to avoid the formation of degenerated Voronoi cells as they frequently occur for completely random sets of seed points, the seeds were initially chosen such that the Voronoi cells are hexagonal. However, 2D Voronoi diagrams are usually not periodic due to irregularities that occur at their boundaries (e.g. cells that are not closed). In order to still obtain a periodic RVE from a Voronoi tesselation, the seeds of the actual RVE are usually duplicated with an offset of $\pm w$ in x and $\pm h$ in y direction where w and h denote the width and the height of the RVE. This is illustrated in Figure 3.4 for an examplary set of 4 seeds.
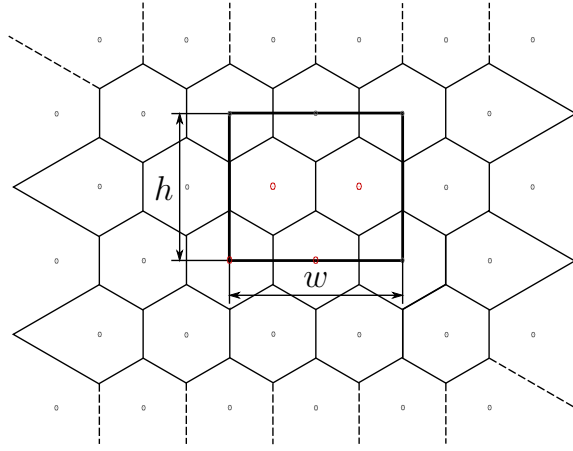
Figure 3.4. 2D Voronoi tesselation for a set of 4 regularly spaced seeds (red dots) that were duplicated in a 3 by 3 pattern to obtain periodic cells in the center region.

In order to obtain less regular shaped colonies while still avoiding degenerated cells, the initial seeds were randomly displaced within a circular region around their initial positions. The duplicated seeds were displaced according to their parent seeds to ensure that the periodicity of the Voronoi diagrams center region (i.e. of the actual RVE) is maintained. The radius of the region in which the seeds are displaced is $r = \zeta r_i$ where r_i is the inner radius of the hexagonal Voronoi cells and $0 \leq \zeta \leq 1$ is a constant. This randomization is illustrated in Figures 3.5(a) and (b) for the center region of the Voronoi diagram from Figure 3.4.

For the RVE used here, this process was carried out for a set of 36 seeds, representing 36 colonies. The parameter ζ was set to 0.9. The resulting Voronoi cells were then imported as x, y sketches to ABAQUS and extruded in z direction. By boolean intersection of the single colonies and a set of coplanar planes, the lamellae were introduced. The orientation of the lamella plane in each colony is uniquely defined by only one angle φ_i rotating around the z-axis, i.e. the normal vectors of the lamella planes of all colonies are assumed to lie within the x, y plane. To minimize the influence of texture, the orientations of the colonies are evenly distributed between $\varphi_i = 0°$ and $\varphi_i = 360°$ (i.e. $\varphi_i = i\frac{360°}{n_{\text{col}}}$ for $i = 1, 2, ..., n_{\text{col}}$). As reviewed in Section 3.1.2, it is unfavorable to set up a one to one discretization of a polycolony microstructure for FEM calculations. Thus, only a reduced number of 15 lamellae with all the same thickness was considered in each colony. Each lamella was assigned to be either of the α_2 phase or of one of the 6 orientation variants of the γ phase while attention was paid to correctly reproduce the corresponding volume fractions in each colony. The different
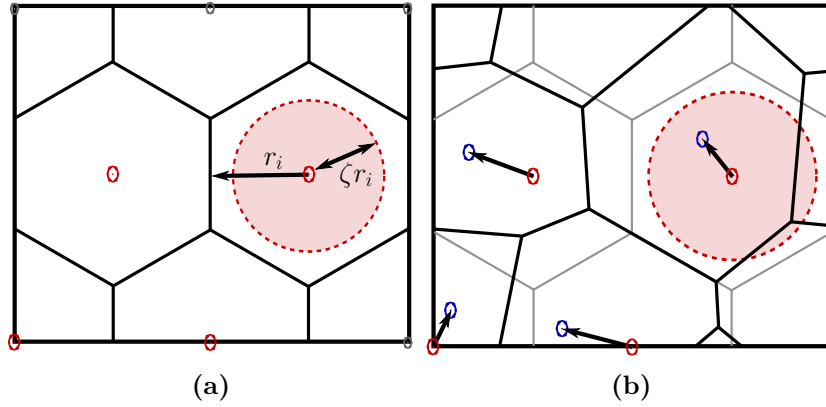
Figure 3.5. Randomization of the initially regular hexagonal Voronoi diagram. (a): The red circle indicates the region in which the initially regular spaced seeds are randomly displaced. The radius of the circle is determined by ζr_i where r_i is the inner radius of the hexagonal Voronoi cells and $0 \leq \zeta \leq 1$ is a constant (b): Voronoi diagram after displacing the initial seeds. The initial seeds are marked in red, blue dots mark the location off the displaced seeds

γ orientation variants were all assumed to occur with the same volume fraction. It was found that the 15 lamellae per colony are sufficient to reproduce most of the common volume fractions to a good accuracy. The created RVE is shown in Figure 3.6 for an assigned α_2 volume fraction of 10%.

This RVE was subjected to periodic boundary conditions (see Section 3.6.1) and meshed using linear wedge elements with a temperature degree of freedom (C3D6T).

3.6 Boundary conditions

In the context of micromechanical modeling of periodic unit cells, the applied boundary conditions are of particular interest. Thus, the here used boundary conditions will be presented in the following.

3.6.1 Periodic boundary conditions

The idea of periodic RVEs is that they yield a space filling continuous representation of the microstructure when being repeated in a tile pattern. For the undeformed state this is easily fulfilled if the geometry of the RVE is set up periodically. However, the opposing faces of the RVE have to fit into each other for any deformation state. This is achieved by applying periodic boundary conditions which constrain the deformation of the RVEs opposing boundaries accordingly as illustrated for an exemplary 2D unit cell in Figure 3.7.

In the context of FEM, these constraints are prescribed in terms of the displacements of nodes that lie on opposing faces of the unit cell. With x^+ and x^- denoting opposing faces of the unit cell with normal vectors of the undeformed face in x direction, the coupling of the displacements $\boldsymbol{u}$ of the ith pair of opposite nodes is described by

$$\boldsymbol{u}_i^{x^+} - \boldsymbol{u}_i^{x^-} = \boldsymbol{u}_{M_x} - \boldsymbol{u}_0 \tag{3.53}$$

$$\boldsymbol{u}_i^{y^+} - \boldsymbol{u}_i^{y^-} = \boldsymbol{u}_{M_y} - \boldsymbol{u}_0 \tag{3.54}$$
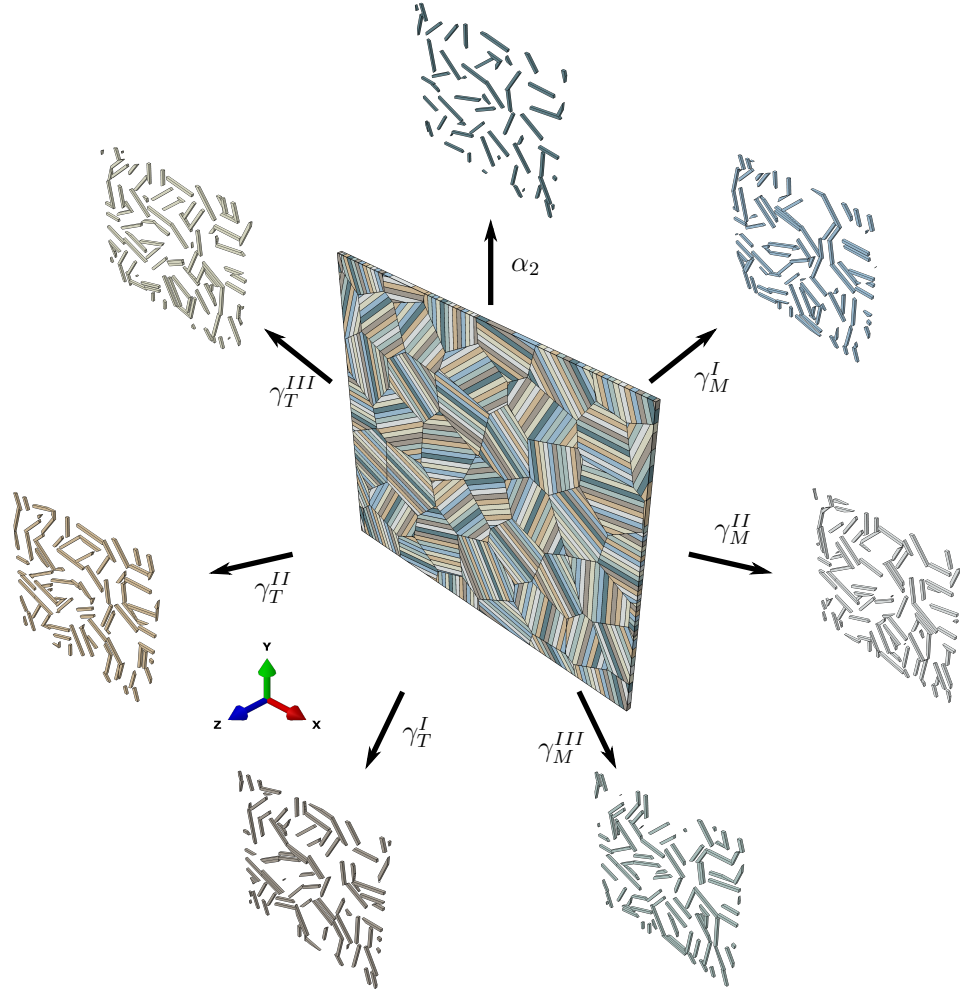
Figure 3.6. RVE of polycolony fully lamellar microstructure consisting of 36 lamellar colonies. Separate depiction of the α_2 phase and the 6 orientation variants of the γ phase ($\gamma_{M/T}^{I-III}$ according to Figure 2.5) shows their distribution within the colonies. Figure taken from Schnabel & Bargmann [2].

which reduces to

$$\boldsymbol{u}_i^{x^+} = \boldsymbol{u}_i^{x^-} + \boldsymbol{u}_{M_x} \tag{3.55}$$

$$\boldsymbol{u}_i^{y^+} = \boldsymbol{u}_i^{y^-} + \boldsymbol{u}_{M_y} \tag{3.56}$$

when fixing node 0 in order to prevent rigid body translations. From this definition, it follows

$$\boldsymbol{u}_{N_{xy}} = \boldsymbol{u}_{M_x} + \boldsymbol{u}_{M_y} \tag{3.57}$$

for the node N_{xy}.

The nodes M_x and M_y are called master nodes since the deformation of all faces is coupled to their displacement. Consequently, the displacements of the master nodes are usually prescribed to load the RVE.
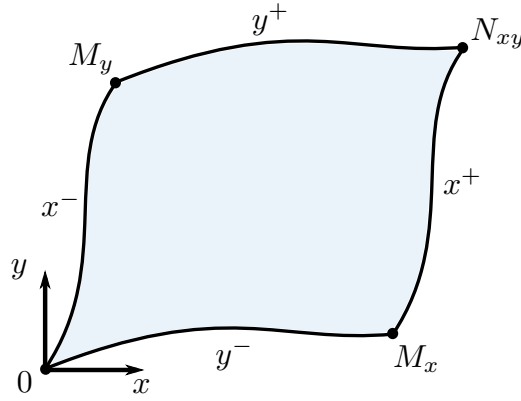
Figure 3.7. Exemplary 2D unit cell subjected to periodic boundary conditions.

The temperature boundary conditions are treated analogically and thus read [5]

$$\theta_i^{x^+} - \theta_i^{x^-} = \theta_{M_x} - \theta_0 \tag{3.58}$$

$$\theta_i^{y^+} - \theta_i^{y^-} = \theta_{M_y} - \theta_0. \tag{3.59}$$

The periodic boundary conditions for 3D RVEs are set up analogically to the 2D case by introducing a third master node M_z and corresponding equations for the displacements and temperature

$$\boldsymbol{u}_i^{z^+} = \boldsymbol{u}_i^{z^-} + \boldsymbol{u}_{M_z} \tag{3.60}$$

$$\theta_i^{z^+} - \theta_i^{z^-} = \theta_{M_z} - \theta_0. \tag{3.61}$$

3.6.2 Rotation of load on representative volume element of a polysynthetically twinned crystal

In the course of this thesis, several aspects of the plastic anisotropy of polysynthetically twinned crystals/single colonies ought to be investigated. Thus, the angle between the uniaxial load and the lamella plane of the corresponding RVE (see Section 3.5.1) has to be adjustable. This is achieved by adopting the approach that was presented in [72]. In this approach, the RVE of a polysynthetically twinned crystal is subjected to periodic boundary conditons and then embedded into a single finite element with the same size as the RVE. This dummy element is defined here as a linear hexahedral element with reduced integration (C3D8R) – i.e. only contains one integration point – and has a negligible stiffness of $0.01\,\text{MPa}$ assigned to it. Figure 3.8 shows the nodes of the dummy element. The dummy element is subjected to periodic boundary conditions and its rigid body translations and rotations are suppressed

---

[5]It has to be noted that periodic boundary conditions are somewhat ill-defined for heat conduction problems. The idea of hypothetically repeating the periodic RVE in a tile pattern to represent the microstructure introduces a paradox for the temperatures. While this concept requires the temperatures of opposite nodes on opposing faces to be identical in order to yield a continous temperature field, the absence of a temperature gradient normal to the RVEs surface inhibits heat conduction over the RVEs boundaries. In contrary, assuming the temperature gradient to be equal between all opposite nodes of opposing faces – as it is done in Equations (3.58) and (3.59) – results in a periodic heat flux but introduces discontinuities in the temperature field [128].

by setting $u_1^x = u_1^y = u_1^z = u_2^x = u_2^z = u_4^z = 0$ while uniaxial loading is prescribed in terms of the displacement u_5^z of the master node of its z^+ surface.
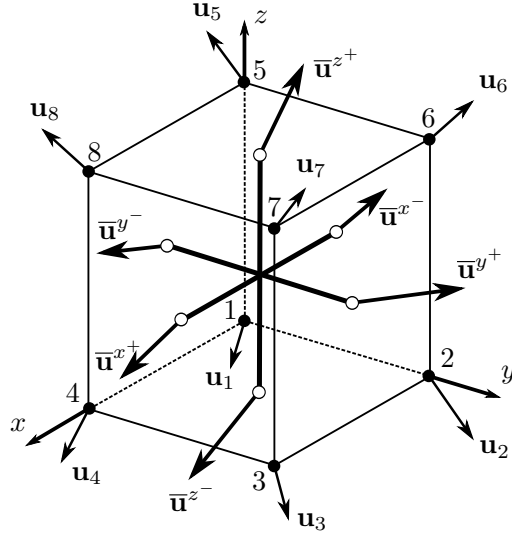
Figure 3.8. Nodes and displacements of the dummy element. Following [29].

The deformation of the dummy element from Figure 3.8 is calculated by averaging the displacements of each of its faces and then determining the difference between the averaged displacements of opposing faces. With the nomenclature from Figure 3.8, the averaged displacements of the dummy element are defined as (cf. [29, 72])

$$\overline{\boldsymbol{u}}_x = \overline{\boldsymbol{u}}^{x^+} - \overline{\boldsymbol{u}}^{x^-} = [\boldsymbol{u}_3 + \boldsymbol{u}_4 + \boldsymbol{u}_7 + \boldsymbol{u}_8]/4 - [\boldsymbol{u}_1 + \boldsymbol{u}_2 + \boldsymbol{u}_5 + \boldsymbol{u}_6]/4 \tag{3.62}$$

$$\overline{\boldsymbol{u}}_y = \overline{\boldsymbol{u}}^{y^+} - \overline{\boldsymbol{u}}^{y^-} = [\boldsymbol{u}_2 + \boldsymbol{u}_3 + \boldsymbol{u}_6 + \boldsymbol{u}_7]/4 - [\boldsymbol{u}_1 + \boldsymbol{u}_4 + \boldsymbol{u}_5 + \boldsymbol{u}_8]/4 \tag{3.63}$$

$$\overline{\boldsymbol{u}}_z = \overline{\boldsymbol{u}}^{z^+} - \overline{\boldsymbol{u}}^{z^-} = [\boldsymbol{u}_5 + \boldsymbol{u}_6 + \boldsymbol{u}_7 + \boldsymbol{u}_8]/4 - [\boldsymbol{u}_1 + \boldsymbol{u}_2 + \boldsymbol{u}_3 + \boldsymbol{u}_4]/4. \tag{3.64}$$

By implementing a rotational relation between the averaged displacements $\overline{\boldsymbol{u}}_x$, $\overline{\boldsymbol{u}}_y$ and $\overline{\boldsymbol{u}}_z$ of the dummy element and the displacements $\boldsymbol{u}_{Mx}$, $\boldsymbol{u}_{My}$ and $\boldsymbol{u}_{Mz}$ of the RVE's master nodes, it is possible to simulate uniaxial loading of the rotated RVE without having to change the simulation set up. In the course of this thesis, the RVE presented in Figure 3.3 is solely rotated within the x,z plane, i.e. around its y axis. Following [29, 72], the corresponding rotational relation reads

$$\boldsymbol{U}_{\mathrm{RVE}} = \boldsymbol{R}_y^T \cdot \boldsymbol{U}_{\mathrm{dummy}} \cdot \boldsymbol{R}_y \tag{3.65}$$

where $\boldsymbol{U}_{\mathrm{RVE}} = (\boldsymbol{u}_{Mx}, \boldsymbol{u}_{My}, \boldsymbol{u}_{Mz})^T$ is the matrix of the displacements of the RVE's master nodes, $\boldsymbol{R}_y$ is the rotation matrix about the y axis (cf. Figure 3.3) and $\boldsymbol{U}_{\mathrm{dummy}} = (\overline{\boldsymbol{u}}_x, \overline{\boldsymbol{u}}_y, \overline{\boldsymbol{u}}_z)^T$ is the matrix of the averaged displacements of the dummy element.

4 Work hardening

The work hardening behavior of fully lamellar TiAl has been investigated in comparatively few experimental studies which can largely be explained by its limited (tensile) ductility at room temperature [39, 129, 130]. Nevertheless, the work hardening behavior of fully lamellar TiAl can be investigated in compression tests in which considerable plastic strains can be achieved. Due to the pronounced plastic anisotropy of the single lamellar colonies (cf. Figure 2.7) polycolony microstructures show a highly inhomogeneous microplasticity, i.e. the plastic deformation is mainly accomplished by weakly oriented colonies which in consequence experience considerable plastic strains (and thus work hardening) even prior to macroscopic yield (see, e.g., digital image correlation (DIC) results in [131–133]). Due to this phenomenon – which will be investigated in Chapter 6 and is referred to as *microyield* in the following – it is crucial to model the anisotropic work hardening behavior of the lamellar colonies up to several % plastic strain when aiming to accurately predict the plastic deformation behavior of a polycolony microstructure.

In the crystal plasticity framework introduced above, work hardening was simply described as the – so far not further specified – increment of the critical resolved shear stresses due to plastic deformation (cf. Equations (3.22) and (3.23)). In this chapter, the work hardening terms in Equations (3.22) and (3.23) will be specified with respect to the evolving defect densities in the deformed volume. The presented work hardening model will then be calibrated against macroscopic stress strain curves obtained from experiments with polysynthetically twinned crystals reported in [52]. In order to supplement the somewhat fragmented experimental data available, the calibrated model will subsequently be used to investigate the post yield behavior of polysynthetically twinned crystals/single colonies in terms of the relative activity of deformation systems as it results from their work hardening interactions.

4.1 Modeling

As it becomes evident by reviewing the reported crystal plasticity models of fully lamellar TiAl (cf. Section 3.1.1), most numerical studies did not aim to investigate the deformation behavior beyond the yield point, i.e. for higher plastic strains. While some of the reported numerical studies showed that the applied linear or saturation work hardening relations were generally suitable to reproduce the stress-strain response of differently oriented polysynthetically twinned crystals [29], polycolony microstructures [75, 80] or nanoindentation tests [41] for higher plastic strains, a detailed discussion of the active deformation systems and work hardening interactions was, apparently, not in the focus of these contributions. Further, the work hardening relations that have been applied in the respective numerical studies were formulated in terms of the accumulated plastic shear $\overline{\gamma}$ (cf. Equations (3.15) and (3.17)) on the respective slip and twinning systems as it is common for classical crystal plasticity models [56]. Keeping in mind the earlier formulated aim to model recovery of work hardening (see Section 1.2), the accumulated shears $\overline{\gamma}$ are, however, unsuitable variables for the work hardening model in this thesis since they can only increase per definition (see Equations (3.15) and (3.17)). A decrease of the critical resolved shear stresses due to annealing at elevated temperatures thus requires the work hardening model to be formulated in terms of a different set of internal variables (see, e.g., [134]). Therefore, the dislocation densities ρ_α^{dis} and the

twinned volume fractions f_β were introduced in Section (3.2.5) as additional internal variables which increase with accumulating shear $\overline{\gamma}$ (cf. Equations (3.18) and (3.21)) while the dislocation densities may also decrease as a function of temperature and time (cf. Equation (3.18)). Thus, the work hardening model is set up in terms of the current dislocation densities ρ_α^{dis} on slip systems α and the current twinned volume fractions f_β of twinning systems β.

Besides interactions between dislocations on both coplanar and non-coplanar slip systems, the latent hardening due to evolving twins in the γ lamellae is of particular interest for the overall work hardening behavior of fully lamellar TiAl since the evolving twin boundaries further reduce the anyway restricted free path length of the deformation systems [11, 39, 130]. Thus, in the following a work hardening model is presented which accounts for the respective work hardening interactions in more detail.

Evolution of slip system strength   Once plastic deformation started (i.e. the resolved shear stress on any deformation system exceeded its initial critical resolved shear stress), the strength τ_α^Y of slip system α increases due to the emerging slip and/or twinning activity. Thus, the hardening term $\Delta\tau_\alpha^Y$ of slip system α (cf. Equation (3.22)) is defined by

$$\Delta\tau_\alpha^Y = \Delta\tau_{\alpha,\text{s}|\text{s}}^Y + \Delta\tau_{\alpha,\text{s}|\text{t}}^Y \tag{4.1}$$

where $\Delta\tau_{\alpha,\text{s}|\text{s}}^Y$ denotes strengthening due to dislocation interactions and $\Delta\tau_{\alpha,\text{s}|\text{t}}^Y$ denotes strengthening by twin activity.

The slip–slip interaction $\Delta\tau_{\alpha,\text{s}|\text{s}}^Y$ is described by the well-known relation [111, 134][6]

$$\Delta\tau_{\alpha,\text{s}|\text{s}}^Y = aGb_\alpha\sqrt{\rho^{\text{dis}}}. \tag{4.2}$$

As defined before, G denotes the shear modulus, b_α is the magnitude of the Burgers vector of slip system α and $a \approx 0.5$ [11] is a material specific constant.

The twin/matrix interfaces of evolving twins on a twinning system β are strong barriers for dislocation motion (cf. e.g. [79, 136–138]) effectively reducing the free path lengths of all non-coplanar (ncp) slip systems α (i.e. systems with slip plane normals $\boldsymbol{n}_\alpha \nparallel \boldsymbol{n}_\beta$). The resultant (Hall-Petch type) strengthening was modeled by several authors (not only in the context of crystal plasticity) [79, 114, 136, 139, 140]. However, explicitly modeling this strengthening effect requires knowledge of the spacing of parallel twins since it denotes the free path length of the non-coplanar slip systems. In the present crystal plasticity formulation, twins are represented by their volume fractions f_β which neither provides information about their number nor their thickness and consequently does not allow to determine their spacing. Thus, the work hardening effect by evolving twins can not be modeled as an explicit function of their spacing as it was e.g. done in [79, 114, 139]. Based on the formulation from [140], the hardening term $\Delta\tau_{\alpha,\text{s}|\text{t}}^Y$ was thus set up in terms of the twinned volume fractions f_β instead and reads

$$\Delta\tau_{\alpha,\text{s}|\text{t}}^Y = \frac{\sum_\beta^{\text{ncp}} h_{\alpha\beta} f_\beta}{1.0 - \sum_\beta^{\text{ncp}} f_\beta}. \tag{4.3}$$

In this, $h_{\alpha\beta}$ denotes a coefficient for hardening of slip system α due to twinning on the non-coplanar twinning system β.

---

[6] A more general description of this hardening term would read $\Delta\tau_{\alpha,\text{s}|\text{s}}^Y = aGb_\alpha\sqrt{\sum q_{\alpha\alpha'}\rho_{\alpha'}^{\text{dis}}}$ where $q_{\alpha\alpha'} > 0$ is the hardening interaction coefficient that describes the effect of dislocations on slip system α' on the strength of slip system α (see, e.g., [114, 135]). In Equation (4.2), it was assumed that $q_{\alpha\alpha'} = 1$ for all slip systems.

Evolution of twinning system strength While there is effectively no self hardening of twinning systems β, they nevertheless experience work hardening from nucleation of twins on non-coplanar systems β' (i.e. twinning plane normals $\boldsymbol{n}_\beta \nparallel \boldsymbol{n}_{\beta'}$) and from interactions of the twinning dislocations with the slip dislocation network [114, 138, 140]. In a general form the corresponding hardening term of twinning systems β (cf. Equation (3.23)) can be written as

$$\Delta\tau_\beta^T = \Delta\tau_{\beta,\mathrm{t|t}}^T + \Delta\tau_{\beta,\mathrm{t|s}}^T, \tag{4.4}$$

introducing $\Delta\tau_{\beta,\mathrm{t|t}}^T$ as the strengthening due to nucleation of non-coplanar twins and $\Delta\tau_{\beta,\mathrm{t|s}}^T$ to account for interactions of twinning dislocations with the slip dislocation network.

The strengthening effect by non-coplanar twins is modeled analogically to Equation (4.3) and reads

$$\Delta\tau_{\beta,\mathrm{t|t}}^T = \frac{\sum_{\beta'}^{\mathrm{ncp}} h_{\beta\beta'} f_{\beta'}}{1.0 - \sum_{\beta'}^{\mathrm{ncp}} f_{\beta'}}. \tag{4.5}$$

Herein, $h_{\beta\beta'}$ is again a hardening interaction coefficient which describes the strengthening effect of twins on the non-coplanar twinning systems β' on twinning system β.

As described in [114], twinning dislocations may interact with the slip dislocation network. Since this effect is probably more subtle than the other strengthening mechanisms, it is, however, often neglected [78]. In the present hardening model, the hardening interactions between twinning and slip dislocations are nevertheless incorporated by adopting the respective formulation from [114] which reads

$$\Delta\tau_{\beta,\mathrm{t|s}}^T = Gb_\beta \sum_\alpha^{N^{\mathrm{sl}}} C_{\beta\alpha} b_\alpha \rho_\alpha^{\mathrm{dis}}. \tag{4.6}$$

In this, $C_{\beta\alpha}$ denotes the hardening interaction coefficient between twinning system β and slip system α.

Figure 4.1 qualitatively shows the evolution of slip/twinning system strengths as it is described by Equations (4.2), (4.3), (4.5) and (4.6).

In the context of thermomechanical modeling it is worth mentioning that the introduced hardening relations (Equations (4.2), (4.3), (4.5) and (4.6)) do not explicitly depend on temperature, which is reasonable for the modeled defect structures, as they can not easily be overcome by thermal activation [11]. However, there still is a slight temperature dependence in Equations (4.2) and (4.6) that results from considering the temperature dependence of the shear modulus G (see the temperature dependent formulation of Young's modulus and Poisson's ratio in Table 3.3).

4.2 Parameter identification

Experimental investigation of work hardening interactions between specific deformation systems requires these systems to be activated selectively. Even though this can be achieved for certain experimental set ups, it is not clear how to derive quantitative parameters for continuum models from the observed hardening interactions. Thus, the work hardening parameters of crystal plasticity models are usually determined by calibration against (macroscopic) experimental stress strain curves. Naturally, the work hardening part of a crystal plasticity model is best calibrated against experiments with single crystals of the crystalline phase that ought to be modeled. However, due to the strong effect of composition on their mechanical behavior, experiments with γ and α_2 single crystals are not suitable for the calibration process as it was
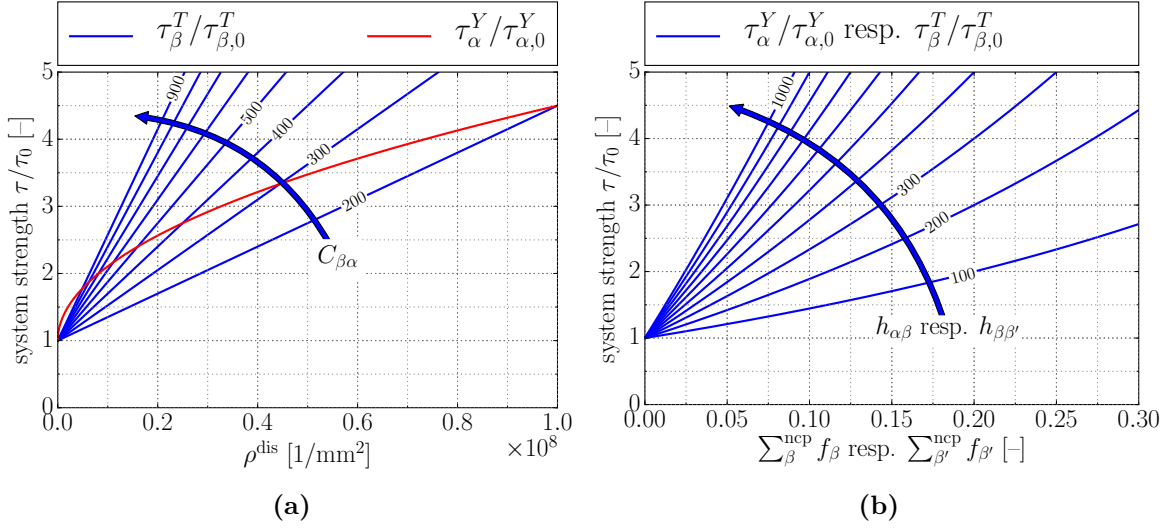
Figure 4.1. Qualitative illustration of hardening laws as defined by Equations (4.2), (4.3), (4.5) and (4.6). (a): Evolution of strengths τ_α^Y and τ_β^T of slip systems α (red line) and twinning systems β (blue lines) normalized to their initial strengths $\tau_{\alpha,0}^Y$ and $\tau_{\beta,0}^T$ with the total dislocation density ρ^{dis}; the different blue lines illustrate the influence of the interaction coefficient $C_{\beta\alpha}$. (b): Evolution of strengths τ_α^Y and τ_β^T of slip systems α and twinning systems β with volume fraction $f_{\beta'}$ of twins on non-coplanar twinning systems β' normalized to their initial strengths $\tau_{\alpha,0}^Y$ and $\tau_{\beta,0}^T$; the different lines illustrate the effect of hardening coefficients $h_{\alpha\beta}$ resp. $h_{\beta\beta'}$.

briefly discussed in Section 2.3.1. Alternatively, the introduced defect density-based hardening model may be calibrated against experiments with polysynthetically twinned crystals or micropillar compression tests since both allow to investigate the anisotropic micromechanical behavior of single lamellar colonies. Although micropillar compression has the clear advantage that it allows to analyze single colonies within actual microstructures [40, 53, 141], at the moment significantly more data is available on the plastic deformation of polysynthetically twinned crystals.

In [52], the plastic deformation of polysynthetically twinned crystals was studied for eight different loading angles φ between 0° (loading in the plane of the lamella interfaces) and 90° (loading perpendicular to the lamella interfaces) for plastic strains of up to 15%, yielding a good data base for the here intended model calibration.

4.2.1 Constitutive assumptions

The high number of parameters in crystal plasticity models renders their identification a formidable task. Therefore, certain constitutive assumptions are usually established that facilitate to identify the missing model parameters by, e.g., identifying groups of deformation systems that can be described by the same parameter set or by narrowing down the range of values certain parameters may take.

Morphological classification

As it was stated in [28] and frequently confirmed by other authors (see, e.g., [72, 75, 80]), assigning the same set of model parameters to each slip and twinning system of a morphological class (see Table 2.1) allows to reproduce the plastic anisotropy of polysynthetically twinned crystals/single colonies very well. While in [28] only the initial critical resolved shear stresses

were assumed to be the same for all deformation systems of a morphological class, this idea was generalized in [29, 72] to also assigning the same work hardening parameters to all deformation systems of a morphological class. This assumption drastically reduces the number of model parameters that have do be identified[7]. Modeling all deformation systems solely according to their morphological classification does, however, neglect differences as they result from the crystallography of the single phases like, e.g., the potentially different strengths of ordinary slip, super slip and twinning in the γ phase that was discussed earlier (see Section 2.3.1).

Consequently, the initial critical resolved shear stresses from Equations (3.22) and (3.23) are defined as

$$\tau_{\mathrm{long},0} = \tau_{\alpha,0}^{Y} = \tau_{\beta,0}^{T} \qquad \text{for } (\alpha = 1-3) \text{ and } (\beta = 1), \qquad (4.7)$$

$$\tau_{\mathrm{mix},0} = \tau_{\alpha,0}^{Y} \qquad \text{for } (\alpha = 4-6), \qquad (4.8)$$

$$\tau_{\mathrm{trans},0} = \tau_{\alpha,0}^{Y} = \tau_{\beta,0}^{T} \qquad \text{for } (\alpha = 7-12) \text{ and } (\beta = 2-4) \qquad (4.9)$$

with the indices α and β from Table 2.1. The model parameters that remain to be identified are summarized in Table 4.1.

Table 4.1. Model parameters that remain to be identified when assuming that all deformation systems of a morphological class can be described by the same parameters. ls: longitudinal slip, ms: mixed slip, ts: transversal slip, lt: longitudinal twinning, tt: transversal twinning, n.a.: not applicable. Indices α and β of the individual deformation systems according to Table 2.1.

γ and α_2 phase (evolution of dislocation density)				
parameter	equation	ls (α = 1-3)	ms (α = 4-6)	ts (α = 7-12)
$A_{\alpha,0}$	(3.19)	$A_{\mathrm{ls},0}$	$A_{\mathrm{ms},0}$	$A_{\mathrm{ts},0}$
$\rho_{\alpha,\mathrm{sat}}^{\mathrm{dis}}$	(3.19)	$\rho_{\mathrm{ls,sat}}^{\mathrm{dis}}$	$\rho_{\mathrm{ms,sat}}^{\mathrm{dis}}$	$\rho_{\mathrm{ts,sat}}^{\mathrm{dis}}$
p_{α}	(3.19)	p_{ls}	p_{ms}	p_{ts}
$R_{\alpha,0}$	(3.20)	$R_{\mathrm{ls},0}$	$R_{\mathrm{ms},0}$	$R_{\mathrm{ts},0}$
$\rho_{\alpha,\mathrm{min}}^{\mathrm{dis}}$	(3.20)	$\rho_{\mathrm{ls,min}}^{\mathrm{dis}}$	$\rho_{\mathrm{ms,min}}^{\mathrm{dis}}$	$\rho_{\mathrm{ts,min}}^{\mathrm{dis}}$
q_{α}	(3.20)	q_{ls}	q_{ms}	q_{ts}
γ phase (slip–twin interaction)				
parameter	equation	ls (α = 1-3)	ms (α = 4-6)	ts (α = 7-12)	interaction
$h_{\alpha\beta}$	(4.3)	n.a.	$h_{\mathrm{ms\vert lt}}$	$h_{\mathrm{ts\vert lt}}$	lt (β = 1)
		$h_{\mathrm{ls\vert tt}}$	$h_{\mathrm{ms\vert tt}}$	$h_{\mathrm{ts\vert tt}}$	tt (β = 2 − 4)
γ phase (twin–twin interaction)				
parameter	equation	lt (β = 1)	tt (β = 2-4)	interaction
$h_{\beta\beta'}$	(4.5)	n.a.	$h_{\mathrm{tt\vert lt}}$	lt (β' = 1)
		$h_{\mathrm{lt\vert tt}}$	$h_{\mathrm{tt\vert tt}}$	tt (β' = 2 − 4)
γ phase (twin–slip interaction)				
parameter	equation	lt (β = 1)	tt (β = 2-4)	interaction
$C_{\beta\alpha}$	(4.6)	$C_{\mathrm{lt\vert ls}}$	$C_{\mathrm{tt\vert ls}}$	ls (α = 1 − 3)
		$C_{\mathrm{lt\vert ms}}$	$C_{\mathrm{tt\vert ms}}$	ms (α = 4 − 6)
		$C_{\mathrm{lt\vert ts}}$	$C_{\mathrm{tt\vert ts}}$	ts (α = 7 − 12)

---

[7]Instead of a complete parameter set for each deformation systems in the γ and the α_2 phase, only a total of three parameter sets (one for each morphological class) have to be identified.

Strengthening by evolving twins in the γ phase

As stated in Section 2.2, all twinning systems of the γ phase are crystallographically equivalent and should thus have the same effect on non-coplanar deformation systems. However, the extent to which evolving twins strengthen the non-coplanar deformation systems still differs depending on their morphological classification. As it was observed in, e.g., [17], transversal twinning activity leads to the formation of a high number of equaly spaced thin twins. Thus, transversal twinning activity strongly reduces the free path lengths of longitudinal and potentially of mixed deformation systems. However, due to the small lamella thickness, non-coplanar tranversal twins do not necessarily have to cross each other and thus presumably have a lower strengthening interaction. The same holds for transversal slip systems that do not necessarily have to cross the boundaries of non-coplanar transversal twins. This is schematically illustrated in Figure 4.2.
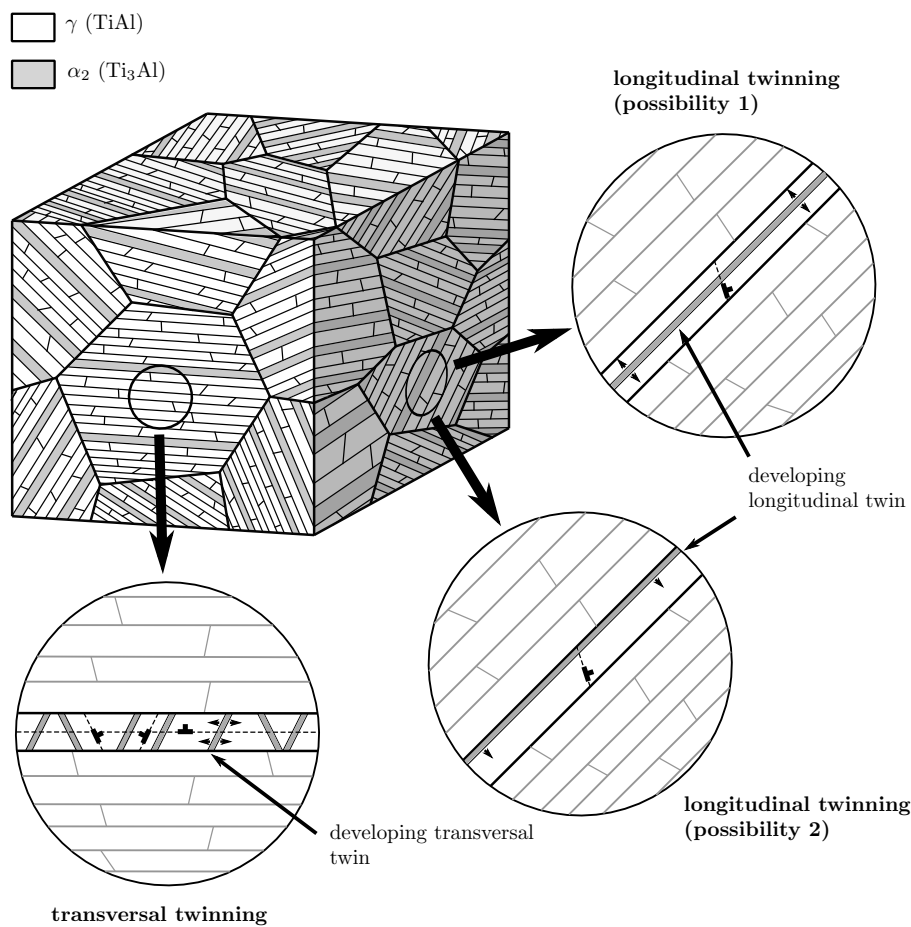
Figure 4.2. Schematic illustration of possible ways in which longitudinal and transversal twins may evolve in the γ lamellae. While longitudinal deformation systems have to interact with transversal twins, transversal deformation systems do not necessarily have to cross each other resulting in a lower hardening interaction. Figure taken from Schnabel & Bargmann [2].

Experimental investigation of the evolution of longitudinal twins is challenging since they can not always be easily distinguished from pre-existing lamellae. In principle, longitudinal twins can be thought to evolve in two ways: as many parallel thin twins that subdivide the lamellae or as single twins that nucleate from lamella boundaries and grow until the lamella is twinned

completely. This is schematically illustrated in Figure 4.2. In fact, both forms of longitudinal twinning have been observed experimentally. In [55], longitudinal twinning was found to form many very thin twins subdividing the lamellae of polysynthetically twinned crystals while in recent investigations [133, 141] longitudinal twins were found to nucleate from lamella boundaries and to grow until the complete lamella is twinned. While the former case results in a further reduction of the anyway small free path length (and thus in high strengthening) of transversal deformation systems, longitudinal twins that grow from one lamella boundary to the other initially reduce the free path length but end up having the same thickness as the initial lamella. Although it is not yet clear what causes the different observed behaviors [141], the author is inclined to believe that it is energetically more favorable for longitudinal twins to nucleate from lamella boundaries instead of evolving as many thin twins within the lamellae. This would result in a negligible contribution of longitudinal twinning to work hardening. However, in lamella orientations that favor the activation of longitudinal twinning (as a soft deformation mode), mixed and transversal deformation (i.e. the hard deformation modes) will not likely be activated so that the work hardening by longitudinal twinning either way plays a minor role from the modeling perspective.

With these preliminary thoughts, the following assumptions are made for the parameters for slip–twin and twin–twin hardening interaction in the γ phase as they were defined in Table 4.1

$$h_{\mathrm{ls|tt}} > h_{\mathrm{ts|tt}}, \tag{4.10}$$

$$h_{\mathrm{ms|tt}} > h_{\mathrm{ts|tt}}, \tag{4.11}$$

$$h_{\mathrm{lt|tt}} > h_{\mathrm{tt|tt}}. \tag{4.12}$$

Modeling super slip in the γ phase

As briefly mentioned in Sections 2.3.1, it has been frequently observed experimentally that super slip systems are less preferably activated in the γ phase of two phase alloys than ordinary slip or twinning systems. This was frequently modeled by assuming that super slip systems have a higher initial critical resolved shear stress [73, 75, 76] or by neglecting them completely [63]. However, in domains that are oriented such that ordinary slip and twinning are both not possible, super slip systems have to be activated in order to ensure a compatible co-deformation of neighboring lamellae/domains and are thus not neglected in this work. Since the plastic anisotropy of polysynthetically twinned crystals/single colonies is dominated by the microstructural interfaces (see Section 2.3.2), potential differences between deformation systems that solely stem from the crystallography of the single phases are not considered throughout this thesis, i.e. the initial critical resolved shear stress of a deformation system is assumed to be determined solely by its morphological classification (cf. Table 4.1).

Although their initial strength was assumed to be the same, there is still a difference in the deformation behavior of super and ordinary slip systems as it is modeled here. Since the magnitude b_α of the Burgers vectors of super slip systems is approximately two times larger than the one of ordinary slip systems (cf. Figure 2.3), the work hardening of super slip systems due to slip–slip interaction as described by Equation (4.2) is approximately twice as high as for ordinary slip systems. This nicely represents the fact that two superpartial dislocations that form the perfect super dislocation (cf. Section 2.2) are bound by the antiphase boundary between them and thus both have to cross the forest of dislocations to propagate further.

Modeling the plastic deformation behavior of the α_2 phase

In common two phase alloys, the volume fraction of the α_2 phase is usually rather low. Consequently, the (direct) effect of the plastic deformation behavior of the α_2 phase on the overall deformation of two phase alloys is assumed to be low as well. Due to the small volume fraction of the α_2 phase it is, furthermore, questionable whether two separate parameter sets for both phases can be derived from the experiments with polysynthetically twinned crystals against which the model will be calibrated. Thus, some simplifications were introduced in the description of the deformation behavior of the α_2 phase.

First of all, basal slip systems are not considered throughout this work since in lamella orientations which favor their activation, the deformation is primarily carried by the much weaker slip and twinning systems of the soft deformation mode in the γ lamellae [35, 37, 47].

Despite the concerns discussed in Section 2.3.1, the initial critical resolved shear stresses $\tau_{\mathrm{mix},0}^{\alpha_2}$ and $\tau_{\mathrm{trans},0}^{\alpha_2}$ of the prismatic (mixed) and the pyramidal (transversal) slip systems were taken from α_2 single crystal experiments [27] with a composition of Ti-24.4Al at.% and read

$$\tau_{\mathrm{mix},0}^{\alpha_2} = 67\,\mathrm{MPa} \tag{4.13}$$

$$\tau_{\mathrm{trans},0}^{\alpha_2} = 450\,\mathrm{MPa}. \tag{4.14}$$

In reality, these critical resolved shear stresses would be even higher due to the strengthening effect of the lamella boundaries (cf. Chapter 5). Further, it was assumed that dislocation accumulation on prismatic (mixed) slip systems in the α_2 phase and mixed slip systems in the γ phase can be described by the same parameters $A_{\mathrm{ms},0}$, $\rho_{\mathrm{ms,sat}}^{\mathrm{dis}}$ and p_{ms}. The same is assumed for the pyramidal (transversal) slip systems in the α_2 phase and the transversal slip systems in the γ phase sharing the parameters $A_{\mathrm{ts},0}$, $\rho_{\mathrm{ts,sat}}^{\mathrm{dis}}$ and p_{ts}.

Initial defect densities

Even in an undeformed state, crystalline materials always contain a certain dislocations density. In the presented model, this is represented by the initial dislocation density $\rho_\alpha^{\mathrm{dis}}|_{t=0} = \rho_{\alpha,0}^{\mathrm{dis}} > 0$ (see Equation (3.18)). In [11] and [142] it has been stated that at the beginning of deformation the total dislocation density ρ^{dis} in TiAl alloys is typically in the range of $10^6\,\frac{1}{\mathrm{mm}^2} < \rho^{\mathrm{dis}} < 10^7\,\frac{1}{\mathrm{mm}^2}$. Therefore, the initial dislocation density is set to $\rho_{\alpha,0}^{\mathrm{dis}} = 1 \times 10^5\,\frac{1}{\mathrm{mm}^2}$ on all slip systems α in the γ and the α_2 phase.

The initial twinned volume fraction is, however, set to be $f_\beta = 0$ on all twinning systems β.

Thermal recovery

For the moment, only the (temperature independent) work hardening behavior is of interest. Hence, all terms in equations (3.18) and (3.20) that are related to thermal recovery are neglected in this chapter. The thermal recovery behavior and the corresponding model parameters are discussed in Chapter 7.

4.2.2 Calibration

In order to calibrate the model against the experimental stress-strain curves from [52], simulations were carried out using the RVE from Section 3.5.1 together with the rotational boundary conditions described in Section 3.6.2. As in [52], a compressive strain rate of $\dot{\varepsilon} = 10^{-4}\mathrm{s}^{-1}$ was applied for all simulations. Since it was not reported in [52], the α_2 volume fraction was assumed to be as low as 2%.

With the above introduced constitutive assumptions, the parameters from Table 4.1 were identified by successively adjusting them until the simulated stress-strain curves sufficiently matched the experimental results for the differently oriented polysynthetically twinned crystals tested in [52]. Figure 4.3 shows the stress-strain curves obtained by the calibrated model in comparison to the experimental results from [52].
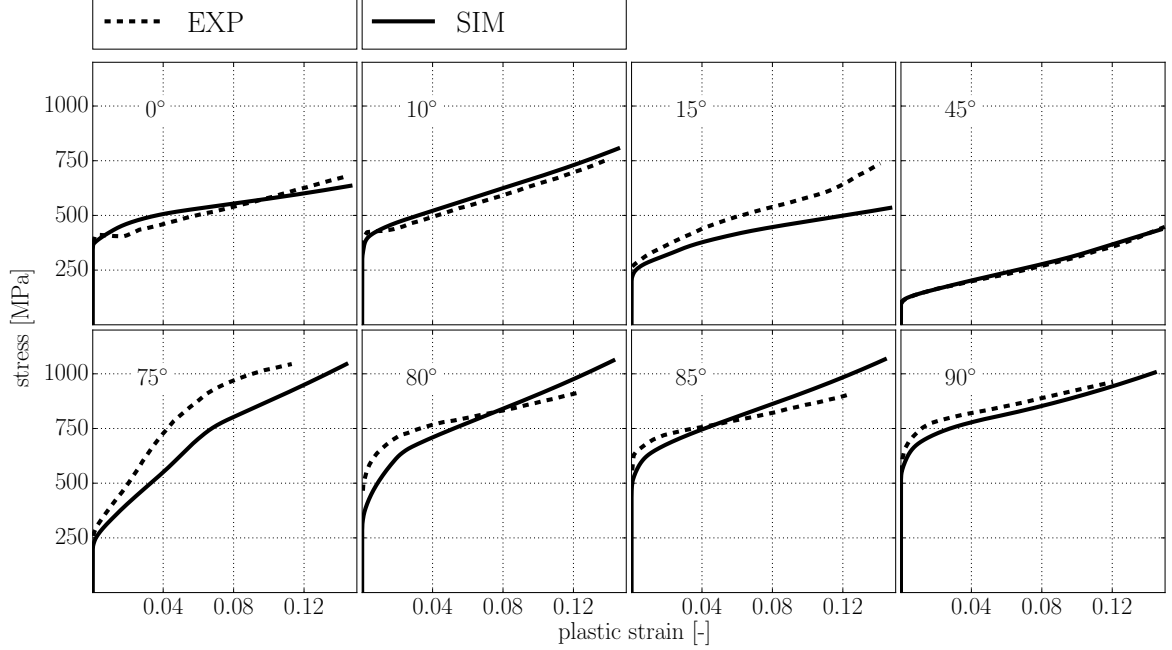
Figure 4.3. Results of the calibration of the work hardening model against experimentally determined stress-strain curves of differently oriented polysynthetically twinned crystals. Experimental data taken from [52].

Given the high number of deformation systems that determine the plastic deformation behavior of polysynthetically twinned crystals (6 γ orientation variants with 12 slip systems and 4 twinning systems each + 9 considered slip systems for the α_2 phase), the agreement between simulation and experiment is assessed as very good.

Plotting the yield stress as it is obtained from the calibrated simulations over the loading angle φ (i.e. the angle between uniaxial load and the plane of the lamella interfaces), shows that its anisotropy is well reproduced by the model, see Figure 4.4.

4.2.3 Model parameters

This section summarizes the model parameters that were identified from the calibration process. In the calibration process, the initial yield point (not to be confused with the 0.2% yield point) of the experimental results from [52] was found to be reproduced well for all loading angles by choosing the initial critical resolved shear stresses

$$\tau^{\gamma}_{\text{long},0} = 38\,\text{MPa}, \tag{4.15}$$

$$\tau^{\gamma}_{\text{mix},0} = 139\,\text{MPa}, \tag{4.16}$$

$$\tau^{\gamma}_{\text{trans},0} = 139\,\text{MPa} \tag{4.17}$$
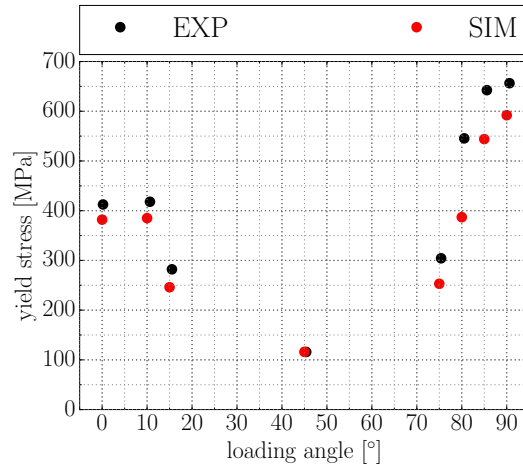
Figure 4.4. Yield stress of polsysnthetically twinned crystals over loading angle (i.e. angle between uniaxial load and lamella plane) as obtained from the calibrated work hardening model compared to experimental results from [52].

for the deformation systems of the three morphological classes in the γ phase. However, the initial critical resolved shear stresses depend on temperature, composition and microstructural lengths and are thus no fixed model parameters. Consequently, the critical resolved shear stresses identified here are only valid for room temperature and the investigated set of experiments. In Chapters 5 and 8, these parameters will be defined in a more general way taking into account their microstructure and temperature dependence.

The work hardening behavior is, however, independent of microstructural parameters and temperature [11, 39] so that the identified work hardening parameters that are summarized in Table 4.2 can be applied to other sets of experiments as well.

4.3 Relative activity of deformation systems in polysynthetically twinned crystals/single colonies

In the previous section, the crystal plasticity model was calibrated to match the macroscopic stress-strain curves of differently oriented polysynthetically twinned crystals. The qualitative features of these stress-strain curves (like e.g. changes in work hardening rate) were reproduced well by the calibrated model (see Figure 4.3). Thus, it is suitable to be used in the following to investigate which deformation systems dominate the plasticity of polysynthetically twinned crystals for different lamella orientations. Further, it will be analyzed in which way the work hardening interactions between the deformation systems are correlated to the specifics of the macroscopic stress-strain response of differently oriented polysynthetically twinned crystals. In order to allow a direct comparison between simulation results and the experimental investigations of active deformation systems in [52], the simulation set up, the model parameters and the constitutive assumptions were taken to be the same as in Section 4.2. In order to validate the model predictions, they were compared to findings of other experimental studies.

4.3.1 Numerical results

In order to visualize which slip and twinning systems contribute to the plastic deformation at a certain deformation stage, their relative activities were extracted from the crystal plasticity

Table 4.2. Identified parameters for the work hardening model. ls: longitudinal slip, ms: mixed slip, ts: transversal slip, lt: longitudinal twinning, tt: transversal twinning, n.a.: not applicable, n.n.: not needed

γ and α_2 phase (evolution of dislocation density)					
parameter	unit	ls (α = 1-3)	ms (α = 4-6)	ts (α = 7-12)	
$A_{\alpha,0}$	$[\frac{1}{\text{mm}^2}]$	2×10^8	2×10^8	4×10^8	
$\rho_{\alpha,\text{sat}}^{\text{dis}}$	$[\frac{1}{\text{mm}^2}]$	1×10^9	1×10^9	1×10^9	
p_α	$[-]$	1	1	1	
γ phase (slip–twin interaction)					
parameter	unit	ls (α = 1-3)	ms (α = 4-6)	ts (α = 7-12)	interaction
$h_{\alpha\beta}$	[MPa]	n.a.	n.n.	n.n.	lt (β = 1)
		1500	1500	100	tt (β = 2 − 4)
γ phase (twin–twin interaction)					
parameter	unit	lt (β = 1)		tt (β = 2-4)	interaction
$h_{\beta\beta'}$	[MPa]	n.a.		n.n.	lt (β' = 1)
		5000		100	tt (β' = 2 − 4)
γ phase (twin–slip interaction)					
parameter	unit	lt (β = 1)		tt (β = 2-4)	interaction
$C_{\beta\alpha}$	$[-]$	700		n.n.	ls (α = 1 − 3)
		700		n.n.	ms (α = 4 − 6)
		700		n.n.	ts (α = 7 − 12)

simulations. In this, the cumulative relative activity and the instantaneous relative activity are distinguished. While the cumulative relative activity illustrates which deformation systems contributed to the plastic deformation up to the investigated deformation stage, the instantaneous relative activity shows which deformation systems are currently contributing to the plastic deformation. In order to make slip and twinning activity comparable, the relative activities were expressed in terms of the plastic shear γ on the respective systems. The cumulative relative activity of a slip or twinning system i was defined by dividing its accumulated plastic shear $\overline{\gamma}_i$ (see Equations (3.15) and (3.17)) by the total accumulated plastic shear $\overline{\gamma} = \sum_i \overline{\gamma}_i$ of all systems. The instantaneous relative activity of a slip or twinning system i was defined by dividing its current shear rate $\dot{\gamma}_i$ (i.e. ν_α for slip systems and $\gamma_T g_\beta$ for twinning systems) by the total shear rate $\dot{\gamma} = \sum_i \dot{\gamma}_i$ on all systems.

The relative activity of deformation systems in the interface dominated plasticity of fully lamellar TiAl is best illustrated by grouping them according to the morphological classification introduced in Section 4.2.1. In Figure 4.5, the relative activity of deformation modes in differently oriented polysynthetically twinned crystals is illustrated as it was predicted by the crystal plasticity model.

Displaying the relative activities of slip and twinning systems grouped by their morphological classes does not only allow to identify active deformation modes at one glance but also enables a straightforward identification of transitions between predominant deformation modes. It is thus easily seen from Figure 4.5 that different groups of slip and twinning systems accomplish the plastic deformation for different loading angles. For the investigated range of loading angles $0° \leq \varphi \leq 90°$, three principal deformation characteristics can be identified:

- φ near 0°: predominant deformation by mixed slip (ms) with considerable contributions of transversal slip (ts) and twinning (tt),

- $15° < \varphi < 75°$: predominant deformation by longitudinal slip (ls) with parallel activity
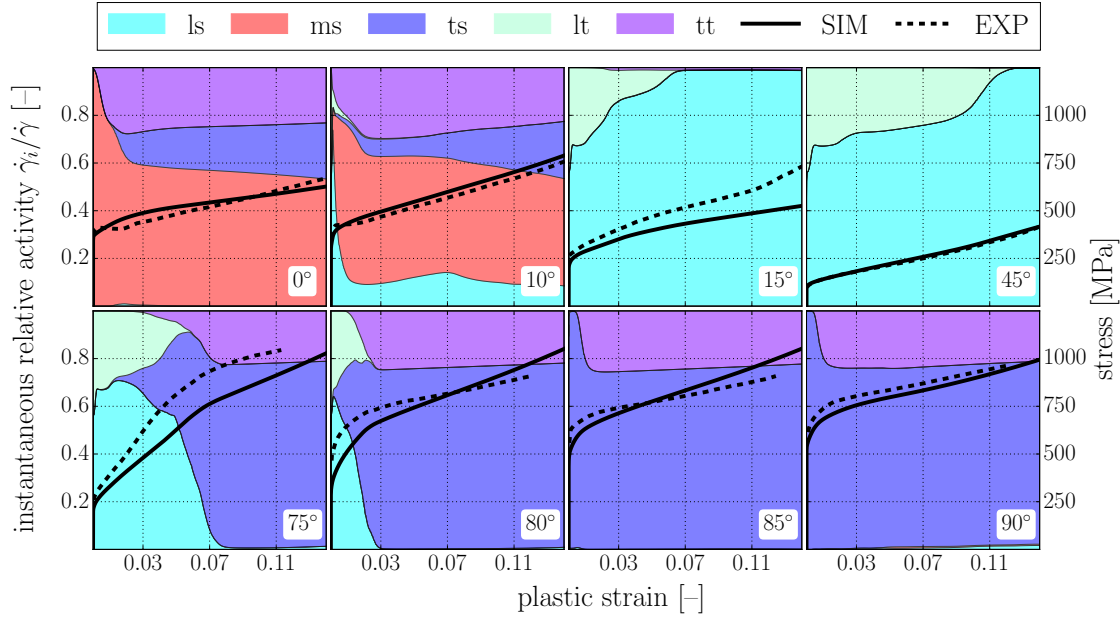
(a) instantaneous relative activity
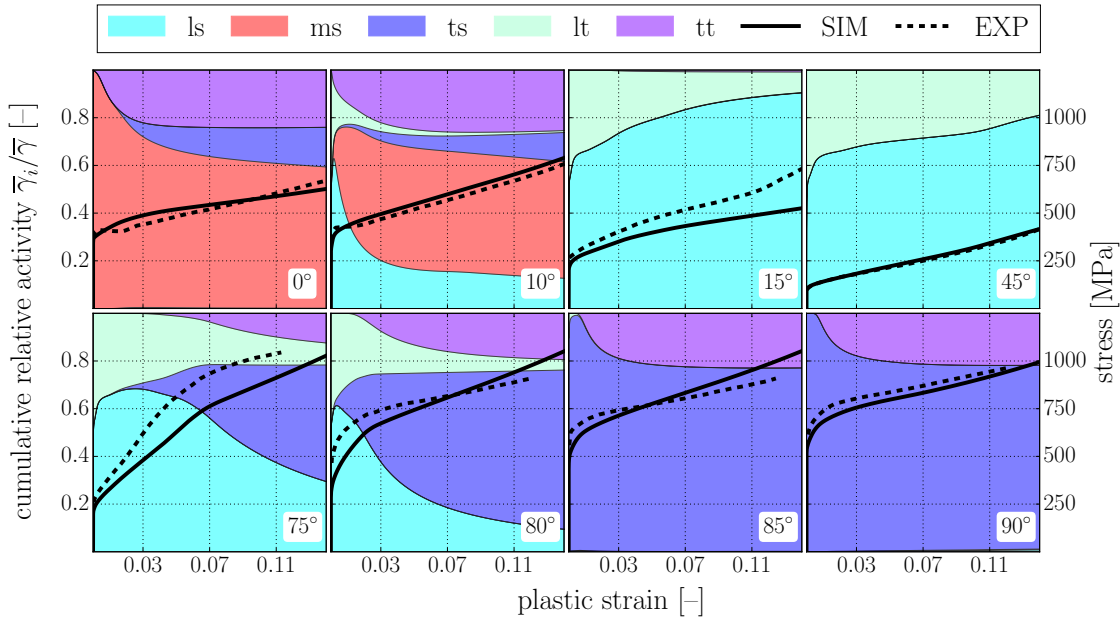
(b) cumulative relative activity

Figure 4.5. Simulated (a) instantaneous and (b) cumulative relative activity of deformation systems in the γ lamellae of differently oriented polysynthetically twinned crystals grouped by morphological class (ls: longitudinal slip; ms: mixed slip; ts: transversal slip; lt: longitudinal twinning; tt: transversal twinning). Simulated (solid lines) and experimental (dashed lines) stress strain curves are added in order to allow attribution of changes in relative activity to specifics of the macroscopic stress strain response. The experimental stress-strain curves are taken from [52]. The simulation set up, the model parameters and the constitutive assumptions were taken to be the same as in Section 4.2.

of longitudinal twinning (lt) and

- φ near 90°: predominant deformation by transversal slip (ts) with considerable contributions of transversal twinning (tt).

For loading angles between 0° and 45° and between 45° and 90° respectively, a gradual transition between these predominant deformation modes occurs.

The predominant activity of slip and twinning systems of only one or two morphological classes as well as the transitions between these principal deformation modes are also reflected in the macroscopic deformation behavior of polysynthetically twinned crystals. Figure 4.6 illustrates the macroscopic deformation of differently oriented polysynthetically twinned crystals in terms of the lateral strains as they were determined in [52]. In [52], the lateral strains ε_x and ε_y in x and y direction (according to the coordinate system introduced in Figure 3.3), were identified at the end of deformation and normalized to the corresponding compression strain ε_z which ranged between 0.10 and 0.15. If both relative transversal strains take values of -0.5, the deformation is isotropic. If one relative transversal strain does, however, take a value of -1 while the other is 0, a plane strain deformation is present. Illustrating the macroscopic deformation of polysynthetically twinned crystals in terms of the transversal strains helps to quantify what was qualitatively observed on the deformed specimens in [55].
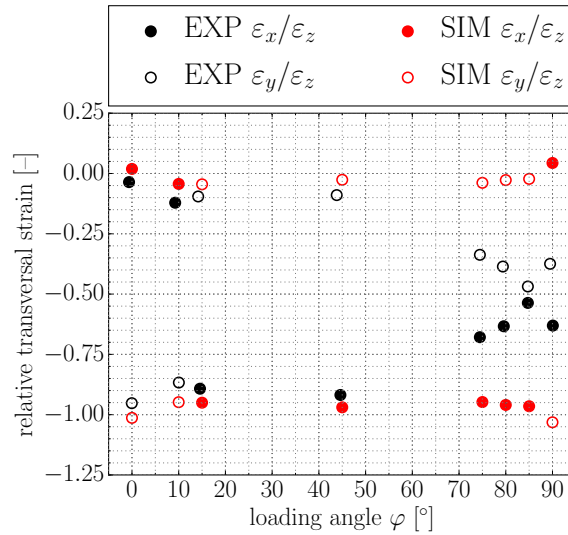
Figure 4.6. Relative transversal strains of polysynthetically twinned crystals as function of loading angle φ. Experimental data are taken from [52]. The relative transversal strains are defined with respect to the coordinate system introduced in Figure 3.3.

For loading angles φ between 0° and 45°,the simulated relative transversal strains match well the experimental findings including the switch from plane strain deformation in the yz plane to plane strain deformation in the xz plane that occurs for 10°$< \varphi <$15°. However, the applied model fails to capture the details in the relative transversal strains for loading angles of 75° $< \varphi <$ 90°. Instead of the experimentally observed trend towards an isotropic deformation, the model predicts a plane strain deformation in the xz plane. This behavior has been observed in previous modeling approaches [28, 72] and has been identified to result from modeling the deformation system strengths according to their morphological instead of their mechanism based classification [28]. For a loading angle of exactly 90°, the model predicts a plane strain deformation in the yz plane rather than the experimentally observed nearly

isotropic deformation. Since the Schmid factors for loading perpendicular to the lamella boundaries (90°) are the same on several transversal slip and twinning systems on oblique shear planes (see, e.g., [55]), this lamella orientation is particularly prone to misalignment in experiments and to the choice of the strength of the different deformation mechanisms and their mutual work hardening interaction parameters in modeling. The observed behavior interestingly also occurred in a previously reported crystal plasticity model [72] and indicates that despite the symmetry in the Schmid factors, the model favors plastic deformation on a single shear plane.

4.3.2 Literature experimental findings

Since the shear rates on individual slip and twinning systems are the main state variables of crystal plasticity models, the relative activity of deformation systems is an inherent result of crystal plasticity simulations. Investigating the activity of deformation systems experimentally, is however much more demanding.

While deformation markings on the surface of polysynthetically twinned crystals [25, 37, 47] or micro compression specimens of single colonies [40, 53, 141] allow a qualitative in situ identification of active deformation modes (parallel or across the lamella interfaces) by scanning electron or even optical microscopy, a detailed investigation of the activated deformation systems within the thin lamellae usually requires destructive sample preparation for, e.g., transmission electron microscopy (TEM)[40, 55]. Consequently, these studies are limited to investigate which deformation systems were activated up to the given deformation state. Thus, the order in which the deformation systems are activated can only be studied by a series of experiments with different final deformation states. Since the preparation of the test specimens and the samples for the subsequent microscopy studies as well as the data analysis are time-consuming, it is extremely laborious to identify the order in which the deformation systems are activated for a certain lamella orientation.

In the so far only reported attempt to in situ investigate in which order the deformation systems are activated, the authors of [52, 54] analyzed the evolution of pole figures of polysynthetically twinned crystals with plastic deformation. Two lamella orientations were tested in [52, 54], 0° and 90°. The inherently strong texture of polysynthetically twinned crystals enabled to analyze whether or not the individual γ orientation variants experience any rotations with plastic deformation which in turn allow conclusions to be drawn about the activity of certain deformation systems. While the activation of transversal twinning systems was directly observable as newly occuring intensities in the measured pole figures, longitudnal twinning activity could not be identified since longitudinal twins reproduce preexisting crystal orientations [54].

Thus, a complete picture of the activated slip and twinning systems in differently oriented polysynthetically twinned crystals/single colonies can only be achieved by summarizing results of different experimental studies as it is done in Table 4.3 for the most commonly studied lamella orientations. In fact, experimental data on the active deformation systems for lamella orientations other than the ones listet in Table 4.3 are scarce.

Despite being obtained by different experimental techniques, the results of the different studies summarized in Table 4.3 yield a consistent picture of the deformation systems that accomplish the plastic deformation for the most commonly studied lamella orientations of 0° (loading in the plane of the lamella interfaces), 31°, 45° and 90° (loading perpendicular to the lamella interfaces). However, there are still remaining questions concerning the order in which deformation systems are activated even for the most commonly studied lamella orientations. Further, an assessment of the relative activity of deformation systems is not possible with either of these experimental techniques.

Table 4.3. Experimentally determined deformation systems that are active in characteristic orientations of polysynthetically twinned crystals/single colonies under uniaxial loading.

orientation		active deformation modes	ref.
0°	qualitatively	across lamella interfaces	[25, 26, 37, 47]
	explicitly	mixed slip	[40, 52, 54, 55]
		transversal slip	[55]
		transversal twinning	[52, 54, 55]
31°	qualitatively	parallel to lamella interfaces	[25, 26, 37]
	explicitly	longitudinal slip	[55]
		longitudinal twinning	[55]
45°	qualitatively	parallel to lamella interfaces	[25, 26, 47]
	explicitly	longitudinal slip	[40, 52]
		longitudinal twinning	[40]
90°	qualitatively	across lamella interfaces	[25, 26, 37, 47]
	explicitly	transversal slip	[52, 55]
		transversal twinning	[52, 55]

4.3.3 Discussion

Comparing the relative activities shown in Figure 4.5 to the experimentally observed active deformation systems in Table 4.3 shows that the deformation modes which were predicted by the simulations to be active for loading angles of 0°, 45° and 90° match the experimental findings. For these characteristic lamella orientations, activity on certain deformation systems can, however, largely be explained by comparing their Schmid factors while considering that mixed and transversal slip and twinning systems are stronger than longitudinal slip and twinning systems (cf. Section 2.3.2).

For a loading angle of 45°, longitudinal slip and twinning systems have the highest Schmid factors. Thus, it is obvious that the considerably stronger mixed and transversal slip and twinning systems are not activated for this lamella orientation. If the load acts in the plane of the lamella interfaces, i.e. for a loading angle of 0°, the Schmid factors of longitudinal deformation systems are zero since their deformation plane is parallel to the load (cf. Figure 2.6). Thus, for a loading angle of 0° the plastic deformation has to be accomplished by mixed and/or transversal deformation systems. For a loading angle of 90° (load perpendicular to the lamella interfaces), the Schmid factor is zero on all longitudinal and mixed deformation systems since for this lamella orientation the deformation planes and directions of longitudinal systems as well as the deformation directions of mixed systems are perpendicular to the load (cf. Figure 2.6). Consequently, for a loading angle of 90° only transversal deformation systems can be activated.

Due to the high strength of mixed and transversal deformation systems, the plastic deformation of polysynthetically twinned crystals/single colonies was found to be dominated by longitudinal slip and twinning for a wide range of intermediate loading angles around the ideal 45° orientation (cf. 31° in Table 4.3). This explains the low yield stresses that have been observed for intermediate loading angles (cf. Figure 2.7). However, the Schmid factors on the longitudinal deformation systems gradually decrease between their maximum at a loading angle of 45° and their minimum of 0 at loading angles of 0° or 90°. Consequently, the initial flow stress increases towards lamella orientations of 0° and 90°. Finally, near 0° and 90° the stresses reach sufficient levels to activate mixed and transversal deformation systems. However, the plastic deformation for loading angles at which this transition from a purely

longitudinal deformation to a deformation by mixed and transversal systems occurs is not investigated well experimentally and can not be assessed by simple Schmid factor comparison anymore. Thus, the transition between the principal deformation modes near loading angles of 0° and 90° will be investigated in the following by having a closer look at the simulation results for loading angles of 15° and 75° (see Figure 4.5).

Both the experimental and the simulated stress-strain curves for loading angles of 15° and 75° show distinct changes in work hardening rate with deformation (cf. Figure 4.5). Such changes in work hardening rate were not observed for the other tested orientations and were thus suspected in [52] to be correlated to the transition between principal deformation modes. While the initial yield stress is rather low and nearly the same in both orientations, their post yield behavior is substantially different. The stress-strain response for the 75° orientation initially shows a very high work hardening rate which leads to stress levels that are even higher than the ones observed for the initially way stronger 90° orientation. After a few percent of plastic strain, the work hardening rate for the 75° orientation decreases to a much lower value. In contrast, the stress-strain response for a lamella orientation of 15° is characterized by a moderate initial work hardening rate that slightly decreases with plastic deformation and finally increases again. These consecutive changes in the macroscopic work hardening rate are most likely related to the onset of slip and/or twinning activity on additional deformation systems and their strengthening effect on the initially active systems.

The simulated relative activities reveal that longitudinal systems initially contribute significantly to the plastic deformation in both orientations which explains the comparatively low yield point. However, for the 75° orientation the stress rapidly reaches levels high enough to activate the hard deformation modes of the ideal 90° orientation. With the onset of transversal slip and twinning activity, longitudinal deformation dies out completely causing the pronounced change in hardening rate. Since transversal twins significantly reduce the free path length of longitudinal deformation systems, this strong reduction of longitudinal slip and twinning activity is clearly attributed to the increasing transversal twinning activity. As suspected in [52], the experimentally observed increase of the work hardening in the 15° orientation tests after ≈ 0.1 plastic strain might be related to a similar process. However, as for this lamella orientation the stress-strain response is underestimated by the model, the simulations do, unfortunately, not provide insight into potential causes for the experimentally observed sudden increase in the work hardening rate.

The closer to the ideal 0° or 90° orientation the load angle is chosen, the less longitudinal slip and twinning activity occurs before the stresses are sufficient to activate the deformation modes that are characteristic for these ideal lamella orientations (cf. Figure 4.5 for 10° and 80°). A comparison of the instantaneous to the cumulative relative activities does, however, show that a deformation mode which is only active at the beginning of plastic deformation (e.g. longitudinal twinning) may still contribute a significant part of the overall accumulated plastic shear.

The range of loading angles between which the transition from predominant deformation by longitudinal systems to predominant deformation by transversal/mixed systems occurs is related to the relative strength of the corresponding deformation systems which is in turn determined by the microstructural parameters (for polysynthetically twinned crystals/single colonies: domain size λ_D and lamella thickness λ_L) as discussed in more detail in Chapter 5. This means, the higher the ratio between the strength of the hard mode deformation systems (mixed and transversal) and the strength of soft mode deformation systems (longitudinal), the closer to the ideal orientations of 0° and 90° longitudinal slip and twinning activity will be observed.

By carefully evaluating the effective shear deformation of the different γ domains in case of (simultaneous) activation of specific slip and twinning systems, it was possible in the past

to relate the experimentally observed activity of deformation systems to the macroscopic deformation of polysynthetically twinned crystals [11, 52, 55]. These – mostly analytical – considerations allowed to explain the observed deformation behavior in the three loading angle regimes, i.e. $0° < \varphi < 10°$, $15° < \varphi < 75°$ and $75° < \varphi < 90°$.

The plane strain deformation which is observable for intermediate loading angles between 15° and 75° as well as the nearly isotropic deformation that occurs close to a loading angle of 90° (cf, Figure 4.6) coincide well with the predominant deformation by longitudinal and transversal deformation systems respectively [11, 52, 55]. The macroscopic deformation of polysynthetically twinned crystals under loading angles between 0° and 10° seems, however, not to be in line with the deformation systems that have been observed to be active. For such orientations near 0°, polysynthetically twinned crystals show almost no strain perpendicular to the lamella boundaries (cf. Figure 4.6). While a respective shear deformation parallel to the lamellae is naturally accomplished by the predominant deformation by mixed slip systems (cf. Figure 4.5), the simultaneously activated transversal deformation systems – per definition – lead to a shear across the lamella boundaries and should thus yield a non-zero strain perpendicular to the lamellar boundaries. However, as it has been elaborately discussed in [11, 52, 55, 143] the transversal deformation systems that have been found to be active for loading angles near 0° act in such a way that their net shear lies parallel to the lamella boundaries, i.e. their shear components perpendicular to the lamella boundaries cancel out each other [11, 52, 55, 143].

4.3.4 Summary

By comparing the numerical results presented in this section to experimental findings [25, 26, 37, 40, 47, 52, 54, 55], it was shown that the calibrated crystal plasticity model is not only able to reproduce the work hardening behavior of differently oriented polysynthetically twinned crystals/single colonies (see Figure 4.3) but also correctly predicts which deformation systems are activated during deformation of the most commonly investigated lamella orientations (i.e. 0°, 45° and 90°). Further, the model was used to investigate details of the transition between predominant deformation by longitudinal slip and twinning at intermediate loading angles and predominant deformation by mixed/transversal deformation systems at loading angles of 0° and 90°. In this it was possible to attribute specifics of the experimentally observed macroscopic stress-strain curves to work hardening interactions between slip and twinning systems of different morphological classes. The respective findings support some presumptions reported in previous experimental work [52].

5 Microstructure sensitive yield strength

As frequently mentioned in the previous chapters, the yield strength of fully lamellar TiAl alloys is very sensitive to changes in the microstructural parameters. A well-designed constitutive model of fully lamellar TiAl alloys thus has to take into account the corresponding micromechanical effects in order to enable an accurate prediction of the yield strength for different combinations of microstructural parameters. In the following, the presented crystal plasticity model from Chapter 3 is extended accordingly. In the present chapter, the microstructure sensitive yield strength is modeled for room temperature only. A model for the temperature dependence of the yield strength is, however, proposed in Chapter 8.

5.1 Influence of microstructural interfaces on the yield strength

Microstructural interfaces like grain boundaries represent strong barriers for dislocation motion and twin propagation, i.e. dislocations pile up at such interfaces while twins abruptly stop at them. Once the stress that is caused by the pile-up of defects against a microstructural interface reaches a certain level, the interface can be overcome and the deformation is transmitted to the next crystal. This effect delays the onset of plastic deformation and consequently increases the yield strength. Thus, the yield strength of a polycrystalline material increases with the number of microstructural interfaces, i.e. with decreasing grain size D. The dependence of the yield stress $\sigma_{0.2}$ of a conventional polycrystalline material on its grain size D, i.e. the (average) spacing of the grain boundaries, was found to follow the relation [144, 145]

$$\sigma_{0.2} = \sigma_R + \frac{K}{\sqrt{D}} \tag{5.1}$$

which is frequently referred to as Hall-Petch equation. In this, σ_R denotes the material's (theoretical) yield stress for grain size $D \to \infty$ (i.e. without the influence of grain boundaries) and K is the Hall-Petch strengthening coefficient.

In fact, lamella, domain and colony boundaries all have been found to be strong obstacles for dislocations and twins (see, e.g., [146] for an image of the observed pile up of dislocations and twins against a lamella boundary) and are thus generally believed to give rise to Hall-Petch strengthening [11, 18, 23, 42–49]. Besides the lamella thickness λ_L[8], the γ domain size λ_D and the colony size λ_C, the spacing λ_{α_2} of the α_2 lamellae is an additional microstructural parameter (cf. Figure 5.1) that contributes to Hall-Petch strengthening since γ/α_2 lamella boundaries have been found to be stronger obstacles for dislocations and twins than the interfaces between neighboring γ lamellae [12, 47].

Thus, the microstructure sensitive yield strength of fully lamellar TiAl alloys can generally be described as a function of four Hall-Petch coefficients and the corresponding microstructural lengths (cf. Figure 5.1):

---

[8]For a better readability, throughout this thesis λ_L is used for the lamella thickness in general. If the thickness of the α_2 and the γ lamellae (which is usually different) ought to be addressed explicitly, $\lambda_L^{\alpha_2}$ and λ_L^{γ} are used respectively.
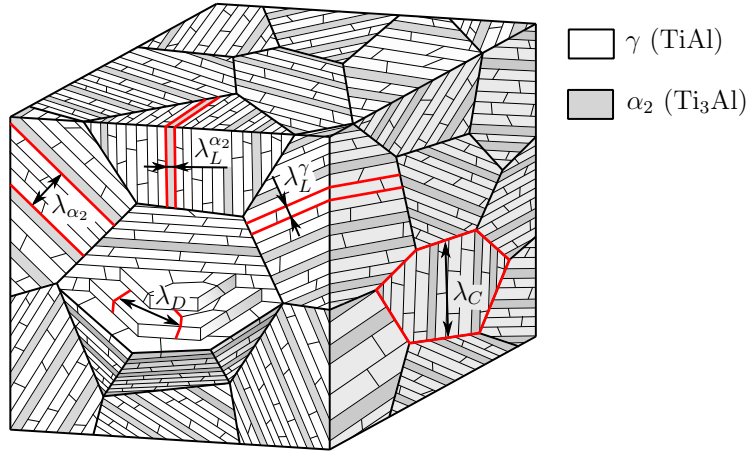
Figure 5.1. Schematic illustration of microstructural interfaces that contribute to Hall-Petch strengthening in fully lamellar TiAl. The spacing of the interfaces is denoted by λ_C: colony size, λ_D: γ domain size, λ_L^γ: thickness of γ lamellae, $\lambda_L^{\alpha_2}$: thickness of α_2 lamellae, λ_{α_2}: spacing of α_2 lamellae.

$$\sigma_{0.2}^{\text{TiAl}} = f\left(\frac{K_C}{\sqrt{\lambda_C}}, \frac{K_D}{\sqrt{\lambda_D}}, \frac{K_L}{\sqrt{\lambda_L}}, \frac{K_{\alpha_2}}{\sqrt{\lambda_{\alpha_2}}}\right). \tag{5.2}$$

However, since λ_{α_2} was not reported in most experimental studies and the corresponding strengthening effect has not been comprehensively investigated yet, this source of Hall-Petch strengthening is not explicitly considered in the following.

In conventional polycrystalline materials the Hall-Petch coefficient K in Equation (5.1) can be determined from a series of experiments with altered grain size D [144, 145]. Separating the strengthening effect of the different coexisting microstructural interfaces in fully lamellar TiAl is, however, much more demanding since it is difficult to independently vary only one microstructural parameter while keeping the others unchanged [11]. While the strengthening by lamella and domain boundaries can be separately investigated in polysynthetically twinned crystals/single colonies with certain orientations, the strengthening effect of the colony boundaries can naturally only be studied in polycolony specimens in which all types of microstructural interfaces coexist and is thus not quantified easily. Therefore, as a first step the microstructure sensitive yield strength of polysynthetically twinned crystals/single colonies will be modeled. Subsequently, a procedure will be shown which allows to identify the strengthening effect of the colony boundaries by combining experimental results and numerical simulations.

5.2 Modeling

In general, gradient extended crystal plasticity models (see, e.g., [113, 118, 126]) allow to intrinsically capture size effects like Hall-Petch strengthening. In order to do so, it is, however, necessary to set up a one to one discretization of the microstructure that is to be investigated. Due to the highly different coexisting length scales, a one to one discretization of a fully lamellar microstructure would lead to an extremely high number of finite elements and with this to unreasonable computational costs (cf. discussion in Section 3.1.2). In order to allow the geometrically simplified RVEs of the fully lamellar microstructure (cf. Section 3.5) to

be used, a local (i.e. not gradient extended) crystal plasticity formulation was presented in Chapter 3. In a local formulation of crystal plasticity models (i.e. in a formulation on Gauss point level), size effects like Hall-Petch strengthening are not captured intrinsically and thus have to be incorporated into the constitutive formulation of the model.

In local crystal plasticity models, all effects that influence the strain independent part of a material's strength are usually combined in the initial critical resolved shear stresses. Thus, the Hall-Petch strengthening by the different types of microstructural interfaces is incorporated into the model by formulating the initial critical resolved shear stresses $\tau_{\alpha,0}^Y$ and $\tau_{\beta,0}^T$ of slip systems α and twinning systems β (see Equations (3.22) and (3.23)) analogically to the macroscopic Hall-Petch relation Equation (5.1) to read

$$\tau_{\alpha,0}^Y = \tau_{\alpha,R} + \sum_i \frac{k_i}{\sqrt{\lambda_i}} \tag{5.3}$$

$$\tau_{\beta,0}^T = \tau_{\beta,R} + \sum_i \frac{k_i}{\sqrt{\lambda_i}}. \tag{5.4}$$

In this, $\tau_{\alpha,R}$ and $\tau_{\beta,R}$ denote the lattice resistance (Peierl's barrier) to slip and twinning which generally is a function of composition and temperature and may have different values for different deformation mechanisms like e.g. ordinary slip, super slip and twinning in the γ phase. The Hall-Petch coefficients k_i describe the strengthening effect by microstructural interfaces of type i with average spacing λ_i.

In the present form, Equations (5.3) and (5.4) contain several simplifications. First of all, it was assumed that there is only one Hall-Petch coefficients k_i that describes the strengthening effect of interfaces of type i on all affected deformation systems. However, the actual strengthening effect of a microstructural interface on a specific slip or twinning system depends on many factors like, e.g., the corresponding misorientation angles so that individual Hall-Petch coefficients would have to be defined for all possible γ/γ or γ/α_2 interfaces. This would lead to a very high number of additional parameters to be identified and thus would counteract the simplicity of the empirical Hall-Petch relation. Further, it is questionable that these subtle differences are relevant for the intended modeling purpose. As a second simplification it was assumed in Equations (5.3) and (5.4) that the microstructural length which determines the Hall-Petch strengthening by interfaces of type i coincides with their average spacing λ_i. Actually, the strengthening effect of interfaces of type i on a specific deformation system is determined by its free path length d_i with respect to these interfaces, i.e. the maximum distance a slip or twinning dislocation can move before encountering an interface of respective type. For equiaxed colonies, the free path length of all deformation systems with respect the colony boundaries coincides well with the colony size, i.e. $d_i \approx \lambda_i$ (for $i = C$). Which microstructural interfaces further contribute to the strength of a specific deformation system strongly depends on its orientation with respect to the lamellae, i.e. on its morphological classification (cf. Section 2.2.3). Since longitudinal deformation systems act parallel to the lamellae (see Figure 2.6), they are not strengthened by the lamella interfaces. Longitudinal deformation systems in γ lamellae are, however, strengthened by the domain boundaries (see Figure 2.6) with a free path length that corresponds well to the domain size, i.e. the assumption of $d_i = \lambda_i$ is met well (for $i = D$). Transversal deformation systems have to cross the lamella interfaces and are thus strengthened by them (see Figure 2.6). Their free path length with respect to the lamella boundaries is, however, generally $d_i > \lambda_i$ (for $i = L$) since their shear planes are inclined with respect to the lamella interfaces. Since the lamella thickness is usually at least one order of magnitude smaller than the γ domain size and even two orders of magnitude smaller than the colony size λ_C, it is still assumed that $d_i = \lambda_i$

(for $i = L$) for the sake of simplicity. Which microstructural interfaces affect the strength of mixed deformation systems is, however, not as obvious. Although the free path length of mixed deformation systems corresponds to the γ domain size (respectively the colony size in the α_2 lamellae), their shear plane crosses the lamella interfaces potentially making the lamella thickness the relevant microstructural parameter for their strength (see Figure 2.6). Experiments with polysynthetically twinned crystals under a loading angle of 0° showed that for this lamella orientation the yield strength is determined by the lamella thickness [47]. Since up to the yield point (plastic strain of 0.2%) polysynthetically twinned crystals with 0° orientation solely deform by mixed slip (cf. Figure 4.5), it can thus be concluded that the strength of mixed deformation systems is determined by the spacing of the lamella boundaries [37, 47].

Consequently, the following definitions for the initial critical resolved shear stresses in Equations (3.22) and (3.23) are introduced:

slip systems in the γ phase

$$\tau_{\alpha,0}^Y = \tau_{\alpha,R} + \frac{k_D}{\sqrt{\lambda_D}} + \frac{k_C}{\sqrt{\lambda_C}} \qquad \qquad \text{for } \alpha = 1 - 3 \qquad \qquad (5.5)$$

$$\tau_{\alpha,0}^Y = \tau_{\alpha,R} + \frac{k_L}{\sqrt{\lambda_L^\gamma}} + \frac{k_C}{\sqrt{\lambda_C}} \qquad \qquad \text{for } \alpha = 4 - 12 \qquad \qquad (5.6)$$

twinning systems in the γ phase

$$\tau_{\beta,0}^T = \tau_{\beta,R} + \frac{k_D}{\sqrt{\lambda_D}} + \frac{k_C}{\sqrt{\lambda_C}} \qquad \qquad \text{for } \beta = 1 \qquad \qquad (5.7)$$

$$\tau_{\beta,0}^T = \tau_{\beta,R} + \frac{k_L}{\sqrt{\lambda_L^\gamma}} + \frac{k_C}{\sqrt{\lambda_C}} \qquad \qquad \text{for } \beta = 2 - 4 \qquad \qquad (5.8)$$

slip systems in the α_2 phase

$$\tau_{\alpha,0}^Y = \tau_{\alpha,R} + \frac{k_C}{\sqrt{\lambda_C}} \qquad \qquad \text{for } \alpha = 1 - 3 \qquad \qquad (5.9)$$

$$\tau_{\alpha,0}^Y = \tau_{\alpha,R} + \frac{k_L}{\sqrt{\lambda_L^{\alpha_2}}} + \frac{k_C}{\sqrt{\lambda_C}} \qquad \qquad \text{for } \alpha = 4 - 12 \qquad \qquad (5.10)$$

The indices α and β correspond to the definition in Table 2.1.

5.2.1 Constitutive assumptions

Like before in Section 4.2.1, some constitutive assumption will be introduced in the following in order to facilitate the identification of the model parameters that were newly introduced by Equations (5.5)-(5.10).

Modeling the plastic deformation behavior of the α_2 phase

Due to the reasons discussed before, basal slip systems ($\alpha = 1 - 3$) are not considered here (see Section 4.2.1). In addition to the constitutive assumptions from Section 4.2.1, the Hall-Petch strengthening by lamella boundaries – i.e. the term $k_L/\sqrt{\lambda_L^{\alpha_2}}$ in Equation (5.10) – is neglected in the following and the lattice resistances $\tau_{\alpha,R}$ are defined to be the same for all slip systems of the same morphological classification. Thus the initial critical resolved shear stresses in the α_2 lamellae reduce to

$$\tau_{\text{mix},0}^{\alpha_2} = \tau_{\alpha,0}^{Y} = \tau_{\text{mix},R}^{\alpha_2} + \frac{k_C}{\sqrt{\lambda_C}} \qquad\qquad \text{for } \alpha = 4 - 6 \qquad\qquad (5.11)$$

$$\tau_{\text{trans},0}^{\alpha_2} = \tau_{\alpha,0}^{Y} = \tau_{\text{trans},R}^{\alpha_2} + \frac{k_C}{\sqrt{\lambda_C}} \qquad\qquad \text{for } \alpha = 7 - 12 \qquad\qquad (5.12)$$

with the lattice resistances

$$\tau_{\text{mix},R}^{\alpha_2} = 67 \, \text{MPa} \qquad\qquad \text{for } \alpha = 4 - 6 \qquad\qquad (5.13)$$

$$\tau_{\text{trans},R}^{\alpha_2} = 450 \, \text{MPa} \qquad\qquad \text{for } \alpha = 7 - 12. \qquad\qquad (5.14)$$

which again correspond to the single crystal findings from [27] (cf. Section 4.2.1).

Lattice resistance to slip and twinning in the γ phase

As mentioned above, the lattice resistance to slip and twinning $\tau_{\alpha,R}$ and $\tau_{\beta,R}$ is generally different for different deformation mechanisms (i.e. ordinary slip, super slip and twinning). Since the respective differences were assumed to be negligible in the γ phase (which – according to [37]) – appears to be reasonable in two phase alloys), the corresponding lattice resistance is modeled to be the same for all deformation systems, i.e.

$$\tau_{\alpha,R} = \tau_{\beta,R} = \tau_R \qquad\qquad \text{for } \alpha = 1 - 12 \text{ and } \beta = 1 - 4. \qquad\qquad (5.15)$$

Thus, the microstructure sensitive initial critical resolved shear stresses of the γ phase (Equations (5.5)-(5.8)) can again be written according to their morphological classification:

$$\tau_{\text{long},0}^{\gamma} = \tau_{\alpha,0}^{Y} = \tau_{\beta,0}^{T} = \tau_R + \frac{k_D}{\sqrt{\lambda_D}} + \frac{k_C}{\sqrt{\lambda_C}} \qquad \text{for } \alpha = 1 - 3 \text{ and } \beta = 1 \qquad (5.16)$$

$$\tau_{\text{mix},0}^{\gamma} = \tau_{\alpha,0}^{Y} = \tau_R + \frac{k_L}{\sqrt{\lambda_L^{\gamma}}} + \frac{k_C}{\sqrt{\lambda_C}} \qquad\qquad \text{for } \alpha = 4 - 6 \qquad\qquad (5.17)$$

$$\tau_{\text{trans},0}^{\gamma} = \tau_{\alpha,0}^{Y} = \tau_{\beta,0}^{T} = \tau_R + \frac{k_L}{\sqrt{\lambda_L^{\gamma}}} + \frac{k_C}{\sqrt{\lambda_C}} \qquad \text{for } \alpha = 7 - 12 \text{ and } \beta = 2 - 4. \qquad (5.18)$$

Work hardening

The work hardening behavior was described using the parameters from Table 4.2 in Chapter 4.

5.3 Lamella and domain boundary strengthening

The strengthening by lamella and domain boundaries is best investigated in polysynthetically twinned crystals/single colonies, i.e. in the absence of colony boundaries. Thus, the terms in Equations (5.11), (5.12) and (5.16)-(5.18) that correspond to the colony boundary strengthening – namely $k_C/\sqrt{\lambda_C}$ – are neglected in this section. The remaining parameters for lamella and domain boundary strengthening will be calibrated against experimental results with polysynthetically twinned crystals/single colonies.

5.3.1 Model parameters

With the introduced constitutive assumptions, only the lattice resistance τ_R and the Hall-Petch coefficients k_D and k_L for the γ phase remain to be identified. These parameters can be determined from experimental studies in which polysynthetically twinned crystals with systematically altered lamella and domain size were tested [44, 47]. Since under a loading angle of 45° the plastic deformation of polysynthetically twinned crystals is solely accomplished by longitudinal deformation systems (see Figure 4.5 and Table 4.3), the yield strength for this lamella orientation is determined by the γ domain size λ_D and can be written in analogy to Equation (5.1)

$$\sigma_{0.2}^{\mathrm{PST},45°} = \sigma_R + \frac{K_D}{\sqrt{\lambda_D}}. \tag{5.19}$$

By varying λ_D, the corresponding Hall-Petch coefficient K_D can be determined from interpolation of the resultant yield stresses. Extrapolating the results to $\lambda_D \to \infty$, further yields σ_R. Analogically, experiments with polysynthetically twinned crystals under loading angles of 0° or 90° have a yield stress that can be described by

$$\sigma_{0.2}^{\mathrm{PST},0°/90°} = \sigma_R + \frac{K_L}{\sqrt{\lambda_L}} \tag{5.20}$$

since for these orientations only mixed respectively transversal deformation systems are active up to the yield point (see Figure 4.5 and Table 4.3) and the yield strength is thus determined by the lamella thickness λ_L. From experimental results with different lamella thicknesses λ_L, the corresponding Hall-Petch coefficient K_L can be derived and extrapolation to $\lambda_L \to \infty$ yields σ_R. In Table 5.1, some Hall-Petch coefficients K_L and K_D are summarized that were determined this way.

Table 5.1. Experimentally obtained Hall-Petch coefficients K for differently oriented polysynthetically twinned crystals.

	loading angle φ	K [MPa$\sqrt{\mathrm{m}}$]	ref.
$\sigma_{0.2}$=f(λ_L)	0°	$K_L = 0.41$	[47]
$\sigma_{0.2}$=f(λ_D)	45°	$K_D = 0.27$	[47]
$\sigma_{0.2}$=f(λ_L)	90°	$K_L = 0.5$	[47]

However, the Hall-Petch coefficients k_D and k_L in Equations (5.16), (5.17) and (5.18) are not directly comparable to experimentally determined, macroscopic Hall-Petch coefficients K_D and K_L. A rough estimate for the lamella and domain boundary strengthening cofficients k_L and k_D may still be obtained by multiplying the experimentally determined Hall-Petch coefficients K_L and K_D from Table 5.1 by the highest Schmid factor that occurs in the respective lamella orientations [44, 63] as the corresponding deformation system(s) will most likely dominate the plastic deformation. With maximum Schmid factors of $f_{\mathrm{SF}} = 0.41$ for 0° orientation, $f_{\mathrm{SF}} = 0.43$ for 45° orientation and $f_{\mathrm{SF}} = 0.27$ for 90° orientation [55, 63], the experimentally determined Hall-Petch coefficients K_D and K_L from Table 5.1 yield $k_D = 0.1161\,\mathrm{MPa}\sqrt{\mathrm{m}}$ for 45° and $k_L = 0.135\,\mathrm{MPa}\sqrt{\mathrm{m}}$ for 90° respectively $k_L = 0.1681\,\mathrm{MPa}\sqrt{\mathrm{m}}$ for 0°. In [44], the Hall-Petch coefficients k_L and k_D were determined similarly but were reported to be the same for strengthening by lamella and domain boundaries with $k_L = k_D = 0.1\,\mathrm{MPa}\sqrt{\mathrm{m}}$. In view of these experimental results, the Hall-Petch coefficients k_D and k_L in Equations (5.16), (5.17) and (5.18) are chosen to be

$$k_L = k_D = 0.125\,\mathrm{MPa}\sqrt{\mathrm{m}} \tag{5.21}$$

in the following.

As the plastic deformation is mainly accomplished by the γ lamellae, the (approximate) lattice resistance τ_R of the γ phase in Equations (5.16), (5.17) and (5.18) can in principal be obtained the same way – i.e. by multiplying the extrapolated stress σ_R by the highest occurring Schmid factor in the γ lamellae of the tested orientations of the polysynthetically twinned crystal – and has been reported to be $\approx 30\,\mathrm{MPa}$ for the experimental results from [47] and [44]. However, determining the lattice resistance by extrapolation of experimental results includes a variety of uncertainties. First of all, the extrapolation is inherently prone to the – sometimes significant – scatter in the experimental data. Further, the yield strength includes some work hardening already as it is – per definition – determined after a plastic strain of 0.2%. However, even when ignoring the rather small plastic deformation prior to the yield point, the strengthening effect of the dislocation density in the undeformed specimen is still remaining. As this initial dislocation density was determined to be as high as $10^6\frac{1}{\mathrm{mm}^2}$ to $10^7\frac{1}{\mathrm{mm}^2}$ (cf. Section 4.2.1 and [11, 142]), this effect may account for $10\,\mathrm{MPa}$ to $30\,\mathrm{MPa}$ (cf. Equation (4.2)) of the apparent lattice resistance. Thus, the de facto lattice resistance is most likely lower than expected by the extrapolation of experimental results. Another important influence on the lattice resistance is the alloy chemistry, i.e. the composition and potential impurities of the tested alloy. All in all, the lattice resistance can, thus, unfortunately not be determined uniquely from the experimental studies at hand. From the described extrapolation of experimental results, the (apparent) lattice resistance was frequently reported to lie in the range of $30\,\mathrm{MPa}\leq \tau_R \leq 50\,\mathrm{MPa}$ [23, 44, 46] (including the mentioned uncertainties) but has been assumed to be as high as $65\,\mathrm{MPa}$ in [147]. Consequently, the applied lattice resistance in the γ phase is always given when discussing simulation results throughout the present work.

5.3.2 Model validation

In order to check whether the model is able to reproduce the microstructure sensitive yield strength of polysynthetically twinned crystals with the chosen Hall-Petch coefficients k_L and k_D (Equation (5.21)), simulations were carried out using the microstructural parameters of the polysynthetically twinned crystals tested in [47]. These microstructural parameters are summarized in table 5.2 together with the corresponding initial critical resolved shear stresses $\tau_{\mathrm{long},0}^{\gamma}$, $\tau_{\mathrm{mix},0}^{\gamma}$ and $\tau_{\mathrm{trans},0}^{\gamma}$ as they result from Equations (5.16), (5.17) and (5.18) with the choice of k_D and k_L given in Equation (5.21) and a lattice resistance of τ_R=20 MPa. In [47], the average lamella thickness was given without distinguishing between the thickness of the α_2 or the γ lamellae. Since the γ phase is the majority phase, the lamella thickness λ_L^{γ} in the model was assumed to coincide with the reported lamella thickness λ_L summarized in Table 5.2.

The simulations were carried out by again using the RVE from Section 3.5.1 and applying the rotational boundary conditions from Section 3.6.2 to it. A compressive strain rate of $\dot{\varepsilon} = 1.2\times 10^{-4}\mathrm{s}^{-1}$ was chosen according to the experiments [47]. The corresponding simulation results are shown in Figure 5.2[9].

While Figure 5.2 shows a good agreement between the simulated and the experimentally determined yield stresses for loading angles of 45° and 90°, the results for a loading angle of 0° require some discussion. Although the Hall-Petch coefficient of $k_L = 0.125\,\mathrm{MPa}\sqrt{\mathrm{m}}$ that was chosen for the simulations is lower than the value of $k_L = 0.1681\,\mathrm{MPa}\sqrt{\mathrm{m}}$ that was

---

[9]As the microstructural parameters were not reported for all tested specimens in [47], some experimental data points in Figure 5.2 miss a simulated counterpart.

Table 5.2. Microstructural parameters of polysynthetically twinned crystals tested in [47] and corresponding initial critical resolved shear stresses for the simulations obtained by Equations (5.16), (5.17) and (5.18) with $k_D = k_L = 0.125\,\mathrm{MPa}\sqrt{\mathrm{m}}$ and $\tau_R = 20\,\mathrm{MPa}$

	experimental study			simulation input		
Composition	α_2 volume fraction	λ_D	λ_L	$\tau^{\gamma}_{\mathrm{long},0}$	$\tau^{\gamma}_{\mathrm{mix},0}$	$\tau^{\gamma}_{\mathrm{trans},0}$
Ti-48.1at%Al	15 Vol%	7 µm	0.37 µm	67 MPa		225 MPa
Ti-48.1at%Al	15 Vol%	22 µm	0.53 µm	47 MPa		192 MPa
Ti-49.1at%Al	8 Vol%	24 µm	0.75 µm	46 MPa		164 MPa
Ti-49.1at%Al	8 Vol%	20 µm	0.57 µm	48 MPa		186 MPa
Ti-50.8at%Al	2 Vol%	64 µm	1.13 µm	36 MPa		138 MPa
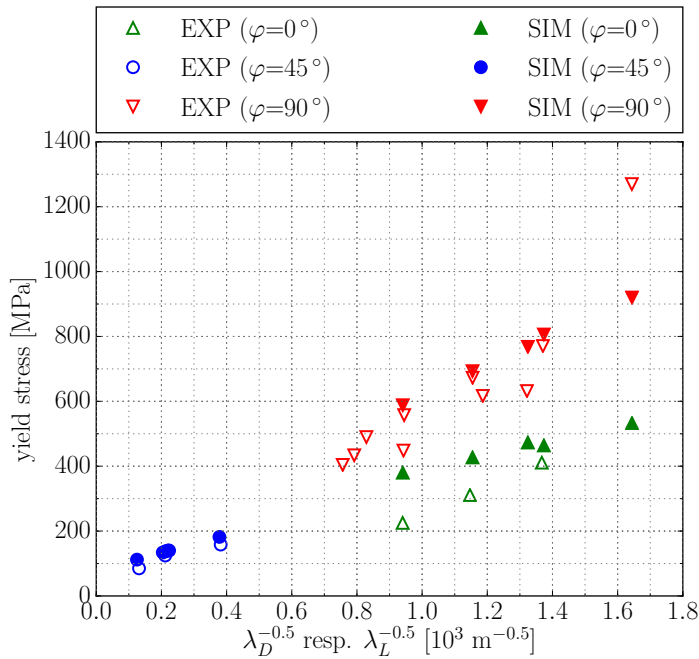
Figure 5.2. Comparison of simulated and experimentally obtained yield stress of differently oriented polysynthetically twinned crystals for different combinations of γ domain size λ_D and lamella thickness λ_L. Simulations were obtained for the microstructural parameter sets summarized in Table 5.2. The corresponding experimental results are taken from [47].

determined above from the experiments, the simulations still overestimate the corresponding experimental yield stresses under loading angles of $0°$. Having a closer look at the experimental results for this orientation, it appears that linear extrapolation of the only 3 experimental points to $\lambda_L \to \infty$ and thus $\lambda_L^{-0.5} \to 0$ does, however, yield a negative value for σ_R in the corresponding Equation (5.20) which is unphysical. The respective Hall-Petch coeffcient that was reported in [47] thus is inconsistent with the Hall-Petch relation. Since at the yield point of polysynthetically twinned crystals under a loading angle of $0°$ only mixed slip systems are active (see Figure 4.5 and Table 4.3), the overestimated yield stress is correlated to the formulation of their initial critical resolved shear stress. While the experimental results still suggest that the strength of mixed slip systems is determined by the lamella thickness, the way mixed slip systems interact with the lamella interfaces does not agree with the Hall-Petch

effect. Since mixed slip acts on shear planes that cross the plane of the lamella interfaces (see Figure 2.6), respective dislocations do not pile-up against the lamella interfaces but rather bow out between them indicating that their propagation is still hindered by the lamella interfaces [52]. In [52], it was thus suggested that the strength of mixed slip systems might be described by the inverse of the lamella thickness $\frac{1}{\lambda_L}$ instead of its inverse square root $\frac{1}{\sqrt{\lambda_L}}$. However, the initial yield stresses of the experiments from [52] were very well met for both $0°$ and $90°$ (see Figures 4.3 and 4.5) by assigning the same initial critical resolved shear stresses to mixed and transversal deformation systems in the simulations (cf. Equations (4.16) and (4.17)). Thus, a modification of the initial critical resolved shear stress of mixed slip systems, i.e of Equation (5.17) would impair the respective results. With the chosen values for $k_L = k_D = 0.125\,\text{MPa}\sqrt{\text{m}}$ and Equations (5.17) and (5.18), the initial critical resolved shear stresses from Equations (4.15)-(4.17) that allowed to reproduce the experimental results from [52], correspond to a lamella thickness of $\lambda_L = 1.1\,\text{µm}$ and a γ domain size of $\lambda_D = 50\,\text{µm}$ for $\tau_R = 20\,\text{MPa}$ which seems a reasonable combination of microstructural parameters as compared to the micrographs given in [52][10]. Further it is possible to reproduce the anisotropic yield stress of the polysynthetically twinned crystals tested in [26] by using the present formulation of the initial critical resolved shear stresses (i.e. Equations (5.16)-(5.18)) for an α_2 volume fraction of 5%, a lamella thickness of $\lambda_L = 2\,\text{µm}$, a γ domain size $\lambda_D = 100\,\text{µm}$[11] and a lattice resistance of $\tau_R = 20\,\text{MPa}$ as shown in Figure 5.3. As in the experiments, a compressive strain rate of $\dot{\varepsilon} = 2 \times 10^{-4}\,\text{s}^{-1}$ was applied.
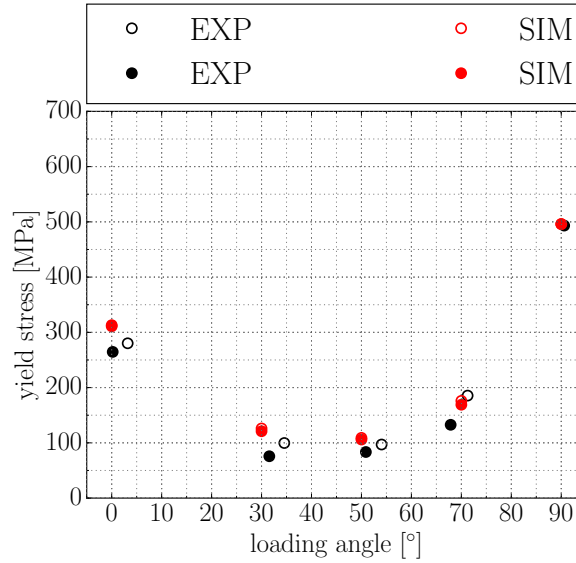
Figure 5.3. Comparison of the anisotropic yield strength of differently oriented polysynthetically twinned crystals as obtained by simulation and experiment. The microstructural parameters were chosen to be α_2 volume fraction=5%, $\lambda_L = 2\,\text{µm}$, $\lambda_D = 100\,\text{µm}$ and $\tau_R = 20\,\text{MPa}$ for the simulations. The experimental results were taken from [26].

Thus, it can be stated, that with the formulated initial critical resolved shear stresses (Equations (5.16)-(5.18))) and a choice of $k_L = k_D = 0.125\,\text{MPa}\sqrt{\text{m}}$, the microstructure sensitive yield strength of polysynthetically twinned crystals can be reproduced reasonably well. However, additional experimental data were required to ultimately reveal the functional de-

---

[10]In [52], the microstructural parameters were unfortunately not given explicitly.

[11]These microstructural parameters agree reasonably well with the ones reported in another publication of the group in the same year [24]

pendence of the initial critical resolved shear stresses of mixed slip systems on the lamella thickness.

5.4 Colony boundary strengthening

While the Hall-Petch strengthening effect by lamella and domain boundaries can be separately investigated by experiments with polysynthetically twinned crystals, colony boundary strengthening can naturally only be investigated in polycolony specimens in which all types of microstructural interfaces coexist. Determining the corresponding colony boundary Hall-Petch strengthening coefficient K_C experimentally thus requires a series of experiments with specimens that all have the same γ domain size λ_D and lamella thickness λ_L but systematically altered colony sizes λ_C. Since it is difficult to independently vary the microstructural parameters [11], conducting a respective series of experiments is challenging. Consequently, most of the reported K_C values [18, 23, 42, 43, 45, 48, 49] were determined from experiments in which not only the colony size was altered but also the lamella thickness and γ domain size varied[12]. However, the reported colony boundary strengthening coefficients K_C differ significantly even between studies in which K_C was determined from experiments with – at least nearly – constant lamella thickness λ_L (and thus constant domain size λ_D) [23, 42, 48]. Thus, it was suggested in [22] that the strengthening effect of the colony boundaries might be a function of the anisotropy of the lamellar colonies, i.e. of the relative strength of hard mode (mixed and transversal) and soft mode (longitudinal) deformation systems. Since K_C represents the colony boundary strength, i.e. the stress of the dislocation pile-up against a colony boundary that has to be reached in order to activate deformation systems in the neighboring colony, it is in fact evident that K_C is a function of the strengths of the respective slip and twinning systems to be activated. This is illustrated in Figure 5.4.
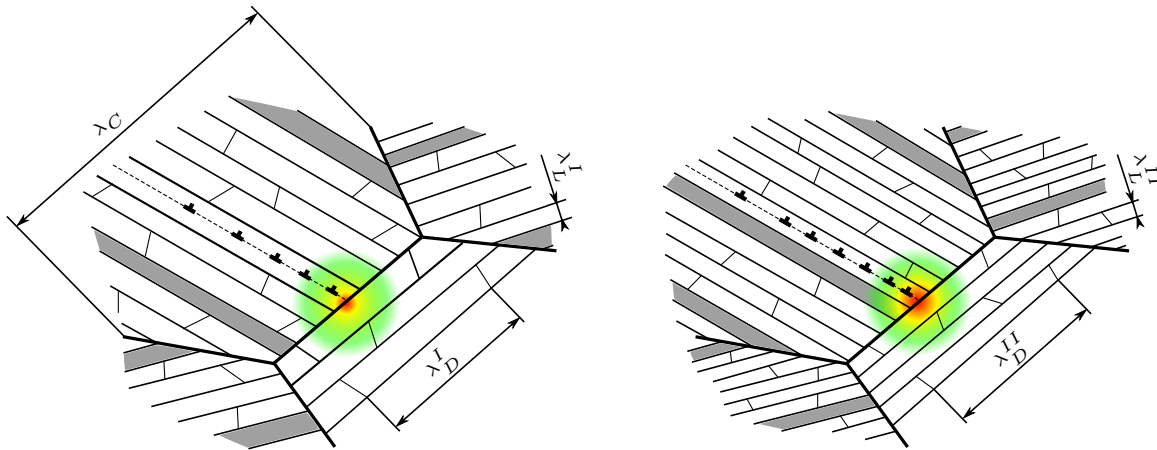
Figure 5.4. Illustration of the dislocation pile-up against a colony boundary that is necessary to activate slip/twinning systems in the adjacent colony. For $\lambda_C^{II} = \lambda_C^I$ but $\lambda_L^{II} < \lambda_L^I$ and $\lambda_D^{II} < \lambda_D^I$ the strength of respective systems in the right image will be higher than in the left one, consequently requiring a higher pile-up stress to be activated and thus making colony boundary strengthening a function of λ_L and λ_D. Figure taken from Schnabel & Bargmann[2].

---

[12]Actually, the γ domain size λ_D was reported in neither of the cited references [18, 23, 42, 43, 45, 48, 49]. However, λ_D was suspected in [22, 148] to be correlated to the lamella thickness λ_L. Thus, specimens with a similar lamella thickness λ_L may be assumed to have a similar domain size λ_D as well.

This statement implies that

- the colony boundary strengthening coefficient K_C has to be a function of the lamella thickness λ_L and the domain size λ_D, since lamella and domain boundary strengthening determine the strength of the deformation systems in the neighboring colony and in consequence

- the experimentally determined coefficients K_C are valid only for the specific combination of λ_L and λ_D for which they were determined.

The second statement rationalizes the differences in the reported colony boundary strengthening coefficients K_C since they were in fact identified for different combinations of λ_L and λ_D in the different studies.

Given the difficulties in microstructure control, identifying the functional relation $K_C = f(\lambda_L, \lambda_D)$ experimentally is, however, unreasonably labor intensive. Unlike experiments, numerical studies are not restricted regarding the choice of microstructural parameters, consequently enabling to investigate any combination of lamella thickness, domain size and colony size. Thus, the presented crystal plasticity model can help to identify $K_C = f(\lambda_L, \lambda_D)$ which then ultimately allows to predict the microstructure sensitive yield strength of fully lamellar TiAl alloys. In the following, a procedure will be shown that allows to identify $K_C = f(\lambda_L, \lambda_D)$ by a combination of simulations and experimental data.

5.4.1 Calculation scheme

In order to predict the yield stress $\sigma_{0.2}$ of a conventional polycrystalline material from its grain size D by the use of the classical Hall-Petch relation, i.e. Equation (5.1), σ_R and the Hall-Petch coefficient K have to be known. As mentioned earlier, σ_R represents the (theoretical) yield stress of a polycrystalline material with grain size $D \to \infty$, i.e. without grain boundary strengthening. In the context of colony boundary strengthening of fully lamellar TiAl alloys the respective Hall-Petch relation would read

$$\sigma_{0.2} = \sigma_R + \frac{K_C}{\sqrt{\lambda_C}} \tag{5.22}$$

where σ_R consequently represents the (theoretical) yield stress of an alloy with a colony size $\lambda_C \to \infty$, i.e. in the absence of colony boundary strengthening. Although a polycolony microstructure with infinitely large colonies is obviously a paradox, it is still possible to set up a model representation of such a hypothetical material by setting the colony boundary strengthening terms $k_C/\sqrt{\lambda_C}$ in the initial critical resolved shear stresses (Equations (5.11), (5.12) and (5.16)-(5.18)) to 0, and applying the resultant model to the polycolony RVE from Section 3.5.2. The simulated yield strength of this model set up in fact represents σ_R in Equation (5.22). Due to the lamella and domain boundary strengthening effect that – in the absence of colony boundaries – determines the strength of the lamellar colonies (cf. Section 5.3), σ_R and thus the simulated σ_R^{SIM} depend on lamella thickness λ_L and domain size λ_D. Adapting the lamella and domain boundary strengthening coefficients k_L and k_D as well as the constitutive assumptions from the previous section (Section 5.3), σ_R^{SIM} can be determined for any combination of lamella thickness λ_L[13] and domain size λ_D. For any yield stress $\sigma_{0.2}^{\text{EXP}}$ which was experimentally determined for a specific combination of λ_L^i, λ_D^i and λ_C^i, it is thus possible to determine the corresponding σ_R^{SIM}. Knowing the yield strength $\sigma_{0.2}^{\text{EXP}} \left(\lambda_L^i, \lambda_D^i, \lambda_C^i \right)$

---

[13]or more precisely λ_L^γ since in Section 5.3 the strengthening of the α_2 lamellae by lamella boundaries was neglected.

and $\sigma_R^{\mathrm{SIM}}\left(\lambda_L^i, \lambda_D^i\right)$ for a specific combination of λ_L^i, λ_D^i and λ_C^i, the corresponding Hall-Petch coefficient $K_C\left(\lambda_L^i, \lambda_D^i\right)$ for this specific combination of microstructural parameters can be determined by rearranging Equation (5.22) to

$$K_C\left(\lambda_L^i, \lambda_D^i\right) = \frac{\sigma_{0.2}^{\mathrm{EXP}}\left(\lambda_L^i, \lambda_D^i, \lambda_C^i\right) - \sigma_R^{\mathrm{SIM}}\left(\lambda_L^i, \lambda_D^i\right)}{\lambda_C^{i^{-0.5}}}. \tag{5.23}$$

Equation (5.23) allows to determine $K_C\left(\lambda_L^i, \lambda_D^i\right)$ for a specific combination of λ_L^i and λ_D^i from only one experimentally determined yield stress instead of the regularly required series of experiments with systematically altered colony size λ_C and constant λ_L and λ_D. This interpolation scheme is illustrated in Figure 5.5.
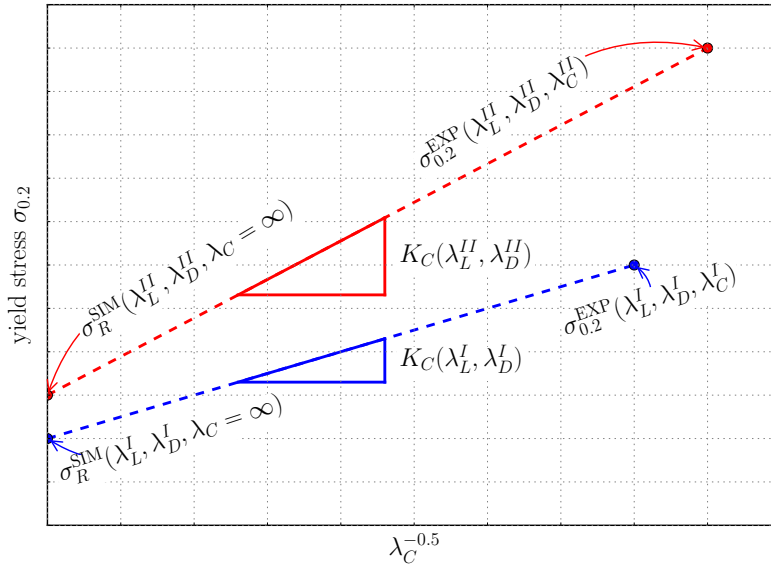
Figure 5.5. Illustration of the presented interpolation scheme which allows to determine $K_C(\lambda_L^i, \lambda_D^i)$ by combining simulation and experimental results. By applying the crystal plasticity model of a polysynthetically twinned crystal/single colony (i.e. without colony boundary strengthening) to the polycolony RVE from Section 3.5.2, $\sigma_R^{\mathrm{SIM}}(\lambda_L^i, \lambda_D^i, \lambda_C = \infty)$ can be determined for any given combination of λ_L^i and λ_D^i. With the corresponding experimental results, the relation $K_C(\lambda_L^i, \lambda_D^i) = \frac{\sigma_{0.2}^{\mathrm{EXP}}(\lambda_L^i, \lambda_D^i, \lambda_C^i) - \sigma_R^{\mathrm{SIM}}(\lambda_L^i, \lambda_D^i)}{\lambda_C^{i^{-0.5}}}$ is evaluated which was obtained by re-arranging the Hall-Petch relation (5.22).

Repeating this for a sufficient number of experimental data points, finally reveals $K_C = f\left(\lambda_L, \lambda_D\right)$. Further, this procedure does not impose any restrictions on the combination of microstructural parameters that have to be tested in the respective experiments.

5.4.2 Determining the colony boundary strengthening coefficient K_C

With the presented interpolation scheme it is possible to determine the functional dependence of the colony boundary Hall-Petch coefficient K_C on the lamella thickness λ_L and the γ domain size λ_D by combining simulation results with the experimental results reported in [18, 23, 42]. The microstructural parameters of the tested samples in respective studies are summarized in Table 5.3.

Unfortunately, the γ domain size is reported in neither of the cited studies. Since the γ domain

Table 5.3. Microstructural parameters of fully lamellar TiAl alloys tested in [18, 23, 42]. Compressive and tensile strain rates are denoted by (C) and (T) respectively. *: not reported. If the α_2 content was not reported, it was assumed to be 10 Vol.-%. Since the γ domain size was reported in neither of the studies, it was assumed to be $\lambda_D = 50 \times \lambda_L$. **: from this study only results for alloys with a maximum α_2 content of 32% were considered.

| composition	α_2 [Vol.-%]	λ_C [μm]	λ_D [μm]	λ_L [μm]	$\sigma_{0.2}^{\text{EXP}}$ [MPa]	$\dot{\varepsilon}$		ref.
Ti-45.3Al-2.1Cr-2Nb	20	75	4.4*	0.088	714	$5 \times 10^{-4}\text{s}^{-1}$	(C)	[23]**
Ti-45.3Al-2.1Cr-2Nb	29	78	2.9*	0.058	835	$5 \times 10^{-4}\text{s}^{-1}$	(C)	[23]**
Ti-45.3Al-2.1Cr-2Nb	32	56	1.75*	0.035	968	$5 \times 10^{-4}\text{s}^{-1}$	(C)	[23]**
Ti-45.5Al-2Cr-1.5Nb-1V	10*	260	8*	0.16	515	$2 \times 10^{-4}\text{s}^{-1}$	(C)	[42]
Ti-45.5Al-2Cr-1.5Nb-1V	10*	390	8*	0.16	546/491	$2 \times 10^{-4}\text{s}^{-1}$	(C)	[42]
Ti-45.5Al-2Cr-1.5Nb-1V	10*	690	8*	0.16	469	$2 \times 10^{-4}\text{s}^{-1}$	(C)	[42]
Ti-45.5Al-2Cr-1.5Nb-1V	10*	920	8.5*	0.17	454	$2 \times 10^{-4}\text{s}^{-1}$	(C)	[42]
Ti-45.5Al-2Cr-1.5Nb-1V	10*	370	0.75*	0.015	823	$2 \times 10^{-4}\text{s}^{-1}$	(C)	[42]
Ti-45.5Al-2Cr-1.5Nb-1V	10*	360	4.75*	0.095	584	$2 \times 10^{-4}\text{s}^{-1}$	(C)	[42]
Ti-45.5Al-2Cr-1.5Nb-1V	10*	380	25*	0.5	466	$2 \times 10^{-4}\text{s}^{-1}$	(C)	[42]
Ti-47Al-2Cr-2Nb	10*	65	5*	0.1	969	$4.4 \times 10^{-3}\text{s}^{-1}$	(T)	[18]
Ti-47Al-2Cr-2Nb	10*	62	19.5*	0.39	646	$4.4 \times 10^{-3}\text{s}^{-1}$	(T)	[18]
Ti-47Al-2Cr-2Nb-0.15B	10*	33	22*	0.44	492	$4.4 \times 10^{-3}\text{s}^{-1}$	(T)	[18]
Ti-47Al-2Cr-1.8Nb-0.2W-0.15B	10*	31	15*	0.3	549	$4.4 \times 10^{-3}\text{s}^{-1}$	(T)	[18]
Ti-47Al-2Cr-1.8Nb-0.2W-0.15B	10*	25	7.05*	0.141	756	$4.4 \times 10^{-3}\text{s}^{-1}$	(T)	[18]
Ti-46Al-2Cr-1.8Nb-0.2W-0.15B	10*	26	5.25*	0.105	895	$4.4 \times 10^{-3}\text{s}^{-1}$	(T)	[18]
Ti-47Al-2Cr-1Nb-1Ta	10*	60	4.3*	0.086	938	$4.4 \times 10^{-3}\text{s}^{-1}$	(T)	[18]

size is, however, suspected to be proportional to the lamella thickness [22, 148], it was assumed to be $\lambda_D = 50 \times \lambda_L$ which seems reasonable when comparing the reported lamella and domain sizes of polysynthetically twinned crystals summarized in Table 5.2. For the simulations the lattice resistance τ_R was set to 30 MPa in the γ phase. The RVE of a polycolony microstructure from Section 3.5.2 was used for the simulations. The RVE was subjected to periodic boundary conditions (cf. Section 3.6.1) and the strain rate for the simulations was set according to the reported values $\dot{\varepsilon}$ (see Table 5.3). The work hardening as well as the lamella and domain boundary strengthening were modeled by applying the model parameters and constitutive assumptions from Chapter 4 and Section 5.3 respectively.

For every experimentally investigated combination of microstructural parameters in Table 5.3, one simulation was carried out to determine the corresponding σ_R^{SIM}. With the results of this simulation and the experimentally determined yield stress $\sigma_{0.2}^{\text{EXP}}$, the K_C value that corresponds to the respective combination of λ_L and λ_D was determined by Equation (5.23). In Figure 5.6(a), the respectively calculated colony boundary Hall-Petch coefficients K_C are plotted together with the experimentally determined K_C values.

Although the correlation of the calculated K_C values in Figure 5.6(a) is compromised by the incompletely reported microstructural parameters (see Table 5.3) which in consequence had to be estimated, the dependence of K_C on the lamella thickness λ_L is apparent. Thus, the simulation results successfully demonstrate that the colony boundary strengthening coefficient K_C is in fact a function of the lamella thickness and the γ domain size[14] as suggested in [22]. In order to finally implement the colony boundary strengthening effect into the initial critical resolved shear stresses of the deformation systems, i.e. into Equations (5.11), (5.12) and (5.16)-(5.18), K_C has to be defined as an explicit function of λ_L and λ_D. As mentioned earlier, it was suspected in [22], that K_C depends on λ_L and λ_D via the relative strength of the hard (mixed and transversal) and the soft (longitudinal) deformation systems of the lamellar colonies. These strengths are themselves determined by the inverse square root of

---

[14]As in the present results the γ domain size was assumed to be $\lambda_D = 50 \times \lambda_L$, the dependence of K_C on λ_D is, however, distorted here.
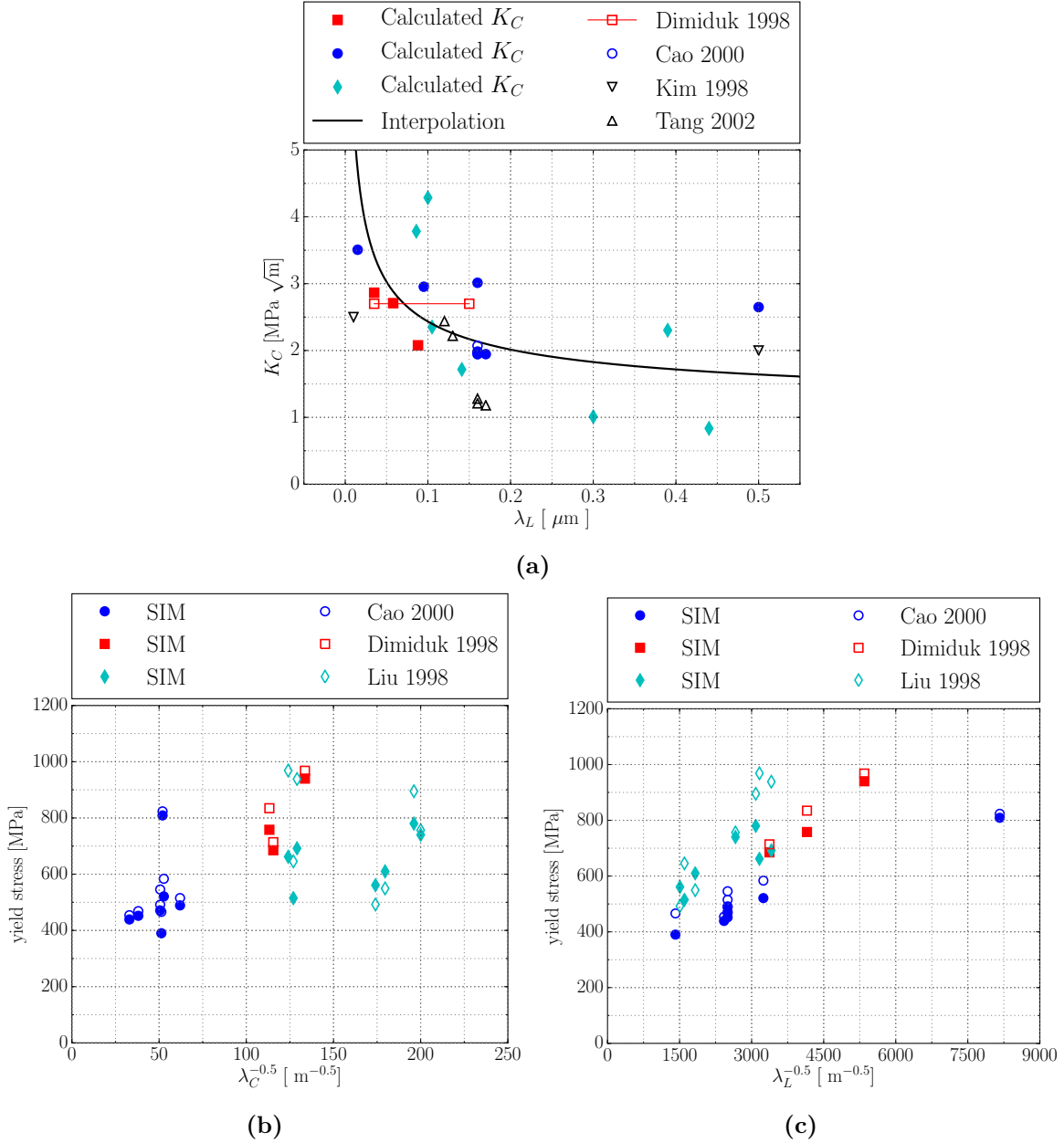
Figure 5.6. (a): Colony boundary Hall-Petch coefficient K_C plotted over the lamella thickness λ_L. Full symbols: determined via the interpolation scheme illustrated in Figure 5.5; open symbols: experimentally determined K_C values from [22, 23, 42, 48]. In [23], K_C was determined from experiments with the indicated range of lamella thicknesses; solid line: interpolation of calculated Hall-Petch coefficients by $K_C(\lambda_L) = K_{C,0} + K_{C,\lambda_L} \frac{1}{\sqrt{\lambda_L}}$; (b) and (c): Comparison of experimentally determined $\sigma_{0.2}^{\mathrm{EXP}}(\lambda_L, \lambda_D, \lambda_C)$ from [18, 23, 42] to simulated yield stresses $\sigma_{0.2}^{\mathrm{SIM}}(\lambda_L, \lambda_D, \lambda_C)$. In the simulations, colony boundary strengthening was considered by introducing the functional relation $K_C = f(\lambda_L, \lambda_D)$ determined from Figure 5.6(a) to the initial critical resolved shear stresses of all deformation systems in both phases like shown in Equations (5.11), (5.12) and (5.16)-(5.18).

λ_L and λ_D (cf. Section 5.3) so that $K_C = f\left(\frac{1}{\sqrt{\lambda_L}}, \frac{1}{\sqrt{\lambda_D}}\right)$ is assumed in the following. Since $\lambda_L \ll \lambda_D$, the term $\frac{1}{\sqrt{\lambda_D}}$ is much smaller than $\frac{1}{\sqrt{\lambda_L}}$ and the sensitivity of K_C to changes in λ_L

is assessed to be much higher than to changes in λ_D. Therefore, K_C is defined as a function of the inverse square root of λ_L only

$$K_C(\lambda_L) = K_{C,0} + K_{C,\lambda_L} \frac{1}{\sqrt{\lambda_L}}. \tag{5.24}$$

For an infinite lamella thickness, i.e. $\lambda_L \to \infty$, Equation (5.24) has to approach the colony boundary strengthening coefficient of a near-γ microstructure which mainly consists of globular γ grains (cf. Figure 1.2). The corresponding Hall-Petch coefficient was stated to be $\approx 1\,\mathrm{MPa}\sqrt{\mathrm{m}}$ [22] so that $K_{C,0}$ is chosen to be $1\,\mathrm{MPa}\sqrt{\mathrm{m}}$. With this assumption, K_{C,λ_L} in Equation (5.24) was determined to be $K_{C,\lambda_L} = 4.3165 \times 10^{-4}\,\mathrm{MPa}[\sqrt{\mathrm{m}}]^2$ by interpolating the calculated K_C values in Figure 5.6(a). The resultant function for $K_C(\lambda_L)$ has been added to Figure 5.6(a).

In order to incorporate the determined function for the macroscopic colony boundary Hall-Petch coefficient K_C into the initial critical resolved shear stresses, Equation (5.24) has to be resolved to the slip and twinning systems. This is done by multiplying it by a factor of 0.3[23] so that the colony boundary strengthening coefficient k_C in Equations (5.11), (5.12) and (5.16)-(5.18) reads

$$k_C(\lambda_L) = k_{C,0} + k_{C,\lambda_L} \frac{1}{\sqrt{\lambda_L}} = 0.3\mathrm{MPa}\sqrt{\mathrm{m}} + 1.295 \times 10^{-4}\mathrm{MPa}[\sqrt{\mathrm{m}}]^2 \frac{1}{\sqrt{\lambda_L}}. \tag{5.25}$$

With the determined functional relation of the Hall-Petch coefficient k_C on the lamella thickness λ_L given by Equation (5.25), it can be checked whether the model is able to reproduce the experimentally determined yield stresses for the microstructural parameters in Table 5.3. As depicted in Figure 5.6 (b) and (c), including $k_C(\lambda_L)$ into the initial critical resolved shear stresses of both phases and rerunning the simulations reproduces the experimentally determined yield stresses reasonably well for most combinations of microstructural parameters in Table 5.3.

5.5 Summary

In the present Chapter, the crystal plasticity model from Section 3.2 was extended to take into account the strengthening effect of the different coexisting microstructural interfaces in fully lamellar TiAl alloys. The corresponding Hall-Petch strengthening was incorporated into the initial critical resolved shear stresses. It was shown that the microstructure sensitive yield strength of differently oriented polysynthetically twinned crystals could be reproduced with the extended model. Subsequently, a procedure was shown that allowed to identify the colony boundary Hall-Petch strengthening coefficient as a function of the other microstructural parameters which was to date not possible by experiments.

6 Micro yield in polycolony microstructures

As briefly mentioned in the introduction to Chapter 4, polycolony microstructures exhibit a distinct micro yield behavior which results from the strong plastic anisotropy of the lamellar colonies. While the anisotropy of the lamellar colonies does not directly appear in the macroscopic yield stress[15] of polycolony microstructures, it still has a pronounced effect on their plastic deformation behavior. This manifests in two ways:

1. in a very inhomogeneous microplasticity since plastic deformation concentrates in weakly oriented colonies and correspondingly

2. in a transient onset of yield since the plastic deformation starts in the colonies that are in weakest orientation while colonies in stronger orientations are only successively activated at higher stresses, i.e. at later deformation stages.

While the transient onset of yield is visible in macroscopic stress-strain curves (see e.g. [22, 23, 131, 149]), the localization of plasticity in weakly oriented colonies was recently observed by DIC analyses of polycolony microstructures [131–133]. The strong gradients that occur in the local plastic strains of polycolony microstructures were frequently suspected to promote pre-yield cracking (see e.g. [132, 149, 150]) so that it is of technical interest to better understand the micro yield behavior in order to ultimately identify combinations of microstructural parameters that reduce the tendency to form pre-yield cracks. Investigating the influence of different combinations of microstructural parameters on the microplasticity of several interacting colonies by experiments is, however, challenging. Compared with the experimental effort that is necessary to investigate the local plastic strain fields in polycolony microstructures and to draw conclusions on how the different microstructural parameters affect the micro yield behavior, it is comparatively easy to assess these issues by the presented crystal plasticity model. In fact, the influence of the relative strength of hard (transversal and mixed) and soft mode (longitudinal) deformation systems on the micro yield behavior was already investigated in the very first, yet still 2D, numerical studies on lamellar TiAl [57, 58]. More recently, the micro stress and strain fields that arise from the strong plastic anisotropy of the differently oriented colonies in polycolony microstructures were investigated by crystal plasticity studies on 3D polycolony RVEs [71, 80]. However, like the 2D numerical studies before [57, 58], these 3D numerical investigations of the microyield in fully lamellar TiAl [71, 80] were based on a homogenized single phase model of the lamellar colonies that does not explicitly incorporate the Hall-Petch strengthening effect (cf. Section 3.1.1). Therefore, the numerical studies presented in [57, 58, 71, 80] enabled a qualitative assessment of the influence of relative strength of hard (transversal/mixed) and soft (longitudinal) deformation systems on the micro yield behavior but do not allow to explicitly relate the findings to the choice of microstructural parameters as it will be done in the following.

6.1 Numerical study

With the work hardening formulation introduced in Chapter 4 and the microstructure sensitive formulation of the initial critical resolved shear stresses introduced in Chapter 5, the

---

[15]provided there is no pronounced texture

presented crystal plasticity model allows to investigate the micro yield behavior of polycolony microstructures as it will be shown in the following. In contrast to experimental investigations, numerical studies allow to directly relate the deformation within the lamellae of the single colonies (i.e. on the micro scale) to the microplasticity of several interacting colonies (i.e. on the meso scale) and finally to the macroscopic stress-strain response. Thus, conclusions can be drawn on how specific combinations of microstructural parameters affect the micro yield behavior.
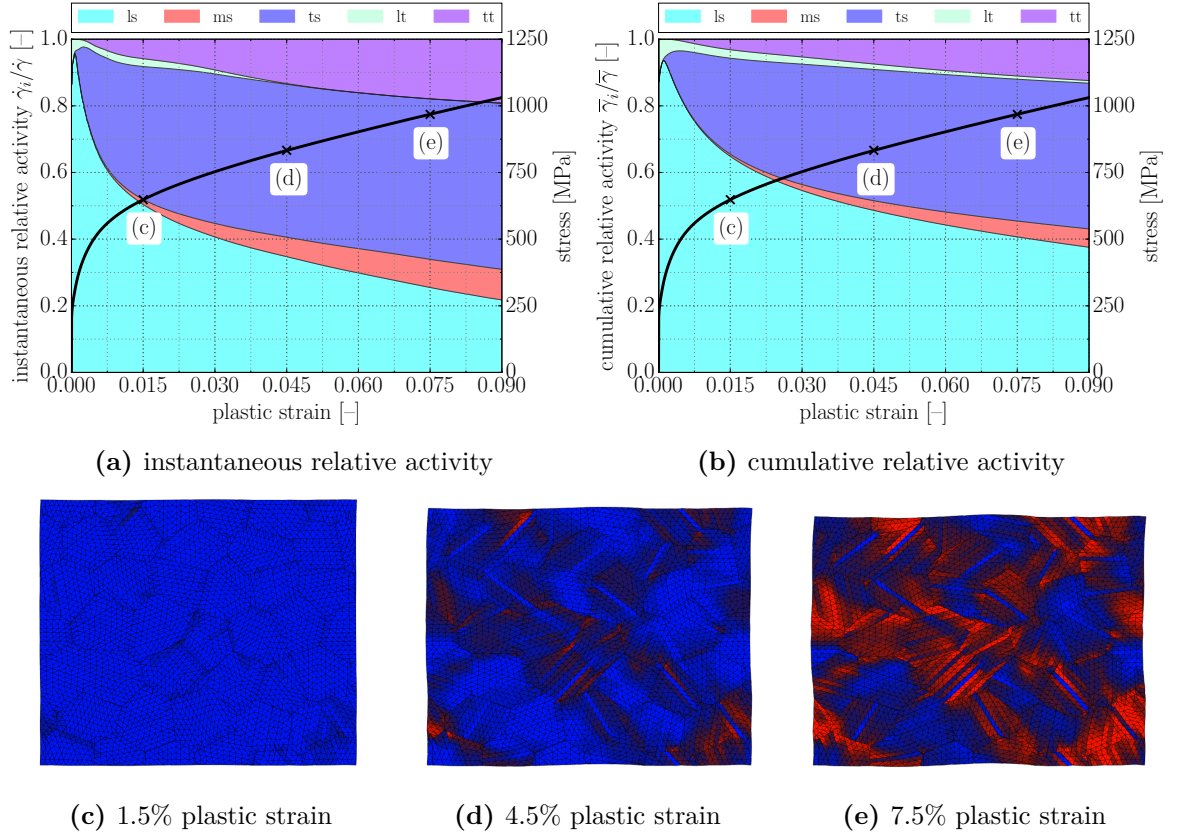
6.1.1 Numerical results

The subsequently presented simulations were carried out using the RVE of a polcolony microstructure from Section 3.5.2. Periodic boundary conditions were applied (see Section 3.6.1) and the RVE was loaded uniaxially with a compressive strain rate of $\dot{\varepsilon} = 1 \times 10^{-4}\text{s}^{-1}$. The work hardening behavior was modeled according to Chapter 4 and the microstructure sensitive initial critical resolved shear stresses were modeled according to Chapter 5.

In order to investigate the relative activity of deformation systems in polycolony microstructures, a simulation was set up with an exemplary microstructure that is characterized by an α_2 volume fraction of 10%, a colony size of λ_C=250 µm, a domain size of λ_D=25 µm and a lamella thickness of λ_L=0.5 µm. The instantaneous as well as the cumulative relative activity of deformation systems in the γ lamellae as obtained by the respective simulation is shown together with the corresponding macroscopic stress-strain curve in Figure 6.1(a) and (b). The relative activities were determined as described in Section 4.3.

The simulated stress-strain curve in Figures 6.1(a) and (b) nicely illustrate the transient onset of yield in fully lamellar TiAl. The relatively low initial yield stress is followed by a high (apparent) work hardening rate which gradually decreases with ongoing plastic deformation until ultimately an approximately constant work hardening rate is reached. The instantaneous relative activity in Figure 6.1(a) indicates that at the very beginning of plastic deformation only longitudinal slip and twinning systems are active. However, directly after beginning plasticity, activity on transversal slip and twinning systems is observed which rapidly increases with ongoing plastic deformation until finally the activity on tranvsersal systems is even higher than on longitudinal systems. Mixed deformation systems show only a moderate activity, obviously playing a subordinate role in the plastic deformation of polycolony microstructures.

As mentioned above, plastic deformation of polycolony microstructures starts in weakly oriented colonies while colonies that are less favorably oriented for plastic deformation start to plasticize only at later deformation stages. The strong concentration of plastic deformation in the weakly oriented colonies is nicely visible in the simulation results as shown in Figure 6.1(c), (d) and (e) by plotting the total plastic shear $\overline{\gamma}$ for different deformation stages.

As the lamella thickness λ_L, the γ domain size λ_D and the colony size λ_C, determine the strengths of the deformation systems of different morphological classes (see Chapter 5), it is evident that the micro yield behavior is influenced by the combination of microstructural parameters. By systematically varying λ_L, λ_D and λ_C in the simulations (while keeping the α_2 volume fraction constant at 10%), it is possible to explicitly investigate the influence of the different microstructural parameters on the microplasticity. For this parameter study, the above used set of exemplary microstructural parameters (λ_C=250 µm, λ_D=25 µm and λ_L=0.5 µm) was taken as a reference. Three additional simulations were carried out in each of which another microstructural parameter was reduced by a factor 5 while keeping the others unchanged. The corresponding simulated stress-strain curves are given in Figure 6.2 together with the stress-strain curve of the reference microstructure (black line).

(a) instantaneous relative activity

(b) cumulative relative activity

(c) 1.5% plastic strain   **(d)** 4.5% plastic strain   **(e)** 7.5% plastic strain

Figure 6.1. Simulation results for of a polycolony microstructure. The simulation was carried out with an α_2 volume fraction of 10%, a colony size λ_C=250 μm, a domain size λ_D=25 μm, a lamella thickness λ_L=0.5 μm and a lattice resistance of τ_R =30 MPa. (a), (b): Simulated macroscopic stress strain curve (solid line) and relative activity of deformation systems in the γ lamellae (colored background areas). ls: longitudinal slip, ms: mixed slip, ts: transversal slip, lt: longitudinal twinning, tt: transversal twinning; (c), (d), (e): Contour plots of total plastic shear $\overline{\gamma}$. Red areas correspond to $\overline{\gamma} > 0.4$; blue areas indicate $\overline{\gamma} < 0.05$.

6.1.2 Discussion

In the following, the presented numerical results are discussed in order to identify trends in the micro yield behavior.

Relative activity of deformation systems

As it was discussed in Section 4.3, the plastic deformation of differently oriented polysynthetically twinned crystals/single colonies under uniaxial load is accomplished by different groups of deformation systems depending on the loading angle. Due to the selective activity of different groups of deformation systems, it was possible to directly relate changes in their relative activity to their work hardening interactions and to specifics of the corresponding macroscopic stress-strain curves. Since the macroscopic stress-strain response of polycolony microstructures is the result of the co-deformation of numerous interacting colonies with different lamella orientations, the relative activity of deformation systems within a single colony can not directly be related to features of the macroscopic stress-strain curve. Unlike in polysynthetically twinned crystals/single colonies, the change in work hardening rate that was observed for the first $\approx$1.5% plastic strain in Figure 6.1(a) and (b), is thus not related to specific work harden-
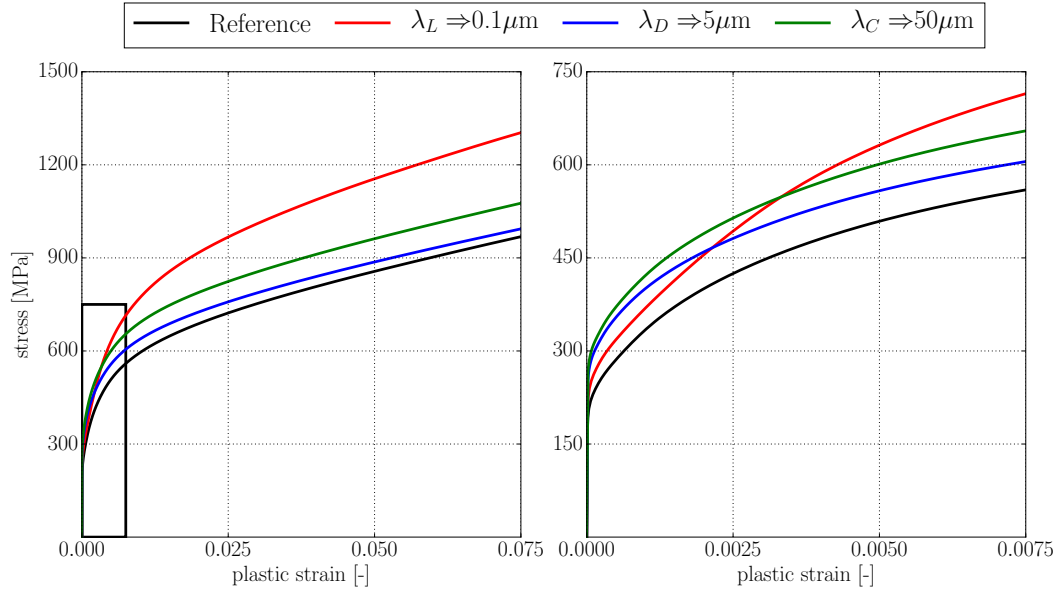
Figure 6.2. Simulated stress-strain response of a polycolony microstructure for systematically altered microstructural lengths. The black line indicates the reference microstructure (λ_C=250 µm, λ_L=0.5 µm, λ_D=25 µm). Microstructural parameters: λ_C: colony size; λ_L: lamella thickness; λ_D: domain size. left: Stress-strain response up to 7.5% plastic strain; right: Magnification of the response for the first 0.75% plastic strain.

ing interactions but is the result of the transient onset of yield in polycolony microstructures. Thus, the relative activity of deformation systems of different morphological classes given in Figure 6.1 provides information to which extent the plastic deformation is accomplished by weakly oriented colonies (in which preferably longitudinal deformation systems will be activated) and at which deformation stage the colonies of stronger orientation start to deform plastically (indicated by activity of mixed and transversal deformation systems) instead.

As expected, the plastic deformation starts in colonies that have sufficiently high Schmid factors on the longitudinal (i.e. the weakest) deformation systems (see Figure 6.1(a) and (b)). However, as long as no fracture occurs, the colonies are forced to undergo a compatible co-deformation. Due to this kinematic constraints between neighboring colonies and the arising constraint stresses it is not surprising that the plastic deformation is not solely accomplished by longitudinal deformation systems in weakly oriented colonies. This explains why shortly after onset of yield, also transversal slip and twinning activity is visible in Figure 6.1(a) and (b). The low activity of mixed slip systems in polycolony microstructures can, however, largely be explained by the fact that they can only be activated for a very narrow range of orientation angles as it was found for polysynthetically twinned crystals (cf. Figure 4.5).

With ongoing plasticity, the relative activity of transversal deformation systems increases which nicely illustrates that the increasing stress levels consecutively trigger plasticity in colonies that are less favorable oriented for plastic deformation. The stress relief by this successive onset of plastic deformation in different colonies causes the gradual decrease of the slope of the macroscopic stress-strain response over the first $\approx 1.5\%$ plastic strain (cf. [39]). After this $\approx 1.5\%$ plastic strain, the slope of the macroscopic stress-strain response (i.e. the macroscopic hardening rate) is relatively constant, indicating that all colonies have started to deform plastically.

Influence of microstructural parameters

As discussed in Chapter 5, the coexisting microstructural interfaces in fully lamellar TiAl have a strong influence on the relative strength of deformation systems. Consequently, changes in microstructural parameters unquestionably will have an influence on the micro yield behavior which is dominated by the relative strength of soft (longitudinal) and hard mode (mixed and transversal) deformation systems.

Thus, the changes in micro yield behavior for systematically altered microstructural parameters as it shown by the simulation results in Figure 6.2 are best understood by combining the Hall-Petch arguments from Chapter 5 with the simulated relative activities obtained for the exemplary reference microstructure (see Figure 6.1(a) and (b)).

Influence of the γ domain size The γ domain size λ_D determines the strength of the longitudinal deformation systems and thus of the weakly oriented colonies in polycolony microstructures. Consequently, a reduced domain size leads to an increase of the initial yield stress as compared with the reference microstructure (see the blue line in Figure 6.2). The characteristics of the transient onset of yield seems, however, not to be influenced by the domain size as the stress-strain curve of the simulations with altered λ_D are approximately parallel to the stress-strain response of the reference microstructure.

Influence of colony size As discussed in Chapter 5, the colony size λ_C equally affects the strength of all deformation systems. Thus, decreasing λ_C equally strengthens longitudinal deformation systems (and consequently the weakly oriented colonies) and mixed/transversal deformation systems (and consequently the colonies that are less favorably oriented for plastic deformation). Compared to the reference microstructure, the increased strength of weakly oriented colonies leads to a higher initial yield stress (see the green line in Figure 6.2). The increased strength of the colonies that are less favorably oriented for plastic deformation results in a slightly higher initial slope of the macroscopic stress-strain response as higher stress levels are required to trigger plasticity in these colonies (cf. Figure 6.2). After 1.5% plastic strain, i.e. in the strain regime in which presumably all colonies have started to deform plastically, the macroscopic hardening rate of the simulation with altered colony size matches again the hardening rate obtained for the reference microstructure.

Influence of lamella thickness The spacing of the lamella interfaces directly determines the strength of mixed and transversal deformation systems but also has a secondary influence on the strength of all deformation systems since the colony boundary strengthening coefficient k_C depends on the lamella thickness λ_L as discussed in Section 5.4. Consequently, reducing λ_L results in a slight increase of the initial yield stress through the strengthening of longitudinal deformation systems and thus weakly oriented colonies (see the red line in Figure 6.2). The strengthening of the mixed and transversal deformation systems leads to a strong increase of the initial slope of the macroscopic stress strain curve as compared with the reference microstructure. Further, the constant hardening rate, i.e. the hardening rate that indicates that all colonies have started to deform plastically, is reached at higher stress levels and for a slightly higher macroscopic plastic strain. Therefore, decreasing the lamella thickness prolongs the transient onset of yield.

Strain localization

As mentioned earlier, the micro yield of fully lamellar TiAl is accompanied by a strong localization of the plastic strains in weakly oriented colonies. This strain localization has

been observed by DIC analysis [131–133] and in previously reported numerical simulations [57, 58, 71, 80].

Since the RVE of a polycolony microstructure that was used for the current simulations (see Figure 3.6) only models a reduced number of lamellae per colony, the obtained micro strain field can obviously only be a rough estimate of the micro strain field in a real microstructure. However, the effect of the kinematic constraints between the colonies on the microplasticity can still be assessed at least qualitatively from contour plots of the total plastic shear $\overline{\gamma}$ (see Figure 6.1 (c), (d) and (e)). The respective contour plot at 7.5% plastic strain (Figure 6.1 (e)) is shown again in Figure 6.3 together with the orientations of colonies on the undeformed RVE.

(a)   **(b)**
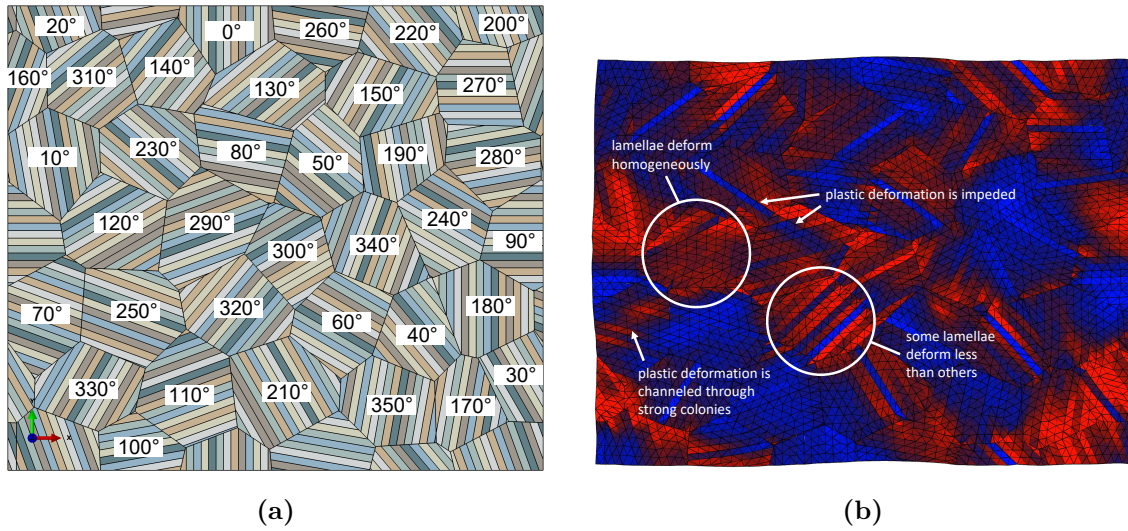
Figure 6.3. (a): orientation angles of the colonies in the used RVE with respect to the loading direction, i.e. the y axis; (b): contour plot of total plastic shear $\overline{\gamma}$ for a macroscopic plastic strain of 7.5%. Red areas correspond to $\overline{\gamma} > 0.4$; blue areas indicate $\overline{\gamma} < 0.05$.

From this contour plot, the following characteristics of the inhomogeneous microplasticity can be identified:

- Due to the kinematic constraints in the microstructure, the weakly oriented colonies are not simply identified by the angle between their lamella plane and the macroscopic loading direction alone.

- The total plastic shear $\overline{\gamma}$ in weakly oriented colonies is several times higher than in colonies that are less favorably oriented for plastic deformation.

- Some colonies show a homogeneous plastic deformation, i.e. all lamellae deform plastically.

- Some colonies contain α_2 lamellae that are nearly undeformed although the other lamellae deform plastically.

- α_2 lamellae that do not deform plastically may locally impede plastic deformation in neighboring colonies.

- The plastic deformation may be channeled through regions with only strong colonies.

Combining such simulations with experimental investigations, would potentially allow to relate the sites at which (pre-yield) cracks typically occur to specifics in the micro strain field.

6.2 Summary

In the present Chapter, the micro yield behavior of polycolony microstructures was investigated using the work hardening formulations and the microstructure sensitive model extension introduced in the previous chapters. This allowed to analyze the influence of the microstructural parameters (λ_L, λ_D and λ_C) on the specifics of micro yield. The results of this numerical study correspond well to findings of previous numerical studies [57, 58, 71, 80] but in contrast allowed to specifically attribute the observed phenomena to the microstructural length scale. Furthermore, the localization of plastic strains in weakly oriented colonies of polycolony microstructures was investigated and some characteristics of the micro strain field that result from the kinematic constraints in the microstructure were identified.

7 Static recovery

7.1 Introduction

Work hardening obviously has a significant effect on basically all technical applications and processes that involve plastic deformation. Since it is well-known that work hardening can be recovered by annealing at elevated temperatures, it is, however, possible to control its – in most cases detrimental – effect on respective applications and processes by systematic heat treatment. In forming processes such heat treatments are, e.g., commonly used to limit the forming forces and correspondingly the tool wear. Processes like, e.g., shot peening on the other hand aim to benefit from systematically introduced work hardening (and compressive residual stresses) in the surface layer of a component, see e.g. [151]. The surface hardening that is introduced by shot peening significantly increases the component's mechanical performance in terms of, .e.g, fatigue life as investigated for lamellar γ TiAl in [21]. For shot peened γ TiAl components under service conditions (i.e. at elevated temperature), potential recovery of the introduced surface hardening is, thus, disadvantageous since it counteracts the intended improvement of the mechanical performance. Being able to predict the static recovery behavior would consequently help to optimize the load/annealing path in forming applications and would further allow to assess the potential of improving the mechanical performance of TiAl components by systematic work hardening.

Thus, in the following the recovery part of the crystal plasticity model from Section 3.2 (i.e. Equation (3.20)) will be calibrated against experiments and subsequently be applied to investigate basic trends in the static recovery behavior of polysynthetically twinned crystals/single colonies and polycolony microstructures.

7.2 Parameter identification

To date, the recovery behavior of γ TiAl alloys was investigated in only few studies [21, 39, 83, 129, 152, 153]. Therefore, the available data to calibrate the recovery part of the crystal plasticity model from Section 3.2 (i.e. Equation (3.20)) are scarce. In order to model the recovery behavior of slip systems α by Equation (3.20), the reference recovery rate $R_{\alpha,0}$, the activation energy for static recovery Q_R, the minimum dislocation density for recovery $\rho_{\alpha,\min}^{\mathrm{dis}}$, the reference dislocation density $\rho_{\mathrm{ref}}^{\mathrm{dis}}$ and the exponent q_α have to be identified.

The activation energy for static recovery Q_R has been found to correlate reasonably well with the activation energy for self diffusion Q_{SD} in γ TiAl [39] . Together with the Boltzmann constant k_B, the temperature dependent part of Equation (3.20), i.e. $\exp\left(-\frac{Q_R}{k_B \theta}\right)$, is thus known. The reference dislocation density $\rho_{\mathrm{ref}}^{\mathrm{dis}}$ serves for normalization purposes only and is thus set to $1\,\mathrm{mm}^{-2}$. For the sake of simplicity, $\rho_{\alpha,\min}^{\mathrm{dis}}$ is set to zero for all slip systems. As proposed in previous modeling approaches for recovery [56, 111], the exponents q_α are set to 2, i.e. the recovery rates of all slip systems α are assumed to increase with $\left(\rho_\alpha^{\mathrm{dis}}\right)^2$. With this, only the reference recovery rates $R_{\alpha,0}$ remain to be identified.

Due to their different initial strength and hardening behavior, it is likely that the evolving dislocation densities vary significantly between slip systems of different morphological classification. Since a higher dislocation density results in a higher recovery rate for a given

temperature, the effective recovery rate presumably also differs between systems of different morphological classification. However, there is no reason to assume that the functional relation between the current dislocation density and the recovery rate, i.e. the actual recovery behavior, is significantly different for systems of different morphological classification. Therefore, it is assumed in the following that the recovery on all slip systems α in the γ and the α_2 phase can be described by the same $R_{\alpha,0}$ irrespective of their mechanistic (super or ordinary slip) and their morphological classification.

7.2.1 Calibration

In order to obtain a data base for the model calibration, static recovery experiments with polysynthetically twinned crystals were carried out by Jonathan D.H. Paul (department of Materials Physics at the Helmholtz-Zentrum Geesthacht). Polysynthetically twinned crystals with the three characteristic lamella orientations of 0°, 45° and 90° were deformed at room temperature with a compressive strain rate of $2.38 \times 10^{-5} \mathrm{s}^{-1}$ to a plastic strain of 5%. The deformed specimens were then annealed at 650°C for either 4 or 8 hours. After annealing, the specimens were retested at room temperature to an additional 1% plastic strain in order to determine how much of the introduced work hardening has been recovered. Further details on the experimental set up can be found in [3]. The microstructural parameters of the tested polysynthetically twinned crystals are summarized in Table 7.1.

Table 7.1. Microstructural parameters of the tested polysynthetically twinned crystals. The 0° and 45° specimens were prepared from a different parent crystal than the 90° specimens. *: α_2 volume fraction used in the simulations. The microstructural parameters were kindly provided by Michael Oehring (department of Materials Physics at the Helmholtz-Zentrum Geesthacht)

	composition	γ		α_2	α_2 content [Vol.-%]	
	EDX	λ_L^γ [μm]	λ_D [μm]	$\lambda_L^{\alpha_2}$ [μm]	image analysis	XRD*
0°/45°	Ti-49 at.% Al	2.3±0.4	26.8	0.66±0.12	6.6±2.40	4.6
90°	Ti-48.5 at.% Al	1.7±0.3	29.4	0.37±0.19	2.6±0.38	1.5

The calibration simulations were carried out again using the RVE of a polysynthetically twinned crystal presented in Section 3.5.1. The RVE was subjected to the rotational boundary conditions from Section 3.6.2. The work hardening behavior and the microstructure sensitive initial critical resolved shear stresses were modeled as described in Chapters 4 and 5 with the respective constitutive assumptions and model parameters. As described in Chapter 5, the lattice resistance τ_R is the only remaining model parameter that can not be identified uniquely as it, a.o., depends on composition and impurities of the tested specimens. In the current simulations the lattice resistance in the γ phase had to be set to $\tau_R = 55\,\mathrm{MPa}$ for the 0° and 45° tests and to $\tau_R = 65\,\mathrm{MPa}$ for the 90° tests respectively in order to match the experimentally determined yield stresses.

Figure 7.1 shows the results of the static recovery experiments compared to the simulations that were obtained for the microstructural parameters from Table 7.1 and the chosen lattice resistance τ_R.

For a better assessment of the results, Figures 7.2(a) and (b) show the simulated and experimentally determined yield stresses and the stresses that were reached at the end of the predeformation, i.e. after 5% plastic strain. Figure 7.2(c) shows the comparison of the experimental and simulated yield stresses after annealing.

Overall, the simulated stress strain curves in Figure 7.1 correspond well to the experimental results for both the predeformation and the retest after annealing. The yield stress as well as the post yield behavior are reproduced well within the experimental error for 0° and 45°
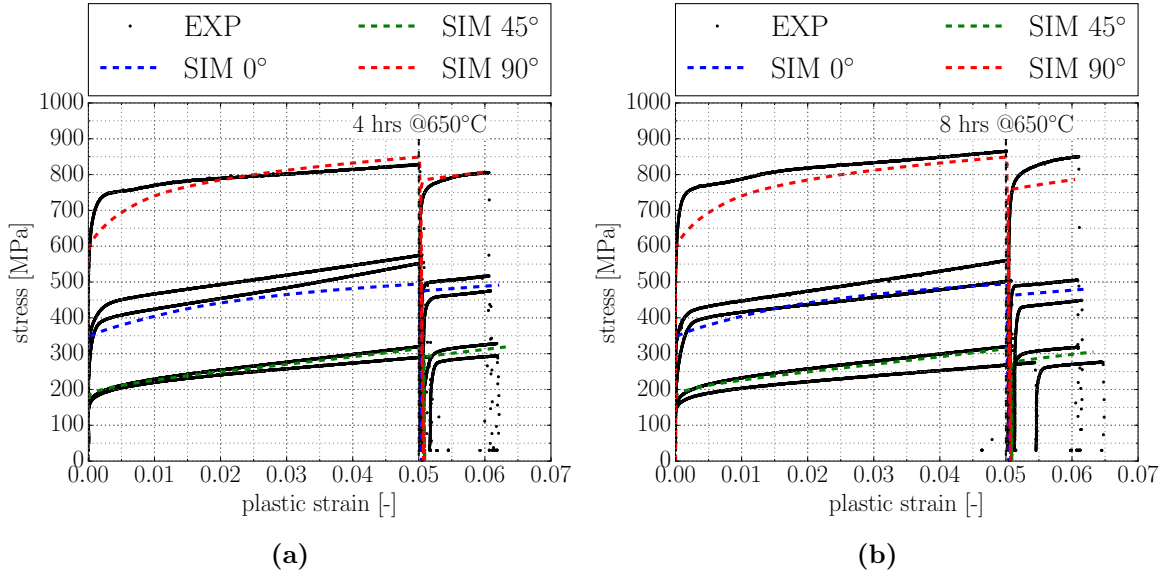
Figure 7.1. Comparison of the experimental results for room temperature compression of polysynthetically twinned crystals under loading angles of 0°, 45° and 90° to the results obtained by the calibrated simulations. The specimens were compressed to a plastic strain of 5% and subsequently annealed at 650°C for (a) 4 hours and (b) 8 hours. The annealed specimens were retested at room temperature to an additional 1% plastic strain. The microstructural parameters of the tested specimens are summarized in Table 7.1. The experimental data were kindly provided by Jonathan D.H. Paul (Department of Materials Physics at the Helmholtz-Zentrum Geesthacht).

orientations (see Figures 7.1 and 7.2(a)). For a loading angle of 90°, the initial hardening rate and thus the yield stress are, however, underestimated by the model. The stress after 5% plastic strain is again met well for all investigated orientations (see Figure 7.2(b)).

7.2.2 Model parameters

The parameters of the recovery model that were applied to obtain the simulation results presented in Figures 7.1 and 7.2 are summarized in Table 7.2.

Table 7.2. Parameters of the recovery model. The same parameters were applied for all slip systems α in the γ as well as in the α_2 phase.

| phase	parameter	value	unit	ref.
γ/α_2	k_B	8.617×10^{-5}	$\left[\frac{\text{eV}}{\text{K}}\right]$	
	Q_R	3.0	$[\text{eV}]$	[39]
	$R_{\alpha,0}$	0.5×10^5	$\left[\frac{1}{\text{mm}^2\text{s}}\right]$	this work
	$\rho_{\alpha,\min}^{\text{dis}}$	0	$\left[\frac{1}{\text{mm}^2}\right]$	this work
	$\rho_{\text{ref}}^{\text{dis}}$	1	$\left[\frac{1}{\text{mm}^2}\right]$	this work
	q_α	2	$[-]$	this work
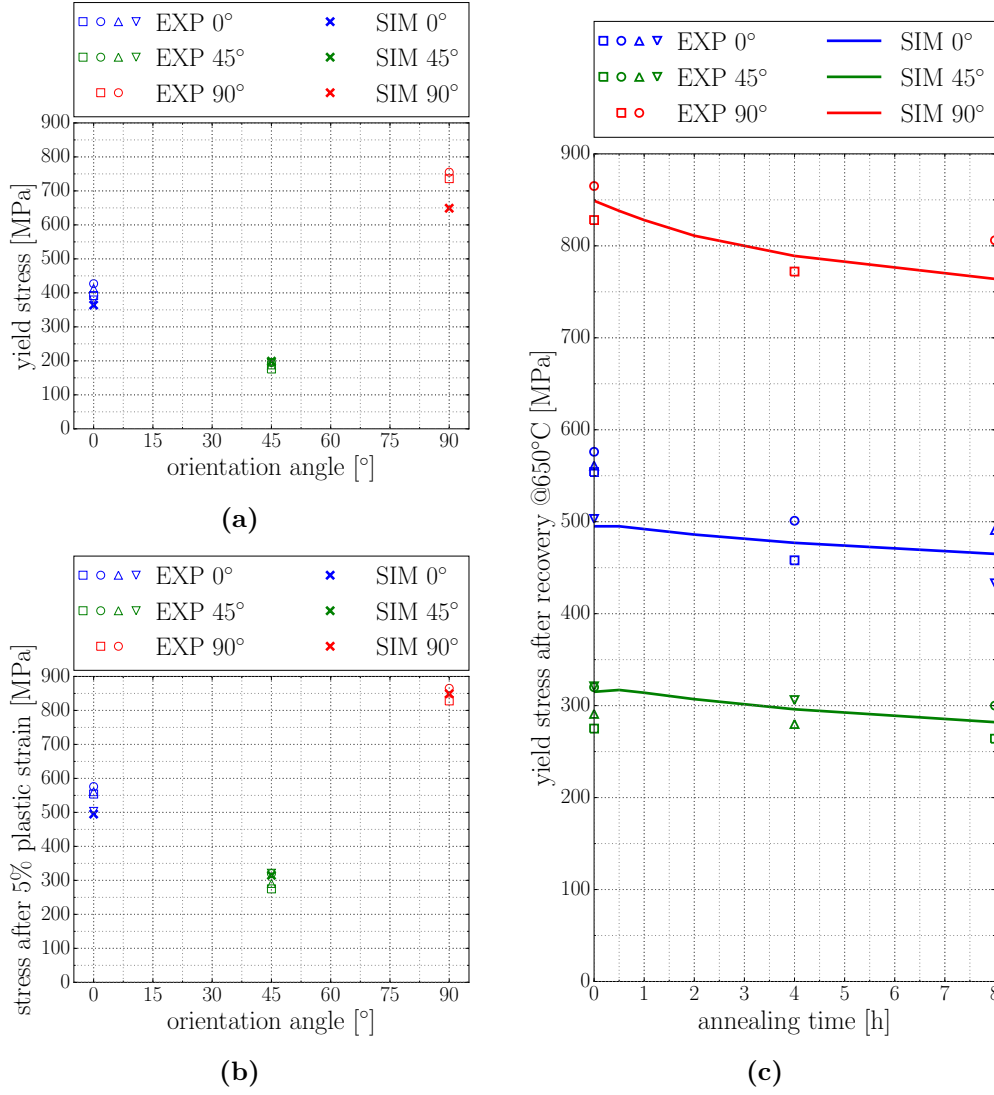
Figure 7.2. Experimental and simulated results of static recovery experiments with polysynthetically twinned crystals under loading angles of 0°, 45° and 90°. (a): yield stresses; (b): stresses at the end of predeformation to 5% plastic strain; (c): yield stress over recovery time for annealing at 650°C. The microstructural parameters of the tested polysynthetically twinned crystals can be found in Table 7.1. The experimental data were kindly provided by Jonathan D.H. Paul (Department of Materials Physics at the Helmholtz-Zentrum Geesthacht).

7.3 Recovery in polysynthetically twinned crystals/single colonies

With the calibrated recovery model it is now possible to investigate basic trends in the static recovery behavior of polysynthetically twinned crystals. Due to the defect density based formulation of the work hardening/recovery model, the simulation results allow to evaluate the evolution of the dislocation density with deformation and annealing time. In Figure 7.3, the simulated evolution of the dislocation density in differently oriented polysynthetically twinned crystals is shown for a predeformation to 5% plastic strain followed by annealing at 650°C for different times and a subsequent room temperature re-test to an additional 1% plastic strain.

Further, the model allows to investigate the recovery behavior for different annealing tem-
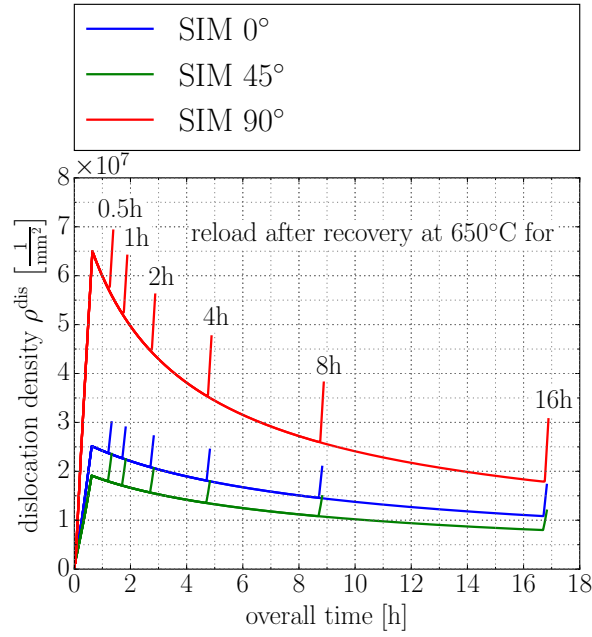
Figure 7.3. Evolution of dislocation density with deformation and annealing time in polysynthetically twinned crystals under loading angles of 0°, 45° and 90° as it was predicted by the model. The simulations were carried out with the microstructural parameters from Table 7.1 and the model parameters from Table 7.2. The test sequence was: room temperature predeformation to 5% plastic strain followed by annealing at 650°C and room temperature retest to an additional 1% plastic strain.

peratures. Figure 7.4 shows the yield stress of differently oriented polysynthetically twinned crystals over annealing time as it was predicted by the model for different annealing temperatures up to 900°C. The simulations were carried out again using the microstructural parameters from Table 7.1.

7.3.1 Discussion

As shown in Figure 7.2(c), the simulated yield stress after recovery agrees well with the experimental results for all three tested lamella orientations. The results in Figure 7.2(c) further show that the effective recovery rate, i.e. the rate at which the yield stress decreases with annealing time, is highest for a lamella orientation of 90° and lowest for 45°. Since the effective recovery rate is a function of the current dislocation density in the material, this indicates that specimens of the different tested lamella orientations exhibited different dislocation densities at the beginning of the heat treatment, i.e. after the predeformation to 5% plastic strain. The model predicts the dislocation density to be in the order of $10^7 \frac{1}{\text{mm}^2}$ for all investigated lamella orientations (see Figure 7.3) which matches the findings in [142]. As illustrated in Figure 7.3, the estimated total dislocation density after predeformation (i.e. at the peak of the depicted curves) is in fact different for different loading angles, i.e. the estimated dislocation density for the 90° orientation is ≈3 times higher than the estimated dislocation density for 45°. This corresponds well to the observed differences in the effective recovery rates depicted in Figure 7.2(c).

Although the effective recovery rate differs with lamella orientation (i.e. is anisotropic), it was successfully modeled by assigning the same recovery model parameters (see Table 7.2) to the recovery Equation (3.20) for all slip systems irrespective of their mechanism based or
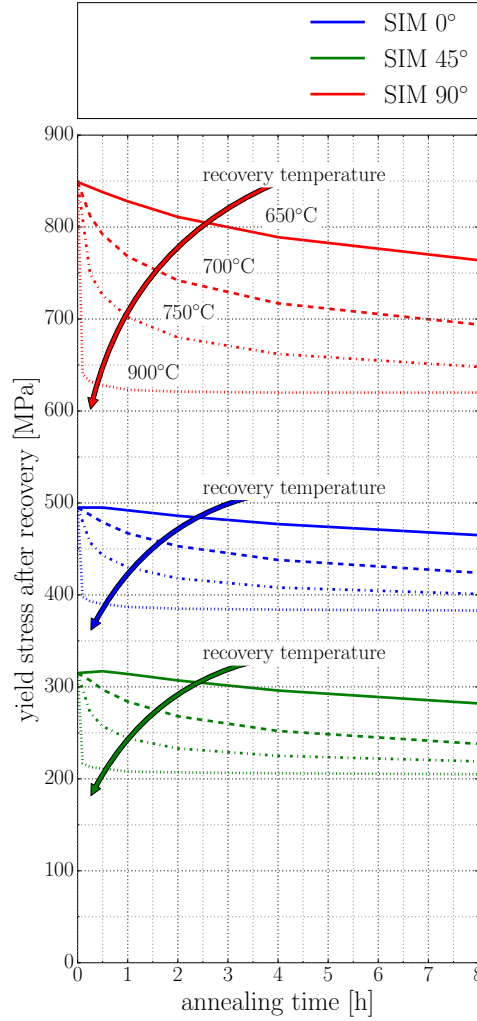
Figure 7.4. Simulated yield stress of differently oriented polysynthetically twinned crystals after recovery at different temperatures over annealing time. The simulations were carried out with the microstructural parameters from Table 7.1 and the model parameters from Table 7.2. The test sequence was: room temperature predeformation to 5% plastic strain followed by annealing and subsequent room temperature retest to determine the yield stress after recovery.

morphological classification. Thus, the prior assumption that the functional relation between the recovery rate and the current dislocation density does not differ between deformation systems appears to be justifiable.

The simulation results shown in Figure 7.4 illustrate nicely how the recovery of work hardening is accelerated with increasing annealing temperature. For typical service temperatures of γ TiAl alloys of 700°C to 750°C, most of the introduced work hardening is predicted to be recovered after a few hours already. This matches the qualitative observations that were reported in [21].

7.4 Recovery in polycolony microstructures

The recovery of work hardening in polycolony microstructures can generally be investigated by the experimental procedures shown in [39, 129, 152]. While respective experiments allow

to investigate how the (macroscopic) work hardening is recovered for different annealing temperatures and times, they do not allow statements on how the dislocation density evolves at the meso scale. Due to the strongly inhomogeneous microplasticity in polycolony microstructures (cf. Chapter 6), it is likely that the recovery behavior on the meso scale is also highly inhomogeneous. While an in situ experimental investigation of the recovery behavior on the meso scale is impeded by the destructive nature of the necessary imaging techniques, it can be studied by the presented crystal plasticity model as it will be shown in the following.

The static recovery simulation that will be shown in the following starts from the simulated deformation state that was obtained from room temperature compression of the exemplary polycolony microstructure investigated earlier (α_2 volume fraction 10%, λ_C=250μm, λ_D=25μm, λ_L=0.5μm, τ_R=30 MPa) to 10% plastic strain. Based on this deformation state, annealing was simulated for 8 hours at 700°C. Then, the RVE is compressed to an additional 1% plastic strain at room temperature. The results of this simulation are depicted in Figure 7.5 in terms of the evolving total dislocation density and the accumulated plastic shear. Further, contour plots are shown in Figure 7.5 that illustrate the inhomogeneous distribution of the accumulated plastic shear and the dislocation density within the polycolony microstructure for different stages of the numerical experiment.

In order to illustrate trends in the recovery of work hardening with annealing temperature and annealing time, additional recovery simulations were carried out for temperatures up to 900°C, see Figure 7.6.

7.4.1 Discussion

Figure 7.5 nicely illustrates how both the accumulated plastic shear and the dislocation density increase during predeformation. As expected, the accumulated plastic shear remains constant during annealing while the dislocation density decreases (see Figure7.5(a)). The contour plots of the accumulated plastic shear (see Figure 7.5(b)-(f)) again show the inhomogeneous microplasticity, i.e. the localization of plastic shear, investigated in Chapter 6. The contour plots in Figures 7.5(g)-(k), show the corresponding inhomogeneous distribution of the dislocation density in the microstructure. As the recovery rate is directly related to the dislocation density, it is to be expected that the recovery behavior also strongly differs locally. Thus, it is generally possible that after annealing other regions of the microstructure are the weakest and the plasticity localizes in a different pattern than in the predeformation. However, the contour plots of the dislocation density at the end of the re-test (i.e. Figures 7.5(f) and (k)) suggest that the microplasticity localizes in the same regions of the microstructure as during predeformation (i.e. Figures 7.5(b) and (g)).

As in the case of polysynthetically twinned crystals, the simulations predict that most of the work hardening in polycolony colony microstructures is recovered after several hours at typical operating temperatures of TiAl components, see Figure 7.6.

7.5 Summary

In this chapter, the recovery behavior of polysynthetically twinned crystals/single colonies and polycolony microstructures was investigated. Based on static recovery experiments with polysynthetically twinned crystals, the recovery part of the crystal plasticity model was calibrated. In this, it has been shown that the anisotropic effective recovery rate of polysynthetically twinned crystals can be reproduced reasonably well by assigning the same model parameters to all slip systems in both phases irrespective of their mechanism based or morphological classification.

(a)

(b)   **(c)**   **(d)**   **(e)**   **(f)**

(g)   **(h)**   **(i)**   **(j)**   **(k)**
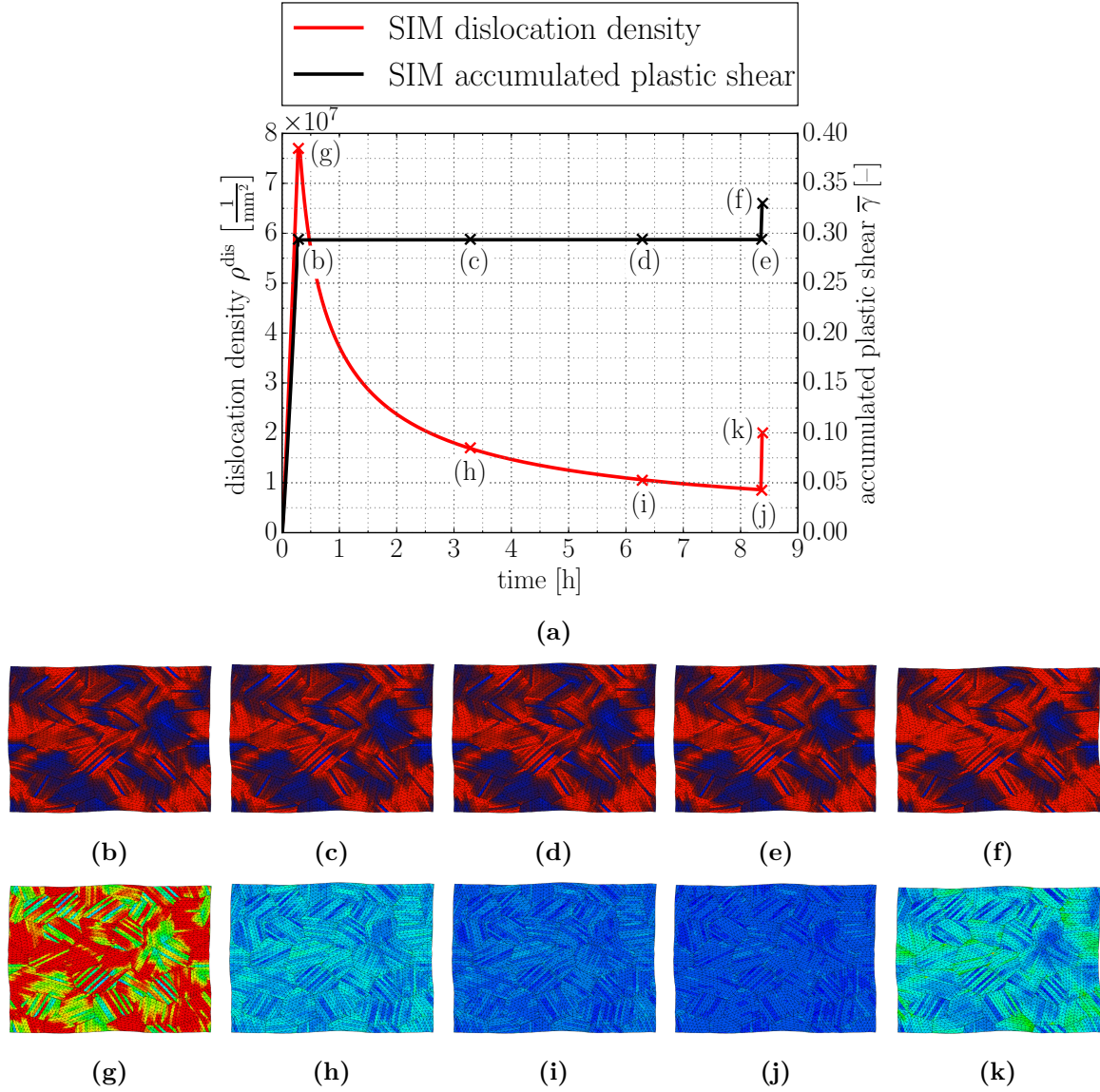
Figure 7.5. Simulated evolution of the total dislocation density and the accumulated plastic shear in an exemplary polycolony microstructure (α_2 volume fraction 10%, λ_C=250 µm, λ_D=25 µm, λ_L=0.5 µm, τ_R=30 MPa). The polycolony RVE was compressed at room temperature to a plastic strain of 10%. Annealing was simulated at 700°C for 8 hours. The room temperature retest was done to an additional 1% plastic strain. (a): Evolution of the volume averaged total dislocation density and the volume averaged accumulated plastic shear in the polycolony RVE over time. (b)-(f): accumulated plastic shear (red: $\overline{\gamma} > 0.4$, blue: $\overline{\gamma} < 0.05$). (g)-(k): total dislocation density (red: $\rho^{\mathrm{dis}} > 8 \times 10^7 \frac{1}{\mathrm{mm}^2}$, blue: $\rho^{\mathrm{dis}} < 1 \times 10^6 \frac{1}{\mathrm{mm}^2}$)
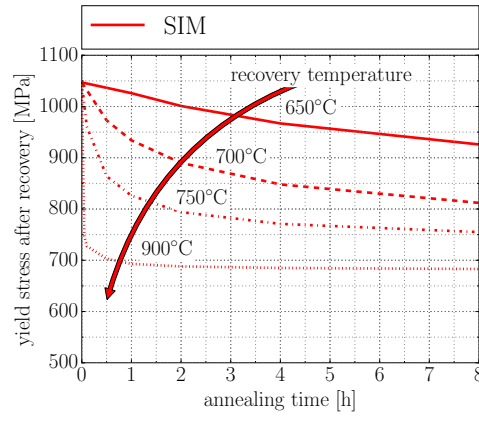
Numerical studies with the calibrated model allowed to investigate basic trends in the static recovery behavior of polysynthetically twinned crystals/single colonies and polycolony microstructures. These simulations predicted that at typical operating temperatures for TiAl alloys most of the work hardening is recovered within a few hours.

Figure 7.6. Simulated yield stress of an exemplary polycolony microstructure (α_2 volume fraction 10%, λ_C=250 µm, λ_D=25 µm, λ_L=0.5 µm, τ_R=30 MPa) for different annealing temperatures and times after room temperature predeformation to a plastic strain of 10%.
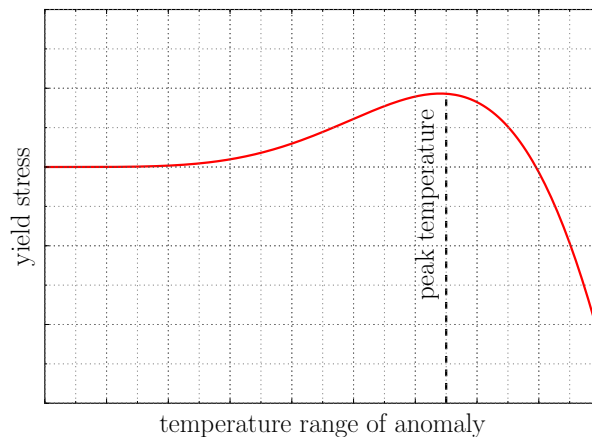
8 Temperature sensitive yield strength

As TiAl alloys are generally deployed at elevated temperatures, a comprehensive constitutive model should be able to predict their mechanical behavior not only at room temperature but also at the temperatures TiAl components typically encounter in service. As mentioned in Section 3.1.1, except for a single other study [81] all proposed crystal plasticity models for lamellar TiAl alloys did so far not take into account the temperature dependence of the material's behavior and are hence only valid near a certain temperature, i.e. the temperature for which the models were calibrated. As a first step to overcome this limitation to isothermal conditions, the presented crystal plasticity model is extended in the following in order to account for the temperature dependence of the yield strength of fully lamellar TiAl between room temperature and 900°C.

8.1 Yield stress anomaly

It has been observed experimentally, that the yield strength of most intermetallic alloys exhibits an anomalous dependence on temperature [154]. While the yield strength of conventional metallic materials usually decreases monotonically with increasing temperature, the yield strength of intermetallic alloys has frequently been found to exhibit a temperature range in which the yield strength anomalously increases with increasing temperature up to a certain peak strength. For temperatures above the corresponding peak temperature the yield strength is decreasing again. This behavior is qualitatively depicted in Figure 8.1 for the temperature range in which the anomaly occurs.

Figure 8.1. Qualitative illustration of the yield stress anomaly that has frequently been observed in intermetallic alloys. In the indicated temperature range, the yield strength is anomalously increasing with increasing temperature. This trend continues up to a certain peak strength. Above the corresponding peak temperature, the yield strength decreases again.

The specific appearance of the anomaly (e.g. the peak strength and/or peak temperature) depends on the intermetallic system at hand and is usually a function of the crystal orien-

tation [154]. In some intermetallics, the anomaly is, e.g., attributed to specific deformation systems only (e.g. pyramidal slip systems in Ti_3Al, i.e. the α_2 phase [27, 36]) so that crystal orientations exist in which no anomalous peak occurs.

8.1.1 Yield stress anomaly in single phases

It has been found that single crystals of both the γ and the α_2 phase exhibit a yield stress anomaly [27, 33, 34, 36, 155]. However, the specific appearance of the anomaly differs significantly between both phases.

γ single crystals

In experiments with Al-rich γ single crystals a distinct yield stress anomaly occurred in all tested crystal orientations [11, 33, 34, 155]. Thus, the anomaly can not be attributed to a specific deformation system [11]. Depending on the crystal orientation and composition, the anomalous peak was observed at temperatures between 700°C and 1000°C. An extensive discussion of the different mechanisms that were proposed to cause the yield stress anomaly in γ single crystals can, e.g., be found in [11, 154].

α_2 single crystals

In α_2 single crystals, an anomalous increase of the yield strength was only observed for crystal orientations which favor the activation of pyramidal slip systems [27, 36]. The anomalous peak that was observed for the respective crystal orientations was located around 500°C to 600°C [11, 27, 36] (see Figure 8.2(b)). For all other tested crystal orientations, the yield strength – and thus the strength of the activated basal and prismatic slip systems – decreases monotonically with increasing temperature [11, 27, 36] (see Figure 8.2(a)). According to [11], the mechanisms that cause the observed yield stress anomaly of the pyramidal slip systems in the α_2 phase are, however, not yet fully understood.

8.1.2 Yield stress anomaly in lamellar two phase alloys

The temperature dependence of the yield strength of fully lamellar TiAl alloys interestingly deviates from the behavior that was observed for γ and α_2 single crystals. While this can partly be explained by compositional effects[16], there is evidence that the fully lamellar microstructure, i.e. the dense arrangement of crystallographic interfaces, has a severe influence on the temperature dependence of the yield strength.

Polysynthetically twinned crystals

The temperature dependence of the yield strength of polysynthetically twinned crystals was experimentally investigated for different loading angles φ in [37, 46]. In [46], different sets of microstructural parameters (i.e. lamella thicknesses λ_L and domain sizes λ_D) were tested in order to investigate the potential influence of the microstructural interfaces on the temperature dependent yield strength.

In both studies, polysynthetically twinned crystals in weak orientations (30° in [37] and 45° in [46]) showed no distinct yield stress anomaly. Instead, the yield strength has been observed to remain relatively constant over the temperature range investigated and – if at all – only

---

[16]Some of the mechanisms that were discussed to cause the yield stress anomaly in Al-rich γ single crystals like, e.g., the presence of Al_5Ti_3 precipitates [155] are particularly linked to their high aluminum content and are thus not present in near-stoichiometric two phase alloys [11].

showed a very small anomalous peak at around 700°C to 800°C (see Figures 8.3 and 8.6). As discussed in Section 4.3, polysynthetically twinned crystals in weak orientation exclusively deform by shear parallel to the lamellae, i.e. by longitudinal deformation systems. Since the longitudinal (basal) slip systems in the α_2 phase are much stronger than the longitudinal systems in the γ phase, the plastic deformation is mainly accomplished by the γ lamellae for this lamella orientation [35, 37, 47]. Thus, it was concluded in [37, 46] that the γ phase in polysynthetically twinned crystals unlike γ single crystals does not exhibit a distinct yield stress anomaly.

However, for loading angles of 0° and 90°, i.e. in the hard orientations, a yield stress anomaly was still observed [37, 46]. As discussed in Section 4.3, in hard orientations the plastic deformation has to act across the lamella boundaries. Since the γ phase apparently does not exhibit a yield stress anomaly in near-stoichiometric two phase alloys (see line of arguments above), the observed peak in yield strength has thus been assumed in [37, 46] to be related to the deformation mechanisms of the α_2 phase or directly to the existence of the lamella interfaces.

For loading perpendicular to the lamella boundaries, i.e. a loading angle of 90°, the reported studies [37, 46] – at least at first glance – yield contradictory results. While in [46] a distinct yield stress anomaly has been observed for all tested combinations of microstructural parameters and α_2 volume fractions, the results from [37] show a plateau rather than an anomalous increase of the yield strength. The anomalous peak as well as the plateau are located around 500°C to 600°C (see Figures 8.3 and 8.6).

For loading perpendicular to the lamella boundaries, the α_2 lamellae can only deform by the very strong pyramidal (transversal) slip systems (loading parallel to the c axis). As the anomalous peak that has been observed in α_2 single crystals for orientations that favor deformation by pyramidal slip is also located around 500°C [27, 36] (see Figure 8.2(b)), it has been proposed in [46] that the yield stress anomaly of the pyramidal slip systems may cause the observed peak in the yield strength of polysynthetically twinned crystals under a loading angle of 90°. This idea is in line with the arguments from Section 5.4 as with an increase of the strength of the pyramidal slip systems the Hall-Petch strengthening effect of the γ/α_2 lamella interfaces increases as well. Assuming that the temperature dependent strengthening effect of the γ/α_2 lamella interfaces causes the observed yield stress anomaly, the peak should be more pronounced if their spacing λ_{α_2} is reduced. In fact, the peak was found to be more pronounced in specimens with higher α_2 volume fraction and thus – assuming that the α_2 lamella thickness is not altered – a reduced distance of the γ/α_2 lamella interfaces [46]. The α_2 volume fraction is inversely related to the Al content of the alloy, that is, decreasing the Al content leads to an increase in α_2 volume fraction (see Figure 1.2). However, the lamella thickness is also changing when altering the Al content, i.e. a reduction in the Al content leads to a reduced lamella thickness [51]. Thus, the anomaly is also apparent when plotting the the yield strengths of 90° specimens at different temperatures against the inverse square root of the lamella thickness, i.e. in a Hall-Petch plot[17] [46] (see Figure 8.4(b)). In this representation of the results (yield strength against inverse square root of lamella thickness), the anomaly manifests in terms of a temperature dependence of the Hall-Petch slope [46]. Beginning from the room temperature value (see Section 5.3), the Hall-Petch slope increases to a peak at $\approx$ 500°C and then reduces to a very low value at 900°C [46]. Thus, the anomalous peak appeared to be less pronounced for higher lamella thicknesses in [46]. This observation might rationalize the discrepancies between the experimental results from [46] and [37]. As the lamella thickness in the experimental results from [37] was $\approx$ 2µm, i.e. twice the biggest lamella thickness that

---

[17]In [46] the lamella thickness is given without differentiating γ and α_2 lamellae. Due to the high γ volume fraction, the average thickness of the γ lamellae should, however, be close to the reported lamella thickness.

was investigated in [46] (cf. Table 5.2), the absence of a distinct anomalous peak in the result from [37] seems reasonable.

While the observed yield stress anomaly of polysynthetically twinned crystals under a loading angle of 90° can – at least – potentially be explained by the temperature dependence of the pyramidal slip systems in the α_2 lamellae, no explanation is at hand for the anomaly that has been observed for loading parallel to the lamella boundaries (0°) [37, 46]. Under a loading angle of 0°, the anomalous peak in the yield strength occurred at temperatures that correspond to the peak temperature of γ single crystals, i.e. around 700°C to 800°C [37, 46] (see Figures 8.3 and 8.6). As discussed above, the γ phase in polysynthetically twinned crystals does not exhibit a yield stress anomaly and can thus not cause the observed anomalous peak. However, for loading parallel to the lamella boundaries the plastic deformation is not solely accomplished by the γ lamellae but also by prismatic (mixed) slip systems in the α_2 lamellae [37]. As it has been found in α_2 single crystal experiments [27, 36] that the prismatic slip systems do not exhibit a yield stress anomaly either, the observed peak can, however, not be attributed to the deformation of the α_2 lamellae. Therefore, it was concluded in [37, 46] that the observed yield stress anomaly in polysynthetically twinned crystals under a loading angle of 0° has to be directly related to the existence of the lamella interfaces. Thus, the anomalous peak should be more pronounced for smaller lamella thicknesses as observed for a loading angle of 90°. Unfortunately, in [37] respectively [46] the temperature dependent yield strength of polysynthetically twinned crystals under a loading angle of 0° have been reported for a single lamella thickness only.

Polycolony microstructures

In contrast to polysynthetically twinned crystals and γ respectively α_2 single crystals, polycolony microstructures do not show an anomalous peak of the yield strength [11, 18, 20, 82, 146]. Instead, the yield strength is essentially constant between room temperature and 700°C to 800°C. Above this temperature, the yield strength decreases rapidly. This behavior can potentially be explained by combining the yield stress - temperature profiles that have been observed for the three characteristic lamella orientations of polysynthetically twinned crystals (i.e. 0°, 45° and 90°) with the microyield behavior investigated in Chapter 6. As discussed in Chapter 6, up to the macroscopic yield point the plastic deformation is nearly exclusively accomplished by weakly oriented colonies. As polysynthetically twinned crystals in weak orientation have been found to exhibit no yield stress anomaly [37, 46], the predominant deformation by weakly oriented colonies can be expected to show no anomalous behavior either. However, as the anomalous peaks in the hard orientations of polysynthetically twinned crystals are located at different temperatures (500°C in 90° orientation and 700°C in 0° orientation, cf. Figures 8.3 and 8.6), limited deformation in strong colonies may macroscopically still yield a plateau in the yield stress below 800°C, a hypothesis which might be tested by numerical simulation.

8.2 Modeling

At the moment, there is no comprehensive theory at hand which explicitly allows to relate the yield stress anomaly of lamellar TiAl alloys to the different pinning mechanisms that were observed in the single phases [11]. In particular the observed influence of the microstructural interfaces on the temperature dependent yield strength of fully lamellar TiAl alloys seems not yet to be understood well. Given the current level of knowledge, the yield stress anomaly of fully lamellar TiAl can, thus, not be modeled in terms of, e.g., detailed dislocation pinning

mechanisms as it has been successfully done for single phase γTiAl alloys [156, 157] and Ni$_3$Al single crystals [158].

Despite the lacking knowledge on the details that cause the observed temperature dependence of the yield strength of fully lamellar TiAl alloys, it may still be modeled in a phenomenological way as it will be shown in the following. As discussed in Chapter 5 in terms of the Hall-Petch strengthening effect, the mechanisms that cause the yield stress anomaly impede the onset of dislocation motion and twin nucleation in the indicated temperature range which results in an increase of the yield strength. Thus, this effect is best included into the initial slip and twinning system strengths $\tau_{\alpha,0}^Y$ and $\tau_{\beta,0}^T$ (see Equations (3.22) and (3.23)). In the temperature range of interest, i.e. between room temperature and 900°C, the yield stress anomaly can be phenomenologically described by the following sinusoidal powerlaw

$$f(\theta) = f_0 + \sin(A\,\theta) \left[B\,\theta^C \right] \tag{8.1}$$

in which f_0 is a temperature independent term and A, B and C are constants.

8.2.1 Constitutive assumptions

Morphological classification

As throughout this entire thesis, the deformation systems are modeled grouped by their morphological classification, i.e. by assigning the same initial critical resolved shear stresses, the same work hardening and the same recovery behavior to all deformation systems of a morphological class.

Modeling the plastic deformation behavior of the α_2 phase

As in previous chapters, the deformation behavior of the α_2 phase is modeled according to the findings from single crystal experiments [27]. Due to the reasons discussed before, basal slip is not modeled explicitly.

Work hardening and recovery

The work hardening and recovery behavior is modeled using the relations, constitutive assumptions and model parameters that have been introduced in the respective chapters of this thesis (see Chapter 4 and 7).

8.2.2 Temperature dependent critical resolved shear stresses of the α_2 phase

The temperature dependence of the initial critical resolved shear stresses in the α_2 lamellae is modeled according to the single crystal experimental findings reported in [27]. This is done by making the lattice resistance $\tau_{\text{mix},R}^{\alpha_2}$ of the prismatic (mixed) slip systems and the lattice resistance $\tau_{\text{trans},R}^{\alpha_2}$ of the pyramidal (transversal) slip systems in Equations (5.11) and (5.12) a function of temperature. The colony boundary Hall-Petch strengthening term remains unaffected in the respective equations.

The monotonic decrease of the initial critical resolved shear stresses of the prismatic (mixed) slip systems with increasing temperature is captured by a polynomial fit, while the anomalous temperature dependence of the pyramidal (transversal) slip systems is fitted using Equation (8.1). This yields

$$\tau_{\text{mix},R}^{\alpha_2} = 67\,\text{MPa} - 0.059\,\theta\,\frac{\text{MPa}}{°\text{C}} - 27.83\,\theta^2\,\frac{\text{Pa}}{[°\text{C}]^2} + 0.0575\,\theta^3\,\frac{\text{Pa}}{[°\text{C}]^3} \tag{8.2}$$

and

$$\tau_{\text{trans},R}^{\alpha_2} = 450\,\text{MPa} + \sin\left(0.00453\,\theta\,\frac{1}{°\text{C}}\right)\left[0.1196\,\theta^{1.21}\,\frac{\text{MPa}}{[°\text{C}]^{1.21}}\right]. \tag{8.3}$$

The obtained fits for the temperature dependent lattice resistances $\tau_{\text{mix},R}^{\alpha_2}$ and $\tau_{\text{trans},R}^{\alpha_2}$ (i.e. Equations (8.2) and (8.3)) are plotted in Figure 8.2.
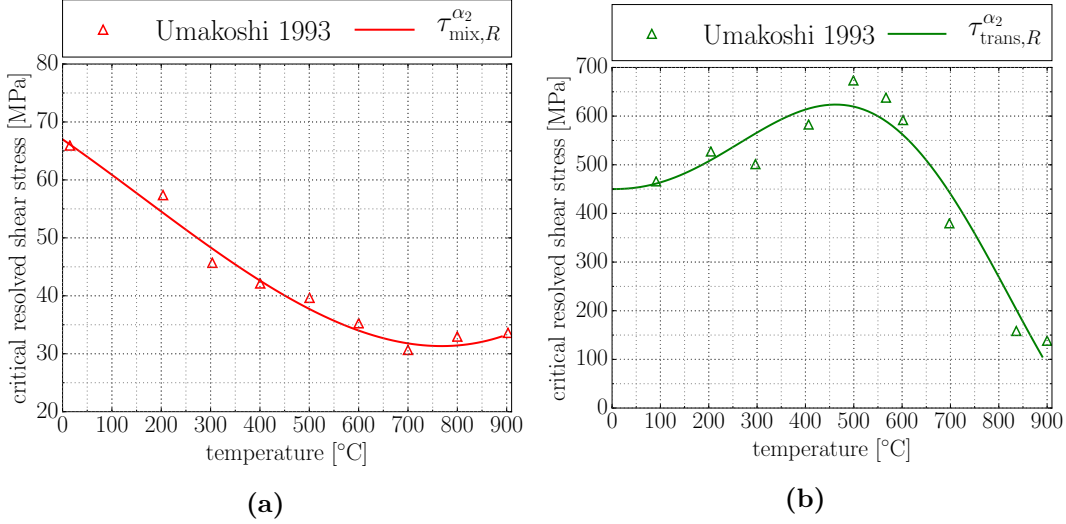
Figure 8.2. Temperature dependent lattice resistance of (a) prismatic (mixed) and (b) pyramidal (transversal) slip systems in α_2 single crystals as experimentally determined in [27] and fitted by Equations (8.2) and (8.3).

8.2.3 Temperature dependent critical resolved shear stresses of the γ phase

As discussed in Section 8.1.2, the experiments with differently oriented polysynthetically twinned crystals at different testing temperatures [37, 46] yielded two main results:

1. in orientations in which the plastic deformation is solely accomplished by longitudinal deformation systems in the γ lamellae, no distinct (or only a very small) anomalous peak occurred in the yield strength and

2. the anomalous peaks that have been observed in the hard orientations (0° and 90°) seem to be directly related to the lamella boundaries.

These findings have clear implications for modeling the temperature dependent initial critical resolved shear stress of the γ lamellae. As in the absence of microstructural interface (or more precisely in the presence of the widely spaced domain boundaries), the γ phase shows no distinct yield stress anomaly, the lattice resistance τ_R in Equations (5.16), (5.17) and (5.18) is assumed to be temperature independent. The assumed influence of the lamella (and potentially domain) boundaries on the yield stress anomaly is modeled by making the respective Hall-Petch strengthening coefficients in Equations (5.16), (5.17) and (5.18) a function of temperature with the general form proposed in Equation (8.1) thus reading

$$k_D(\theta) = k_{D,0} + \sin(A_D\,\theta)\left[B_D\,\theta^{C_D}\right] \tag{8.4}$$

$$k_L^{\mathrm{mix}}(\theta) = k_{L,0} + \sin(A_L^{\mathrm{mix}}\,\theta)\left[B_L^{\mathrm{mix}}\,\theta^{C_L^{\mathrm{mix}}}\right] \tag{8.5}$$

$$k_L^{\mathrm{trans}}(\theta) = k_{L,0} + \sin(A_L^{\mathrm{trans}}\,\theta)\left[B_L^{\mathrm{trans}}\,\theta^{C_L^{\mathrm{trans}}}\right]. \tag{8.6}$$

In this, the superscripts mix and trans indicate that the influence of the lamella boundaries on the temperature dependent initial critical resolved shear stress of the mixed and the transversal deformation systems is most likely not the same as the respective yield stress peaks have been found to occur at different temperatures for lamella orientations of 0° respectively 90°, i.e. for loading angles under which mixed respectively transversal deformation systems are predominantly activated (see Figure 8.3). The colony boundary strengthening coefficient k_C is assumed to be temperature independent.

8.3 Polysynthetically twinned crystals

Firstly, the temperature dependent model is applied to differently oriented polysynthetically twinned crystals before its transferability to polycolony microstructures is investigated.

8.3.1 Parameter identification

In the following, the above presented model for the yield stress temperature anomaly is calibrated against the experimental results reported in [46]. In [46], uniaxial compression tests with differently oriented polysynthetically twinned crystals were carried out for temperatures between 0°C and 900°C. As for the room temperature simulations in the Chapters 4 and 5.3, the lattice resistance to slip and twinning in the γ lamellae was set to $\tau_R = 20\,\mathrm{MPa}$. The temperature independent parts $k_{D,0}$ and $k_{L,0}$ of the Hall-Petch coefficients $k_D(\theta)$, $k_L^{\mathrm{mix}}(\theta)$ and $k_L^{\mathrm{trans}}(\theta)$ in Equations (8.4)-(8.6) were set to coincide with the room temperature Hall-Petch coefficients, identified in Section 5.3 (see Equation (5.21)).

With the identified parameters in Table 8.1, the model reproduces the experimentally determined temperature dependent yield stress well for loading angles of 0°, 45° and 90°, see Figure 8.3.

Further, the introduced temperature dependence of the Hall-Petch coefficients for lamella and domain boundaries allows to sufficiently reproduce the change in the Hall-Petch slope with temperature that has been experimentally observed in [46] for loading angles of 90° and 45°, see Figure 8.4.

Figure 8.5 shows the identified temperature dependent Hall-Petch coefficients, i.e. Equation (8.4) and (8.6) evaluated for the model parameters from Table 8.1.

From Figure 8.5 it can be seen that two different temperature characteristics were identified, one for the Hall-Petch coefficient of the transversal deformation systems with a peak at $\approx$ 500°C and one for the Hall-Petch coefficients of the deformation systems of the longitudinal and mixed morphological class with a peak at $\approx$ 700°C. The locations of these peaks were to be expected as they coincide to the temperatures at which the anomalous peaks occurred in tests with the characteristic lamella orientations of 0°, 45° and 90°.

8.3.2 Discussion

The results from the calibration process show that the presented modeling approach – despite being of purely phenomenological nature – allows to sufficiently reproduce the experimental results from [46, 47] for the investigated range of temperatures and microstructural parameters. The calibrated model can thus potentially help to rationalize the qualitative differences that have been observed between the experimental results from [46] and [37].
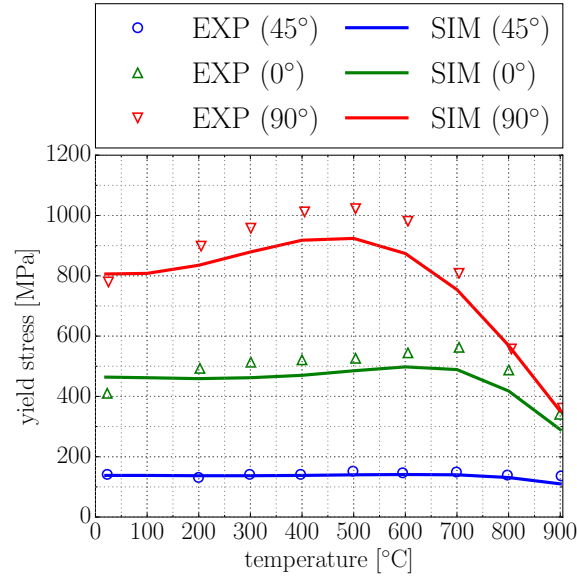
Figure 8.3. Calibration results against the temperature dependent yield strength of polysynthetically twinned crystals under a loading angle of 0°, 45° and 90°, tested in [46] between room temperature and 900°C. The microstructure parameters were taken to be $\lambda_L = 0.53 \, \mu m$, $\lambda_D = 22 \, \mu m$ and α_2 volume fraction $= 15 \, Vol\%$ as reported in [46] (cf. Table 5.2). The lattice resistance was chosen to be $\tau_R = 20 \, MPa$.
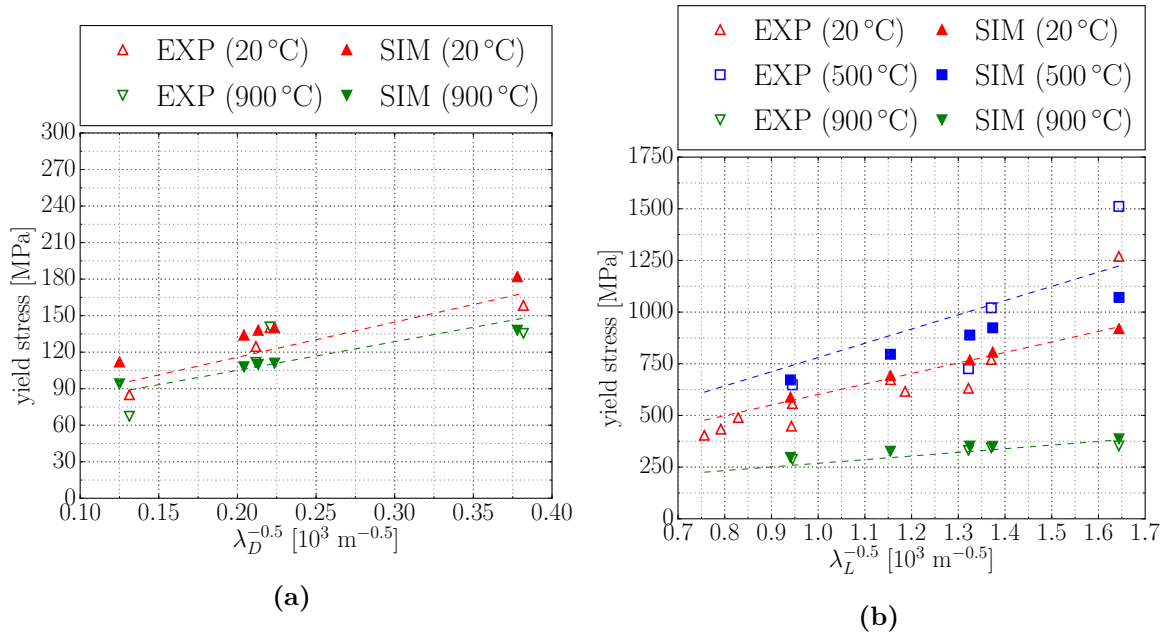
Figure 8.4. Yield strength of polysynthetically twinned crystals under a loading angle of (a) 45° and (b) 90°, tested in [46] for different temperatures between room temperature and 900°C. The microstructural parameters of the specimens tested in [46] are summarized in Table 5.2. The dashed lines indicate the linear interpolation of the experimental results. The lattice resistance was chosen to be $\tau_R = 20 \, MPa$.
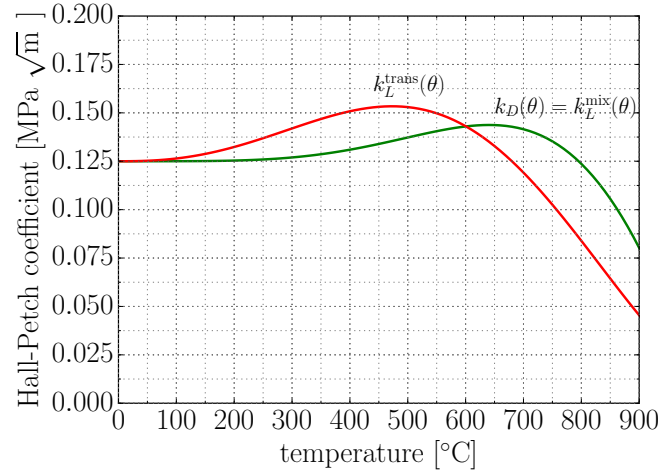
Figure 8.5. Temperature dependent Hall-Petch coefficients for lamella and domain boundary strengthening as obtained by calibrating Equations (8.4) and (8.6) against the experimental results from [46].

Table 8.1. Parameters for the temperature dependent formulation of the Hall-Petch coefficients for lamella and domain boundary strengthening, i.e. Equations (8.4) and (8.6).

$k_D(\theta)$		$k_L^{\mathrm{mix}}(\theta)$		$k_L^{\mathrm{trans}}(\theta)$	
symbol	value	symbol	value	symbol	value
$k_{D,0}$	$0.125\,\mathrm{MPa}\sqrt{\mathrm{m}}$	$k_{L,0}$	$0.125\,\mathrm{MPa}\sqrt{\mathrm{m}}$	$k_{L,0}$	$0.125\,\mathrm{MPa}\sqrt{\mathrm{m}}$
A_D	$0.00395\,\frac{1}{°\mathrm{C}}$	A_L^{mix}	$0.00395\,\frac{1}{°\mathrm{C}}$	A_L^{trans}	$0.00462\,\frac{1}{°\mathrm{C}}$
B_D	$2.41\times10^{-6}\,\frac{\mathrm{Pa}\sqrt{\mathrm{m}}}{[°\mathrm{C}]^{C_D}}$	B_L^{mix}	$2.41\times10^{-6}\,\frac{\mathrm{Pa}\sqrt{\mathrm{m}}}{[°\mathrm{C}]^{C_L^{\mathrm{mix}}}}$	B_L^{trans}	$2.64\,\frac{\mathrm{Pa}\sqrt{\mathrm{m}}}{[°\mathrm{C}]^{C_L^{\mathrm{trans}}}}$
C_D	3.61	C_L^{mix}	3.61	C_L^{trans}	1.54

As mentioned earlier, in contrast to the experimental results the model was calibrated against, in [37] the temperature dependent yield strength of polysynthetically twinned crystals under a loading angle of 90° showed a plateau rather than an anomalous peak. As the polysynthetically twinned crystals that have been tested in [37] exhibited relatively broad lamellae of $\approx 2\,\mu$m thickness and correspondingly domain sizes of up to 100 µm, it might be expected that the yield stress anomaly is predicted by the model to be less pronounced. Simulations with an α_2 volume fraction of 5%, $\lambda_L = 2\,\mu$m, $\lambda_D = 100\,\mu$m and $\tau_R = 20$ MPa do, in fact, show that the calibrated model reproduces the experimental findings from [37] to a certain degree (see Figure 8.6).

The magnitude of the predicted yield strength fits the experimental observations for the three tested orientations. For the weak orientation (loading angle of 31°), the simulation results reproduce well the yield stress – temperature profile. For loading parallel to the lamella boundaries (loading angle of 0°), the strength of the anomalous peak is, however, underestimated by the model and occurs at a lower temperature than in the experiments. Despite the high lamella thickness, the model predicts a slight anomalous peak under a loading angle of 90°. While the magnitude of the anomalous peak in the 90° simulations lies within the experimental scatter, it is still too pronounced to unambiguously explain the differences between the experimental results from [46] and [37] solely based of the different microstructural parameters investigated. Despite the models ability to sufficiently reproduce the temperature
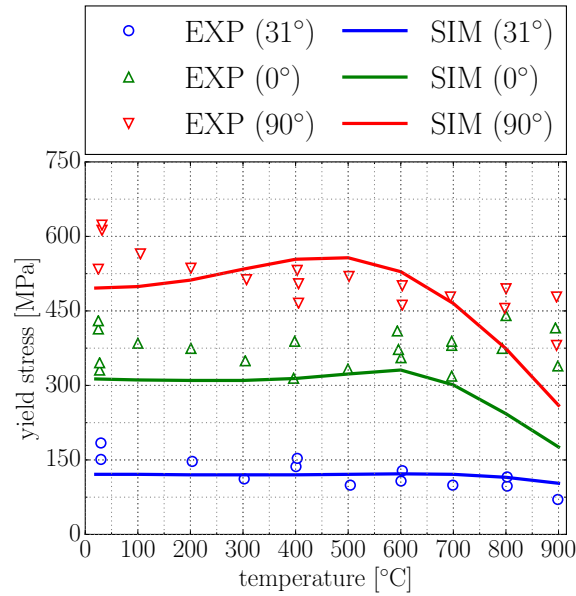
Figure 8.6. Yield strength of differently oriented polysynthetically twinned crystals tested in [37] between room temperature and 900°C. The simulations were carried out with α_2=5 Vol%, $\lambda_L = 2\,\mu\text{m}$, $\lambda_D = 100\,\mu\text{m}$ and $\tau_R = 20$ MPa.

and microstructure dependent experimental results from [46], obviously further – particularly experimental – work is needed to reveal in detail the influence of the microstructure on the yield stress anomaly of polysynthetically twinned crystals.

8.4 Polycolony microstructures

Although the details that cause the yield stress anomaly in certain orientations of polysynthetically twinned crystals are not fully understood yet, the presented model sufficiently captures their microstructure and temperature dependent yield strength on a phenomenological basis. Thus, it will be applied to study the temperature dependent yield strength of polycolony microstructures in the following.

While the general characteristics of the temperature dependence of polycolony microstructures (constant yield strength up to $\approx$ 700°C to 800°C) has been reported in various works (see, e.g., [11, 18, 20, 82, 146]), reports of systematic studies on how the microstructural parameters influence the high temperature yield strength are rare. Also, the microstructural parameters are often not or only incompletely reported in these studies. In [18], the yield strength of polycolony microstructures was investigated at 800°C for different combinations of lamella thickness and colony size. By plotting the determined yield stresses against the lamella thickness, it has been shown in [18] that the (apparent) Hall-Petch coefficient is lower at 800°C than at room temperature.

Presuming that the colony boundaries do not influence the temperature dependence of the yield strength (i.e. assuming the colony boundary strengthening Hall-Petch coefficent k_C to be temperature independent), the model can directly be applied to the polycolony RVE shown in Section 3.5.2. With the microstructural parameters from 5.3 (the ones from [18]) and a lattice resistance of $\tau_R = 30\,\text{MPa}$ (cf. Section 5.4), the model in fact predicts yield stresses comparable to the experimental findings from [18] for both, room temperature (see also Figure 5.6) and 800°C (see Figure 8.7).
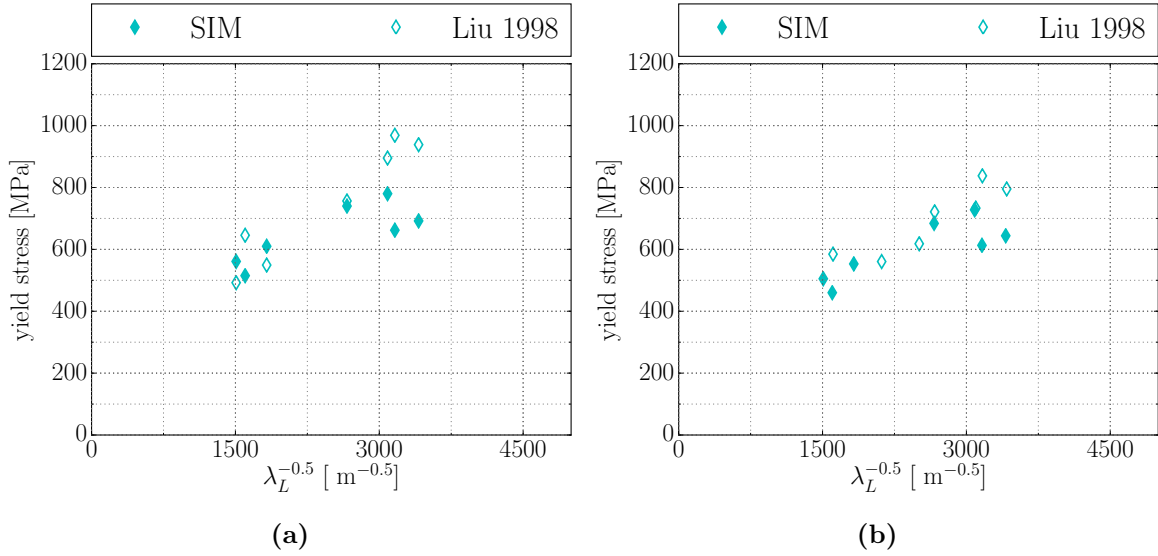
Figure 8.7. Yield strength of polycolony microstructures with different sets of microstructural parameters (see Table 5.3) tested at (a) room temperature and (b) 800 °C in [18]. For the simulations a lattice resistance of $\tau_R = 30$ MPa was chosen.

However, these results show the microstructure sensitive yield strength at only two different temperatures and do thus only grant limited insight into its temperature dependence. Therefore, the simulated temperature dependent yield stress of a polycolony microstructure is shown in Figure 8.8. The simulations were carried out with a lattice resistance of $\tau_R = 20$ MPa, an α_2 volume fraction of 10 Vol%, $\lambda_C = 330$ µm, $\lambda_L = 1$ µm and $\lambda_D = 50$ µm. The experimental results for a nearly lamellar microstructure with 0.05 µm $< \lambda_L < 1$ µm and $\lambda_C = 330$ µm from [146] are shown for a qualitative comparison.

The model shows a similar behavior as the experimental results, i.e. the predicted yield strength remains relatively constant up to 700 °C and above this temperature decreases rapidly.

8.4.1 Discussion

As mentioned earlier, the influence of the microstructural interfaces in fully lamellar TiAl on the temperature dependent yield strength is not yet fully understood. Thus, the simulation results obtained by applying the phenomenological model of the microstructure and temperature dependent yield strength of polysynthetically twinned crystals to a polycolony microstructure while assuming the colony boundary strengthening to remain temperature independent have some implications for future investigations.

First of all, the model allowed to sufficiently reproduce the experimentally determined yield strengths at room temperature and 800°C for the different combinations of microstructural parameters tested in [18]. This indicates that the colony boundary strengthening might in fact be temperature independent.

Secondly, the simulated yield strengths of polycolony microstructures do not exhibit any pronounced yield stress anomaly but instead show a nearly constant yield strength up to temperatures of 700°C similar to experimental findings (see Figure 8.8). This observation is of particular interest since in the model mixed and transversal deformation systems in the γ phase exhibit a distinct yield stress anomaly at 700°C respectively 500°C (cf. Section
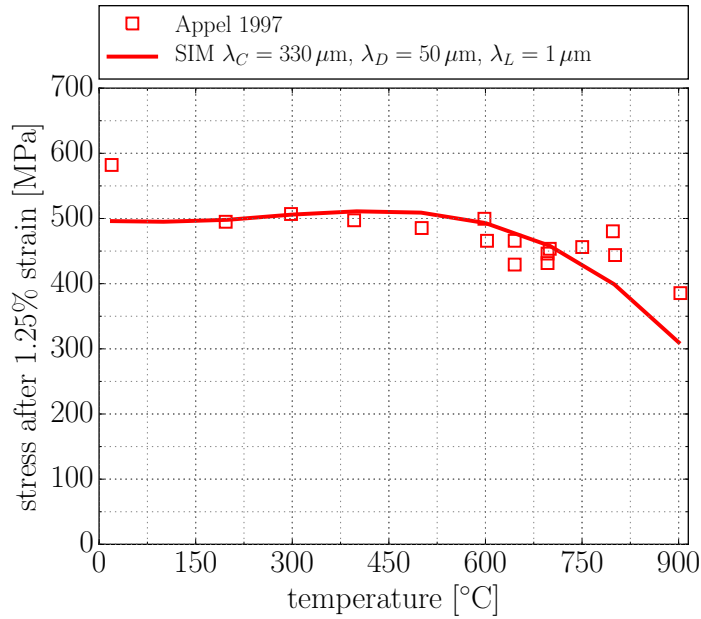
Figure 8.8. Yield strength of polycolony microstructures as function of temperature. Experimental results taken from [146] for a nearly lamellar microstructure with $0.05\,\mu m < \lambda_L < 1\,\mu m$ and $\lambda_C = 330\,\mu m$. The simulations were carried out with a lattice resistance of $\tau_R = 20\,\mathrm{MPa}$, an α_2 volume fraction of $10\,\mathrm{Vol\%}$, $\lambda_C = 330\,\mu m$, $\lambda_L = 1\,\mu m$ and $\lambda_D = 50\,\mu m$.

8.3). This finding is most likely explained by the fact that at the onset of yield the plastic deformation is nearly exclusively accomplished by longitudinal deformation systems in weakly oriented colonies which both experimentally and in the model do not exhibit a pronounced yield stress anomaly (cf. Section 8.3). Thus, the differences between the experimental findings on the temperature dependent yield strength of polysynthetically twinned crystals [37, 46] and polycolony microstructures may be rationalized.

8.5 Summary

At the moment, there is no theory at hand which comprehensively explains the distinct features in the temperature dependence of the yield strength of fully lamellar TiAl alloys. Especially the influence of the microstructural interfaces on the yield stress anomaly of polysynthetically twinned crystals remains unclear. While the presented modeling approach allowed to reproduce experimental results on the microstructure and temperature dependent yield strength of differently oriented polysynthetically twinned crystals, it is of phenomenological nature and thus has limited predictive capabilities. However, the presented phenomenological model still allowed to rationalize some of the observed differences in the temperature dependent yield strength of polysynthetically twinned crystals and polycolony microstructures and allowed to identify starting points for further investigations of the underlying micromechanical phenomena.

9 Summary and outlook

In the present thesis, a microstructure sensitive, defect density based, thermomechanically coupled crystal plasticity model for γ based fully lamellar TiAl alloys was presented. In this crystal plasticity model, the evolution of crystallographic defects – namely dislocations and twins – with deformation and thermal recovery is accounted for through internal state variables as proposed in [110, 111]. These internal state variables (i.e. the dislocation densities and twinned volume fractions) allowed to set up a physics based work hardening model and enabled a physically meaningful representation of the dissipation and the stored energy of cold work in the applied thermomechanical framework. The dominant effect of the microstructural interfaces on the mechanical behavior of fully lamellar TiAl was considered throughout all stages of the modeling process.

9.1 Work hardening

In the presented work hardening model, dislocation interactions are accounted for through a classical Taylor hardening formulation. The reduction of the free path length of slip and twinning systems due to evolving twin-matrix interfaces on non-coplanar twinning systems is incorporated into the hardening model via a Hall-Petch type relation based on the ideas from [78]. Further, the hardening interaction of twinning dislocations with the slip dislocation network is accounted for as proposed in [114].

With this defect density based crystal plasticity model it is possible to reproduce the specifics of the stress-strain response of polysynthetically twinned crystals to a degree that was not reached by previously reported models. Detailed comparison of simulation results for differently oriented polysynthetically twinned crystals to literature experimental findings showed a very good agreement. Especially the deformation systems that were predicted by the model to be active in polysynthetically twinned crystals under different loading angles matched well the experimental findings, indicating that the introduced defect density based hardening model represents a noticeable improvement as compared to formerly applied phenomenological work hardening formulations. In contrast to experiments, the simulations further allowed detailed investigation of the transition between predominant deformation modes for specific lamella orientations which were attributed to their work hardening interactions.

Further details of the work hardening behavior may be introduced into the model by, e.g., accounting for different types of dislocation interactions through suitable interaction coefficients (see, e.g., [113, 115, 135]) or by distinguishing different dislocation based defect populations (see,e.g., [114, 115]), however, by the cost of an increasing number of model parameters that have to be identified.

9.2 Microstructure sensitive yield strength

The influence of the different coexisting microstructural interfaces on the yield strength of fully lamellar TiAl alloys was incorporated into the model via three distinct Hall-Petch relations. The Hall-Petch strengthening coefficients of lamella and domain boundaries were extracted from reported experiments with differently oriented polysynthetically twinned crystals and

enabled the model to reproduce the corresponding microstructure sensitive yield strengths reasonably well.

Due to the limitations in systematically varying the microstructural parameters of fully lamellar TiAl, quantifying the Hall-Petch coefficient for colony boundary strengthening – which itself is a function of the lamella thickness and domain size [22] – was so far not possible by experiments (see, e.g., [23, 42]). By applying the microstructure sensitive model of a polysynthetically twinned crystal to an RVE of a polycolony microstructure and combining respective simulation results with experimental findings on the microstructure sensitive yield strength of polycolony fully lamellar TiAl, it was possible to extract the Hall-Petch strengthening coefficient for the colony boundaries as a function of the other microstructural parameters.

While the model proved its ability to reproduce the microstructure sensitive yield strength of fully lamellar TiAl alloys sufficiently well, there are still some open questions remaining. First of all, it is still unclear how the lattice resistance τ_R in the γ phase depends on composition and impurities. Although most experimental results were reproduced well with the presented microstructure sensitive model by choosing the lattice resistance to be in the range of $20\,\mathrm{MPa} < \tau_R < 30\,\mathrm{MPa}$, τ_R had to be chosen as high as $65\,\mathrm{MPa}$ in order to reproduce the experimental results shown in Chapter 7. While the applied values for the lattice resistance lie within the reported range (cf. Section 5.3), the uncertainties in the choice of τ_R lead to a certain span in the predicted yield strength. This counteracts the aim of precisely predicting the yield strength only based on microstructural parameters.

Further, the model does not explicitly incorporate the Hall-Petch strengthening effect by the γ/α_2 lamella interfaces so far. From a modeling perspective, the strengthening effect of the relatively strong (but widely spaced) γ/α_2 lamella interfaces might be accounted for in the same manner as the strengthening effect of the other microstructural interfaces, i.e. by Equations (5.3) and (5.4). However, an enhanced experimental data base would be needed to isolate the subtle effect of the γ/α_2 interfaces.

Finally, additional experiments with polysynthetically twinned crystals/single colonies under a loading angle of $0°$ would be helpful in order to ultimately identify the relation between the strength of mixed deformation systems and the lamella thickness.

9.3 Micro yield in polycolony microstructures

With the calibrated work hardening model and the microstructure sensitive formulation of the initial slip and twinning systems strengths at hand, is was possible to analyze the typical microyield behavior of polycolony microstructures. As opposed to previous numerical studies of the microyield behavior [41, 57, 58, 71, 80], the microstructure sensitive description of the yield strength shown here allowed to distinctly analyze the influence of the microstructural parameters on the microyield behavior. Since the employed RVE of a polycolony microstructure explicitly considers the lamellar structure of the colonies, it was further possible to (qualitatively) identify certain specifics in the highly localized plastic deformation that occurs on the micro scale.

Here, a comparison to experimental results on the microstrain fields (e.g. DIC analyses) would be interesting to validate the simulation results and to study how many lamellae per colony have to be discretized in order to capture the details in the meso scale deformation sufficiently well. Further, a more realistic RVE of a polycolony microstructure – as e.g. the one presented in [100] – would allow a more detailed analysis of the three dimensional microstrain fields than the pseudo 3D (or 2.5D) approach applied here.

9.4 Static recovery

In order to consider the elevated temperatures that TiAl components encounter in service, the recovery of the introduced work hardening was modeled. Therefore, the evolution equation for the dislocation density was extended according to [110, 111] in order to account for dislocation removal during annealing. The recovery model was calibrated against static recovery experiments with differently oriented polysynthetically twinned crystals and was subsequently applied to investigate basic trends in the static recovery behavior of polysynthetically twinned crystals as well as polycolony microstructures, a topic that to date has not been addressed in crystal plasticity modeling of fully lamellar TiAl.

From a thermodynamic point of view, a consequent next step would be to incorporate the contribution of the evolving twin-matrix interfaces to the stored energy of cold work. It is, however, unclear whether it is possible to model this contribution to the stored energy of cold work by simply formulating the Helmholtz free energy as a function of the twinned volume fractions since they are no direct measure for the energy stored in the form of twin-matrix interfaces. Here, a modeling approach that explicitly accounts for the number of twins (and their thickness) similar to the ones presented in [79, 114, 139, 159] could be useful, as the energy stored in terms of twin-matrix interfaces is directly related to their number.

9.5 Temperature sensitive yield strength

In an attempt to overcome the limitation of previously reported crystal plasticity models to isothermal conditions, the here presented model was extended in order to account for the (anomalous) temperature dependence of the yield strength of fully lamellar TiAl. In accordance to literature experimental findings on the microstructure and temperature dependent yield strength of differently oriented polysynthetically twinned crystals, this was done in a phenomenological way by making the Hall-Petch coefficients for lamella and domain boundary strengthening a function of temperature. In this, the experimentally observed yield stress anomaly was considered in terms of a sinusoidal powerlaw. This model did not only enable to reproduce the temperature (and microstructure) sensitive yield strength of differently oriented polysynthetically twinned crystals but also allowed to rationalize, to a certain degree, the observed discrepancies between different experimental studies.

In an attempt to explain why there is no yield stress anomaly observed in experiments with polycolony microstructures, the model for the temperature dependent yield strength of polysynthetically twinned crystals was applied to an RVE of a polycolony microstructure. In this, the colony boundary strengthening was assumed to be temperature independent. The model showed the typical characteristics of the temperature dependent yield strength of polycolony microstructures. This is particularly interesting as the strengths of the hard deformation modes were modeled to exhibit distinct yield stress anomalies as observed in polysynthetically twinned crystals. Since at the onset of yield, polycolony microstructures deform mainly by weakly oriented colonies (i.e. by deformation systems that do not show a stress anomaly), the simulation results potentially allow to rationalize the apparently contradicting experimental findings on the temperature dependence of the yield strengths of polysynthetically twinned crystals and polycolony microstructures.

More than the other micromechanical phenomena examined in this thesis, setting up a physics based model of the temperature dependent yield strength of fully lamellar TiAl alloys would benefit from further experimental investigations. High temperature micromechanical tests could, e.g., show whether or not single colonies in hard orientations (0° or 90°) show the same yield stress anomaly that has been observed in polysynthetically twinned crystals in the

same orientations. Further, such experiments could potentially reveal the micromechanisms behind the observed anomaly. Based on a respective series of experiments, it would likely be possible to model the temperature dependent yield strength of fully lamellar TiAl in more detail, ideally based on experimentally identifiable material parameters only.

9.6 Prospective applications

From a theoretical point of view, modeling the evolution of crystallographic defect densities is desirable since it enables a physics based formulation of the work hardening/recovery model and allows a physically meaningful assessment of the stored energy of cold work and the corresponding dissipative processes [111]. However, the presented defect density based crystal plasticity model for fully lamellar TiAl can also be of some practical use.

Numerical investigation of polycolony microstructures using the presented crystal plasticity model can greatly contribute to the understanding of their microplasticity. While it is probably not reasonable to model complete components of TiAl by explicitly discretizing the colonies and lamellae, localized plastic deformation as it might, e.g., appear due to surface treatments can be investigated by a detailed microstructural representation. Since the presented crystal plasticity model proved its ability to precisely capture the work hardening behavior of the lamellar colonies, it also allows to investigate localized deformation effects like, e.g., kinking of the lamellae [21]. Due to the incorporated recovery model, respective simulations may further help to optimize load-annealing paths in forming applications and allow to assess whether or not it is suitable to systematically introduce work hardening to improve a component's mechanical behavior at a certain operating temperature.

As the onset of recrystallization is closely related to the stored energy of cold work, the presented defect density based model – although not explicitly capturing recrystallization processes – may be useful to relate the local evolution of the defect density due to deformation and recovery to the experimentally observed tendency for recrystallization.

Although not incorporating damage evolution so far, the presented crystal plasticity model may further help to understand the causes for the frequently observed pre yield cracking [132, 149, 150] by, e.g., investigating the strong gradients in the simulated microstrain fields near microstructural sites at which pre yield cracks were experimentally observed to occur.

In conclusion, it might thus be stated that the presented defect density based crystal plasticity model opens up many new possibilities to support the understanding of experimental findings on the microplasticity in fully lamellar TiAl and further allows to relate the respective findings to the macroscopic material's behavior.

10 Bibliography

[1] J.E. Butzke and S. Bargmann. Thermomechanical Modeling of Polysynthetically Twinned TiAl Crystals. *Philosophical Magazine*, 95(24):2607–2626, 2015.

[2] J.E. Schnabel and S. Bargmann. Accessing Colony Boundary Strengthening of Fully Lamellar TiAl Alloys via Micromechanical Modeling. *Materials*, 10(8):896, 2017.

[3] J.E. Schnabel, S. Bargmann, J.D.H. Paul, M. Oehring, and F. Pyczak. Work Hardening and Recovery in Fully Lamellar TiAl: Relative Activity of Deformation Systems. *Philosophical Magazine*, 99(2):148–180, 2019.

[4] S. Bargmann, B. Klusemann, J. Markmann, J.E. Schnabel, K. Schneider, C. Soyarslan, and J. Wilmers. Generation of 3D Representative Volume Elements for Heterogeneous Materials: A Review. *Progress in Materials Science*, 96:322–384, 2018.

[5] A. Lasalmonie. Intermetallics: Why is it so Difficult to Introduce Them in Gas Turbine Engines? *Intermetallics*, 14:1123–1129, 2006.

[6] M. Yamaguchi, H. Inui, and K. Ito. High-Temperature Structural Intermetallics. *Acta Materialia*, 48:307–322, 2000.

[7] D. M. Dimiduk. Gamma Titanium Aluminide Alloys – An Assessment Within the Competition of Aerospace Structural Materials. *Materials Science and Engineering A*, 263:281–288, 1999.

[8] E.A. Loria. Gamma Titanium Aluminides as Prospective Structural Materials. *Intermetallics*, 8:1339–1345, 2000.

[9] H. Clemens and S. Mayer. Development Status, Applications and Perspectives of Advanced Intermetallic Titanium Aluminides. *Materials Science Forum*, 783-786:15–20, 2014.

[10] B.P. Bewlay, S. Nag, A. Suzuki, and M.J. Weimer. TiAl Alloys in Commercial Aircraft Engines. *Materials at High Temperatures*, 33(4–5):549–559, 2016.

[11] F. Appel, J.D.H. Paul, and M. Oehring. *Gamma Titanium Aluminide Alloys.* Wiley-VCH Verlag & Co. KGaA, 2011.

[12] F. Appel and R. Wagner. Microstructure and Deformation of Two-Phase γ-Titanium Aluminides. *Material Science and Engineering*, R22:187–268, 1998.

[13] H. Clemens and W. Smarsley. Light-Weight Intermetallic Titanium Aluminides – Status of Research and Development. *Advanced Materials Research*, 278:551 – 556, 2011.

[14] H. Clemens and S. Mayer. Design, Processing, Microstructure, Properties, and Applications of Advanced Intermetallic TiAl Alloys. *Advanced Engineering Materials*, 15(4):191 – 215, 2013.

[15] Y.-W. Kim. Ordered Intermetallic Alloys, Part III: Gamma Titanium Aluminides. *JOM*, 46(7):30–39, 1994.

[16] T. Tetsui. Development of a TiAl Turbocharger for Passenger Vehicles. *Material Science and Engineering A*, 329-331:582–588, 2002.

[17] Y.-W. Kim. Microstructural Evolution and Properties of a Forged Gamma Titanium Aluminide Alloy. *Acta metallurgica et materialia*, 40(6):1121–1134, 1992.

[18] C.T. Liu and P.J. Maziasz. Microstructural Control and Mechanical Properties of Dual-Phase TiAl Alloys. *Intermetallics*, 6:653–661, 1998.

[19] Y. Chen, Y. Chen, F. Kong, and S. Xiao. Fabrication and Processing of Gamma Titanium Aluminides – a Review. *Materials Science Forum*, 638-642:1281–1287, 2010.

[20] T. Tetsui, K. Shindo, S. Kobayashi, and M. Takeyama. A Newly Developed Hot Worked TiAl Alloy for Blades and Structural Components. *Scripta Materialia*, 47:399–403, 2002.

[21] J. Lindemann, C. Buque, and F. Appel. Effect of Shot Peening on Fatigue Performance of a Lamellar Titanium Aluminide Alloy. *Acta Materialia*, 54:1155–1164, 2006.

[22] Y.-W. Kim. Strength and Ductility in TiAl Alloys. *Intermetallics*, 6:623–628, 1998.

[23] D. M. Dimiduk, P. M. Hazzledine, T. A. Parthasarathy, S. Seshagiri, and M. G. Mendiratta. The Role of Grain Size and Selected Microstructural Parameters in Strengthening Fully Lamellar TiAl Alloys. *Metallurgical and Materials Transactions A*, 29:37–47, 1998.

[24] H. Inui, M.H. Oh, A. Nakamura, and M. Yamaguchi. Ordered Domains in TiAl Coexisting with Ti$_3$Al in the Lamellar Structure of Ti-rich TiAl Compounds. *Philosophical Magazine A*, 66(4):539–555, 1992.

[25] T. Fujiwara, A. Nakamura, M. Hosomi, S. R. Nishitani, Y. Shirai, and M. Yamaguchi. Deformation of Polysynthetically Twinned Crystals of TiAl with a Nearly Stoichiometric Composition. *Philosophical Magazine A*, 61(4):591–606, 1990.

[26] H. Inui, M.H. Oh, A. Nakamura, and M. Yamaguchi. Room-Temperature Tensile Deformation of Polysynthetically Twinned (PST) Crystals of TiAl. *Acta metallurgica et materialia*, 40(11):3095–3104, 1992.

[27] Y. Umakoshi, T. Nakano, T. Takenaka, K. Sumimoto, and T. Yamane. Orientation and Temperature Dependence of Yield Stress and Slip Geometry of Ti$_3$AI and Ti$_3$Al-V Single Crystals. *Acta metallurgica et materialia*, 41(4):1149–1154, 1993.

[28] R. Lebensohn, H. Uhlenhut, C. Hartig, and H. Mecking. Plastic Flow of γ-TiAl-Based Polysynthetically Twinned Crystals: Micromechanical Modeling and Experimental Validation. *Acta Materialia*, 46(13):4701–4709, 1998.

[29] M. Werwer. *Mikromechanische Modellierung des Verformungs- und Bruchverhaltens von Lamellarem TiAl*. PhD thesis, University of Technology Hamburg, 2005.

[30] W.F. Hosford. *Mechanical Behavior of Materials*. Cambridge University Press, first edition edition, 2005.

[31] Y. He, R.B. Schwarz, T. Darling, M. Hundley, S.H. Wang, and Z.M. Wang. Elastic Constants and Thermal Expansion of Single Crystal γ–TiAl from 300 to 750 K. *Materials Science and Engineering A*, 239–240:157–163, 1997.

[32] M.H. Yoo, J. Zou, and C.L. Fu. Mechanistic Modeling of Deformation and Fracture Behavior in TiAl and Ti$_3$Al. *Materials Science and Engineering A*, 192/193:14–23, 1995.

[33] H. Inui, M. Matsumuro, D.-H. Wu, and M. Yamaguchi. Temperature Dependence of Yield Stress, Deformation Mode and Deformation Structure in Single Crystals of TiAl (Ti-56 at.% Al). *Philosophical Magazine A*, 75(2):395–423, 1997.

[34] T. Kawabata, T. Kanai, and O. Izumi. Positive Temperature Dependence of the Yield Stress in TiAl L1$_0$ Type Superlattice Intermetallic Compound Single Crystals at 293-1273 K. *Acta metallurgica*, 33(7):1355–1366, 1985.

[35] H. Inui, Y. Toda, and M. Yamaguchi. Plastic Deformation of Single Crystals of a DO$_{19}$ Compound with an Off-Stoichiometric Composition (Ti–36.5 at. % Al) at Room Temperature. *Philosophical Magazine A*, 67(6):1315–1332, 1993.

[36] Y. Minonishi. Plastic Deformation of Single Crystals of Ti$_3$Al with D0$_{19}$ Structure. *Philosophical Magazine A*, 63(5):1085–1093, 1991.

[37] H. Inui, K. Kishida, M. Misaki, M. Kobayashi, Y. Shirai, and M. Yamaguchi. Temperature Dependence of Yield Stress, Tensile Elongation and Deformation Structures in Polysynthetically Twinned Crystals of Ti-Al. *Philosophical Magazine A*, 72(6):1609–1631, 1995.

[38] T. Nakano, K. Hayaashi, Y. Umakoshi, Y.-L. Chiu, and P. Veyssière. Effects of Al Concentration and Resulting Longperiod Superstructures on the Plastic Properties at Room Temperature of Al-rich TiAl Single Crystals. *Philosophical Magazine*, 85(22):2527–2548, 2005.

[39] F. Appel, U. Sparka, and R. Wagner. Work Hardening and Recovery of Gamma Base Titanium Aluminides. *Intermetallics*, 7:325–334, 1999.

[40] A.J. Palomares-García, M.T. Pérez-Prado, and J.M. Molina-Aldareguia. Effect of Lamellar Orientation on the Strength and Operating Deformation Mechanisms of Fully Lamellar TiAl Alloys Determined by Micropillar Compression. *Acta Materialia*, 123:102–114, 2017.

[41] C. Zambaldi. *Micromechanical Modeling of γ-TiAl Based Alloys*. PhD thesis, Rheinisch-Westfälische Technische Hochschule Aachen, 2010.

[42] G. Cao, L. Fu, J. Lin, Y. Zhang, and C. Chen. The Relationships of Microstructure and Properties of a Fully Lamellar TiAl Alloy. *Intermetallics*, 8:647–653, 2000.

[43] K. Maruyama, M. Yamaguchi, G. Suzuki, H. Zhu, Hee Y. Kim, and M.H.Yoo. Effects of Lamellar Boundary Structural Change on Lamellar Size Hardening in TiAl Alloy. *Acta Materialia*, 52:5185–5194, 2004.

[44] K. Kishida, D.R. Johnson, Y. Masuda, H. Umeda, H. Inui, and M. Yamaguchi. Deformation and Fracture of PST Crystals and Directionally Solidified Ingots of TiAl-Based Alloys. *Intermetallics*, 6:679–683, 1998.

[45] K. Maruyama, N. Yamada, and H. Sato. Effects of Lamellar Spacing on Mechanical Properties of Fully Lamellar Ti-39.4mol% Al Alloy. *Materials Science and Engineering A*, 319-321:360–363, 2001.

[46] Y. Umakoshi and T. Nakano. Plastic Behaviour of TiAl Crystals Containing a Single Set of Lamellae at High Temperatures. *ISIJ International*, 32:139–1347, 1992.

[47] Y. Umakoshi and T. Nakano. The Role of Ordered Domains and Slip Mode of α_2 Phase in the Plastic Behaviour of TiAl Crystals Containing Oriented Lamellae. *Acta metallurgica et materialia*, 41(4):1155–1161, 1993.

[48] J. Tang, B. Huang, Y. He, W. Liu, K. Zhou, and A. Wu. Hall-Petch Relationship in Two-Phase TiAl Alloys with Fully Lamellar Microstructures. *Materials Research Bulletin*, 37:1315–1321, 2002.

[49] P.J. Maziasz and C.T. Liu. Development of Ultrafine Lamellar Structures in Two-Phase γ-TiAl Alloys. *Metallurgical and Materials Transactions A*, 29:105–117, 1998.

[50] K.-F. Yao, H. Inui, K. Kishida, and M. Yamaguchi. Plastic Deformation of V- and Zr-Alloyed PST TiAl in Tension and Compression at Room Temperature. *Acta metallurgica et materialia*, 43(3):1075 – 1086, 1995.

[51] H. Umeda, K. Kishida, H. Inui, and M. Yamaguchi. Effects of Al-Concentration and Lamellar Spacing on the Room-Temperature Strength and Ductility of PST Crystals of TiAl. *Materials Science and Engineering A*, 239–240:336 – 343, 1997.

[52] H. Uhlenhut. *Ursachen Plastischer Anisotropie von γ-TiAl-Basislegierungen*. PhD thesis, Technische Universität Hamburg-Harburg, 1999.

[53] A.J. Palomares-García, I. Sabirov, M.T. Pérez-Prado, and J.M. Molina-Aldareguia. Effect of Nanoscale Thick Lamellae on the Micromechanical Response of a TiAl Alloy. *Scripta Materialia*, 139:17–21, 2017.

[54] A. Bartels and H. Uhlenhut. Anisotropy of Plastic Flow in Strongly Textured γ-TiAl-Based Alloys. *Intermetallics*, 6:685–688, 1998.

[55] K. Kishida, H. Inui, and M. Yamaguchi. Deformation of Lamellar Structure in TiAl-Ti$_3$Al Two-Phase Alloys. *Philosophical Magazine A*, 78(1):1–28, 1998.

[56] F. Roters, P. Eisenlohr, L. Hantcherli, D.D. Tjahjanto, T.R. Bieler, and D. Raabe. Overview of Constitutive Laws, Kinematics, Homogenization and Multiscale Methods in Crystal Plasticity Finite-Element Modeling: Theory, Experiments, Applications. *Acta Materialia*, 58:1152–1211, 2010.

[57] B.K. Kad, M. Dao, and R.J. Asaro. Numerical Simulations of Stress-Strain Behavior in Two-Phase $\alpha_2 + \gamma$ Lamellar TiAl Alloys. *Material Science and Engineering A*, 192/193:97–103, 1995.

[58] B.K. Kad, M. Dao, and R.J. Asaro. Numerical Simulations of Plastic Deformation and Fracture Effects in Two Phase γ-TiAl + α_2-Ti$_3$Al Lamellar Microstructures. *Philosophical Magazine A*, 71(3):567–604, 1995.

[59] M. Dao, B.K. Kad, and R.J. Asaro. Deformation and Fracture Under Compressive Loading in Lamellar TiAl Microstructures. *Philosophical Magazine A*, 74(3):569–591, 1996.

[60] B.K. Kad and R.J. Asaro. Apparent Hall-Petch Effects in Polycrystalline Lamellar TiAl. *Philosophical Magazine A*, 75(1):87–104, 1997.

[61] E. Parteder, T. Siegmund, F.D. Fischer, and S. Schlögl. Numerical Simulation of the Plastic Behavior of Polysynthetically Twinned Ti-Al Crystals. *Materials Science and Engineering A*, 192/193:149–154, 1995.

[62] S.M. Schlögl and F.D. Fischer. Micromechanical Modelling of TiAl Intermetallics. *Computational Materials Science*, 7:34–39, 1996.

[63] S.M. Schlögl and F.D. Fischer. The Role of Slip and Twinning in the Deformation Behaviour of Polysynthetically Twinned Crystals of TiAl: A Micromechanical Model. *Philosophical Magazine A*, 75(3):621–636, 1997.

[64] S.M. Schlögl and F.D. Fischer. Numerical Simulation of Yield Loci for PST Crystals of TiAl. *Materials Science and Engineering A*, 239-240:790–803, 1997.

[65] R. Lebensohn. Modelling the Role of Local Correlations in Polycrystal Plasticity Using Viscoplastic Self-Consistent Schemes. *Modelling and Simulation in Materials Science and Engineering*, 7:739–746, 1999.

[66] R.A. Lebensohn and C.N. Tomé. A Self-Consistent Anisotropic Approach for the Simulation of Plastic Deformation and Texture Development of Polycrystals: Application to Zirconium Alloys. *Acta Metallurgica Materialia*, 41(9):2611–2624, 1993.

[67] M. Grujicic and Y. Zhang. Crystal Plasticity Analysis of the Effect of Dispersed β-Phase on Deformation and Fracture of Lamellar $\gamma + \alpha_2$ Titanium Aluminide. *Material Science and Engineering A*, 265:285–300, 1999.

[68] M. Grujicic and G. Cao. Crack Growth in Lamellar Titanium Aluminides Containing Beta Phase Precipitates. *Journal of Materials Science*, 37:2949–2963, 2002.

[69] M. Grujicic and S. Batchu. A Crystal Plasticity Materials Constitutive Model for Polysynthetically-Twinned γ-TiAl $+\alpha_2$-Ti$_3$Al Single Crystals. *Journal of Materials Science*, 36:2851–2863, 2001.

[70] M. Grujicic, G. Cao, and S. Batchu. Crystal Plasticity-Based Finite Element Analysis of Deformation and Fracture of Polycrystalline Lamellar γ-TiAl $+\alpha_2$-Ti$_3$Al Alloys. *Journal of Materials Science*, 38:307–322, 2003.

[71] R.A. Brockmann. Analysis of Elastic-Plastic Deformation in TiAl Polycrystals. *International Journal of Plasticity*, 19:1749–1772, 2003.

[72] M. Werwer and A. Cornec. Numerical Simulation of Plastic Deformation and Fracture in Polysynthetically Twinned (PST) Crystals of TiAl. *Computational Materials Science*, 19:97–107, 2000.

[73] M. Werwer and A. Cornec. The Role of Superdislocations for Modeling Plastic Deformation of Lamellar TiAl. *International Journal of Plasticity*, 22:1683–1698, 2006.

[74] M.R. Kabir. *Modeling and Simulation of Deformation and Fracture Behavior of Components Made of Fully Lamellar γ TiAl Alloy*. PhD thesis, Christian-Albrechts-Universität zu Kiel, 2008.

[75] M.R. Kabir, L. Chernova, and M. Bartsch. Numerical Investigation of Room-Temperature Deformation Behavior of a Duplex Type γTiAl Alloy Using a Multi-Scale Modeling Approach. *Acta Materialia*, 58:5834–5847, 2010.

[76] A. Cornec, M.R. Kabir, and N. Huber. Numerical Prediction of the Stress-Strain Response of a Lamellar γTiAl Polycrystal Using a Two-Scale Modelling Approach. *Materials Science & Engineering A*, 620:273–285, 2015.

[77] A. Roos, J.-L. Chaboche, L. Gélébart, and J. Crépin. Multiscale Modelling of Titanium Aluminides. *International Journal of Plasticity*, 20:811–830, 2004.

[78] K. Kowalczyk-Gajewska. *Micromechanical Modelling of Metals and Alloys of High Specific Strength.* Instytut Podstawowych Problemów Techniki Polskiej Akademii Nauk, 2011.

[79] I. Karaman, H. Sehitoglu, A.J. Beaudoin, Y.I. Chumlyakov, H.J. Maier, and C.N. Tomé. Modeling the Deformation Behavior of Hadfield Steel Single and Polycrystals due to Twinning and Slip. *Acta Materialia*, 48:2031–2047, 2000.

[80] C. Zambaldi, F. Roters, and D. Raabe. Analysis of the Plastic Anisotropy and Pre-Yielding of (γ/α_2)-Phase Titanium Aluminide Microstructures by Crystal Plasticity Simulation. *Intermetallics*, 19:820–827, 2011.

[81] M.U. Ilyas and M.R. Kabir. A Temperature Sensitive Crystal Plasticity Model for the Prediction of High Temperature Mechanical Behaviour of Multi-Phase TiAl Alloy. In M. Papadrakakis, V. Papadopoulos, G. Stefanou, and V. Plevris, editors, *VII European Congress on Computational Methods in Applied Sciences and Engineering*, 2016.

[82] F. Appel, H. Clemens, and F.D. Fischer. Modeling Concepts for Intermetallic Titanium Aluminides. *Progress in Materials Science*, 81:55–124, 2016.

[83] W.T. Marketz, F.D. Fischer, and H. Clemens. Deformation Mechanisms in TiAl Intermetallics – Experiments and Modeling. *International Journal of Plasticity*, 19:281–321, 2003.

[84] R. Mohr. *Modellierung des Hochtemperaturverhaltens Metallischer Werkstoffe.* PhD thesis, Technische Universität Hamburg-Harburg, 1999.

[85] M.F. Bartholomeusz and J.A. Wert. Modeling Creep Deformation of a Two-Phase TiAI/Ti$_3$AI Alloy With a Lamellar Microstructure. *Metallurgical and Materials Transactions A*, 25:2161–2171, 1994.

[86] M.V. Kral, M.A. Mangan, G. Spanos, and R.O. Rosenberg. Three-Dimensional Analysis of Microstructures. *Materials Characterization*, 45:17–23, 2000.

[87] S. Zaefferer, S.I. Wright, and D. Raabe. Three-Dimensional Orientation Microscopy in a Focused Ion Beam–Scanning Electron Microscope: A New Dimension of Microstructure Characterization. *Metallurgical and Materials Transactions A*, 39:374–389, 2008.

[88] Y. Adachi, M. Ojima, S. Morooka, and Y. Tomota. Hierarchical 3D/4D Characterization on Deformation Behavior of Austenitic and Pearlitic Steels. *Materials Science Forum*, 638–642:2505–2510, 2010.

[89] Y.-T. Wang, Y. Adachi, K. Nakajima, and Y. Sugimoto. Quantitative Three-Dimensional Characterization of Pearlite Spheroidization. *Acta Materialia*, 58:4849–4858, 2010.

[90] M. Simonelli. *Microstructure Evolution and Mechanical Properties of Selective Laser Melted Ti-6Al-4V.* PhD thesis, Loughborough University, 2014.

[91] E.P. Barry. Three-Dimensional Reconstruction of Microstructures in $\alpha + \beta$ Titanium Alloys. Master's thesis, Ohio State University, 2008.

[92] A. Yamanaka, T. Takaki, and Y. Tomita. Coupled Simulation of Microstructural Formation and Deformation Behavior of Ferrite-Pearlite Steel by Phase-Field Method and Homogenization Method. *Materials Science and Engineering A*, 480:244–252, 2008.

[93] J. Hötzer, M. Jainta, P. Steinmetz, B. Nestler, A. Dennstedt, A. Genau, M. Bauer, H. Köstler, and U. Rüde. Large Scale Phase-Field Simulations of Directional Ternary Eutectic Solidification. *Acta Materialia*, 93:194–204, 2015.

[94] P. Steinmetz, M. Kellner, J. Hötzer, A. Dennstedt, and B. Nestler. Phase-Field Study of the Pattern Formation in Al–Ag–Cu Under the Influence of the Melt Concentration. *Computational Materials Science*, 121:6–13, 2016.

[95] J. Yang, G. Hu, and Y. Zhang. Prediction of Yield Stress for Polysynthetically Twinned TiAl Crystals. *Script Materialia*, 45:293–299, 2001.

[96] X. Peng, W. Pi, and J. Fan. A Microstructure-Damage-Based Description for the Size Effect of the Constitutive Behavior of Pearlitic Steels. *International Journal of Damage Mechanics*, 19:821–849, 2010.

[97] M. Ekh, N. Larijani, and E. Lindfeldt. A Comparison of Approaches to Model Anisotropy Evolution in Pearlitic Steel. In *11th World Congress on Computational Mechanics (WCCM XI) 5th European Conference on Computational Mechanics (ECCM V) 6th European Conference on Computational Fluid Dynamics (ECFD VI)*, 2014.

[98] E. Lindfeldt and M. Ekh. Multiscale Modeling of the Mechanical Behaviour of Pearlitic Steel. *Technische Mechanik*, 32(2–5):380–392, 2012.

[99] D. Deka, D.S. Joseph, S. Ghosh, and M.J. Mills. Crystal Plasticity Modeling of Deformation and Creep in Polycrystalline Ti-6242. *Metallurgical and Materials Transactions A*, 37:1371–1388, 2006.

[100] S. Dodla, A. Bertram, and M. Krüger. Finite Element Simulation of Lamellar Copper-Silver Composites. *Computational Materials Science*, 101:29–38, 2015.

[101] T. Schaden, F.D. Fischer, H. Clemens, F. Appel, and A. Bartels. Numerical Modelling of Kinking in Lamellar γ-TiAl Based Alloys. *Advanced Engineering Materials*, 8(11), 2006.

[102] R. Morrissey, C.-H. Goh, and D.L. McDowell. Microstructure-Scale Modeling of HCF Deformation. *Mechanics of Materials*, 35:295–311, 2003.

[103] M. Abouridouane, F. Klocke, D. Lung, and O. Adams. A New 3D Multiphase FE Model for Micro Cutting Ferritic-Pearlitic Carbon Steels. *CIRP Annals - Manufacturing Technology*, 61:71–74, 2012.

[104] G. Venkatramani, S. Ghosh, and M. Mills. A Size-Dependent Crystal Plasticity Finite-Element Model for Creep and Load Shedding in Polycrystalline Titanium Alloys. *Acta Materialia*, 55:3971–3986, 2007.

[105] G. Venkatramani, D. Deka, and S. Ghosh. Crystal Plasticity Based FE Model for Understanding Microstructural Effects on Creep and Dwell Fatigue in Ti-6242. *Journal of Engineering Materials and Technology*, 128:356–365, 2006.

[106] M. Zhang, J. Zhang, and D.L. McDowell. Microstructure-Based Crystal Plasticity Modeling of Cyclic Deformation of Ti-6Al-4V. *International Journal of Plasticity*, 23:1328–1348, 2007.

[107] J.R. Rice. Inelastic Constitutive Relations for Solids: An Internal-Variable Theory and its Application to Metal Plasticity. *Journal of Mthe Mechanics and Physics of Solids*, 19:433–455, 1971.

[108] S.R. Kalidindi. Incorporation of Deformation Twinning in Crystal Plasticity Models. *Journal of the Mechanics and Physics of Solids*, 46(2):267–290, 1998.

[109] D. Pierce, R.J. Asaro, and A. Needleman. Material Rate Dependence and Local Deformation in Crystalline Solids. *Acta metallurgica*, 31:1951–1976, 1983.

[110] A. McBride, S. Bargmann, and B.D. Reddy. A Computational Investigation of a Model of Single-Crystal Gradient Thermoplasticity that Accounts for the Stored Energy of Cold Work and Thermal Annealing. *Computational Mechanics*, 55:755–769, 2015.

[111] L. Anand, M.E. Gurtin, and B.D. Reddy. The Stored Energy of Cold Work, Thermal Annealing, and Other Thermodynamic Issues in Single Crystal Plasticity at Small Length Scales. *International Journal of Plasticity*, 64:1–25, 2015.

[112] H. Mecking and F. Kocks. Kinetics of Flow and Strain-Hardening. *Acta Metallurgica*, 29:1865 – 1875, 1981.

[113] L.P. Evers, W.A.M. Brekelmans, and M.G.D. Geers. Non-Local Crystal Plasticity Model with Intrinsic SSD and GND Effects. *Journal of the Mechanics and Physics of Solids*, 52:2379–2401, 2004.

[114] I.J. Beyerlein and C.N. Tomé. A Dislocation-Based Constitutive Law for Pure Zr Including Temperature Effects. *International Journal of Plasticity*, 24:867–895, 2008.

[115] A. Ma, F. Roters, and D. Raabe. A Dislocation Density Based Constitutive Model for Crystal Plasticity FEM Including Geometrically Necessary Dislocations. *Acta Materialia*, 54:2169–2179, 2006.

[116] J. Lemaitre and J.L. Chaboche. *Mechanics of Solid Materials*. Cambridge University Press, 1990.

[117] R. Seghir, E. Charkaluk, P. Dufrenoy, and L. Bodelot. Thermomechanical Couplings in Crystalline Plasticity Under Fatigue Loading. *Prodcedia Engineering*, 2:1155–1164, 2010.

[118] S. Bargmann and M. Ekh. Microscopic Temperature Field Prediction During Adiabatic Loading Using Gradient Extended Crystal Plasticity. *International Journal of Solids and Structures*, 50(6):899–906, 2013.

[119] M. Scheidler and T.W. Wright. A Continuum Framework for Finite Viscoplasticity. *International Journal of Plasticity*, 17:1033–1085, 2001.

[120] G.A. Holzapfel. *Nonlinear Solid Mechanics - A Continuum Approach for Engineering*. Wiley-VCH Verlag GmbH, 2008.

[121] S. Bargmann. *Theory and Numerics of Non-Classical Thermo-Hyperelasticity*. PhD thesis, Technische Universität Kaiserslautern, 2008.

[122] R.E. Schafrik. Dynamic Elastic Moduli of the Titanium Aluminides. *Metallurgical Transactions A*, 8:1003–1006, 1977.

[123] T. Novoselova, S. Malinov, W. Sha, and A. Zhecheva. High-Temperature Synchrotron X-Ray Diffraction Study of Phases in a Gamma TiAl Alloy. *Material Science and Engineering A*, 371:103–112, 2004.

[124] I. Egry, R. Brooks, D. Holland-Moritz, R. Novakovic, T. Matsushita, E. Ricci, S. Seetharaman, R. Wunderlich, and D. Jarvis. Thermophysical Properties of γ - Titanium Aluminide: the European IMPRESS Project. *International Journal of Thermophysics*, 28:1026–1036, 2007.

[125] W.J. Zhang, B.V. Reddy, and S.C. Deevi. Physical Properties of TiAl-Base Alloys. *Scripta Materialia*, 45:645–651, 2001.

[126] S. Bargmann, B. Svendsen, and M. Ekh. An Extended Crystal Plasticity Model for Latent Hardening in Polycrystals. *Computational Mechanics*, 48:631–645, 2011.

[127] C. Miehe. Numerical Computation of Algorithmic (Consistent) Tangent Moduli in Large-Strain Computational Inelasticity. *Computational Methods in Applied Mechanics and Engineering*, 134:223–240, 1996.

[128] H.J. Böhm. A Short Introduction to Basic Aspects of Continuum Micromechanics. *ILSB Report / ILSB-Arbeitsbericht*, 206, 2017.

[129] J.D.H. Paul and F. Appel. Work Hardening and Recovery Mechanisms in Gamma-Based Titanium Aluminides. *Metallurgical and Materials Transactions A*, 34:2103–2111, 2003.

[130] F. Appel, D. Herrmann, F.D. Fischer, J. Svoboda, and E. Kozeschnik. Role of Vacancies in Work Hardening and Fatigue of TiAl Alloys. *International Journal of Plasticity*, 42:83–100, 2013.

[131] E. Héripré, D. Caldemaison, A. Roos, and J. Crépin. Microstrain Analysis of Titanium Aluminides. *Materials Science Forum*, 638-642:1330–1335, 2010.

[132] C. Içöz, L. Patriaca, M. Filipini, and S. Beretta. Strain Accumulation in TiAl Intermetallics via High-Resolution Digital Image Correlation (DIC). *Procedia Engineering*, 74:443–448, 2014.

[133] T.E.J. Edwards, F. Di Gioacchino, R. Muñoz-Moreno, and W.J. Clegg. The Interaction of Borides and Longitudinal Twinning in Polycrystalline TiAl Alloys. *Acta Materialia*, 140:305–316, 2017.

[134] D. Kuhlmann-Wilsdorf. The Theory of Dislocation-Based Crystal Plasticity. *Philosophical Magazine A*, 79(4):955–1008, 1999.

[135] A. Arsenlis and D.M. Parks. Modeling the Evolution of Crystallographic Dislocation Density in Crystal Plasticity. *Journal of the Mechanics and Physics of Solids*, 50:1979–2009, 2002.

[136] L. Remy. Kinetics of F.C.C. Deformation Twinning and its Relationship to Stress-Strain Behaviour. *Acta Metallurgica*, 26:443–451, 1978.

[137] S.R. Kalidindi. Modeling Anisotropic Strain Hardening and Deformation Textures in Low Stacking Fault Energy FCC Metals. *International Journal of Plasticity*, 17:837–860, 2001.

[138] J.W. Christian and S. Mahajan. Deformation Twinning. *Progress in Materials Science*, 39:1–157, 1995.

[139] G. Proust, C.N.Tomé, and G.C. Kaschner. Modeling Texture, Twinning and Hardening Evolution During Deformation of Hexagonal Materials. *Acta Materialia*, 55:2137–2148, 2007.

[140] K. Kowalczyk-Gajewska. Modelling of Texture Evolution in Metals Accounting for Lattice Reorientation due to Twinning. *European Journal of Mechanics A/Solids*, 29:28–41, 2010.

[141] T.E.J. Edwards, F. Di Gioacchino, R. Muñoz-Moreno, and W.J. Clegg. Deformation of Lamellar TiAl Alloys by Longitudinal Twinning. *Scripta Materialia*, 118:46–50, 2016.

[142] M. Rester, F.D. Fischer, C. Kirchlechner, T. Schmoelzer, H. Clemens, and G. Dehm. Deformation Mechanisms in Micron-Sized PST TiAl Compression Samples: Experiment and Model. *Acta Materialia*, 59:3410–3421, 2011.

[143] Z.-W. Ji, S. Lu, Q.-M. Hu, D. Kim, R. Yang, and L. Vitos. Mapping Deformation Mechanisms in Lamellar Titanium Aluminide. *Acta Materialia*, 144:835–843, 2018.

[144] E.O. Hall. The Deformation and Ageing of Mild Steel: III Discussion of Results. *Proceedings of the Physical Society. Section B*, 64:747 – 753, 1951.

[145] N.J. Petch. The cleavage strength of polycrystals. *Journal of the Iron and Steel Institute*, 174(1):25–28, 1953.

[146] F. Appel, U. Lorenz, M. Oehring, U. Sparka, and R. Wagner. Thermally Activated Deformation Mechanisms in Micro-Alloyed Two-Phase Titanium Aluminide Alloys. *Materials Science and Engineering A*, 233:1–14, 1997.

[147] T.A. Partasarathy, M.G. Mendiratta, and D.M. Dimiduk. Flow Behavior of PST and Fully Lamellar Polycrystals of Ti–48Al in the Microstrain Regime. *Acta Materialia*, 46(11):4005 – 4016, 1998.

[148] T. A. Parthasarathy, P. R. Subramanian, M. G. Mendiratta, and D. M. Dimiduk. Phenomenological Observations of Lamellar Orientation Effects on the Creep Behavior of Ti–48at.%Al PST Crystals. *Acta Materialia*, 48:541 – 551, 2000.

[149] D. Hu, A. Huang, H. Jiang, N. Mota-Solis, and Xinhua Wu. Pre-Yielding and Pre-Yield Cracking in TiAl-Based Alloys. *Intermetallics*, 14:82–90, 2006.

[150] R. Botten, X. Wu, D. Hu, and M.H. Loretto. The Significance of Acoustic Emission During Stressing of TiAl-Based Alloys. Part I: Detection of Cracking During Loading Up in Tension. *Acta Materialia*, 49:1687–1691, 2001.

[151] I.F. Pariente and M. Giagliano. About the Role of Residual Stresses and Surface Work Hardening on Fatigue ΔK_{th} of a Nitrided and Shot Peened Low-Alloy Steel. *Surface & Coatings Technology*, 202:3072–3080, 2008.

[152] R. Hoppe. *Thermische und athermische Spannungen bei der Verformung und Ermüdung von TiAl-Legierungen.* PhD thesis, Technische Universität Hamburg-Harburg, 2013.

[153] M.H. Oh, H. Inui, A. Nakamura, and M. Yamaguchi. Recovery and Recrystallization of Cold-Rolled Polysynthetically Twinned (PST) Crystals of TiAl. *Acta Metallurgica et Materialia*, 40(1):167–176, 1992.

[154] P. Veyssière. Yield Stress Anomalies in Ordered Alloys: a Review of Microstructural Findings and Related Hypotheses. *Materials Science and Engineering A*, 309-310:44–48, 2001.

[155] T. Nakano, K. Hagihara, T. Seno, N. Sumida, M. Yamamoto, and Y. Umakoshi. Stress Anomaly in Al-Rich Ti-Al Single Crystals Deformed by the Motion of 1/2«110] Ordinary Dislocations. *Philosophical Magazine Letters*, 78:5:385–391, 1998.

[156] B. Viguier, K. J. Hemker, J. Bonneville, F. Louchet, and J.-L. Martin. Modelling the Flow Stress Anomaly in γ-TiAl I. Experimental Observations of Dislocation Mechanisms. *Philosophical Magazine A*, 71(6):1295–1312, 1995.

[157] F. Louchet and B. Viguier. Modelling the Flow Stress Anomaly in γ-TiAl II. The Local Pinning-Unzipping Model: Statistical Analysis and Consequences. *Philosophical Magazine A*, 71(6):1313–1333, 1995.

[158] S. Keshavarz and S. Ghosh. A Crystal Plasticity Finite Element Model for Flow Stress Anomalies in Ni_3Al Single Crystals. *Philosophical Magazine*, 95(24):2639–2660, 2015.

[159] M. Homayonifar. *Modeling of Deformation-Induced Twinning and Dislocation Slip in Magnesium Using a Variationally Consistent Approach*. PhD thesis, Christian-Albrechts Universität Kiel, 2011.

A Appendix

A.1 Miller index notation for cubic lattices

Crystallographic planes and directions in cubic crystal lattices (e.g. FCC or BCC) are commonly described in terms of so-called Miller indices [30]. In this Miller index notation, crystallographic planes are denoted by (hkl), i.e. using round brackets, whereas for crystallographic directions square brackets are used, i.e. $[uvw]$. Whenever a family of crystallograpically equivalent planes is supposed to be adressed, the notation $\{hkl\}$ is used. Correspondingly, $\langle uvw \rangle$ denotes a family of crystallographically equivalent directions.

Generally, the Miller indices are determined in the cubic unit cell (edge length $= 1$) depicted in Figure A.1.
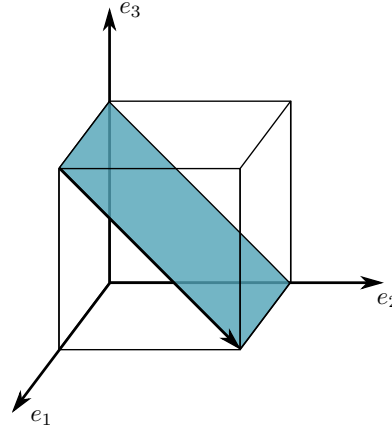
Figure A.1. Cubic unit cell (edge length $= 1$) with cartesian coordinate system (axes e_1, e_2 and e_3)

The indices for a specific crystallographic plane (hkl) are found by the following procedure [30]

1. determine the intersections of the plane with the e_1, e_2 and e_3 axes,

2. take the reciprocals of the found values and

3. find the lowest set of integers with the same ratio.

This procedure is exemplarily shown in the following for the plane that is drawn in Figure A.1:

1. intersections of the plane with the axes e_1, e_2 and e_3: ∞, 1 and 1

2. reciprocals of the found values: $\frac{1}{\infty} = 0$, $\frac{1}{1} = 1$ and $\frac{1}{1} = 1$

3. lowest set of integers with the same ratio: 0, 1 and 1.

Consequently, the plane in Figure A.1 is denoted by (011). It is noteworthy that the Miller index notation of a plane coincides with its normal vector. The family of planes that are crystallographically equivalent to (011), i.e. {011}, is obtained by perturbation of the Miller indices and reads:

$$\{011\} \mathrel{\widehat{=}} (011),\ (01\bar{1}),\ (101),\ (10\bar{1}),\ (110) \text{ and } (1\bar{1}0) \tag{A.1}$$

where per convention $\bar{1} = -1$. Here, only half of the possible perturbations are listed since the negative of a planes index notation denotes the same plane (i.e. $(011) \mathrel{\widehat{=}} (0\bar{1}\bar{1})$ etc.).

The crystallographic directions are determined directly by the lowest set of integers of their vectorial components in the e_1, e_2 and e_3 base. The direction that is shown in Figure A.1 is consequently described by $[01\bar{1}]$. The crystallographically equivalent directions, i.e. $\langle 01\bar{1} \rangle$, are given by

$$\begin{aligned} \langle 01\bar{1} \rangle \mathrel{\widehat{=}} & [01\bar{1}],\ [011],\ [0\bar{1}1],\ [0\bar{1}\bar{1}], \\ & [10\bar{1}],\ [101],\ [\bar{1}01],\ [\bar{1}0\bar{1}], \\ & [\bar{1}10],\ [110],\ [1\bar{1}0] \text{ and } [\bar{1}\bar{1}0]. \end{aligned}$$

While the Miller index notation gives a clear and unified description of crystallographic planes and directions, it has to be kept in mind, that it is dimensionless. Thus, the lattice parameters have to be considered to apply the Miller index notation to a specific crystal. With a being the unit cell base length for a specific lattice and c/a being its potential tetragonality, directions read $[ua\ va\ wc]$ and plane normals read $(h/a\ k/a\ l/c)$.

A.2 Miller-Bravais index notation for hexagonal lattices

Crystallographic planes and directions in hexagonal lattices are commonly described by use of the four digit Miller–Bravais notation [30] described in the following. For this, a four axes coordinate system is defined, see Figure A.2.
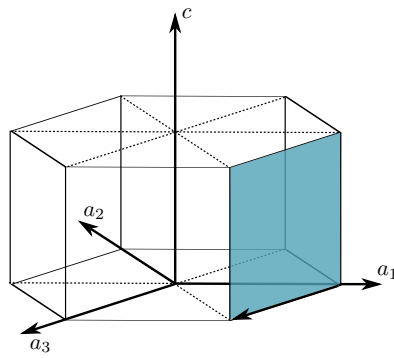
Figure A.2. Hexagonal unit cell with four axes coordinate system (axes a_1, a_2, a_3 and c). The a_1, the a_2 and the a_3 axes lie in the basal plane of the hexagonal unit cell and are 120° apart. The c axis is perpendicular to the a_1, a_2 and a_3 axes.

The unit cell that is depicted in Figure A.2 has an edge length of 1. A plane in this hexagonal unit cell is written as $(hkil)$ and a family of crystallographically equivalent planes is written as $\{hkil\}$ respectively. Further, a crystallographic direction is denoted by $[uvtw]$ whereas a family of crystallographically equivalent directions is denoted by $\langle uvtw \rangle$.

Determining the four Miller–Bravais indices that describe a crystallographic plane follows the same three steps as in the Miller index notation for cubic lattices (see Section A.1), i.e.

1. determine the intersections of the plane with the a_1, a_2, a_3 and c axes,

2. take the reciprocals of the found values and

3. find the lowest set of integers with the same ratio.

The index notation of the plane that is drawn in Figure A.2 is thus derived by:

1. intersections of the plane with the axes a_1, a_2, a_3 and c: 1, −1, ∞, ∞

2. reciprocals of the found values: $\frac{1}{1} = 1$, $\frac{1}{-1} = -1$, $\frac{1}{\infty} = 0$ and $\frac{1}{\infty} = 0$

3. lowest set of integers with the same ratio: 1, -1, 0 and 0

and consequently reads $(1\bar{1}00)$. The corresponding group of crystallographically equivalent planes $\{1\bar{1}00\}$ (i.e. the prismatic planes) reads

$$\{1\bar{1}00\} \triangleq (1\bar{1}00),\ (10\bar{1}0)\ \text{and}\ (01\bar{1}0).$$

Since the three axes in the basal plane, i.e. a_1, a_2 and a_3, are not linearly independent, it is not straightforward to write down the Miller-Bravais index notation of a crystallographic direction in a hexagonal lattice. In a first step, the translations U, V and W parallel to the axes a_1, a_2 and c that produce the given direction are determined. From U, V and W, the Miller–Bravais indices u, v, t and w of the direction $[uvtw]$ can be derived [30] by

$$u = (2U - V)/3, \quad v = (2V - U)/3, \quad t = -(u + v) \quad \text{and} \quad w = W.$$

The direction given in Figure A.2, can be described by translations $U = -1$, $V = -1$ and $W = 0$ along axes a_1, a_2 and c. Thus, the Miller-Bravais indices read

$$u = (-2 + 1)/3 = -1/3, \quad v = (-2 + 1)/3 = -1/3, \quad t = -(u + v) = 2/3 \quad \text{and} \quad w = W = 0,$$

i.e. the direction is described by $1/3[\bar{1}\bar{1}20]$. The group of crystallographically equivalent directions $1/3\langle\bar{1}\bar{1}20\rangle$ reads

$$1/3\langle\bar{1}\bar{1}20\rangle \triangleq 1/3[\bar{1}\bar{1}20],\ 1/3[\bar{1}2\bar{1}0]\ \text{and}\ 1/3[2\bar{1}\bar{1}0]. \tag{A.2}$$

While the four digit Miller–Bravais notation enables a comprehensible description of crystal symmetries, most practical applications require the crystallographic planes and directions to be written in terms of cartesian coordinates. Figure A.3 shows the hexagonal coordinate system of the Miller–Bravais notation together with a cartesian coordinate system. In this, the a_1 axis is defined to be parallel to the e_1 axis and the c axis is defined to be parallel to the e_3 axis.

With this alignment of the coordinate systems, the crystallographic directions $[uvtw]$ and planes $(hkil)$ in a hexagonal lattice can be transformed to cartesian coordinates by the relations in Table A.1 that were obtained by basic trigonometry.

All here shown notations of crystallographic planes and directions in a hexagonal unit cell are dimensionless per definition. To incorporate the length scale of a specific lattice, the respective lattice parameters have to be considered. With a being again the base length of the unit cell of a specific lattice and c being its height, directions read $[ua\ va\ ta\ wc]$ and planes read $(h/a\ k/a\ i/a\ l/c)$.
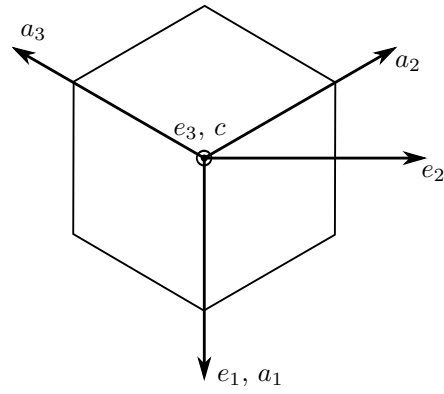
Figure A.3. Overlayed depiction of the hexagonal coordinate system (a_1, a_2, a_3 and c) and a cartesian coordinate system (e_1, e_2 and e_3). View from positive c/e_1 direction.

Table A.1. Transformation relations from Miller-Bravais notation to cartesian coordinates.

Directions:

$$e_1 = \frac{3}{2}u$$

$$e_2 = \frac{\sqrt{3}}{2}(u + 2v)$$

$$e_3 = w$$

Planes:

$$e_1 = h$$

$$e_2 = \frac{1}{\sqrt{3}}(h + 2k)$$

$$e_3 = l$$